Imperial College
London

Characterisation of self-guided laser wakefield accelerators to multi-GeV energies

Kristjan Põder

September 2016

Submitted in partial fulfillment of the requirements for the degree of Doctor of Philosophy of Imperial College London

Department of Physics
Imperial College London
Prince Consort Road
London SW7 2BZ

Abstract

This thesis details experimental and theoretical work in the field of self-guided laser wakefield accelerators, characterising various aspects of the machine related to the driver laser and electron beam generation.

The spectral changes to the laser pulse driving a laser wakefield accelerator were characterised. It was found that the spectral blueshift is directly correlated to the length of the plasma cavity. Spectral phase changes of the driver pulse were measured to dramatically alter the interaction. Positive second order spectral phase was measured to increase electron beam energy, its charge and the spectral blueshifting undergone by the driver pulse.

The suppression of self-injection in laser wakefield accelerators operating in the highly non-linear bubble regime was observed. The use of ionisation impurity to pre-inject electrons into the plasma cavity was measured to alter the fundamental properties of the electron beam. Through particle-in-cell simulations it was shown that this effect arises from the repulsive electrostatic force from the beam load, preventing sufficient transverse momentum gain of sheath electrons.

Record electron beam energies of nearly 3 GeV were measured in the self-injecting, self-guiding regime of laser wakefield accelerators. These results were obtained at higher than expected plasma densities and are thought to be a direct result of increased energy coupling due to the use of a much longer main focussing optic. Very stable injection in the self-injection regime was observed allowing for experimental measurements of peak accelerating field within the bubble. The field $E_z = (590 \pm 180)\,\mathrm{GV\,m^{-1}}$ is the highest value of the electric field reported.

The efficacy and long-term stability of self-guided, self-injecting laser wakefield electron acceleration was evaluated. Highest sustained laser energy to electron beam energy conversion efficiency of nearly 3% was measured. It was also shown the self-injection yields higher overall efficiencies than ionisation induced injection. Stability of injection and acceleration over more than half a thousand consecutive shots was studied and found to be directly dependent on the stability of the driving laser.

Contents

List of Figures

List of Tables

Acknowledgements

The past four years have been the most interesting and testing time throughout my life. I've learned an immeasurable amount of new things and had to relearn some old items as well. Many thanks to Zulfikar, for pointing me in the right way and allowing me to stumble towards the correct answer many a times. Thanks to Stuart for the countless wanders into the office and asking about what I was doing – many of these conversations showed things in a light I had not seen before.

Thanks to (soon to be Dr) Fash for being a good neighbour in the office and on experiments, conferences and summer schools. The particularly dry sense of humour, cynicism and infallible interest in all things Augustus Caeser have been a source of endless fun. Thanks to Nelson for buying me countless electronics components and steadily guiding me towards a slightly more complete understanding of electronics and CAD design. Thanks to Juff, George, Savio, Elias, Will, Nick, Matt, Charlie, and many others for the pleasure of having worked with you. Dan and Steve, the transition of the Prince from what it used to be to what it is now was tricky but we got through it.

Finally, the last four years frame my transition from a bachelor to a (nearly) married man and I am forever in debt to Kris (yes, we have the same name!). You've managed to push me just enough at all times to get me through this and I'm a different man now thanks to you. I would not be anywhere near this position without my parents and the continual support and belief in me.

Author's role

The author of this work performed all the measurements presented in this thesis as part of a larger experimental team, apart from where otherwise credited.

In the experiments performed in Gemini during 2012, the author built and commissioned the forward line diagnostics. Additionally, the author performed daily laser alignment.

During the experimental campaign yielding the data presented in Chapter 5, the author performed the role of Target Area Operator, overseeing day-to-day laser alignment and experimental procedures while also being responsible for the safety of the entire experimental team.

The author participated extensively in planning for the experiment presented in Chapter 6. The main beam layout incorporating the $f/40$ along with the forward line optical layout and vacuum chambers were designed by the author. The new gas delivery system aiming to increase reproducibility was designed with input from N. Lopes and built by the author. The role of the Target Area Operator during the experimental campaign was undertaken by the author.

All PIC simulations presented in this thesis were set up and run by the author on the Imperial College cx1 and cx2 clusters. For the FLASH simulations, invaluable help from N. Dover helped start the simulation campaign, with the author providing the final simulation geometry.

CHAPTER 1
Introduction

THE ADVENT OF FIRST PARTICLE ACCELERATOR changed the field of physics forever. With particle energies reaching far beyond those available to Rutherford,[1] the very fundamental constituents of matter have been probed with precision unimaginable even a mere half-century ago. Driven by the development of particle accelerators, particle physics and the associated Standard Model[2] have achieved unprecedented success as a predictive theory, crowned by the success of identifying the Higgs boson a few years ago.[3] With even larger machines proposed to further test and explore physics beyond the standard model,[4–6] particle accelerators are set to carry on expanding and revolutionising the understanding of Nature by mankind.

However, particle accelerators are not only tools to quench Man's infinite curiosity towards Nature, but have also revolutionised the way we understand ourselves. Since Röntgen's first x-ray picture of his wife's hand, different methods of looking deeper inside our body have been developed with the help from particle accelerators. These have allowed the discovery and cure of many diseases and have played a major role in extending the average lifespan of people by more than 30 years, equivalent to a generation. Today, particle accelerators are employed in ever expanding fields in medicine, including radiotherapy to kill tumours, isotope productions for Positron Emission Tomography studies and equipment sterilisation.[7]

With ever-growing and changing requirements from accelerators, the variety of dif-

[1] E. Rutherford, Philosophical Magazine Series 6 **21**, 1911.
[2] T. Shears, *Phil Trans R Soc A* **370**, 2012.
[3] G. Aad *et al*, *Phys Rev Lett* **114**, 2015.
[4] *The Internatioal Linear Collider Technical Design Report*. Tech. rep. ILC, June 2013. URL: https://www.linearcollider.org/ILC/Publications/Technical-Design-Report.
[5] *A Multi-TeV Linear Collider based on CLIC Technology: CLIC Conceptual Design Report*. Tech. rep. CERN-2012-007. CERN, Jan. 2012. URL: http://project-clic-cdr.web.cern.ch/project-CLIC-CDR/CDR_Volume1.pdf.
[6] A. Ball *et al.* "Future Circular Collider Study". In: *Future Circular Collider Study Kickoff Meeting*. Feb. 2014.
[7] W. H. Scharf. *Biomedical particle accelerators*. American Institute of Physics, 1993.

ferent machines and concepts spans more than a dozen variants by now, with more than 30 000 particle accelerators in operation worldwide. However, for the last 40 years the energy frontier has been pushed to higher center-of-mass energies by building larger machines. The current pinnacle is the Large Hadron Collider, filling a tunnel of 27 km circumference under the border of France and Switzerland. Plans for the International Linear Collider (31 km[4]) and the Compact Linear Collider (48 km[5]) carry on this trend. With obvious complications arising from such vast devices, alternatives to decrease size of the machines by allowing higher accelerating gradients are being increasingly pursued. As one of the most promising options, the field of compact plasma-based accelerators has evolved from a conceptual paper in 1979 to a vibrant research community.[1]

1.1 Particle accelerators

At the heart of the quest for high energy particles, and thus particle accelerators, lies the quantum mechanical principle of corpuscular and wave-like duality of all matter, formulated by de Broglie in 1924.[8] This is contained in the famous expression $\lambda = h/p$, where λ is the de Broglie wavelength and p the momentum of a particle; $h = 6.62 \times 10^{-34}\,\mathrm{J\,s}$ is Planck's constant. Thus all matter behaves as a wave whose wavelength is inversely proportional to its momentum. This is the underlying reason driving physicists to higher particle energies – a smaller wavelength allows for finer resolution and more detailed measurements.

Most elementary particles do not exist as free particles in Nature. This fact leads to the other reason to pursue higher particle energies – the famous energy and mass equivalence principle by Einstein. Expressed as $\mathcal{E} = mc^2$ where $\mathcal{E}$ is collision energy, m is rest-mass and $c = 299\,792\,458\,\mathrm{m\,s^{-1}}$ is the speed of light in vacuum, this Equation states that energy can be converted into mass and vice-versa. Thus in order to create exotic particles, the energy of the accelerated particles must be more than the rest-mass of the new entity. This is why the discovery of particles has progressed from the lighter to the heavier, as the maximum centre-of-mass energy available has increased.

The first accelerator was constructed by Cockroft and Walton in 1930[9] relying on the principle of charged particles gaining energy by moving from a higher potential to a lower one. This can be expressed as $\Delta\mathcal{E} = q\,[\Phi(r_{\mathrm{fin}}) - \Phi(r_{\mathrm{in}})]$, where $\Delta\mathcal{E}$ is the change of energy of the particle, q is its charge and $\Phi(r_{\mathrm{in}})$ and $\Phi(r_{\mathrm{fin}})$ are the initial and final

[1] If the length of a Wikipedia entry is not a measure of the success of a research field, then a CERN accelerator school dedicated to the topic certainly is.

[8] L. V. de Broglie, *Ann. de Phys.* **3**, 1925.

[9] J. D. Cockcroft *et al*, *P Roy Soc A: Math Phy* **129**, 1930.

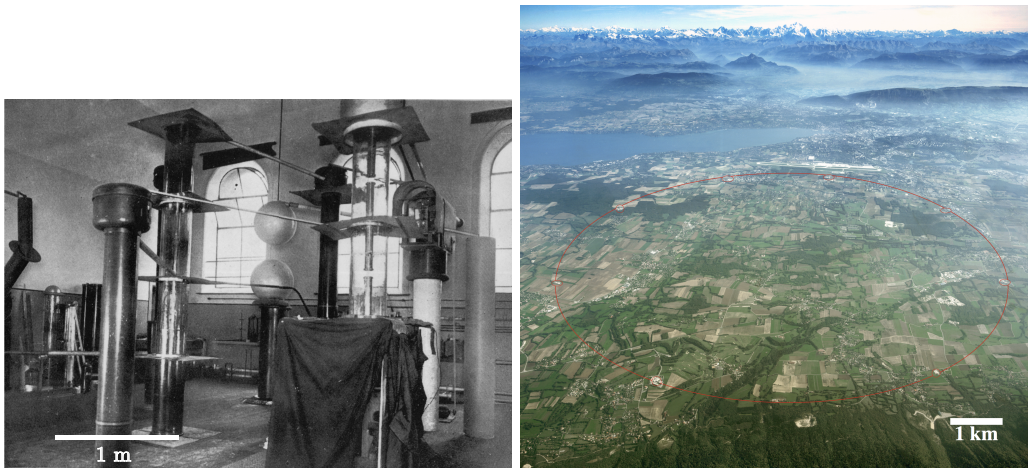

(a) Cockcroft and Walton, 1932 *(b) Large Hadron Collider, 2009*

Figure 1.1: *The first accelerator constructed in the Cavendish laboratory in Cambridge by Cockcroft and Walton in 1932 is shown in Panel (a) and an aerial view of Geneva, with an outline of the Large Hadron Collider is in Panel (b). Images from Refs 10 and 11.*

electrostatic potentials, respectively. As the electric field is defined as $\mathbf{E} = -\nabla\Phi$, the acceleration can be seen to depend on the strength of the accelerating electric field.

The very first machine built by Cockroft and Walton achieved a potential difference of 300 kV,[9] with an improved version of the apparatus allowing for $\Delta\Phi = 800\,\mathrm{kV}$ in 1.83 m.[10] This gives an electric field of $E = 4.37 \times 10^5\,\mathrm{V\,m^{-1}}$. A picture of the device is shown in Figure 1.1a. Since then the progress in increasing the accelerating gradient has been tremendous. Novel technologies have been implemented, the most important of which are phase synchronisation[12,13] and strong focussing.[14,15] Radio frequency cavities, along with other technological and conceptual innovations, have allowed the maximum particle energy to grow almost exponentially with time. Such progress has lead to the construction of the Large Hadron Collider, the outline of which is shown in Figure 1.1b. The Large Hadron Collider accelerats protons up to energies of 7 TeV; Cockcroft and Walton's machine delivered protons with energies of 710 keV.[2] The rapid rise in particle energies was first observed by accelerator pioneer Livingston, compiling the now famous Livingston plot in his 1954 book on accelerators.[16] Shown in Figure 1.2a, the dashed

[10] J. D. Cockcroft *et al*, *P Roy Soc A: Math Phy* **136**, 1932.
[12] V. I. Veksler, J. Phys. **9**, 1945.
[13] E. M. McMillan, *Phys Rev* **68**, 1945.
[14] N. Christofilos. *Focussing system for ions and electrons.* US Patent 2,736,799. 1956. URL: http://www.google.co.uk/patents/US2736799.
[15] E. D. Courant *et al*, *Phys Rev* **88**, 1952.
[2] The SI prefix tera stands for 10^{12}, so 7 tera-electronvolts is 7 000 000 000 000 electronvolts. The prefix kilo is a factor of 10^3, so 710 keV is 710 000 electronvolts.
[16] S. M. Livingston. *High-energy accelerators.* Interscience Publishers, 1954.

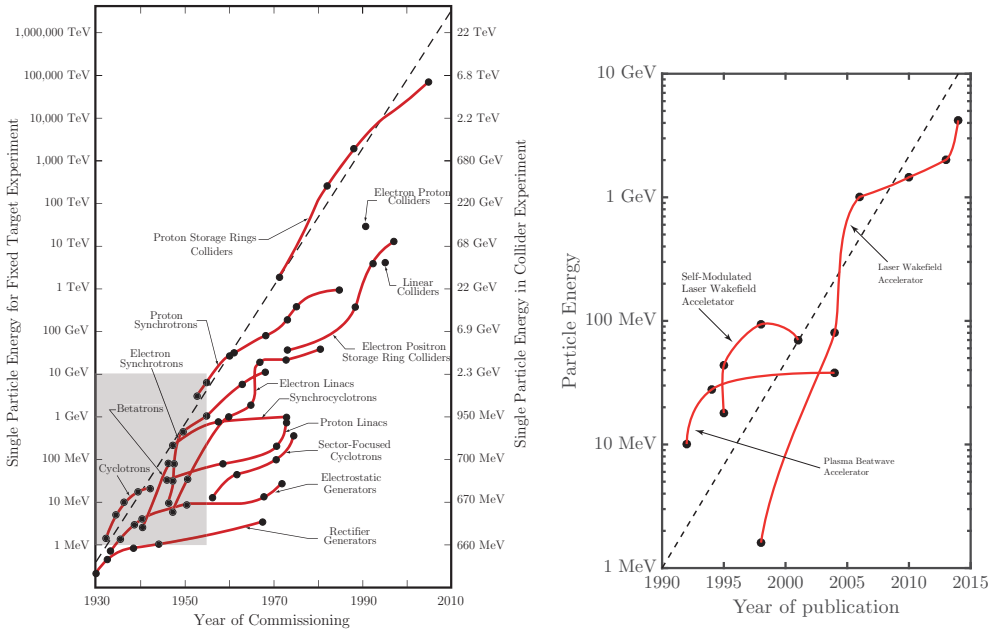

(a) Conventional accelerators *(b) Laser-plasma accelerators*

Figure 1.2: *Livingston plot showing the evolution of maximum particle energy with time for conventional accelerators (a) and laser-plasma based accelerators (b). The progress shown in Panel (b) is equivalent to the the shaded area in Panel (a). The energy axes in Panel (a) are plotted in terms of laboratory energy of particles colliding with a proton at rest on the left and particle energy in a collider setup on the right for a given centre-of-mass energy. The succession of different technologies has driven the progress in both fields. Figure in Panel (a) adapted from Ref 18.*

line shows a tenfold increase in energy every six to eight years,[17] a trend that has been closely followed for many decades since.[18] From Figure 1.2a, it is also clear that the continual progress has largely been due to adapting new technologies.

While the continuous growth of available particle energy is clearly seen in Figure 1.2a, it is also obvious that no new technological innovations have occurred in the last few decades. Instead, continual progress has been driven by building larger facilities. Both these factors have increased the cost[3] of "centre-of-mass GeV of protons" by about a factor of 10 in the forty years up to 2001.[19] The economical impact of constructing a new, energy frontier redefining accelerator facility, has now become almost unpalatable.

The fundamental reason behind the ever-increasing cost of conventional, radio-frequency based accelerators is the breakdown limit of the accelerator cavity. Increasing the accelerating gradient is not possible beyond a certain point due to the field becom-

[17] W. K. Panofsky, SLAC Beam Line , 1997.
[18] A. Chao *et al*, eConf **C010630**, 2001.
[3] Not inflation corrected. Accounting for inflation would increase this by another factor of 6.
[19] M. Tigner, *Phys Today* **54**, 2001.

ing strong enough to strip electrons off atoms that make up the cavity walls. This limits the maximum electric fields to $\sim 100\,\mathrm{MV\,m^{-1}}$ in radio-frequency accelerators.[5,20] Such limitations have motivated the community of accelerator physicists to search for alternative, much higher gradient solutions for new machines.[21]

1.2 Plasma accelerators

As seen above, the main factor driving the cost and size of conventional accelerators is the breakdown limit in the radio-frequency cavity. This happens because the electric fields associated with the accelerating force become large enough to strip off electrons from the atoms making up the structure. So, as the physical limitation is due to the onset of very strong ionisation, why not use a medium which bypasses that limit by already having electrons stripped off the atoms?

Such a medium is a plasma, a quasineutral gas of ions and electrons exhibiting collective effects to external electromagnetic fields. By definition, a fully ionised plasma cannot suffer dielectric breakdown[4] and thus the electric fields that can be supported can be much higher than in radio-frequency cavities. Obviously, the electric field cannot be increased infinitely in a plasma either and there do exist limitations to the peak field, such as the cold wavebreaking limit. However, for a typical plasma density of $n_e \simeq 1 \times 10^{18}\,\mathrm{cm^{-3}}$, the maximum electric field that can be supported is $\sim 100\,\mathrm{GV\,m^{-1}}$, about a thousand times higher than achievable in radio-frequency devices.

The principle behind a laser driven plasma accelerator[22] is the fact that as a laser pulse propagates in a plasma, the electrons feel a force that pushes them away from regions of high intensity. This is somewhat similar to a boat passing in water – the front of the boat pushes water away. After the laser has passed, the electrons try to return to their positions, again much like what happens at the stern of a boat. Completing the analogy, a wake is set up behind the laser pulse, travelling along with the laser plasma. An example of such a plasma wave is shown in Figure 1.3. Switching the water based analogy to larger waves, such as those exploited by surfers, an electron in a wakefield can gain energy from the wave structure as it travels along with it.

Plasma accelerators can also be driven by particle beams. Proposed in 1985,[23]

[20] A. Grudiev *et al*, *Phys Rev Spec Top-Ac* **12**, 2009.
[21] R. W. Aßmann. "Review of Ultra high-gradient acceleration schemes, results of experiments". In: *Proceedings of EPAC 2002*. 2002.
[4] Note this is not the case for a partially ionised plasma where additional ionisation can occur.
[22] T. Tajima *et al*, *Phys Rev Lett* **43**, 1979.
[23] P. Chen *et al*, *Phys Rev Lett* **54**, 1985.

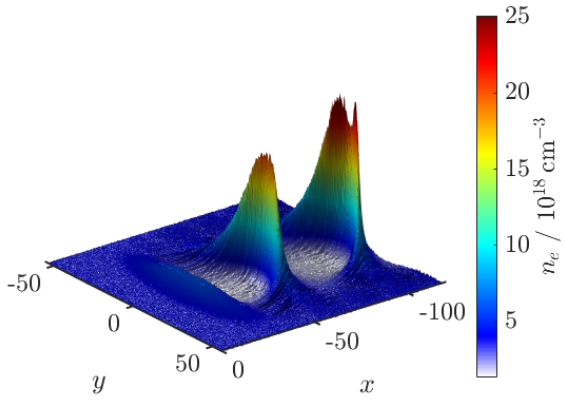

Figure 1.3: *Plasma wave set up by a laser pulse travelling through a plasma. The laser pulse intensity is* $9.5 \times 10^{18}\,\mathrm{W\,cm^{-2}}$*, initial spot size* $w_0 = 31\,\mu\mathrm{m}$ *and pulse length* $\tau = 45\,\mathrm{fs}$*; plasma density is* $n_e = 7.5 \times 10^{17}\,\mathrm{cm^{-3}}$*.*

the electron driven plasma wakefield accelerator[5] was soon demonstrated.[25] The true potential of plasma accelerators was demonstrated recently at the Stanford Linear Accelerator, achieving 42 GeV energy gain in only 85 cm of plasma.[26] The energy gain achieved in less than a metre is identical to the energy of the drive beam, which is accelerated in a conventional 3 km linear accelerator. Experimental work is continuing at the Facility for Advanced Accelerator Experimental Tests at SLAC, with the FLASHForward project soon starting at DESY, Germany.[27] Additionally, the AWAKE experimental campaign will launch soon at CERN, examining the possibility to drive a plasma accelerator with a long proton bunch.[28]

Further highlighting the vast potential of plasma accelerators, Figure 1.4 shows an aerial photo of the Rutherford Appleton Laboratory in Oxfordshire, UK, home to two multi-gigaelectronvolt electron accelerators. One of them is Diamond, a 3 GeV electron synchrotron lightsource with a storage ring diameter of 178 m costing 260 million pounds.[29] The other one is the Gemini laser, with a cost of £5m and housed in a small building, yielding multi-gigaelectronvolt electron beams in merely 2 cm acceleration distance.[6]

[5] Although the concept of acceleration in electron beam driven plasma waves was apparently proposed by Fainberg in 1956[24]

[25] J. B. Rosenzweig *et al*, *Phys Rev Lett* **61**, 1988.

[26] I. Blumenfeld *et al*, *Nature* **445**, 2007.

[27] DESY. *The FLASHForward Project.* URL: https://vi-pwfa.desy.de/e192843/ (visited on 09/18/2016).

[28] R Assmann *et al*, *Plasma Phys Contr F* **56**, 2014.

[29] Diamond. *Diamond facts.* URL: http://www.diamond.ac.uk/Home/About/FAQs/General.html (visited on 09/18/2016).

[6] Cf. Chapter 7 of this thesis.

Figure 1.4: *Aerial view of the Rutherford Appleton Laboratory. Both the Diamond lightsource and the building housing the Gemini laser are shown. Image from Ref 29.*

1.2.1 From beat-wave through self-modulation to pure LWFA

The Livingston plot for laser wakefield accelerators in Figure 1.2b shows that progress and higher particle energies are reached as a succession of novel technologies, similarly to the conventional field. The seminal work by Tajima and Dawson outlined the theory of the laser wakefield accelerator, where a resonant laser pulse drives a plasma wave.[22] For this, the pulse length has to be of the order of an electron plasma wavelength, $c\tau \sim \lambda_p$. However, due to the early stages of laser development, such ultrashort pulses were not available. Another mechanism that was also discussed in the work by Tajima and Dawson had been previously analysed by Rosenbluth and Liu.[30] In what became known as plasma beat wave accelerator (PBWA) two counter propagating laser pulses with frequencies $\omega_1 - \omega_2 = \omega_p$ set up a large amplitude plasma wave. However, as the wave grows it becomes dephased from the beats due to relativistic plasma frequency change, limiting acceleration. Despite this, electron beams with energy gains up to $\sim 40\,\mathrm{MeV}$ have been observed.[31–34]

[30] M. Rosenbluth *et al*, *Phys Rev Lett* **29**, 1972.
[31] Y Kitagawa *et al*, *Phys Rev Lett* **68**, 1992.
[32] C. E. Clayton *et al*, *Phys Plasmas* **1**, 1994.
[33] S. Y. Tochitsky *et al*, *Phys Rev Lett* **92**, 2004.
[34] C. Joshi, *Phys Plasmas* **14**, 2007.

The development of laser technology brought about higher intensities and shorter pulse lengths. With the pulse durations still not at the required femtosecond[7] range, the self-modulated laser wakefield accelerator was proposed.[35,36] Here, an ultrahigh intensity laser pulse drives a plasma wave, which in turn modulates the envelope of the initial pulse and breaks it into beamlets. This process is enhanced at higher plasma densities, but operating in the high n_e regime severely limits maximum energy gains through dephasing. Nevertheless, experiments accelerating large amount of charge up to 100 MeV have been performed.[37–40]

The advent of chirped pulse amplification and mode-locked oscillators[8] gave researchers access to pulse lengths comparable to plasma wavelength, unlocking the full potential of laser wake field accelerators. Here, a very intense pulse with length $L \sim \lambda_p/2$ is used to drive a large amplitude relativistic plasma wave[22,41,42]. Propagating in an underdense plasma, the intense laser pulse expels electrons from the space occupied by the pulse itself via the ponderomotive force. A large electrostatic force pulls the electrons back and a plasma wave moving with a phase velocity of the laser group velocity is set up.

Successful early experiments date back to 1995, when Hamster *et al* inferred radial laser driven plasma currents from the measured $\omega_p/2\pi = 4.6\,\mathrm{THz}$ radiation.[43] Detailed measurements of the plasma wave amplitude were soon performed.[44,45] Early acceleration experiments in the laser wakefield regime were observed to yield electrons with quasi-thermal spectra.[45–47]

The continuing increase in laser powers meant the generation of non-linear plasma waves became realistic with the use of a single driving pulse. The non-linearities arise due to a relativistic effect, namely the mass increase of plasma electrons. In the extreme case, the laser intensity is high enough to expel all electrons and form an ion cavity;[9]

[7] Femto is the SI prefix for 10^{-15}. The ratio of 150 femtoseconds to one heartbeat is the same as that of one heartbeat to the age of mankind.

[35] E. Esarey *et al*, *Phys Rev Lett* **65**, 1990.
[36] J. Krall *et al*, *Phys Rev E* **48**, 1993.
[37] K. Nakajima *et al*, *Phys Rev Lett* **74**, 1995.
[38] A. Modena *et al*, *Nature* **377**, 1995.
[39] D. Gordon *et al*, *Phys Rev Lett* **80**, 1998.
[40] V. Malka *et al*, *Phys Plasmas* **8**, 2001.

[8] Cf. Section 3.1.1 and references therein.

[41] L. Gorbunov *et al*, Soviet Physics JETP **66**, 1987.
[42] P. Sprangle *et al*, *Appl Phys Lett* **53**, 1988.
[43] H Hamster *et al*, *Phys Rev Lett* **71**, 1993.
[44] J. R. Marquès *et al*, *Phys Rev Lett* **76**, 1996.
[45] C. W. Siders *et al*, *Phys Rev Lett* **76**, 1996.
[46] F. Amiranoff *et al*, *Phys Rev Lett* **81**, 1998.
[47] Y. Kitagawa *et al*, *Phys Rev Lett* **92**, 2004.

[9] Extending this regime to the boat in water analogy is slightly more difficult.

known as the bubble regime.[48,49] Successful experiments soon followed with demonstrations of narrow divergence and peaked energy spectra.[50–52] Dubbed the "dream beam", these results gained widespread attention as they showed that high quality electron beam acceleration is possible in laser wakes. Since these groundbreaking results, the energy frontier has been extended up to 4 GeV.[53] Some key points are shown in Figure 1.2b; the results for these datapoints cover the major steps in energy.[46,50,53–56]

1.2.2 Current challenges

Although the energy frontier of LWFA has been pushed beyond 4 GeV, research continues into many issues such as stability of the acceleration, injection, tunability and possibility of staging acceleration.

Stability

The issue of stability has seen widespread attention, with experimental work having shown the importance of target choice[57] and somewhat obviously, the quality of the laser pulse.[58,59] It is not a completely freestanding issue, though, with the chosen injection method playing a very important part. Stability is investigated in the current work for laser wakefield accelerators driven by a ~ 250 TW laser.

While not directly falling under the definition of stability, further diagnosis of the wakefield and the dynamics of the laser will further the understanding of the laser-plasma interaction. Transverse probing, for example, helps to understand the coupling of poor quality focal spots into plasma,[60] allowing conscious design decisions to be made to improve the energy capture. Characterising the driver laser after the interaction can also yield extra information on what occurred during the process as propagation in the plasma wake imprints spectral signatures onto the laser spectrum. Diagnosis of such spectral changes is presented in Chapter 4.

[48] P. Mora *et al*, *Phys Rev E* **53**, 1996.
[49] A. Pukhov *et al*, *Appl Phys B-Lasers O* **74**, 2002.
[50] S. P. D. Mangles *et al*, *Nature* **431**, 2004.
[51] J. Faure *et al*, *Nature* **431**, 2004.
[52] C. G. R. Geddes *et al*, *Nature* **431**, 2004.
[53] W. P. Leemans *et al*, *Phys Rev Lett* **113**, 2014.
[54] W. P. Leemans *et al*, *Nat Phys* **2**, 2006.
[55] C. E. Clayton *et al*, *Phys Rev Lett* **105**, 2010.
[56] X. Wang *et al*, *Nat Comms* **4**, 2013.
[57] J. Osterhoff *et al*, *Phys Rev Lett* **101**, 2008.
[58] S. P. D. Mangles *et al*, *Plasma Phys Contr F* **48**, 2006.
[59] S. Banerjee *et al*, *Phys Rev Spec Top-Ac* **16**, 2013.
[60] J. M. Cole. "Diagnosis and Application of Laser Wakefield Accelerators". Imperial College London, 2015.

Injection

Apart from striving towards improved stability, perhaps the widest research topic now is the injection of electrons into the accelerating structure. Early work involved injecting external electron bunches.[32,46] There are difficulties associated with this approach, though, as the electron bunches are typically much longer than the wake; the femtosecond nature of plasma waves adds further complications with synchronisation. The first quasi-monoenergetic results[50–52] all relied on self-injection, i.e. some background electrons become trapped in the accelerating phase of the bubble. Theoretical models of self-injection soon followed.[61,62] However, due to the extremely high degree of nonlinearity the exact physics of self-injection is still not fully understood. Despite the lack of accurate theoretical descriptions, with properly matched laser and plasma parameters self-injection is the simplest form of achieving high charge and high quality electron bunches.[63]

Partly due to poor theoretical understanding and a perceived lack of controllability of self-injection alternative methods for injection have been proposed. These include ionisation injection, where ionisation causes electrons to be liberated in the correct place in the bubble[55]; colliding pulse injection, where the beat wave pattern of two pulses pre-accelerates some electrons[64,65]; density transition injection, where the change of plasma wavelength dephases some electrons[66–68]; ponderomotive injection, where a second orthogonal laser pulse pre-accelerates some electrons.[69] For most of these methods, it is required to operate in an intensity regime where self-injection does not occur. This is because most self-injection generated beams are measured to be of lower quality; the alternative injection methods are used to provide higher fidelity beams. We show in Chapter 5 that this requirement can actually be bypassed and self-injection can be suppressed in regimes where it would otherwise occur. The implications of this are far-reaching and can change the design of future laser wakefield accelerators.

Further, while ionisation injection has seen widespread adaptation in recent years, a thorough experimental comparison with self-injection has not been published to date. This is rectified in the current work, with Chapter 6 highlighting some important differences between the two methods.

[61] I. Kostyukov *et al*, *Phys Rev Lett* **103**, 2009.
[62] S. Kalmykov *et al*, *Phys Rev Lett* **103**, 2009.
[63] W. Lu *et al*, *Phys Rev Spec Top-Ac* **10**, 2007.
[64] E. Esarey *et al*, *Phys Rev Lett* **79**, 1997.
[65] J Faure *et al*, *Nature* **444**, 2006.
[66] S. Bulanov *et al*, *Phys Rev E* **58**, 1998.
[67] A Buck *et al*, *Phys Rev Lett* **110**, 2013.
[68] M. Burza *et al*, *Phys Rev Spec Top-Ac* **16**, 2013.
[69] D. Umstadter *et al*, *Phys Rev Lett* **76**, 1996.

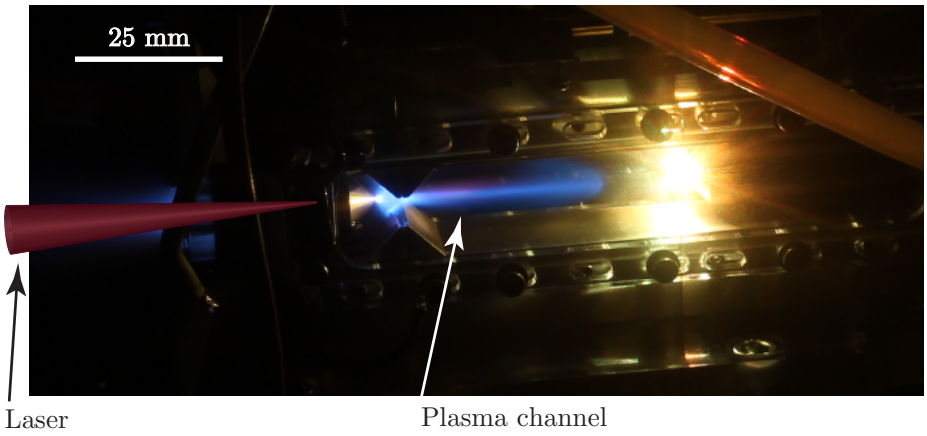

Figure 1.5: *A true colour image of a self-guided laser wakefield accelerator. The direction of laser propagation is schematically shown. The blue channel is the plasma channel created by the self-guided laser; the blue light is from recombination of ions with electrons after the laser has passed.*

Guiding

For maximum acceleration the high intensity interaction should last as long as possible. However, laser beams will not propagate with a small spot size (required for high intensity) for long distance; in fact the intensity that can be reached in vacuum is inversely proportional to the distance it occurs over. This means that laser wakefield accelerators need to impose some form of guiding of the pulse in order to gain as much energy as possible. Due to the properties of plasmas, there is actually a non-linear feedback loop that provides such guiding. Coined self-focussing,[70,71] the plasma responds to high intensity pulses by effectively becoming a focussing lens. This can counterbalance the natural diffraction of the laser pulse and yield stable propagation.[72] External guiding structures can also be used, as a tailored density channel with a minimum on-axis prevents diffraction. This is most often achieved via discharges in capillary channels.[73]

While the highest electron energies to date have been achieved with capillary guiding;[53] some difficulties do arise from their use. For the optimised channel, the hole for the plasma is of comparable size to the laser spot so any small fluctuations in laser pointing can have devastating effects on the guiding structure. Additionally, recent success in imaging the plasma wave itself[74] is impossible in capillary waveguides.

[70] C. Max *et al*, *Phys Rev Lett* **33**, 1974.
[71] G. Z. Sun *et al*, *Phys Fluids* **30**, 1987.
[72] J. E. Ralph *et al*, *Phys Rev Lett* **102**, 2009.
[73] A. Butler *et al*, *Phys Rev Lett* **89**, 2002.
[74] A. Sävert *et al*, *Phys Rev Lett* **115**, 2015.

Such direct measurements are important to understand the laser-plasma interaction as simulations with idealised laser profiles are not sufficient to predict the realistic laser-plasma interaction. Work exploring self-guiding of ultra-intense laser pulses is presented in Chapter 4 in this thesis, demonstrating the effectiveness of guiding. Results presented in Chapter 7 show that self-guided laser wakefield accelerators can actually reach energies comparable to those from externally guided experiments. Further, it is shown that the efficiency can be improved as well.

Efficiency

One of the most important aspects of study is the possibility for staging of multiple laser wakefield stages with an end goal of a large scale collider.[75] A successful demonstration of staging two independent plasma accelerators has recently been completed.[76] However, a capture efficiency of particles on the single percent level from one stage to the next is clearly insufficient for coupling hundreds of stages.[10] Additionally, the efficiency of laser energy to electron beam energy needs to be addressed as currently this is extremely low as well. In order to increase the efficiency, it is imperative to operate in the highly non-linear regime; additional benefits to beam quality further emphasize this point. However, the current thinking suggests that a byproduct of operating in the non-linear regime is self-injection. Work in the current thesis, presented in Chapter 5, shows that this can in fact be suppressed, opening up the prospect of achieving higher efficiencies and better beam quality in staged laser wakefield accelerators.

1.3 Thesis outline

This thesis presents work performed to characterise different aspects of self-guided laser wakefield accelerators in the multi-gigaelectronvolt energy gain regime. The thesis is organised as follows:

Chapter 2 provides a theoretical overview of the concepts underlying the present work.

Chapter 3 describes experimental approaches to realising the work described in this thesis.

Chapter 4 presents experimental measurements of the laser pulse driving the accelerators, looking at the spectral modifications to the pulse and the effects of

[75] W. P. Leemans *et al*, *Phys Today* **62**, 2009.
[76] S. Steinke *et al*, *Nature* **530**, 2016.
[10] Assuming 1.6 nC of charge or 10^{10} electrons at the input to stage 2, only 18 electrons would be captured into stage 7 given a coupling efficiency of 3.5%.

non-perfect compression of the laser pulse. Additionally, characterisation of self-guiding over unprecedented distances is reported.

Chapter 5 describes the suppression mechanism of self-injection in laser wakefield accelerators operating in the highly non-linear regime.

Chapter 6 presents a comparative experimental study between self-injection and ionisation injection. The spectral signatures of alternative injection methods are presented and a characterisation of electron beams is shown, detailing the differences between injection methods.

Chapter 7 details measurements performed with an extended focal length optic, presenting results of multi-GeV electron acceleration in the self-guided, self-injected regime of laser wakefield accelerators employing a 250 TW laser. The stability of the device is analysed, along with with experimental measurements of the accelerating electric field.

CHAPTER 2
Theoretical Background

IN THIS CHAPTER WE WILL REVIEW theoretical aspects underlying the work presented later on in the thesis. We start by describing the ionisation processes and dynamics of atoms in intense laser fields. We then discuss the behaviour of a single electron in an electromagnetic wave. We will look at non-linear effects caused by laser pulses with relativistic intensities. Physics of the fundamental concept underlying laser wakefield accelerators, laser driven plasma waves, will be presented. The laser driven plasma wakefield accelerator is then discussed, with the limitations imposed on the energy gain and efficiency of laser wakefield accelerators presented.

2.1 Ionisation of underdense gas in laser field

Ionisation is the process of atoms changing the number of electrons orbiting them, either gaining an electron to form a negatively charge ion or losing an electron to become a positive ion. This is the fundamental process to create plasmas from initially neutral media by separating electrons from the atoms they orbit such that the electrons become free particles. This is done by transferring a sufficient amount of energy to the bound electrons such that they overcome the Coulomb barrier binding them to the nucleus.

Ionisation by short pulse lasers, in particular, can happen either via multi-photon ionisation,[77] tunnel ionisation[78] or barrier suppression ionisation.[79] The exact mechanism leading to ionisation depends on the ponderomotive potential U_p of the laser[1] and is characterised by the Keldysh parameter[77]:

$$\gamma_K = \sqrt{\frac{E_{\text{ion}}}{2U_p}} = \omega_L \sqrt{\frac{\epsilon_0 m_e c}{2e^2} \frac{E_{\text{ion}}}{I_L}}, \tag{2.1}$$

[77] L. V. Keldysh, Soviet Physics JETP **20**, 1965.
[78] A. M. Perelomov *et al*, Soviet Physics JETP **23**, 1966.
[79] H. R. Reiss, *Phys Rev A* **1**, 1970.
[1] Cf. Section 2.2.2

Ion	E_{ion} (eV)	I_{app} (W cm^{-2})
H^+	13.6	1.4×10^{14}
He^+	24.6	1.5×10^{15}
He^{2+}	54.4	8.8×10^{15}
C^+	11.3	6.4×10^{13}
C^{4+}	64.5	4.3×10^{15}
C^{5+}	392.1	4.4×10^{18}
C^{6+}	490.0	6.4×10^{18}
O^+	13.6	1.4×10^{14}
O^{6+}	138.1	4.0×10^{16}
O^{7+}	739.3	2.4×10^{19}
O^{8+}	871.4	3.6×10^{19}

Table 2.1: *Appearance intensities for a range of ions, calculated with barrier suppression model in Equation 2.2.*

where E_{ion} is the binding energy of an electron and I_L is the laser intensity. The Keldysh parameter effectively expresses the ratio of electron binding energy to the ponderomotive potential. An electron is ionised via multiphoton ionisation for $\gamma_K > 1$, when the ponderomotive potential of the laser is not comparable to the Coulomb potential from the nucleus. This is the case for high laser frequencies and low intensities.

For $\gamma_K < 1$, the laser ponderomotive potential becomes comparable to the binding energy. This occurs for lower laser frequencies and higher intensities. As the laser intensity increases towards this regime, the potential of the oscillating laser field becomes comparable to the Coulomb potential binding electrons to the nucleus. The effective nuclear potential is modified by the field of the laser and is decreased for half of the laser period. This reduction of field increases the probability of quantum tunnelling through the potential barrier and hence this regime is known as tunnelling ionisation.

As the laser intensity is increased further, the Coulomb barrier is reduced until at some point it falls below E_{ion}. At this point the electron will escape spontaneously and thus this regime is known as barrier suppression ionisation. The appearance intensity, where the oscillating laser potential suppresses the Coulomb potential of the nucleus, is given by

$$I_{\text{app}} = \frac{cE_{\text{ion}}^4}{128\pi Z^{*2} e^6}, \tag{2.2}$$

where Z^* is the nuclear charge of the ion created after ionisation. For the simplest case of hydrogen, the binding energy is $E_{\text{ion}} = 13.61\,\text{eV}$ and appearance intensity is $1.4 \times 10^{14}\,\text{Wcm}^{-2}$. This simple model applies reasonably well to a variety of different atoms,[80]

[80] S Augst *et al*, *Phys Rev Lett* **63**, 1989.

with a range of appearance intensities calculated from Equation 2.2 listed in Table 2.1. For laser intensities employed in the present work, of the order of $10^{18}\,\mathrm{W\,cm^{-2}}$, most light gases will be fully ionised before the peak of the laser pulse. Thus ionisation dynamics will be largely neglected henceforth and the peak of the laser pulse is assumed to interact with a fully ionised plasma. Ionisation will be revisited in a later section when relevant to ionisation induced injection.[2]

2.2 Single electron dynamics

In this section, we will look at the interaction of a single electron with the electromagnetic field of a laser pulse. These interactions underpin most of the physics that we observe.

2.2.1 Charged particle motion in electromagnetic field

The Lagrangian for a relativistic charged particle with charge q, moving in a vector potential $\mathbf{A}$ and scalar potential ϕ is given by[81]

$$\mathcal{L} = -mc^2\sqrt{1-\frac{v^2}{c^2}} + q\mathbf{v}\cdot\mathbf{A} - q\phi, \tag{2.3}$$

with m being the rest-mass of the particle and v its velocity. To analyse the particle's motion, we use the Euler-Lagrange equation[82]

$$\frac{\mathrm{d}}{\mathrm{d}t}\frac{\partial\mathcal{L}}{\partial\mathbf{v}} - \frac{\partial\mathcal{L}}{\partial\mathbf{r}} = 0. \tag{2.4}$$

By noting that $\mathbf{A}$ is a function of only position and time, Equation 2.4 simplifies to

$$\frac{\mathrm{d}}{\mathrm{d}t}\left(\mathbf{p} + q\mathbf{A}\right) = q(\nabla\mathbf{A})\cdot\mathbf{v} - q\nabla\phi, \tag{2.5}$$

where $\mathbf{p} = \gamma m\mathbf{v}$ is the kinetic momentum of the particle. Equation 2.4 along with Equation 2.5 provide the definition of conjugate (also known as canonical) momentum:

$$\mathbf{P} \equiv \frac{\partial\mathcal{L}}{\partial\mathbf{v}} = \mathbf{p} + q\mathbf{A}. \tag{2.6}$$

We can now make use of: the vector identity $\mathbf{v}\times\nabla\times\mathbf{A} = (\nabla\mathbf{A})\cdot\mathbf{v} - (\mathbf{v}\cdot\nabla)\mathbf{A}$ and the definition of convective derivative $\frac{\mathrm{d}}{\mathrm{d}t} = \frac{\partial}{\partial t} + (\mathbf{v}\cdot\nabla)$, along with the definitions of $\mathbf{E}$ and $\mathbf{B}$ fields in terms of vector potential $\mathbf{A}$ (cf. Section B.1) to arrive at

[2] Cf. Section 2.5.6

[81] J. D. Jackson. *Classical Electrodynamics*. John Wiley and Sons, 1998.

[82] T. Kibble *et al.* *Classical Mechanics*. Imperial College Press, 2004.

$$\frac{\mathrm{d}\mathbf{p}}{\mathrm{d}t} = q\left(\mathbf{E} + \mathbf{v} \times \mathbf{B}\right) \tag{2.7}$$

which is the well known equation for the Lorentz force. As can be seen, arising from fundamental concepts of Lagrangian mechanics, the Lorentz equation underpins the fundamental interactions between electromagnetic fields and charged particles.

We now analyse the motion of an electron in an infinite plane electromagnetic wave. We proceed by assuming an elliptically polarised, infinite plane electromagnetic wave with vector potential $\mathbf{A} = (\delta A_0 \sin\varphi, (1-\delta^2)^{1/2} A_0 \cos\varphi, 0)$, travelling in the positive z direction.[83,84] Here δ is the polarisation state, with $\delta = \{\pm 1, 0\}$ for linear polarisation and $\delta = \sqrt{2}/2$ for circular polarisation; $\varphi = \omega t - kz$ is the phase of wave. Normalised units[3] are adopted henceforth, with the normalised vector potential defined as $\mathbf{a} = e\mathbf{A}/(m_e c^2)$.

Laboratory frame trajectories of an electron (detailed derivation can be found in Appendix B.2), initially at rest before the arrival of the laser, are given by

$$x = -\delta a_0 \cos\varphi, \tag{2.8}$$

$$y = (1-\delta^2)^{1/2} a_0 \sin\varphi, \tag{2.9}$$

$$z = \frac{a_0^2}{8}\left[2\varphi + (2\delta^2 - 1)\sin 2\varphi\right]. \tag{2.10}$$

It is evident from Equation 2.10 that regardless of polarisation of the wave, the first term in the square brackets increases linearly with time. Physically, this is drift motion, proportional to the pump strength – a charged particle will obtain longitudinal drift momentum in a purely transverse electromagnetic wave. The cycle averaged drift velocity is given by

$$\langle v_D \rangle = \frac{a_0^2}{4 + a_0^2}, \tag{2.11}$$

showing that the longitudinal component becomes relativistic for high pump strength $a_0 > 1$.

For linear polarisation $\delta = 0$ the trajectories reduce to

$$y = a_0 \sin\varphi; \qquad z = \frac{a_0^2}{4}(2\varphi + \sin 2\varphi). \tag{2.12}$$

The lab frame trajectories of an electron for two values of a_0 are depicted in Figure 2.1a, where both x and z scales have been normalised to $1/k_0$. As can be seen, for $a_0 = 0.3$

[83] P. Gibbon. *Short Pulse Laser Interactions with Matter*. Imperial College Press, 2005.
[84] J. N. Bardsley *et al*, *Phys Rev A* **40**, 1989.
[3] Cf. Appendix A.2

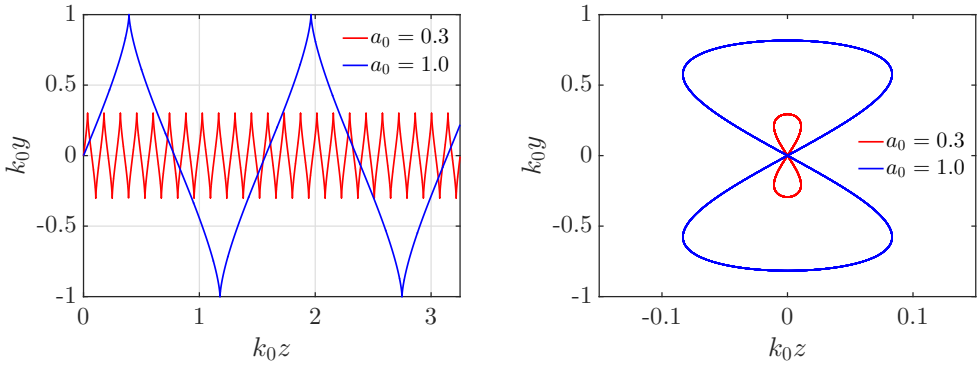

(a) *Charged particle trajectory* ***(b)*** *Charged particle motion in drift frame*

Figure 2.1: *Motion of charged particle in the fields of a laser pulse for two values of* a_0.

the motion of a charged particle is mainly oscillatory in the laser field and dominates over the longitudinal drift. However, as a_0 increases, the longitudinal component of motion becomes more important, resulting in the particle obtaining a large forward momentum.

We can also analyse the trajectories of the particle in its rest frame. Electron orbits in its average rest frame are given by (cf Appendix B.2)

$$x = -\delta \frac{a_0}{\gamma_0} \cos\varphi, \tag{2.13}$$

$$y = (1-\delta^2)^{1/2} \frac{a_0}{\gamma_0} \sin\varphi, \tag{2.14}$$

$$z = (2\delta^2 - 1) \frac{a_0^2}{8\gamma_0^2} \sin 2\varphi, \tag{2.15}$$

where $\gamma_0 = \sqrt{1 + a_0^2/2}$. Again using a linearly polarised pulse with $\delta = 0$ we have the particle trajectories as

$$y = \frac{a_0}{\gamma_0} \sin\varphi; \qquad z = \frac{a_0^2}{8\gamma_0^2} \sin 2\varphi \tag{2.16}$$

Numerical solutions to these equations for two different values of a_0 are depicted in Figure 2.1b, exhibiting the famous "figure-of-eight" motion.

2.2.2 Ponderomotive force on an electron

Equation 2.5 can be simplified by normalising involved quantities (cf. Section A.2) to yield

$$\frac{\mathrm{d}}{\mathrm{d}t}(\mathbf{p} - \mathbf{a}) = c\nabla\phi - c(\nabla\mathbf{a}) \cdot \mathbf{v}. \tag{2.17}$$

The left hand side of Equation 2.17 is again the canonical momentum (cf. Equation 2.6). In normalised units $\mathbf{p} = \gamma\mathbf{v}$, we have

$$\frac{\mathrm{d}\mathbf{P}}{\mathrm{d}t} = c\nabla\phi - c(\nabla\mathbf{a}) \cdot \frac{\mathbf{a}+\mathbf{P}}{\gamma}, \tag{2.18}$$

which is an equation for the rate of change of canonical momentum and can be rewritten as

$$\frac{\mathrm{d}\mathbf{P}}{\mathrm{d}t} = -\frac{c}{\gamma}\nabla\frac{\mathbf{a}^2}{2} - \frac{c}{\gamma}\nabla\mathbf{a}\cdot\mathbf{P} + c\nabla\phi. \tag{2.19}$$

The last term is the electrostatic contribution, which can be neglected as we are looking at the ponderomotive force on a single particle in a laser field. We now consider a laser pulse with a slowly varying envelope both spatially and temporally; that is $\tau \gg 1/\omega_0$ and $w_0 \gg 1/k_0$ with $\omega_0 = |k_0|c$. This allows us to separate out the fast quiver motion and slow scale dynamics of a test electron. We can average Equation 2.19 over a period $\Delta T = 2\pi/\omega_0$ to yield the slow scale dynamics of the electron:

$$\frac{1}{\Delta T}\int_{t_i}^{t_i+\Delta T}\frac{\mathrm{d}\mathbf{P}}{\mathrm{d}t}\,\mathrm{d}t' = -\frac{1}{\Delta T}\int_{t_i}^{t_i+\Delta T}\left(\frac{c}{\gamma}\nabla\frac{\mathbf{a}^2}{2} + \frac{c}{\gamma}\nabla\mathbf{a}\cdot\mathbf{P}\right)\mathrm{d}t'. \tag{2.20}$$

Second term on the right hand side of Equation 2.20 can be integrated by parts, using $\int u'v\mathrm{d}x = uv - \int uv'\mathrm{d}x$, to yield

$$\left\langle\frac{\mathrm{d}\mathbf{P}}{\mathrm{d}t}\right\rangle = -\left\langle\frac{c}{\gamma}\nabla\frac{\mathbf{a}^2}{2}\right\rangle - \left[\frac{c}{\gamma}\nabla\langle\mathbf{a}\rangle\cdot\mathbf{P}\right]_{t_i}^{t_i+\Delta T} + \int_{t_i}^{t_i+\Delta T}\frac{c}{\gamma}\nabla\langle\mathbf{a}\rangle\frac{\partial\mathbf{P}}{\partial t}\,\mathrm{d}t'. \tag{2.21}$$

However, as $\tau \gg \Delta T$, the period average $\langle\mathbf{a}\rangle \simeq 0$ and hence the last two terms in Equation 2.21 can be neglected. What remains is the ponderomotive force on an electron in the field of a relativistic laser pulse[85,86]:

$$\left\langle\frac{\mathrm{d}\mathbf{P}}{\mathrm{d}t}\right\rangle \equiv \mathbf{F}_p = -\left\langle\frac{c}{\gamma}\nabla\frac{\mathbf{a}^2}{2}\right\rangle. \tag{2.22}$$

In the low intensity limit, $a_0 \ll 1$ and $\gamma \simeq 1$, this result reduces to[87,88]

$$\mathbf{F}_p = -m_e c^2\nabla\frac{\langle a^2\rangle}{2}. \tag{2.23}$$

The last equation is similar to a generic equation of a force in terms of a potential. The

[85] B. Quesnel *et al*, *Phys Rev E* **58**, 1998.
[86] E. A. Startsev *et al*, *Phys Rev E* **55**, 1997.
[87] W. L. Kruer. *The Physics of laser plasma interactions*. Westview Press, 1987.
[88] H. A. H. Boot *et al*, Nature **180**, 1957.

ponderomotive potential is defined as $m_e c^2 a_0^2/2$, and a particle in a laser field naturally moves toward areas with lower potential. Thus a particle moving in the ponderomotive potential can typically gain energies of order $m_e c^2 a_0^2/2$. The ponderomotive force can also be thought of as a radiation pressure, again pushing particles towards regions of lower intensity.

The ponderomotive force acts on not only electrons, but all charged particles as to repel them from areas of high intensity. However, as the mass of the ions is much larger than that of electrons they remain immobile for ultrashort laser pulses. Ion motion does become an issue for longer pulse lasers and extremely high intensities. Also, in the slow dynamics regime there is no dependence on polarisation and the plasma response is cylindrically symmetric for radially symmetric pulses. If, however, the pulse is few cycle or very tightly focussed the ponderomotive approximations break down and the plasma response will no longer exhibit spatial symmetry even for radially symmetric pulses.[89]

2.3 Waves in plasmas

Plasmas can support a very wide range of oscillations. These can be divided into electrostatic and electromagnetic waves, with very different wave phenomena depending on plasma temperature, magnetisation or polarisation of incident electromagnetic wave. However, as plasmas we deal with here are mostly cold, non-magnetised and driven by linearly polarised laser pulses, we will not discuss any other wave phenomena apart from electron Langmuir waves.

The simplest oscillation mode in cold, non-magnetised plasma is the Langmuir wave, or plasma electron oscillation. Small perturbations of electron position about their equilibrium act as to set up an electrostatic restoring force, as much heavier ions cannot respond as quickly. This force accelerates electrons back towards their initial position. However, due to the electrons having gained momentum they now overshoot the equilibrium position and an oscillation is set up.

A detailed derivation of the frequency of the resulting oscillation is presented in Appendix B.3. The electron plasma frequency is given by

$$\omega_{pe} = \left(\frac{n_e e^2}{m_e \epsilon_0} \right)^{1/2} \tag{2.24}$$

where $n_e = Z n_i$ is the electron plasma density. It is important to note that frequency

[89] E. N. Nerush *et al*, *Phys Rev Lett* **103**, 2009.

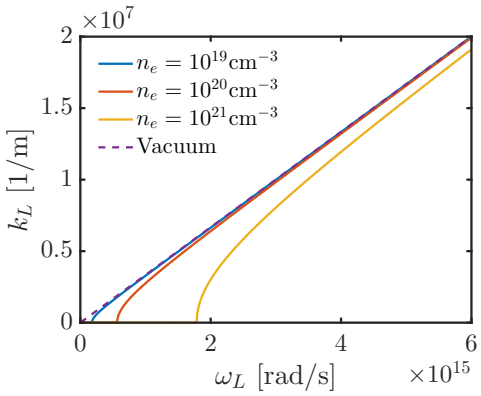

Figure 2.2: *Dispersion relation for electromagnetic radiation in a cold, nonmagnetised plasma. Also shown is the vacuum dispersion relation, $k_L = \omega_L/c$.*

of these waves is independent of wavenumber.[4] This implies that the phase velocity of this perturbation can be chosen arbitrarily, as in laser driven plasma waves where the phase velocity of the wake is equal to the laser group velocity. Lack of dependence on wavenumber also means the group velocity is zero. Hence, these oscillations do not transfer energy or information and merely oscillate about a mean position.

2.3.1 Propagation of laser light in plasma

When a laser pulse[5] is incident on a plasma, its propagation is governed by the dispersion relation for electromagnetic waves in plasmas, derived in detail in Appendix B.4, given by

$$c^2k^2 = \omega_L^2 - \omega_p^2. \tag{2.25}$$

Here, ω_L is angular frequency of the laser and k is the wavenumber of the pulse in a plasma. This dispersion relation is plotted in Figure 2.2 for different plasma densities, along with the vacuum propagation, given by $k_L = \omega_L/c$.

From this expression the phase velocity of the laser light can be calculated as

$$v_p = \frac{\omega_L}{k} = \sqrt{c^2 + \frac{\omega_p^2}{k^2}}. \tag{2.26}$$

Hence the phase velocity of electromagnetic radiation propagating in a plasma is always greater than the speed of light. However, information propagates at the group velocity,

[4] This is true in the cold plasma limit. If temperature of the plasma can no longer be neglected, the Bohm-Gross dispersion relation applies, which has explicit dependence on the wavenumber of the Langmuir wave.[90]

[5] Or indeed any electromagnetic radiation

which is given by

$$v_g = \frac{\partial \omega_L}{\partial k} = \frac{c^2 k}{\omega_L} = \frac{c^2}{v_p}. \tag{2.27}$$

As $v_p > c$ always, group velocity is lower than c. Thus, regardless of the phase velocity of the radiation being larger then c, no information is transmitted at velocities exceeding c.

It is evident from Equation 2.25 that for plasma densities where $\omega_p > \omega_L$, the wavenumber of the laser pulse becomes imaginary. Physically this means that for these densities, electrons in the plasma can oscillate in response to the incident electric field of the laser fast enough to completely cancel the wave out. This means there is no propagation of the radiation into the plasma and it is instead reflected at the boundary. The plasma density corresponding to this cut-off is termed the critical density,

$$n_c = \frac{m_e \epsilon_0 \omega_L^2}{e^2}. \tag{2.28}$$

The critical density is also evident from Figure 2.2; the critical density is the point where the wavenumber becomes zero. The critical density for titanium:sapphire laser systems centred at $\lambda_0 = 800\,\mathrm{nm}$ is $1.4 \times 10^{21}\,\mathrm{cm}^{-3}$.

2.3.2 Wave breaking

Whilst plasmas can support very large electric fields, there exists a limit at which a plasma oscillation will break down. Consider a cold, non-relativistic plasma. We can estimate the magnitude of the largest supported electric field by considering charge separation equal to the plasma density, $n_e = \omega_p^2 m_e \epsilon_0 / e^2$. For a linear plasma wave Gauss' law B.1 then yields $\nabla \cdot E = \omega_p^2 m_e / e$. Assuming a characteristic length of a plasma skin depth c/ω_p, the wavebreaking field[91] can be calculated as

$$E_{\mathrm{wb}} \equiv E_0 = \frac{m_e c \omega_p}{e}. \tag{2.29}$$

If the electric field becomes larger than E_0, neighbouring electron sheets will start to cross and a coherent wave structure will be destroyed. The wavebreaking field is proportional to square root of plasma density and is plotted as the solid black line in Figure 2.3. An engineering formula can be cast to read $E_{\mathrm{wb}} = 96\sqrt{n_e[\,\mathrm{cm}^{-3}]}\,\mathrm{V/m}$ or $E_{\mathrm{wb}} = \sqrt{n_e[\,\mathrm{cm}^{-3}]}\,\mathrm{V/cm}$.

A fully relativistic 1D treatment for a cold plasma is soluble analytically, using non-linear, cold, relativistic fluid equations. The wave breaking limit is then modified

[91] J. M. Dawson, *Phys Rev* **113**, 1959.

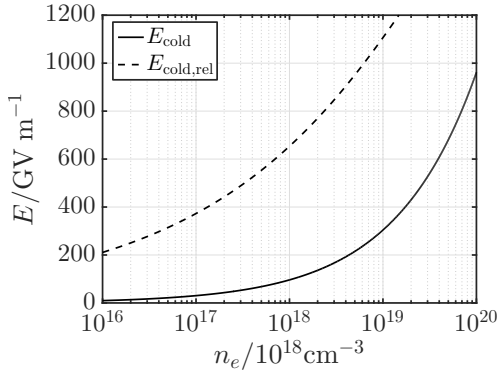

Figure 2.3: *Wavebreaking field as a function of plasma density.*

to read[92]

$$E_{\text{wb,rel}} = \sqrt{2(\gamma_p - 1)} \cdot E_0 \tag{2.30}$$

where γ_p is the relativistic factor associated with the plasma wave, given by $\gamma_p = (1 - v_{\text{ph}}^2/c^2)^{-1/2}$; v_{ph} is the phase velocity of the plasma wave. For laser driven waves, in the low intensity limit, $\gamma_p = \omega_L/\omega_p$. Thus wakes excited by a laser pulse in a tenuous plasma can support much higher fields than E_0. This is illustrated in Figure 2.3, where the cold wavebreaking limit is plotted as the solid black line and the cold relativistic wavebreaking field is sketched with a dashed black line. Thermal effects, such as pressure, will act as to lower the wavebreaking limit and induce incoherence between fluid elements at lower fields, due to fluid elements having a distribution of velocities about the mean.[93]

2.3.3 Laser driven plasma waves

Non-driven electron plasma waves were described in the preceding sections. We now look at electron plasma waves driven by a laser pulse. Consider a radially symmetric laser pulse propagating in an underdense plasma. The ponderomotive force[6] of the laser pulse is thus directed radially outwards, as depicted in Panel (a) in Figure 2.4 by the black arrows. This force pushes all plasma particles outwards, towards regions of lower intensity. The light electrons provide a fast response and move away from the high intensity regions while heavy ions stay immobile for longer. The large charge separation force set up due to this charge imbalance acts as to pull electrons back towards the axis of the laser. This force is depicted in Panel (b) in Figure 2.4 as the green arrows.

[92] A. I. Akhiezer *et al*, *JETP Lett* **3**, 1959.
[93] T. Katsouleas *et al*, *Phys Rev Lett* **61**, 1988.
[6] Cf. Section 2.2.2

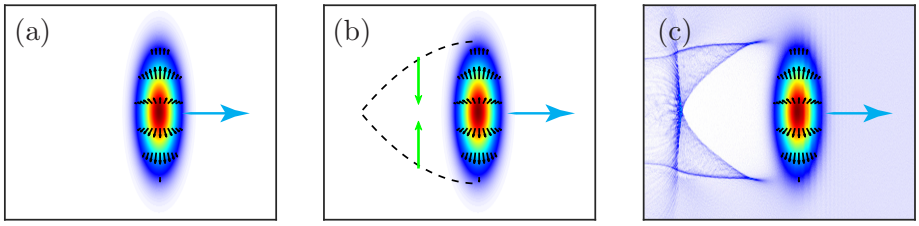

Figure 2.4: *Schematic depicting laser driven plasma wave creation. Panel (a) shows a radially symmetric laser pulse propagating to the right, with the black arrows depicting the ponderomotive force. In Panel (b) the typical path of an electron, after the laser is passed, is shown as the black dashed line; the restoring electrostatic force is shown by the green arrows. Finally, Panel (c) shows the resulting plasma wave.*

The dashed black lines in the same plot depict the path of electrons under this force, thus setting up a plasma wave in the laser's wake. The resulting wakefield is plotted in Panel (c) in Figure 2.4. The phase velocity of this wake is determined by the group velocity of the laser, and in the low intensity limit moves with $\gamma_p = \omega_L/\omega_p$.

Whilst this simple explanation captures the qualitative behaviour of the interaction the exact physics depends heavily on the intensity of the laser. As the normalised vacuum potential $a_0 \to 1$, the motion of the electrons forming the wake becomes relativistic and non-linear effects set in. Secondly, depending on the spot size w_0 of the laser, the motion of the electrons can be mainly one-dimensional ($w_0 \gg c/\omega_p$) or inherently multidimensional ($w_0 \simeq c/\omega_p$). As such, different regimes of applicability can be identified and examined.

3D linear plasma waves

The analytical description of 3D linear plasma waves can be performed using cold fluid equations, i.e. Poisson's equation, the continuity equation and the fluid momentum equation.[41,42] A detailed derivation of equations describing a plasma wave behind a low amplitude laser pulse travelling in an underdense plasma is given in Section B.5.

The plasma wake generated behind a laser pulse is described by

$$\left(\frac{\partial^2}{\partial t^2} + \omega_p^2\right)\frac{n_1}{n_0} = c^2\nabla^2\frac{a^2}{2}, \tag{2.31}$$

$$\left(\frac{\partial^2}{\partial t^2} + \omega_p^2\right)\phi = \omega_p^2\frac{a^2}{2}. \tag{2.32}$$

[41] L. Gorbunov *et al*, Soviet Physics JETP **66**, 1987.
[42] P. Sprangle *et al*, *Appl Phys Lett* **53**, 1988.

It is evident that this is an equation of an undamped driven simple harmonic oscillator. As per the qualitative explanation, the driving term is gradient of the ponderomotive force of the laser pulse. The restoring force is provided by the charge imbalance. The natural frequency of this oscillation is the electron plasma frequency ω_p. Hence, the wake excited by a laser pulse travelling in an underdense plasma is a Langmuir wave.

Solutions describing the density perturbation and the wakefield are given by

$$\frac{n_1}{n_0} = \frac{c^2}{\omega_p} \int_0^t \mathrm{d}t' \sin[\omega_p(t-t')]\nabla^2 \frac{a^2}{2} \tag{2.33}$$

$$\frac{\mathbf{E}}{E_0} = -c \int_0^t \mathrm{d}t' \sin[\omega_p(t-t')]\nabla \frac{a^2}{2}. \tag{2.34}$$

As mentioned before, these solutions describe plasma waves at ω_p. It is also noted that the wakefield is most efficiently excited for $L_0 \sim \lambda_p$, i.e. when the pulse length is of the order of the plasma wavelength. Far behind the laser the plasma wave will be given by

$$\frac{n_1}{n_0} = C \sin(\omega_p t + \varphi), \tag{2.35}$$

where C is a constant depending on initial laser strength and φ describes the phase of the wave. Hence, in the linear regime $E/E_0 \ll 1$, the wakefield is a sinusoidal perturbation.

In order to proceed the quasi-static approximation[7] is applied in a frame with $\xi = z - v_g t$. In the quasi static limit all time derivatives can be neglected as the laser pulse evolution time is much longer than the plasma response. The wakefield is then given by

$$\frac{\mathbf{E}}{E_0} = -c \int_0^\xi \mathrm{d}\xi' \sin[k_p(\xi-\xi')]\nabla \frac{a^2}{2}. \tag{2.36}$$

Panels (a), (c) and (e) in Figure 2.5 depict numerical solutions to Equation 2.36 and the associated plasma response and potential of the wake, in a frame comoving with the laser. The laser has a Gaussian longitudinal profile, $a = a_0 e^{(\xi-\xi_0)^2/L_0^2} e^{ik_0\xi}$, and is linearly polarised with $a_0 = 0.1$, $L_0 = 1/k_p$ and $k_0^2/k_p^2 = 50$. In Figure 2.5a, the electron density modulation arising from the laser interaction is showed. The high frequency oscillations within the envelope of the laser are a consequence of linear polarisation of the laser and their frequency is twice that of the laser. After the laser has passed a sinusoidal density fluctuation remains. In the laboratory frame, this wake is travelling with a phase velocity that is set by the group velocity of the laser. The longitudinal electric field and the potential of the wake are depicted in Figures 2.5c and 2.5e. The electric field is normalised to the cold wavebreaking field $E_0 = m_e c\omega_p/e$. Following

[7] Cf. Section B.6

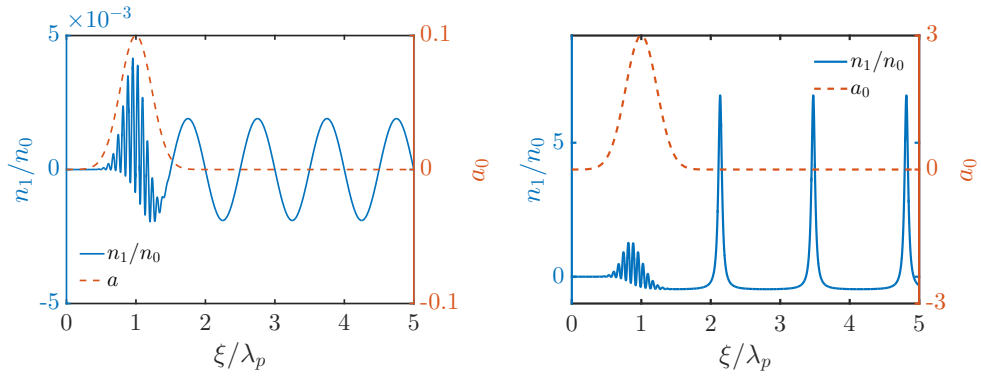

(a) *Density perturbation,* $a_0 = 0.1$ ***(b)*** *Density perturbation,* $a_0 = 3$

(c) *Electric field,* $a_0 = 0.1$ ***(d)*** *Electric field,* $a_0 = 3$

(e) *Potential,* $a_0 = 0.1$ ***(f)*** *Potential,* $a_0 = 3$

Figure 2.5: *Plasma wakefield excited by a Gaussian shaped laser pulse with* $L_0 = 1/k_p$*. Panels (a), (c) and (e) depict the behaviour of linear plasma waves with* $a_0 = 0.1$*, while panels (b), (d) and (e) show characteristics of non-linear regime with* $a_0 = 3$*.*

from the plasma density wave, both are sinusoidal oscillations as well.

It is instructive to discuss the optimum length of a laser pulse to excite a laser plasma wave. Intuitively one would assume the pulse length to excite the largest amplitude is

less than the wavelength of the wave such as to provide a resonant driving term. An analytical expression can be found[41] for low intensity drivers with a circularly polarised Gaussian pulse:

$$\frac{|E_{max}|}{E_0} = \sqrt{\pi}\frac{a_0^2}{2}k_pL\exp\left(-\frac{k_p^2L^2}{4}\right). \tag{2.37}$$

Equation 2.37 has a maximum at $k_pL = \sqrt{2}$ or $L = 0.23\lambda_p$. As L increases beyond this value, the exponential term vanishes and hence for pulse lengths $L \gg \lambda_p$, the amplitude of the excited wave is diminished. Physically, this means that the driving pulse length is longer than the resonant value and hence the back of the pulse starts to damp out the wave. It is also worth noting that for optimum length driver, the maximum field strength scales as $E_{max}/E_0 \simeq 0.76a_0^2$. Hence for $a_0 \ll 1$ the wake is always in the linear regime with $E \ll E_0$.

Another important parameter describing a laser pulse and hence its ability to excite plasma waves is its temporal shape. However, as long as the characteristic pulse length is optimum, its shape has little effect on the total amplitude of the excited wave.

Transverse fields in a multidimensional linear wakefield are related to the axial field by the Panofsky-Wenzel theorem.[94,95] A charged particle moving along the z axis with relativistic velocities will feel radial forces due to $E_r - v_zB_\theta$, which is related to the axial field by

$$\frac{\partial E_z}{\partial r} = \frac{\partial\left(E_r - v_zB_\theta\right)}{\partial\xi}. \tag{2.38}$$

Consider a longitudinal field E_z, given by $E_z \propto \exp(-r^2/r_0^2)\cos k_p\xi$. Equation 2.38 then yields a radial force

$$\left(E_r - v_zB_\theta\right) \propto \frac{4r}{k_pr_0^2}e^{-r^2/r_0^2}\sin k_p\xi,$$

which is $\pi/2$ out of phase with the longitudinal field and is zero on axis.[8] Physically this focussing force arises from charge imbalance, and as $\nabla\cdot\mathbf{E} = \rho/\epsilon_0$, the transverse force is in phase with density modulation n_1/n_0.

1D non-linear plasma waves

In the linear regime discussed in the preceding section, the plasma wave set up by the laser is a sinusoidal oscillation with wavelength $\lambda_p = 2\pi c/\omega_p$. This is valid for weak drivers, $a_0 \ll 1$, and small wakefields, $E \ll E_0$. With increasing a_0 the wakefield E

[94] W. K. H. Panofsky *et al*, *Rev Sci Instrum* **27**, 1956.
[95] R. Keinigs *et al*, *Phys Fluids* **30**, 1987.
[8] Cf. Figure 2.10

will also increase and the wake will cease to be sinusoidal. This is due to electrons in the plasma wave being accelerated to velocities where their trajectories may cross. Hence, electrons can start to 'overtake' one another, leading to a non-linear behaviour of the plasma wave and destruction of its linear structure.[91] This is the physical picture behind the cold wavebreaking limit $E_0 = m_e c\omega_p/e$.[9]

The behaviour of non-linear wakes can be examined in the 1D limit which is valid for large drivers, such that $w_0 k_p \gg 1$, with w_0 being the laser's transverse extent. It is also assumed that the laser is non-evolving, such that the quasi-static approximation[10] holds.[96] A set of non-linear, relativistic cold fluid equations can then be written, describing the wakefield generation for arbitrary laser intensities in the 1D limit.[96,97] For tenuous plasmas, with $\gamma_p = (1 - v_p^2/c^2)^{-1/2} \gg 1$, Poisson's equation describing the wakefield can be written as[97,98]

$$\frac{\partial^2 \phi}{\partial \xi^2} = \frac{k_p^2}{2}\left[\frac{\left(1+a^2\right)}{(1+\phi)^2} - 1\right]. \tag{2.39}$$

Whilst analytical solutions to Equation 2.39 exist for square pulses,[98] we shall proceed to study the properties of non-linear 1D wakes by numerically solving Equation 2.39.

Panels (b), (d) and (f) in Figure 2.5 depict a non-linear plasma wave for $a_0 = 3$. The pulse shape is Gaussian, with its length $L_0 = 1/k_p$, the same as for the linear wave in Figures 2.5a, 2.5c and 2.5f. Remarkedly different behaviour of the wake is evident. In the non-linear case, not only is the plasma wave not sinusoidal any more, its wavelength increases as well. This is caused by the relativistic mass increase of plasma electrons due to a higher laser strength, $m = \gamma m_e$ and $\gamma = \sqrt{1 + a_0^2/2}$ for linear polarisation. In the $a_0 \gg 1$ limit, the non-linear plasma wavelength is given by $\lambda_{\mathrm{Np}} = 2\lambda_p a_0/\pi$.[97,98] The electric field in a non-linear plasma wave is depicted in Figure 2.5d. The characteristic "sawtooth" shape of the field is evident. The potential, depicted in Figure 2.5f, also deviates strongly from the linear behaviour of the low laser strength case.

An interesting artefact of 1D treatment is the minimum density depression within the wake being $n_1/n_0 = -0.5$. Hence full cavitation of the wake structure is not allowed. However, ion spheres completely void of electrons are commonly observed in 3D PIC simulations.[48,49,99] Hence non-linear 3D theory is required to accurately model

[9] Cf. Section 2.3.2
[10] Cf. Section B.6
[96] P Sprangle *et al*, *Phys Rev Lett* **64**, 1990.
[97] P Sprangle *et al*, *Phys Rev A* **41**, 1990.
[98] S. V. Bulanov *et al*, *JETP Lett* **50**, 1989.
[48] P. Mora *et al*, *Phys Rev E* **53**, 1996.
[49] A. Pukhov *et al*, *Appl Phys B-Lasers O* **74**, 2002.
[99] F. S. Tsung *et al*, *Phys Rev Lett* **93**, 2004.

the non-linear plasma wake physics.

3D non-linear plasma waves

As seen in the preceding section, relativistic laser strengths $a_0 \gtrsim 1$ lead to wake shape steepening and lengthening of the plasma wave period. In multiple dimensions, radial nonlinearities will also arise. For example, consider a plasma wave driven by a laser with an intensity maximum on axis. The axial wake is more strongly driven than at radial positions and hence the length of the plasma period will depend on the radial coordinate. This will lead to further phase mixing of plasma electrons. Additionally, for strong enough drivers complete cavitation of a region behind the laser pulse can occur.

An analytical theory was developed by Lu *et al* and describes wake generation in three dimensions for relativistic ($a_0 \gtrsim 2$) drivers in the blow out regime.[100,101] They find that a narrow sheath of electrons is formed around a fully cavitated ion sphere. The ion sphere is surrounded by a high electron density, low thickness sheath shielding out the field from the positive ions. The shape of the bubble is found by using a pseudopotential $\Psi = A_z - \phi$, where A_z is the longitudinal component of vector potential and ϕ is the scalar potential; the Lorentz gauge is employed. This pseudopotential captures the effects from the electrostatic and electrodynamic contributions. The radial position of an electron moving within the sheath, $r_b(\xi)$, where $\xi = z - v_g t$ is the coordinate in the bubble frame, determines the shape of the ion cavity.

The resulting second order non-linear differential equation for r_b has no analytical solutions and is usually solved numerically, as shown in Figure 2.6. The bubble shape obtained for a bi-gaussian laser driver with $a_0 = 4$, $w_0 = 1$ and $L_0 = 1.6$ is depicted in Figure 2.6a. The resulting bubble is indeed very nearly spherical.

The longitudinal electric field inside the bubble is calculated to vary as $E_z = (k_p r/2)E_0$, where r is distance from the bubble centre. Thus, similarly to the 1D non-linear case, the electric field is linear, and reaches a maximum value of $E_{\text{peak}} = \sqrt{a_0}E_0$. Both these characteristic are evident in Figure 2.6b, where the longitudinal electric field for the bubble shape in Figure 2.6a is shown.

The extent of the blowout, or radius of the ion sphere, is found by balancing the ponderomotive force from the laser and the restoring force from the ion column. With a numerical factor based on PIC simulations, the blowout radius is given by

$$r_b = 2\sqrt{a_0}\frac{c}{\omega_p}. \tag{2.40}$$

[100] W. Lu *et al*, *Phys Rev Lett* **96**, 2006.
[101] W. Lu *et al*, *Phys Plasmas* **13**, 2006.

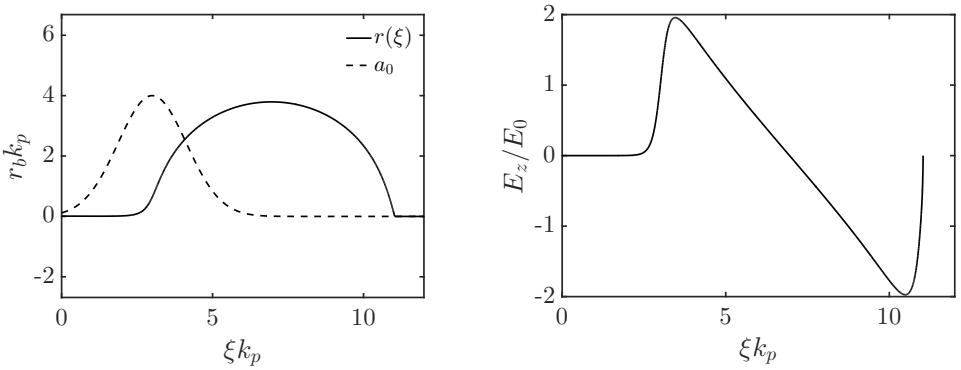

(a) Shape of the bubble *(b) Longitudinal field*

Figure 2.6: *Numerical solutions to 3D non-linear theory showing the bubble shape and the longitudinal field.*

A short pulse duration of the order of r_b is also assumed in deriving this expression. This is also the extent of a matched spot size w_m. Only laser pulses focussed to $w_m \simeq r_b$ yield a narrow and well defined sheath around the ion column.[101] Additionally, there is minimal transverse focussing for laser spot size w_m, i.e. optimum guiding is achieved.

The general expression for the bubble shape can be simplified in the case of ultra-relativistic blowout, defined as $r_m \gtrsim 4$. In this case, the differential equation describing the shape of the bubble reduces to

$$r_b \frac{\mathrm{d}^2 r_b}{\mathrm{d}\xi^2} + 2\left(\frac{\mathrm{d}r_b}{\mathrm{d}\xi}\right)^2 + 1 = 0 \tag{2.41}$$

where the driving term is ignored in this case as the length of the driver is usually much shorter than the bubble length. This equation is similar to the equation of a circle, with an additional $(\mathrm{d}r_b/\mathrm{d}\xi)^2$ term ensuring a faster return to axis near the back of the bubble. In order to be in the ultrarelativistic regime, $a_0 \gtrsim 4$ and $w_0 \sim 2\sqrt{a_0}$; thus laser powers of $P \simeq 8P_c$ are required, where P_c is the critical power for self-focussing.[11]

Due to the ion sphere being completely void of electrons, the electric field always points spherically outwards. Thus, the radial electric field changes linearly with distance. However, when the laser is relativistic but below $a_0 \sim 2$, cavitation will not be complete and there will be a non-linear radial dependence on transverse fields. This has important implications for beam quality conservation, discussed in more detail in Section 2.5.2.

[11] Cf. Section 2.4.3

2.4 Non-linear plasma optics

The propagation of electromagnetic radiation in a medium is determined by the response of the medium itself to the wavelike oscillations. For dielectrics, this can be expressed in terms of the polarisation $\mathbf{P}$:

$$\mathbf{P} = \epsilon_0 \chi^{(1)} \mathbf{E} + \epsilon_0 \chi^{(2)} \mathbf{E}^2 + \epsilon_0 \chi^{(3)} \mathbf{E}^3 + \dots \tag{2.42}$$

where $\chi^{(i)}$ is susceptibility of order i. The refractive index of a medium, used to describe optical phenomena, is defined in terms of susceptibility, $\eta = \sqrt{\epsilon_r \mu_r}$, with $\epsilon_r = (1+\chi)\epsilon_0$.

In everyday situations the electric field strength is weak enough to justify neglecting higher order terms in the polarisation and thus arises the linear behaviour of optics. However, in the case of lasers the coherent nature of radiation means the electric field can be strong enough to make contributions from higher order terms in susceptibility comparable to the linear term.[102] Hence the optical properties of materials can be changed by very high electric fields, by making the terms with $i \geq 2$ relevant in Equation 2.42, thus giving rise to the field of non-linear optics.[12]

2.4.1 Non-linear refractive index of plasma

The dispersion relation of an electromagnetic wave, given by Equation 2.25, can be rearranged to yield the well known expression for the refractive index of a plasma,

$$\eta = \left(1 - \frac{\omega_p^2}{\omega_L^2}\right)^{1/2}, \tag{2.43}$$

from which it is evident that the refractive index can be changed by the interaction of a laser pulse with plasma. This gives rise to a wide range of phenomena commonly referred to as non-linear plasma optics.[96,103]

If the laser pulse is of relativistic strength with $a_0 \to 1$, the motion of plasma electrons becomes relativistic and the effective mass of electrons increases to γm_e, decreasing the electron plasma frequency by $\gamma^{1/2}$. If we assume the plasma is relativistically underdense, i.e. $\omega_p^2 \ll \gamma \omega_L^2$, Equation 2.43 can be expanded to yield

$$\eta \simeq 1 - \frac{\omega_p^2}{2\gamma\omega_L^2}. \tag{2.44}$$

[102] Y. R. Shen. *The Principles of nonlinear optics*. Wiley, 1984.

[12] Indeed, the opening sentence from Shen: *Physics would be dull and life most unfulfilling if all physical phenomena around us were linear. Fortunately, we are living in a nonlinear world. While linearisation beautifies physics, nonlinearity provides excitement in physics.*

[103] W. B. Mori, *IEEE J Quantum Elect* **33**, 1997.

The refractive index can be modulated during the laser-plasma interaction by changes to the plasma frequency, the laser carrier frequency or the laser intensity. The change in plasma frequency is due to changes in electron density, e.g. from ponderomotive effects; hence we can write $n = n_0(1 + \delta n/n_0)$. Time-varying refractive index gradients induce changes in carrier frequency which can be written as $\omega = \omega_L(1 + \delta\omega/\omega_L)$. We also have the period averaged vector potential for a linearly polarised pulse as $\langle\gamma\rangle = 1 + a_0^2/4$. Hence, Equation 2.44 can be expanded to obtain[103]

$$\eta = 1 - \frac{1}{2}\frac{\omega_p^2}{\omega_L^2}\left(1 + \frac{\delta n}{n_0} - \frac{a_0^2}{4} - 2\frac{\delta\omega}{\omega_L}\right). \tag{2.45}$$

The expansion leading to Equation 2.45 is only valid for small perturbations in density and frequency and weakly relativistic laser pulses. However, regardless of the limits imposed to the range of intensities the result applies for, insight can be gained into various phenomena arising from non-linear plasma optics.

In order to advance to the derivations in the subsequent sections we also assume the conservation of photon number within a local volume. This is in effect conservation of classical action,[13] i.e. conservation of photon number,[103,104] and can be expressed as

$$\langle a^2\rangle\omega_L w^2 L = \text{constant}, \tag{2.46}$$

where the angle brackets represent averaging over laser oscillations, ω_L is laser frequency and w^2L represent a volume, with w being the laser spot size and L is the initial length of the laser pulse.

2.4.2 Pulse compression

A laser pulse travelling in a plasma can be compressed when a refractive index gradient is present in the direction of propagation. This gradient can be caused by either the relativistic plasma response to the laser pulse itself or the presence of a relativistic plasma wave. The refractive index also varies in the direction perpendicular to the propagation which will lead to self focussing, discussed in Section 2.4.3.

Pulse compression can arise when the group velocity is larger at the rear of the laser pulse leading to the tail of the pulse "catching" the leading edge, as shown in Figure 2.7. Consider two points in the laser pulse, z_1 and z_2, initially separated by $L = z_2 - z_1$.[103] After some time Δt the change in separation between the points will be

$$\Delta L = (v_{g2} - v_{g1})\Delta t. \tag{2.47}$$

[13] See Ref 103 for an excellent derivation of this.

[104] J. T. Mendonça. *Theory of photon acceleration*. Institute of Physics Publishing, 2001.

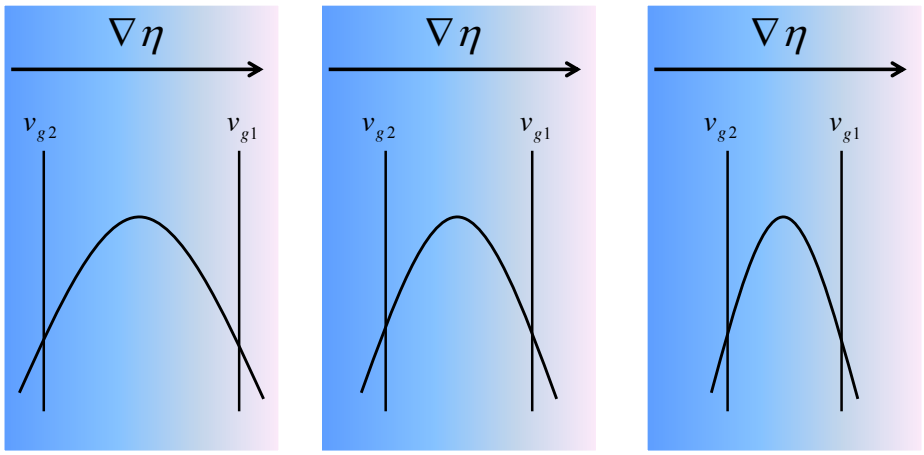

Figure 2.7: *Schematic depicting pulse compression in a refractive index gradient.*

In the limit of the points z_1 and z_2 being closely separated, we have $v_{g2} - v_{g1} = \frac{\partial v_g}{\partial z} L$. Changing to a frame comoving with the laser pulse with $\xi = z - ct$ and $\tau = t$ we obtain

$$\frac{1}{L}\frac{\partial L}{\partial \tau} = \frac{\partial v_g}{\partial \xi} = c\frac{\partial \eta}{\partial \xi}. \tag{2.48}$$

Evidently, longitudinal changes in the refractive index – which can arise due to any of the three terms in Equation 2.45, i.e. density modulations, carrier frequency changes or laser intensity variations – can lead to changes in the pulse envelope shape. Depending on the sign of the refractive index gradient this can be a stretching or compression of the pulse. If there are periodic modulations in the density, say, the laser pulse will also undergo periodic stretching and compression. Despite being derived here for very small modulations, pulse compression has been observed for very relativistic pulses.[105,106]

2.4.3 Relativistic self-focussing

Refractive index gradients in the direction perpendicular to laser propagation lead to focussing or defocussing of a laser pulse. Indeed, this property is realised in the Gradient Index (GRIN) lens.[107] If the refractive index changes so that it is maximum on axis, focussing of the laser pulse occurs.

We can examine the rate of focussing by considering the rate of change of laser phase velocity in the transverse direction. A spatial gradient in phase velocity will

[105] J. Faure *et al*, *Phys Rev Lett* **95**, 2005.
[106] J. Schreiber *et al*, *Phys Rev Lett* **105**, 2010.
[107] E. Hecht. *Optics*. 4th ed. Addison Wesley, 2002.

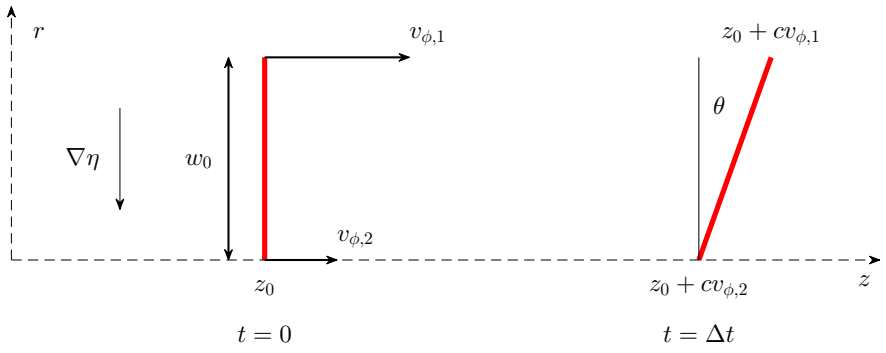

Figure 2.8: *Schematic depicting curving of laser wavefronts due to transverse refractive index gradient.*

cause wavefronts to curve accordingly. As the Poynting vector is perpendicular to the laser wavefront, curvature of the wavefront is equivalent to focussing.

Consider a laser pulse with a flat wavefront at time $t = 0$, as shown in Figure 2.8, with point r_2 on laser axis having phase velocity $v_{\phi 2}$ and point r_1 a distance w_0 from axis with phase velocity $v_{\phi 1}$. After a short time Δt the wavefront curvature will be given by $\tan\theta \approx \theta = \Delta t(v_{\phi 1} - v_{\phi 2})/w_0$. This can be written in terms of phase velocity gradient as $(v_{\phi 1} - v_{\phi 2}) = \frac{\partial v_\phi}{\partial r} w_0$. We can thus express the rate of change of wavefront curvature angle as

$$\frac{\partial \theta}{\partial t} = \frac{\partial v_\phi}{\partial r}. \tag{2.49}$$

As mentioned earlier, energy flows in the direction perpendicular to wavefronts at the group velocity v_g. If the wavefronts are curved by an angle of θ, there is a component $v_g \sin\theta \approx v_g\theta$ of energy flow in the transverse direction. This energy flow towards the laser axis corresponds to focussing, i.e. the rate of change of focal spot size, $\frac{\partial w}{\partial t} = -v_g\theta \approx -c\theta$. Differentiating this with respect to time gives the "acceleration" of spot size as $\partial^2 w/\partial^2 t = -c\partial\theta/\partial t$ and inserting Equation 2.49 here we obtain

$$\frac{\partial^2 w}{\partial t^2} = -c\frac{\partial v_\phi}{\partial r}. \tag{2.50}$$

But $v_\phi = c\eta^{-1}$ and hence we have

$$\frac{\partial^2 w}{\partial t^2} = \frac{c^2}{\eta^2}\frac{\partial \eta}{\partial r}. \tag{2.51}$$

When a plasma channel with electron density minimum on-axis is formed, focussing over

long lengths will occur. Indeed, this is utilised in density channel guiding scenarios.[108] If, however, the refractive index is caused by variations in laser intensity, the resulting phenomenon is called relativistic self-focussing. If the rate of focussing matches natural diffraction of the spot, perfect self-guiding is achieved.

We now look at the threshold of self-focussing. For this we assume that the changes in the refractive index are only due to the laser pulse itself,[70] i.e. the a_0 term in Equation 2.45. The acceleration of the spot size is found from Equation 2.51 to first order (i.e. to order ω_p^2/ω_L^2) as

$$\frac{\partial^2 w}{\partial t^2} = \frac{c^2\omega_p^2}{8\omega_L^2}\frac{\partial a^2}{\partial r}. \tag{2.52}$$

Evaluating the transverse derivative of a Gaussian spot of form

$$a(r,z) = a_0(z)\exp\left(-\frac{r^2}{w^2(z)}\right) \tag{2.53}$$

near focus, i.e. $(z - z_R) \ll 1$, yields

$$\frac{\partial a^2}{\partial r} = -\frac{a_0^2}{w_0}, \tag{2.54}$$

which, when substituted back into Equation 2.52, gives

$$\frac{\partial^2 w}{\partial t^2} = -\frac{c^2\omega_p^2}{8\omega_L^2}\frac{a_0^2}{w_0}. \tag{2.55}$$

Self-focussing occurs when the focussing due to the laser intensity is larger than the natural diffraction of the spot. Hence the threshold for self-focussing is

$$\left.\frac{\partial^2 w}{\partial t^2}\right|_{\text{diff}} + \left.\frac{\partial^2 w}{\partial t^2}\right|_{\text{foc}} = 0 \tag{2.56}$$

For a gaussian beam the spot size varies as

$$w(z) = w_0\left(1 + \frac{z^2}{z_R^2}\right)^{1/2}. \tag{2.57}$$

Expanding this near focus, ie $(z - z_R) \ll 1$, differentiating twice and recognising $\partial z/\partial t \approx c$ yields acceleration of spot size for a gaussian beam,

$$\frac{\partial^2 w}{\partial t^2} = \frac{4c^4}{w_0^3\omega_L^2}, \tag{2.58}$$

[108] A. Zigler *et al*, Journal of the Optical Society of America B **13**, 1996.
[70] C. Max *et al*, *Phys Rev Lett* **33**, 1974.

where we have used definition of Rayleigh range $z_R = \pi w_0^2/\lambda_L$. Equation 2.56 can then be rearranged to yield

$$a_0^2 w_0^2 = \frac{32c^2}{\omega_p^2}. \tag{2.59}$$

Recognising that $(a_0 w_0)^2$ is proportional to laser power,[14] we can obtain from Equation 2.59 the critical power for self-focussing:

$$P_c \equiv P_{\text{crit}} = \frac{8\pi\epsilon_0 m_e^2 c^5}{e^2}\frac{\omega_L^2}{\omega_p^2} = 17.4\,\frac{\omega_L^2}{\omega_p^2}\ \text{GW}. \tag{2.60}$$

The result obtained from this simple argument agrees well with more sophisticated derivations.[71,109] Equation 2.60 can be rewritten in terms of electron density and critical density to yield $P_c = 17.4(n_c/n_e)$ GW. Hence, the critical power for self-focussing decreases with increasing electron density.

For an optimally chosen laser spot size diffraction can thus perfectly balance self-focussing. The rate of spot change is found to vary as[109]

$$\frac{\partial^2 \bar{w}}{\partial t^2} = V_0 \begin{cases} \dfrac{P}{P_c \bar{w}^3} - \dfrac{1}{\hat{w}^3}, & a_0 \ll 1 \\ \dfrac{1}{\bar{w}^3} - 16\dfrac{P}{P_c}, & a_0 \gg 1 \end{cases} \tag{2.61}$$

where $\bar{w} = w/(w_0 a_0)$ and $V_0 = [c\lambda_L/(\pi w_0^2 a_0^2)]^2$. Hence, in the low intensity limit perfect guiding is achieved for $P = P_c$. For $P \neq P_c$, either constant diffraction or focussing to $\bar{w} \to 0$ will occur. In the high intensity regime with $P > P_c$, the spot will self-focus until the diffraction term starts to dominate, at which point the spot will increase in size again. Thus an oscillation of the spot size occurs. Note that if the initial focussing is very tight, such that $|\partial\bar{w}/\partial t|$ is large, the spot will self-focus to a small spot and then diffract indefinitely. Solutions to the envelope equation for $P/P_c = 10$ at $n_e = 2 \times 10^{18}\,\text{cm}^{-3}$ are plotted in Figure 2.9. The focussing term $|\partial\bar{w}/\partial t| \propto w_0^{-3}$ and thus larger spot sizes self-guide, whereas for small initial spot sizes diffraction is never balanced and the spot diverges. Indeed only guiding of large spot sizes is seen in simulations and experiments.[110]

Assuming a small focussing term, the spot will be guided in the $a_0 \gg 1$ regime if $\partial^2\bar{w}^3/\partial t^2 = 0$. Thus $\bar{w}^{-3} = 16P/P_c$, which can be rearranged to yield a matched spot

[14] The total laser power for a Gaussian spot is found by $P = \int_S I(r)\mathrm{d}S$, with $I = \epsilon_0 c E_0^2/2$ and $E_0 = m_e c\omega_0 a_0/e$. As a_0 varies radially as $a_0(r) = a_0 \exp(-r^2/w_0^2)$, the integral yields $P = a_0^2 w_0^2 \frac{\pi\epsilon_0 m_e^2 c^3 \omega_0^2}{4e^2}$.

[71] G. Z. Sun *et al*, *Phys Fluids* **30**, 1987.

[109] P. Sprangle *et al*, *IEEE T Plasma Sci* **15**, 1987.

[110] A. G. R. Thomas *et al*, *Phys Rev Lett* **98**, 2007.

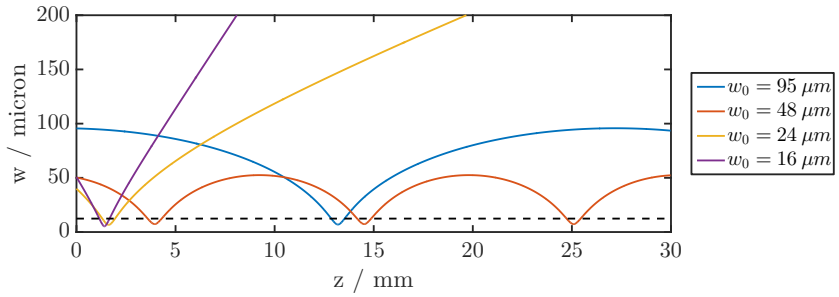

Figure 2.9: *Solutions to envelope equation for* $P/P_c = 10$ *and* $n_e = 2 \times 10^{18}\,\mathrm{cm}^{-3}$ *for different vacuum spot sizes. The black dashed line is the matched spot size given by Equation 2.62,* $w_m =$ 12.4 *microns.*

size:

$$k_p w_m = 2\sqrt[6]{2}\left(\frac{P}{P_c}\right)^{1/6}. \tag{2.62}$$

This scales very weakly with laser power. Interestingly, the 3D nonlinear matched spot size, given by Equation 2.40, can be recast to read

$$k_p w_m = 2\sqrt{2}\left(\frac{P}{P_c}\right)^{1/6}. \tag{2.63}$$

Thus exactly the same scaling with laser power is obtained, differing only by a very small numerical factor.

2.4.4 Photon acceleration

Non-linear refractive index was shown to lead to pulse compression earlier. This was due to the effect on the group velocity of the laser, leading to envelope modulations. However, the phase velocity of the laser is also modulated. This can lead to wavefronts bunching together (photon acceleration) or getting further separated (photon deceleration).

Consider two wavefronts in the laser pulse, z_1 and z_2, with a phase difference of 2π. This is equivalent to $z_2 - z_1 = \lambda_0$. A gradient in the refractive index leads to both wavefronts having a different phase velocity. Hence, after time Δt the separation between the wavefronts will be $z_2' - z_1' = \lambda_0 + (v_{\phi 2} - v_{\phi 1})\Delta t$. We have $(v_{\phi 2} - v_{\phi 1}) \simeq \frac{\partial v_\phi}{\partial z}\lambda_0$ and writing this in terms of refractive index gradient yields

$$\frac{\partial \lambda}{\partial \tau} = -\lambda_0 \frac{c}{\eta^2}\frac{\partial \eta}{\partial \xi}, \tag{2.64}$$

where we have again moved into comoving frame, with variables ξ and τ. We can write

Equation 2.64 in terms of frequency, rather than wavelength:

$$\frac{1}{\omega_L}\frac{\partial\omega}{\partial\tau} = \frac{c}{\eta^2}\frac{\partial\eta}{\partial\xi}. \tag{2.65}$$

Equation 2.65 describes how refractive index gradients that are comoving with the laser can lead to laser frequency shifts. The frequency of photons will increase in the presence of a positive gradient of the refractive index. It is also clear that pulse compression described in Section 2.4.2 and photon acceleration cannot occur on their own and are related phenomena, as both are caused by longitudinal refractive index gradients. Indeed, pulse compression implies frequency modulations, as a wider spectrum is required to support a shorter pulse.

2.5 Laser wakefield accelerator

The main task of a particle accelerator is to add energy to a beam of particles. Hence the most fundamental component of an accelerator is the accelerating field. Secondly, in order to maintain a high beam quality and to avoid space charge effects focussing of the bunch is also required. This is achieved with transverse fields, confining the beam to its axis. In the case of a laser wakefield accelerator, the acceleration cavity is an ion rich void behind the laser pulse, in its wakefield.

The laser wakefield accelerator was first proposed by Tajima and Dawson in 1979.[22] In this paper the authors describe an electron wave, moving behind an electromagnetic wave packet, with a phase velocity given by the group velocity of the driving pulse. This seminal work presented first results for maximum attainable energy gain and dephasing length in the linear regime. Much more work has been performed since then, exploring non-linear regimes in multiple dimensions. In this section we will review the sources of acceleration and focussing fields and discuss the physical limitations of wakefield accelerators.

2.5.1 Accelerating gradient

Acceleration gradient is the longitudinal electric field within the wake. In the linear regime, $a_0 \ll 1$, this is a sinusoidal perturbation. As intensity is increased, the field shape deviates from its sinusoidal behaviour and instead becomes more peaked. In the extreme, fully non-linear regime, the electric field varies linearly with distance behind the laser pulse.[15]

[22] T. Tajima *et al*, *Phys Rev Lett* **43**, 1979.
[15] Cf. Section 2.3.3

The maximum longitudinal electric field attainable is limited by charge separation that can be supported without wavebreaking. Hence the peak field is a function of plasma density. However, the achievable peak field also depends on laser parameters. The maximum electric field in a wake excited by a linearly polarised laser of strength a_0 in a tenuous plasma with $\gamma_p \gg 1$ is given by[41,96,101]

$$\frac{E_{\max}}{E_0} = \begin{cases} \sqrt{\frac{\pi}{2e}} a_0^2, & a_0 \ll 1 \text{ (1D)} \\ \frac{a_0^2/2}{\sqrt{1 + a_0^2/2}}, & a_0 \gtrsim 1 \text{ (1D)} \\ \sqrt{a_0}, & a_0 \gtrsim 2 \text{ (3D)} \end{cases} \tag{2.66}$$

where $E_0 = mc\omega_p/e$ is the cold wavebreaking limit. We see that for low intensities the peak field scales as a_0^2. In the non-linear regime, the field scales as a_0 in the 1D limit while in 3D non-linear limit there is a $\sqrt{a_0}$ scaling.[63]

2.5.2 Focussing fields

An ideal accelerator will add energy to a beam without degrading its quality. A common measure of beam quality is transverse emittance, which is a measure of the focusability of a beam and is defined as an area in the $p_y - y$ phase space, where p_y is transverse momentum and y is transverse coordinate. In order to increase beam energy without degrading emittance, the transverse focussing within the accelerator cavity must be linear with the transverse coordinate.[111]

In the case of a low intensity sinusoidal wake driven by $a(r) = a_0 \exp(-r^2/w_0^2)$,

$$E_r = \frac{\partial \phi}{\partial r} \propto \frac{-4r}{w_0^2} \exp\left(-\frac{2r^2}{w_0^2}\right), \tag{2.67}$$

as depicted in Figure 2.10c. The focussing field is clearly not linear with transverse direction and thus emittance is not be conserved in linear wakes driven by gaussian laser pulses. Furthermore, there is a dependence on the longitudinal coordinate as well, meaning accelerating particles with different phase feel different focussing forces. These effects can be mitigated by correct beam loading and phase space rotation, adding more complexity into the design. In the case of full cavitation, though, the transverse focussing field is given by[101]

$$E_r - B_\theta = \frac{1}{2} r \tag{2.68}$$

[63] W. Lu *et al*, *Phys Rev Spec Top-Ac* **10**, 2007.
[111] T. P. Wangler. *RF Linear Accelerators*, p. 284. Wiley, 2008.

and is obviously linear with radial distance, as illustrated in Figure 2.10d. Note the field is normalised to E_0 and distance to $1/k_p$; the velocity v_z has been set to $c = 1$. Furthermore, in the 3D non-linear case the transverse field stays constant with longitudinal distance, $\partial F_\perp/\partial\xi = 0$. Thus the fully cavitated 3D non-linear regime is ideal for high quality beam acceleration.

2.5.3 Wake phase velocity

The wake set up by a laser pulse propagating in a plasma moves at the group velocity in the linear regime, hence $\gamma_p = \omega_L/\omega_p$. As the amplitude of the laser increases, non-linear corrections to the group velocity need to be made. These were first analysed by Decker and Mori.[112] However, they find that the leading edge of a laser pulse moves at the linear group velocity, regardless of its intensity.

Whilst group velocity of the leading edge remains the same with increasing intensity, energy depletion from the front affects the speed of the wake. The front edge of the laser loses its energy as it drives the wake, thus effectively moving back within the pulse.[113] This happens at an etching rate given by $\nu_{\text{etch}} = \omega_p^2/\omega_L^2$. The front of the laser hence moves with $v_{\text{g,eff}} = v_g - \omega_p^2/\omega_L^2$ and the wake moves at

$$\gamma_p = \left[1 - \left(1 - \frac{3\omega_p^2}{2\omega_L^2}\right)^2\right]^{-\frac{1}{2}} \simeq \frac{\omega_L}{\sqrt{3}\omega_p}. \tag{2.69}$$

Thus in the non-linear regime the phase velocity of the wake is reduced due to depletion. Accurate description of the wake phase velocity is of critical importance in determining the final energy of the electron beam.

2.5.4 Acceleration limits

Acceleration in a wakefield accelerator can be limited by a variety of processes: laser diffraction, electron dephasing, laser pulse depletion or laser-plasma instabilities. Laser diffraction limits acceleration due to the reduction of peak intensity, thus reducing wakefield strength. Diffraction can be avoided by using a guiding structure, such as a preformed plasma channel with suitable transverse profile. However, in a plasma self-focussing[16] can also provide guiding. Hence, we neglect diffractive losses in the following discussion.

[112] C. Decker *et al*, *Phys Rev Lett* **72**, 1994.
[113] C. D. Decker *et al*, *Phys Plasmas* **3**, 1996.
[16] Cf. Section 2.4.3

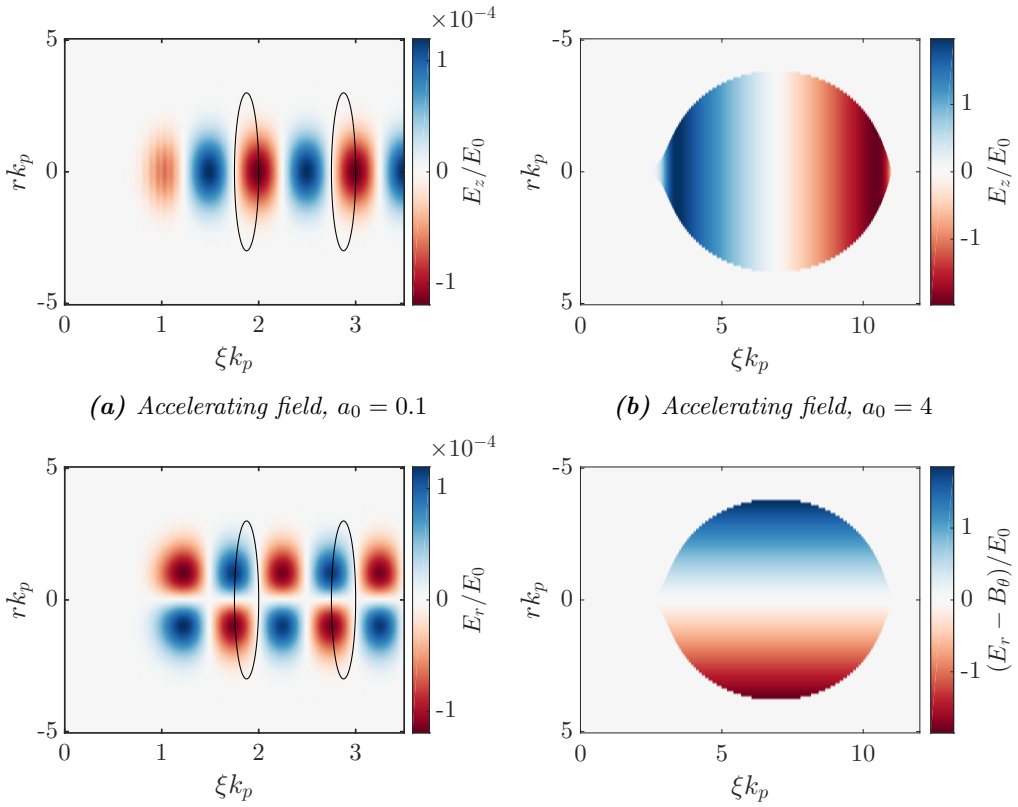

(a) *Accelerating field,* $a_0 = 0.1$

(b) *Accelerating field,* $a_0 = 4$

(c) *Focussing field,* $a_0 = 0.1$

(d) *Focussing field,* $a_0 = 4$

Figure 2.10: *Accelerating and focussing fields in 3D bubbles in the linear and non-linear regimes.*

Dephasing

Acceleration in a wakefield accelerator is limited by an electron effectively overtaking the wake and moving into a decelerating phase of the wave. This is due to the plasma wave moving at $\gamma_p \simeq \omega_L/\omega_p$ whereas the electron will be moving at $\beta \sim 1$. Thus the electron phase slips in the accelerating potential. The length it takes for the electron to move into a decelerating phase is called the dephasing length.

The region of the plasma wave that is a useful accelerator is where the electrons feel both an accelerating and a focussing force. In linear plasma waves the fraction of a wave period where both these conditions are fulfilled is 1/4 of a period. Thus in the linear regime the useful acceleration length is $\lambda_p/4$. This is illustrated in Figure 2.10, Panels (a) and (c), depicting the longitudinal and transverse fields in a linear plasma wave. The ellipses denote regions where electrons feel both a longitudinal accelerating and a transverse focussing force.

In the non-linear 3D regime, there is no dependence on longitudinal coordinate

for the focussing fields. Thus the full length of accelerating gradient can be used for acceleration. The spatial variation of E_z and focussing force $E_r - B_\theta$ is shown in Figure 2.10b and Figure 2.10d. The dephasing length is the full region where $E_z < 0$, and is given by $L_{\mathrm{dph}} = \lambda_{Np}/2$, where λ_{Np} is the total length of the cavity.

The dephasing length in different intensity regimes is given by[63,96]

$$L_{\mathrm{dph}} = \frac{\lambda_p^3}{2\lambda_L^2} \begin{cases} 1, & a_0 \ll 1 \text{ (1D)} \\ \dfrac{\sqrt{2}}{\pi} a_0, & a_0 \gtrsim 1 \text{ (1D)} \\ \dfrac{4}{3\pi}\sqrt{a_0}, & a_0 \gtrsim 2 \text{ (3D)} \end{cases} \tag{2.70}$$

and scales as $n_e^{3/2}$ with plasma density for all intensity regimes. The additional dependence on laser intensity is the largest difference between linear and non-linear regimes. Increase of the dephasing length in the nonlinear regime is a direct consequence of nonlinear plasma period lengthening. Also note the different intensity scaling for the 1D and 3D non-linear regimes. Interestingly, for the 3D non-linear case the dephasing length is actually shorter than in the linear case for $a_0 < 5.6$, despite being able to utilise $\lambda_p/2$ of a nonlinearly lengthened bubble. This is a direct consequence of the wake phase velocity being slower due to accounting for laser depletion.[17]

Laser depletion

Acceleration of an electron in a plasma wake will also cease if the wake is not driven any more, i.e. when the laser has lost all its energy. As a relativistic laser pulse drives a wake, it loses energy from the front to the plasma wave and the leading edge is etched away at $\nu_{\mathrm{etch}} = c\omega_p^2/\omega_L^2$.[113] The depletion length is defined as the length it takes for the entire pulse to etch away:

$$L_{\mathrm{dpl}} \simeq \frac{c}{\nu_{\mathrm{etch}}} c\tau_{\mathrm{FWHM}} = \frac{\omega_0^2}{\omega_p^2} c\tau_{\mathrm{FWHM}} \tag{2.71}$$

where τ_{FWHM} is the full-width-half-maximum (FWHM) duration of the pulse. Whilst somewhat arbitrarily defined in terms of FWHM duration of the pulse, this expression is based on numerous 1D, 2D and 3D simulations.[63] More rigorous analysis can be performed and yields very similar scalings to Equation 2.71.[114]

[17] Cf. Section 2.5.3

[114] B. A. Shadwick *et al*, *Phys Plasmas* **16**, 2009.

2.5.5 Scaling laws

Simple formulae to predict the energy of electrons in laser wakefield accelerators can be found by combining acceleration limitations discussed in the previous sections. These scaling laws can be then used to examine the effect of different parameters on the final energy of electrons. It is instructive to consider first the original result from Tajima and Dawson, namely[22]

$$\Delta\mathcal{E} = 2\gamma_p^2 m_e c^2. \tag{2.72}$$

This simple estimate gives a n_e^{-1} scaling for maximum electron energies as $\gamma_p^2 = n_c/n_e$. However, the derivation of the above result assumes an electric field amplitude equal to E_0. From previous sections, however, we recall that the excited field depends on laser intensity. Thus, whilst being conceptually simple and encapsulating the inverse plasma density scaling, this result provides an estimate that overestimates energy gains in realistic accelerators.

To derive more accurate scaling laws, we consider the limitations presented in previous sections along with the maximum excited wakefield strengths. The energy gain for an electron in an accelerator is given by $\Delta\mathcal{E} = -eE_{\mathrm{acc,av}}L_{\mathrm{acc}}$, where $E_{\mathrm{acc,av}}$ is the average accelerating gradient. We neglect diffraction losses and assume a constant laser intensity for the entire interaction. Thus $L_{\mathrm{acc}} = L_{\mathrm{dph}}$ and for linear plasma waves we have

$$\Delta\mathcal{E} = \sqrt{\frac{2\pi}{e}}\gamma_p^2 a_0^2 m_e c^2. \tag{2.73}$$

This result exhibits the same n_e^{-1} scaling, but additionally has an a_0^2 dependence. Valid for $a_0 \ll 1$, it limits energy gains in linear plasma wakes to very modest values.

Including the dependence of the peak accelerating field with laser intensity, a scaling for maximum electron energy gain in the 1D non-linear regime is given by[115]

$$\Delta\mathcal{E} = \frac{1}{2}\frac{\omega_0^2}{\omega_p^2} a_0^2 m_e c^2, \tag{2.74}$$

which is valid for a linearly polarised laser. Applicable for $a_0 \gg 1$, the above result exhibits energy gains much larger than those predicted from Equation 2.72. Including three dimensional effects yields energy scaling in 3D non-linear regime as[63]

$$\Delta\mathcal{E} = \frac{2}{3}\frac{\omega_0^2}{\omega_p^2} a_0 m_e c^2. \tag{2.75}$$

The last result is valid for lasers with $a_0 \gtrsim 2$ and is thus most applicable to the majority

[115] E. Esarey *et al*, *Phys Plasmas* **2**, 1995.

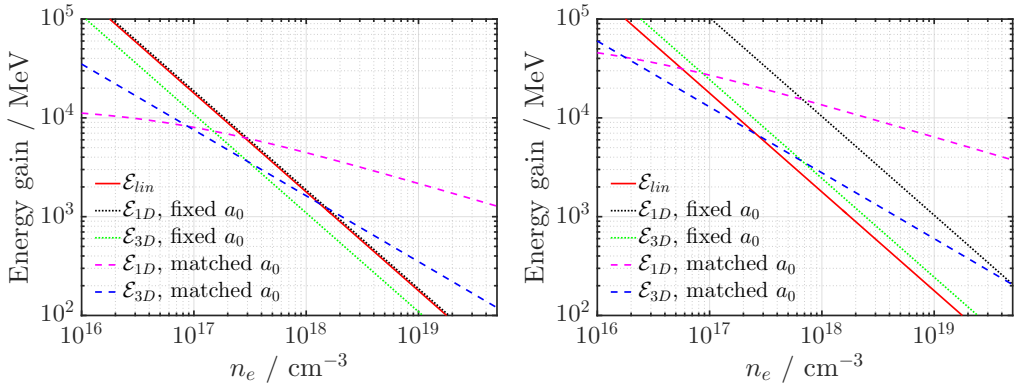

(a) $E = 10\,\mathrm{J}$, $\tau = 50\,\mathrm{fs}$ ***(b)*** $E = 50\,\mathrm{J}$, $\tau = 50\,\mathrm{fs}$

Figure 2.11: *Maximum single stage electron energy gains as predicted by different scaling laws: panel (a) shows the scalings for a 100 TW laser while panel (b) is for a 1 PW laser, both with 800 nm laser focussed with an $f/40$ optic to $w_0 = 26.24$ micron spot size. The resulting normalised vacuum potential is $a_0 = 1.8$ for 100 TW and $a_0 = 4.1$ for 1 PW case.*

of the work presented in this thesis. Additionally it does not require $w_0 \gg c/\omega_p$, hence is valid for spot sizes of the order of the plasma wavelength. Note that $\gamma_p^2 = \omega_L^2/\omega_p^2$ only for low intensities where pump depletion is neglected. Pulse etching rate is also neglected in Equation 2.74, whereas the denominator 3 arises from pump depletion in Equation 2.75.

As discussed earlier in Section 2.4.3, laser pulses self-focus in plasmas for powers exceeding P_c. It has also been shown that the pulse will tend to focus to a matched spot width and propagate with little further size changes.[63,116] Hence, if the plasma density is not matched to the vacuum focal spot size and laser intensity, the pulse will self-focus to achieve the matched size. Assuming no energy loss, the laser intensity for a matched spot size is given by

$$a_{0,m} = \left(\frac{w_0 a_0}{2}\frac{\omega_p}{c}\right)^{2/3}, \tag{2.76}$$

where a_0 and w_0 are the vacuum normalised vector potential and vacuum spot size. Albeit strictly only applicable in 3D non-linear theory, we can use this expression in the 1D non-linear case to explore the scalings of total energy gain as a function of plasma density. These are plotted in Figure 2.11 for a 50 fs, 800 nm linearly polarised laser pulse with either 10 J or 50 J of energy. The initial spot size is that obtained with an $f/40$ parabola, $w_0 = 26.24\,\mu\mathrm{m}$, yielding normalised vacuum potential of $a_0 = 1.8$ for the 100 TW and $a_0 = 4.1$ for the 1 PW case.

The Tajima and Dawson scaling in Equation 2.72 is shown as a red line and is

[116] S. P. D. Mangles *et al*, *IEEE T Plasma Sci* **36**, 2008.

independent of laser intensity. In the case of fixed a_0, both 3D non-linear and 1D non-linear theory energy gain predictions scale identically to Equation 2.72, with an offset provided by the intensity dependency. It is also evident that the 1D non-linear regime predicts extremely high energy gains even at very high plasma densities. This is, however, unphysical as the laser pulse is now longer than the plasma period and thus non-resonant. Although self-modulation of the long pulse would still drive a high amplitude wave, the energy scaling does not apply due to different scaling of peak accelerating field. Secondly, at high densities the laser would in fact self-focus rapidly and thus the $w \gg c/\omega_p$ approximation becomes invalid. Additionally, these simple predictions neglect energy depletion, which happens at a rate proportional to plasma density.

The dashed lines in Figure 2.11 make use of Equation 2.76 and thus include the effects of self-focussing. This invalidates the main assumption of the 1D non-linear theory and thus these scalings are unphysical. Indeed, it would predict 10 GeV energy gains for plasma densities of $10^{19}\,\mathrm{cm}^{-3}$. Of more interest are the 3D non-linear scalings with spot size that self-focusses to matched spot size. These predict energy gains of the order of GeV for $10^{18}\,\mathrm{cm}^{-3}$, which are in line with experimental observations. Interestingly, the energy gains are not too dissimilar to the Tajima and Dawson scaling.

The matched spot size in 3D non-linear regime is given by $w_m = 2\sqrt{a_0}/k_p$. Thus, if the pulse is focussed to $w_0 = w_m$, the energy scaling in Equation 2.75 can be rearranged to yield

$$\Delta\mathcal{E} = \frac{\omega_L^2}{6c^2} w_0^2 m_e c^2. \tag{2.77}$$

Hence, using a matched spot size in the 3D non-linear regime makes energy gain a function of the initial spot size only. This can be understood by remembering the matched spot size is determined by the plasma density and laser intensity. The quadratic dependence means that tripling the initial spot size leads to an almost order of magnitude increase in single stage energy gain for the same laser power. This scaling is depicted in Figure 2.12, showing the maximum electron energy gain as a function of laser spot size w_0 for matched guiding. The spot sizes obtained with standard focussing geometries available in the GEMINI laser are plotted with dashed lines, with the spot sizes being $w_0 = 16\,\mu\mathrm{m}$ for the $f/20$ and $w_0 = 32\,\mu\mathrm{m}$ for the $f/40$.

The simple estimate requires the laser to self-guide at the matched spot size and hence $P > P_\mathrm{c}$ is to be satisfied. Additionally, the laser intensity needs to be $a_0 > 2$ for the 3D non-linear theory to be applicable. The spot widths for which the laser power falls below P_c are also plotted for 300 TW and 1 PW. Thus, assuming perfect guiding with $P = P_\mathrm{crit}$, single stage energy gain of $\sim 20\,\mathrm{GeV}$ is predicted for 1 PW laser. This

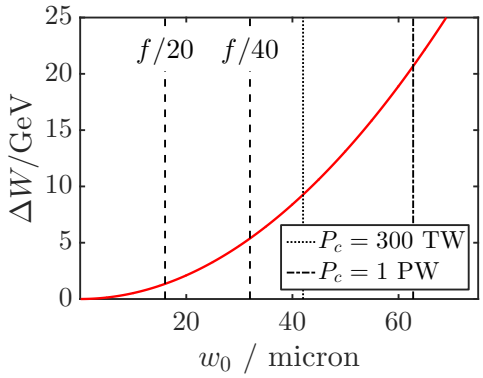

Figure 2.12: *Maximum electron energy gain in 3D nonlinear regime as a function of matched spot size w_0. The dashed lines show the ideal spot widths for* GEMINI *laser focussed with $f/20$ and $f/40$ configuration. The dotted and dotted-dashed lines show the spot size at which the laser power falls below the critical power for self focussing for 300 TW and 1 PW, respectively.*

scaling predicts energies similar to experimental observations.[117]

All the discussion this far has neglected laser depletion and assumed a constant power throughout the interaction. However, for non-linear interactions the laser pulse depletes with a constant rate dependent on the plasma density. Whilst modelling the actual power and spot size of the laser throughout the interaction is very complicated, simpler estimates based on total depletion length can be derived.

If the laser pulse is depleted before dephasing is reached the relevant acceleration length is $L_{\rm acc} = L_{\rm dpl}$. This is independent of laser intensity and instead a function of pulse length. In 3D non-linear regime the electric field is linear in the bubble and thus

$$\mathcal{E}(z) = \sqrt{a_0} E_0 \left(1 - \frac{z}{L_{\rm dpl}}\right). \tag{2.78}$$

The field at the rear of the bubble is simply $E_p = \sqrt{a_0} E_0$ and if an electron accelerates for a distance L the average field felt by it is $E_{\rm acc,av} = [E_p + E(L)]/2$. Hence, the total energy of the particle is

$$\mathcal{E} = \sqrt{a_0} E_0 \left(1 - \frac{L}{2L_{\rm dpl}}\right) L. \tag{2.79}$$

The pump depletion limited energy gain is found by setting $L = L_{\rm dpl}$.

The maximum energy gain in the 3D non-linear regime for both self-matched spot size and a fixed a_0 is shown in Figure 2.13. The laser pulse here is of 50 fs duration and 15 J energy, focussed to a 26 micron spot with an $f/40$ optic. The energy gains are calculated using Equation 2.79 by using the depletion length $L_{\rm dpl}$ as the acceleration

[117] S. Kneip *et al*, *Phys Rev Lett* **103**, 2009.

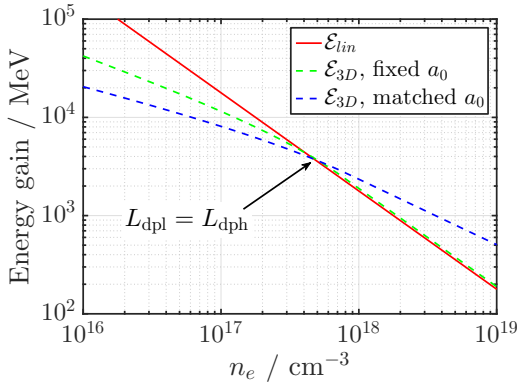

Figure 2.13: *Maximum single stage electron energy gain including pump depletion length for a fixed a_0 and a matched a_0. The 300 TW laser ($E = 15$ J, $\tau = 50$ fs) is focussed with an $f/40$ optic to $w_0 = 26.24$ micron spot size.*

length. The scaling changes at the point where $L_{\mathrm{dpl}} = L_{\mathrm{dph}}$, with the energy gain now limited by pulse depletion. Pump depletion is a limitation for lower density plasmas, where the wake phase velocity is sufficiently high to yield long dephasing lengths. Note this scaling is not plotted for a fixed plasma length. Including a fixed plasma length severely limits energy gain for lower plasma densities, where the accelerating field is lower.[18]

Albeit only strictly valid the under stated assumptions, these scaling laws provide a very useful general estimate of achievable single stage energy gains. They all indicate that energy gain increases with decreasing plasma density and increasing laser intensity. The advent of PW scale laser facilities in the near future will allow for 10 GeV scale single stage energy gains, allowing laser plasma accelerators to be used to their full potential.

2.5.6 Trapping and injection

Injection is the common term used to describe the process of inserting a beam into an accelerator. This needs to be performed with high precision, to ensure the bunch is in the correct phase of the accelerating field. Injection is intimately related to the concept of trapping in plasma waves, as the latter describes the phase an electron needs to be injected into the wake to gain energy from it.

[18] Cf. Section 7.4, Figure 7.22.

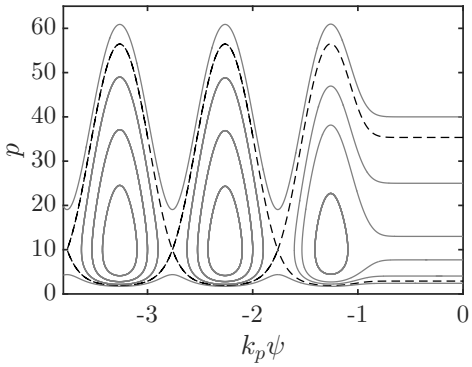

Figure 2.14: *Electron trajectories in (p, ψ) phase space in a plasma wave with $\phi_0 = 0.1$ and $\gamma_p = 10$, excited by a laser pulse centred at $\psi = 0$. The solid grey lines describe trajectories of test electrons, with closed orbits corresponding to trapped electrons. The black dashed lines represent the separatrix.*

Trapping in 1D plasma wave

Particle motion in a 1D plasma wave can be analysed by studying the (p, ψ) phase space, where $\psi = k_p\xi = k_p(z - v_g t)$ is the phase of an electron in a plasma wave.[115] Consider a linear wave with potential given by $\phi = \phi_0 \cos\psi$, where ϕ_0 is the maximum value of potential. Test electrons will follow phase space orbits for which the Hamiltonian

$$\mathcal{H}(\gamma, \psi) = \gamma - \beta_p p - \phi(\psi) = \text{const}, \tag{2.80}$$

with $p = \gamma\beta$ and β_p is the phase velocity of the wake. Numerical solutions for electrons in the (p, ψ) phase space are depicted in Figure 2.14, where the plasma wave is excited by a laser centred at $\xi = -1$ with $\gamma_p = 10$ and $\phi_0 = 0.1$. Test electron phase space orbits are shown as solid lines. Depending on its initial momentum and phase, an electron will either stream backwards in the plasma wave or become trapped in the potential of the wake.

An electron is trapped when it undergoes periodic acceleration and deceleration within one period of the wake. As the particle stays within the potential of the wave its trajectory is manifested as a closed orbit in (p, ψ) phase space. This type of motion occurs if the electron's longitudinal velocity exceeds the phase velocity of the wake at the rear of the bubble, $v_z > v_p$. The trajectory in phase space that separates trapped orbits from untrapped is the separatrix, depicted as the dashed line in Figure 2.14. The separatrix is given by $\mathcal{H}_s \equiv \mathcal{H}(\gamma_p, \psi_{\min})$, where $\phi_{\min} \equiv \phi(\psi_{\min})$. Electrons will be trapped if $\mathcal{H} \leq \mathcal{H}_s$.

Self-injection

A large variety of different injection methods have been proposed for laser plasma accelerators. The most straightforward of these relies on some of the plasma electrons becoming trapped in the wakefield. As in this case an electron is generated from within the plasma this process is called self-injection.

To make some electrons dephase from the collective plasma oscillation the wave needs to be driven to very high amplitudes. Effectively, it is required for the wave to break. Self-injection is hence a highly non-linear process. Self-injection was first observed experimentally by Modena *et al* in 1995.[38] Self-injection in full blowout regime was later observed in 3D PIC simulations by Pukhov and Meyer-ter-Vehn.[49] A number of analytical approaches have since been developed to explain self-injection and find a threshold for it. The first of these to be put forward is a phenomenological theory based on observations from PIC simulations, proposed by Kostyukov *et al* in 2004[118] and further refined in 2009,[61] here referred to as KNPS model. The accelerator is modelled as a static spherical ion cavity, moving at γ_p. The threshold for self injection is formulated by requiring a sufficiently large bubble size,

$$R_m \gtrsim \sqrt{2}\gamma_p k_p^{-1}, \tag{2.81}$$

where R_m is the bubble size. Physically, this condition requires an electron to still be within the boundary of the ion bubble when its transverse momentum changes direction. It is assumed that if an electron is in the bubble at this time point, it will remain in the bubble for all later times.

Thomas put forward a model for self injection by assuming elliptical trajectories within an elliptical bubble.[119] The trapping condition

$$R_m \gtrsim 2\sqrt{\ln(2\gamma_p^2) - 1}k_p^{-1} \tag{2.82}$$

requires an electron, stationary in the lab frame before the laser arrives, not to slip back further than the bubble radius as it loses energy in the fields of the bubble.

Comparing the static bubble models by Thomas and KNPS, plotted in Figure 2.15, shows remarkedly different behaviour. The required a_0 plotted in Figure 2.15 is found from $k_p R_m = 2\sqrt{a_0}$ while the phase velocity $\gamma_p = \omega_L/(\sqrt{3}\omega_p)$ is that of the back of the bubble. The KNPS model severely overestimates the required laser intensities, even for

[38] A. Modena *et al*, *Nature* **377**, 1995.
[118] I. Kostyukov *et al*, *Phys Plasmas* **11**, 2004.
[61] I. Kostyukov *et al*, *Phys Rev Lett* **103**, 2009.
[119] A. G. R. Thomas, *Phys Plasmas* **17**, 2010.

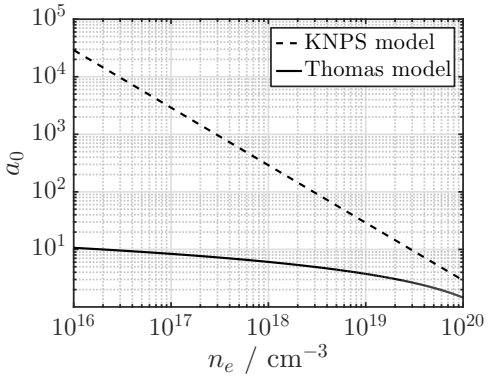

Figure 2.15: *Required laser intensity a_0 for self injection according to the KNPS and Thomas models.*

high densities. This implies the condition used to define self-injection is too restrictive. Thus assuming the velocity of the back of the bubble can be modelled correctly, Thomas' model provides a reasonably accurate and robust self-injection threshold. Experimental evidence suggesting the validity of the Thomas model has also been published.[120]

An alternative approach is to use an expanding bubble model, as proposed by Kalmykov *et al*.[62,121] In this theory, they note that as the bubble expands, the potential inside it evolves and thus the hamiltonian of plasma particles is changing. For initially untrapped particles far from the bubble the potential $A_z = \phi = 0$ and the hamiltonian $H = \sqrt{1+\mathbf{p}^2} - \beta_p p_z > 0$. Hence any particle with $H < 0$ must be trapped in the bubble. As initially $H = 1$, the requirement for injection is $\Delta H < -1$.

The expanding bubble model has shown to be a good way to describe the self-injection process. Shadowgraphy of the bubble as it propagates has shown that the bubble does indeed expand before self-injection, and that there is a threshold rate for this expansion.[74] Additionally, as density transitions modify the bubble size, this theory provides a natural explanation for density downramp injection.

However, a large drawback of this model is the assumption of a perfectly spherical cavity. This yields minimum threshold rates that are too high and diverge from experimental observations. The total change in Hamiltonian ΔH for a test electron as a function of initial bubble size and expansion rate is plotted in Figure 2.16 along with some estimates for recent experiments. Points A,[50] B,[51] C[117] and D[56] correspond to

[120] S. P. D. Mangles *et al*, *Phys Rev Spec Top-Ac* **15**, 2012.
[62] S. Kalmykov *et al*, *Phys Rev Lett* **103**, 2009.
[121] S. A. Yi *et al*, *Plasma Phys Contr F* **53**, 2011.
[74] A. Sävert *et al*, *Phys Rev Lett* **115**, 2015.
[50] S. P. D. Mangles *et al*, *Nature* **431**, 2004.
[51] J. Faure *et al*, *Nature* **431**, 2004.
[56] X. Wang *et al*, *Nat Comms* **4**, 2013.

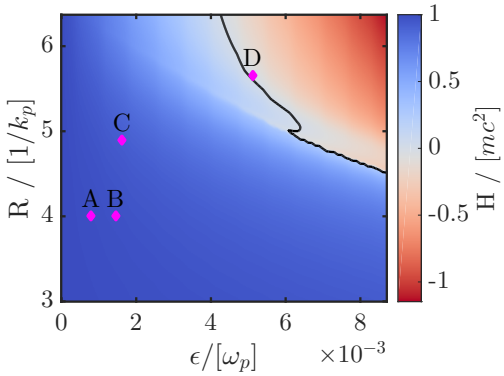

Figure 2.16: *Total change in Hamiltonian of a test particle in an expanding bubble. The bubble expands for 4 plasma periods and the black line separates regions of injection ($\Delta H < 0$, red) and no injection ($\Delta H > 0$, blue). Points A,[50] B,[51] C[117] and D[56] correspond to recent experimental results, where a 20 % expansion over 300 micron distance is assumed. Additionally, for A and B a self-focussed intensity of $a_0 \simeq 4$ is used (hamiltonian data from Ref 122.)*

recent experiments, where for A and B a self-focussed intensity of $a_0 \simeq 4$ is used while for C and D the reported estimate is utilised. The bubble is assumed to expand by 20 % in 300 microns, with the final size corresponding to the value used in Ref 62. Note direct measurements of bubble evolution gives a similar final bubble size and expansion distance.[74] It is clear that while the model does correctly predict self-injection for very large bubble sizes as in the case of D, for a plethora of experiments the theory fails to predict correct threshold.

It was recently shown that the expanding bubble model can be expanded by including charge buildup at the rear of the bubble.[122] It is well documented that due to sheet crossing in multiple dimensions there is a buildup of electrons at the back of the bubble, increasing the potential. Adding this increase in the potential was shown to reduce the threshold for self-injection and correctly predict injection in near-threshold cases.[122] However, this model adds another free parameter η, the fraction of electrons that stay within the sheath in the rear half of the bubble. Additionally, the potentials need to be integrated numerically (similarly to Ref 62) and thus a robust and straightforward determination of the threshold is not possible.

Whilst all presented self-injection models have their merits, one prevailing theory has not yet surfaced. This is in part due to the different density and laser intensity regimes. Terawatt level lasers typically require very high densities to self-inject and rely very heavily on self-compression and self-focussing. These intricate non-linear effects make finding an accurate and versatile self-injection threshold very difficult. For systems with large powers, the vacuum vector potential can be large enough to drive

[122] M. R. Islam *et al*, *New J Phys* **17**, 2015.

a highly non-linear bubble, even in very rarefied plasmas. Semi-empirical models, such as that by Mangles *et al*,[120] have been shown to overcome some of these difficulties predicting self-injection threshold over a large parameter range of experiments.

Ionisation induced injection

As self-injection is a highly non-linear process it is also difficult to control. Additionally, it can result in beams that have many beamlets and poor focussing properties. Hence, much work has been done to develop alternative injection techniques.

One of the simplest alternative injection techniques is ionisation induced injection. Here, a gas with tightly bound inner shell electrons is used as the target. The leading edge of the laser ionises the outer shell electrons, with only the peak of the laser having high enough intensity to suppress the Coulomb barrier of the innermost electrons. Thus these electrons are ionised inside the plasma cavity. Being born in a region of non-zero potential they gain more energy streaming backwards in the bubble and can be trapped in the cavity.

Ionisation injection can be studied in a 1D non-linear plasma wave with hamiltonian analysis by solving Equation 2.39. The hamiltonian is now given by[123]

$$\mathcal{H}(\mathbf{u},\psi) = (\gamma_\perp^2 + u^2)^{1/2} - \beta_p\gamma\beta - \phi(\psi), \tag{2.83}$$

where $\gamma^2 = \gamma_\perp^2 + u^2$ and $\gamma_\perp^2 = 1 + u_\perp^2$. The separatrix is given by $\mathcal{H}_s = \gamma_\perp(\psi_{\min})/\gamma_p - \phi_{\min}$. For electrons ionised at phase ψ_i in the wake, the trapping conditions is[123,124]

$$1 + \phi_{\min} - \phi(\psi_i) \leq \frac{\sqrt{1 + \frac{a^2(\psi_i)}{2}}}{\gamma_p} \tag{2.84}$$

for a linearly polarised laser. Figure 2.17a shows laser intensity required to trap an electron ionised at phase ψ_i in a wakefield for different plasma densities. The laser is centred on $\psi = 0$, pulse length is fixed at $\tau_{\mathrm{FWHM}} = 35$ fs and the wake is calculated using Equation 2.39. It is also assumed the electron is ionised at the phase peak of a laser oscillation, such that $a(\psi_i) = 0$. A pulselength of 35 fs corresponds to a resonant pulse length for $n_e = 2.5 \times 10^{18}\,\mathrm{cm}^{-3}$. For modestly relativistic lasers, $a_0 \simeq 1.5$, trapping of ionised electrons only occurs if the wake is excited by a pulse with a duration close to resonance. Also, it is evident that trapping of electrons ionised near the peak of the laser is only possible for relativistic laser pulses. As seen from Figure 2.17, trapping at the peak of the laser, with $\psi = 0$, requires $a_0 > 1.6$.[123]

[123] M. Chen *et al*, *Phys Plasmas* **19**, 2012.
[124] A. Pak *et al*, *Phys Rev Lett* **104**, 2010.

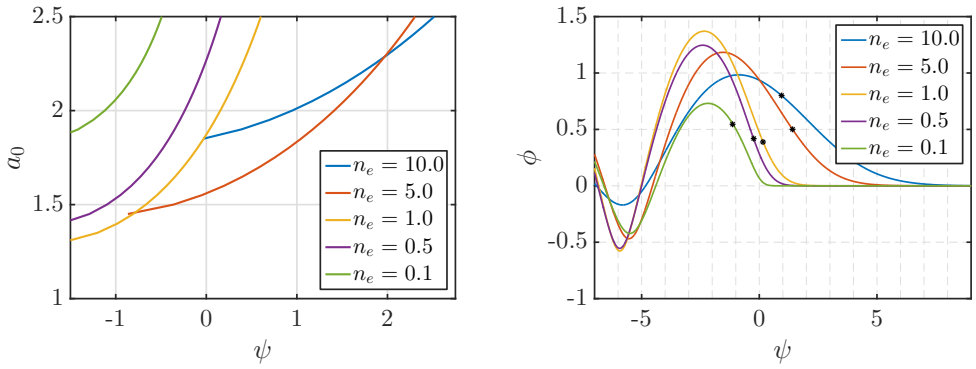

(a) *Intensity threshold* ***(b)*** *Trapping phase*

Figure 2.17: *Trapping threshold for ionisation induced injection into a wake excited by a 30 fs laser pulse centred at $\psi = 0$ for different plasma densities $n_e[\times 10^{18}\,\mathrm{cm}^{-3}]$. Panel (a) shows the required laser intensity to trap and electron ionised at a given phase in the wakefield whereas (b) depicts the potential of the excited wakefield for $a_0 = 2$ along with the phase where ionised electrons are trapped.*

For plasma densities where pulselength is far from resonance, higher initial laser intensity is required to ensure trapping. This can be seen from Figure 2.17a, with trapping requiring a_0 as high as 2.3 for $n_e = 5 \times 10^{18}\,\mathrm{cm}^{-3}$. This behaviour is further illustrated in Figure 2.17b depicting the excited wake for different plasma densities for $a_0 = 2$ along with the phase where ionised electrons will be trapped. For the closely resonant case, $n_e = 5 \times 10^{18}\,\mathrm{cm}^{-3}$, electrons will be trapped if born up to $\psi \sim 1.5$ before the peak of the laser. For non-resonant cases, the electrons can only be trapped if born very close to the peak of the laser.

2.5.7 Beam loading

Beam loading is the general name given to a variety of phenomena that arise when a particle bunch interacts with the accelerator cavity. This topic is covered extensively in radio-frequency cavities, with effects such as phase slip, cavity detuning, cavity harmonic mode excitation by the bunch and energy spread increase arising.[125]

Changes to the accelerator cavity have been analysed in the case of plasma based accelerators. The framework in the linear regime was developed by Katsouleas *et al*.[126,127] They derive a maximum amount of charge that can be loaded into the wake

[125] J. E. Leiss, *IEEE Trans Nucl Sci* , 1965.
[126] T. Katsouleas *et al*, *Part. Accel.* **22**, 1987.
[127] S. Wilks *et al*, *IEEE T Plasma Sci* **15**, 1987.

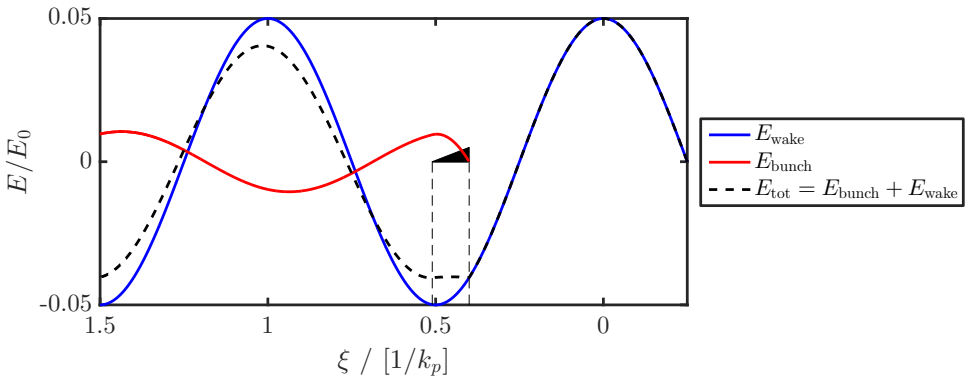

Figure 2.18: *Total wakefield of tailored witness bunch in a linear plasma wave, yielding a flat accelerating gradient in the bunch.*

by considering the number of particles for which the wake vanishes:

$$N_0 = 5 \times 10^5 \left(\frac{\delta n}{n_0}\right) \sqrt{n_0} A, \tag{2.85}$$

where δn is the density perturbation of the wake, n_0 is the plasma density in cm^{-3} and A is the cross sectional area of the wake, in cm^2. However, for maximum number of particles a 100% efficiency in energy conversion is only achieved by allowing a 100% energy spread.

In the linear regime the witness bunch can be tailored to create a non-chromatic accelerating field. This can be be done with a triangularly shaped bunch. As we are working in the linear regime, the total excited wakefield is simply the superposition of the wake from the witness bunch and the driver bunch, as depicted in Figure 2.18. The wake created by the driver bunch is $E_{\text{wake}} = E_0 \cos(k_p \xi)$ and the field created by the witness bunch is found from[127]

$$E_{\text{bunch}} = -c \int_{\xi_0}^{\xi} \mathrm{d}\xi' \rho(\xi') E_0 \cos[k_p(\xi - \xi')] \tag{2.86}$$

where $\rho(\xi)$ is the longitudinal charge density. The total wake is just the linear sum of these two.

As mentioned in preceding sections, the linear wakefield regime suffers some serious drawbacks. Firstly the transverse focussing fields are not linear, thus leading to emittance growth. Secondly, even though the axial wakefield may be flattened by proper tailoring of the linear charge density, the longitudinal fields are dependent on distance from beam axis. Thus regardless of proper beam loading electrons at different radial positions will be accelerated at different rates and thus increase bunch energy spread.

Thirdly, as shown in Ref 126, the total useful area the witness bunch can extract energy from is of the order of skin depth $(c/\omega_p)^2$. Thus Equation 2.85 becomes

$$N_0 = \left(\frac{\delta n}{n_0}\right) n_0 k_p^{-3} \simeq \frac{1.5 \times 10^{17}}{\sqrt{n_e[\,\mathrm{cm}^{-3}]}} \left(\frac{\delta n}{n_0}\right). \tag{2.87}$$

Allowing for a density perturbation of $\delta n/n_0 \sim 1$ yields a maximum value for accelerated charge. For a modest density of $1 \times 10^{18}\,\mathrm{cm}^{-3}$ this gives a maximum charge of just 24 pC. Thus the linear regime is inefficient, as well as not maintaining beam quality.

Beam loading theory in wakefield accelerators was extended to the 3D non-linear regime by Tzoufras *et al*;[128,129] building on the 3D non-linear theory of wakefield generation by Lu *et al*. Within the ion column the pseudopotential describing the electromagnetic fields is given by $\psi(\xi, r) = [(1+\beta)r_b^2 - r^2]/4$, where $r_b \equiv r_b(\xi)$ and $\beta \equiv \beta(\xi)$ is the ratio of sheath thickness to the bubble radius at ξ. The accelerating and focussing fields are given by $E_z = -\partial\psi/\partial\xi$ and $E_r - B_\theta = \nabla_\perp \psi$. It is clear from the definition of ψ that $\partial E_z/\partial r = 0$ and $\partial(E_r - B_\theta)/\partial\xi = 0$. Thus in the non-linear regime there is no transverse dependence on accelerating gradient nor is there longitudinal variation of focussing forces.[19] Introduction of a witness bunch into the cavity can only modify the shape of the sheath r_b. Thus even in the presence of trailing load, focussing forces remain linear and independent of ξ. While the shape of E_z changes, $\partial E_z/\partial r = 0$ still holds.

The shape of the sheath in the presence of a trailing bunch can be calculated analytically for flat top and trapezoidal longitudinal profiles of witness bunches.[20] Assuming relativistic blowout, such that Equation 2.41 can be used, an additional source term arising from the witness bunch is added:[129]

$$r_b \frac{\mathrm{d}^2 r_b}{\mathrm{d}\xi^2} + 2\left(\frac{\mathrm{d}r_b}{\mathrm{d}\xi}\right)^2 + 1 = \frac{4\lambda(\xi)}{r_b^2}, \tag{2.88}$$

with $\lambda(\xi) = \int_0^{r \gg \sigma_r} r n_b \mathrm{d}r$ and $n_b \equiv n_b(\xi, r)$ is the shape of the trailing bunch. Once the shape of the sheath is found, the wakefield is given by $E_z = r_b r_b'/2$ in the ultrarelativistic case. The optimum trailing bunch shape, one that flattens the accelerating field within the load, is found to be trapezoidal as in the linear wake case. The shape of the bubble with and without an optimally tailored beam load is shown in Figure 2.19a. The

[128] M. Tzoufras *et al*, *Phys Rev Lett* **101**, 2008.
[129] M. Tzoufras *et al*, *Phys Plasmas* **16**, 2009.
[19] Cf. Section 2.3.3
[20] Gaussian profiles can also be used by approximating them as flat top bunches with length $\Delta\xi = 2\sqrt{2}\sigma_z$.

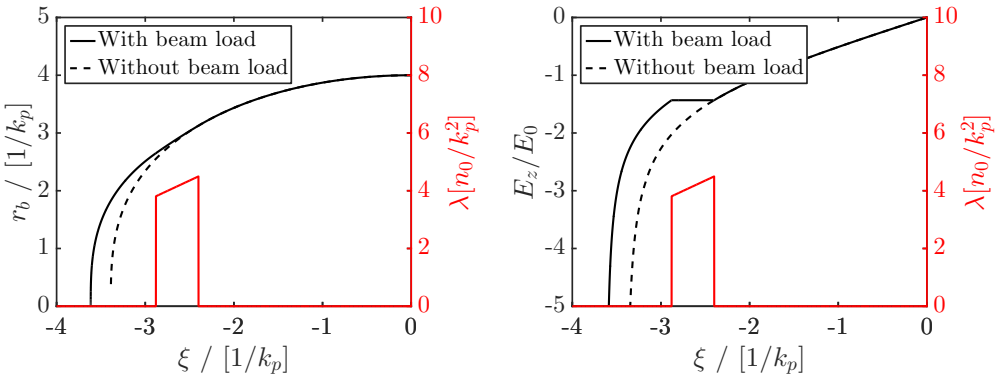

(a) Bubble shape *(b) Longitudinal field*

Figure 2.19: *Beam loading of a non-linear 3D wake for $a_0 = 4$ for the case of optimally tailored bunch profile. Panel (a) depicts the shape of the sheath defining the bubble with and without a witness bunch while panel (b) shows the longitudinal electric field.*

presence of the witness bunch causes electrons in the sheath to slow their return onto the axis and thus lengthens the bubble. The resulting longitudinal electric field in the ion column is plotted in Figure 2.19b along with the current profile of the witness bunch. Note that the constant field within the bunch is of the order of the cold wavebreaking limit.

The maximum amount charge that can be loaded into a non-linear bubble, for a constant wakefield, is given by[129]

$$N_{tr} = \frac{\pi}{16}\frac{R_b^4}{E_t} n_0 k_p^{-3} \simeq \frac{R_b^4}{E_t}\frac{3\times 10^{16}}{\sqrt{n_e[\,\mathrm{cm}^{-3}]}} \tag{2.89}$$

where $R_b = 2\sqrt{a_0}$ is the maximum blowout radius and $E_t = E_z(\xi_t)$ is value of electric field at the front of the witness bunch, both in normalised units. Equation 2.89 assumes the bunch extends from ξ_t to the end of the ion column, where the sheath defining the bubble shape reaches the laser axis. As an example, consider the bubble shown in Figure 2.19, with $a_0 = 4$, $E_t = 1.43$ and background density $n_e = 1\times 10^{17}\,\mathrm{cm}^{-3}$. If the witness bunch depicted in Figure 2.19 extended to the end of the bubble, the total amount of charge that could be accelerated is 2.7 nC. Hence non-linear wakes are ideal for electron beam acceleration, offering very high accelerating fields, emittance conservation and maintaining energy spread for beams with high charge.

CHAPTER 3
Experimental methods

THE MOST CRUCIAL PART OF ANY EXPERIMENT is the suite of diagnostics used to characterise its outcome. Properties of particular diagnostics hence affect experimental physics in the most intimate way. It is a challenge for any experimentalist to become well acquainted with the apparatus being used in order to be certain that what has been measured is what did actually occur. Thus understanding the limitations and working principles of diagnostics form the basis of any successful experiment.

This chapter will explore experimental methods and approaches used in the work presented in this thesis. The fundamentals of high power laser systems will be discussed. We will explore diagnostics used to determine the properties of laser pulses used to drive laser plasma accelerators. Methodology of measuring accelerated electron beams will be presented and software used to analyse data discussed. There will be an overview of gas targets used in the experiments presented in this thesis. Finally, we will explore computer codes used to simulate these very complex phenomena.

3.1 Laser physics

Invented in 1960[130] and first dubbed to be a "solution looking for a problem",[131] the laser[1] has since become ubiquitous in modern life. Indeed, this very document is likely to have been printed by a laser printer. However, unlike the lasers in everyday use where they fulfil tasks from transmitting data to scanning barcodes, the laser systems used in the present work are of very different category. Capable of achieving powers in excess of petawatts, high power laser systems are complex machines capable of producing

[130] T. H. Maiman, *Nature* **187**, 1960.
[131] C. H. Townes. "The first laser". In: *A Century of Nature: Twenty-One Discoveries that Changed Science and the World*. Ed. by L. Garwin *et al.* University of Chicago Press, 2004, pp. 105–119.
[1] Acronym for Laser Amplification by Stimulated Emission of Radiation.

nuclear fusion,[132] compressing matter to pressures comparable to the centre of stars[133] or accelerating particles to high energies in mere centimetres.[134]

3.1.1 High power laser systems

Light Amplification by Stimulated Emission of Radiation

Einstein showed in 1917[135] that in addition to spontaneous quantum transitions an electron can also undergo stimulated transitions.[2] If an atom in an excited state is stimulated by a photon, the excited electron will relax into a lower state, thus emitting another photon. This reaction will only occur, however, if the energy of the stimulating photon is equal to the energy difference between the excited and the lower state of the electron. The emitted photon will be coherent with the initial photon, effectively being a copy of it. Hence, if a volume contains a large fraction of excited atoms, an incident beam of light with the correct wavelength can effectively be amplified – the exiting beam will have a much higher flux due to an increased number of photons.

To achieve amplification of light, the fraction of atoms in an excited state must be large. In fact, it can be shown that amplification can only be achieved when population inversion is established, i.e. when there are more atoms in excited state than in the ground state.[137] This requires energy to be put into the gain medium. This is done by pumping the laser medium, either with electron beams,[138] explosion,[139] flashlamps[130] or by using another laser. The latter option yields higher efficiencies, as from the broad spectrum output by flashlamps only particular wavelengths will couple into exciting atoms in the gain medium. The highest efficiency method is the use of diode pumping, envisaged to dramatically increase the wall-plug efficiency of high power lasers.[140]

Q-switching

The peak output power of lasers has grown more than 10 orders of magnitude since the first demonstration. A lot of that progress is due to making the output pulse shorter. The first innovation to enable the generation of very short pulses was Q-switching.[141]

[132] O. A. Hurricane *et al*, *Nature* **506**, 2014.
[133] R. F. Smith *et al*, *Nature* **511**, 2014.
[134] M. Dunne, *Science* **213**, 2006.
[135] A Einstein, *Phys Z* **18**, 1917.
[2] It was later realised that the spontaneous transitions are actually caused by quantum fluctuations of vacuum, which effectively create virtual photons that stimulate the atom to emit a real photon.[136]
[137] A. Siegman. *Lasers*. University Science Books, 1990.
[138] J. D. Sethian *et al*, *Phys Plasmas* **10**, 2003.
[139] J. Tulip *et al*, *Appl Phys Lett* **19**, 1971.
[140] S. Banerjee *et al*, *Opt Lett* **37**, 2012.
[141] F. J. McClung *et al*, *J Appl Phys* **33**, 1962.

The technique is based on keeping the optical cavity in a high Q, or low gain, mode by disabling positive feedback. Hence, the pump energy is stored in the gain medium instead of being continuously extracted. At some point the feedback is reintroduced and thus the cavity is switched into low Q, high gain mode. Almost all of the energy stored in the cavity is now extracted in a single very short pulse.

Q-switching enables generation of laser pulses with pulse lengths of tens of nanoseconds. As such, in plasma physics Q-switched lasers find most use as pump sources in high power laser systems. These are also extensively used for industrial purposes, such as cutting and welding.

Modelocking

The second major improvement introduced in the 1960s was modelocking. The randomly seeded modes in an oscillator were locked in phase such as to allow the amplification of single, ultrashort pulses.

The modes travelling in an oscillator are separated by $\Delta\omega = 2\pi\frac{c}{2L} = 2\pi/T_c$, where L is the cavity length and T_c is the round trip time. Hence, the cavity will be populated by modes with angular frequencies $\omega_m = \omega_{ce} + m\Delta\omega$, with $m \geq 0$ and ω_{ce} is the cavity off-set frequency.[142] Only modes lying within the gain bandwidth of the lasing medium will actually be amplified. For titanium:sapphire this is $\Delta\omega = 86\,\mathrm{THz}$, meaning up to $N = 10^5$ can be supported.

The electric field of each mode can be written as

$$E(z,t) = E_m \exp\left[i(k_m z \pm \omega_m t + \phi_m)\right], \tag{3.1}$$

where E_m is the amplitude and ϕ_m is the phase of the mode with waves travelling in both positive and negative z directions allowed. If the laser oscillates simultaneously in N such modes the laser radiation leaking from the output coupler will be given by

$$E(z,t) = \sum_{m=1}^{N} E_m \exp\left[i(k_m z - \omega_m t + \phi_m)\right]. \tag{3.2}$$

Assuming equal mode amplitudes $E_m = E_0$ the output will depend most drastically on the relative phase of the different modes. This is illustrated in Figure 3.1, showing oscillator output intensity for 60 equal amplitude modes. If all modes have random phases, the output will be an incoherent addition of all the modes, as depicted in Figure 3.1a. This is referred to as CW mode of an oscillator. However, if all modes have the same phase, they will add constructively to produce short intense pulses separated by

[142] S. Hooker *et al. Laser Physics.* Oxford University Press, 2010.

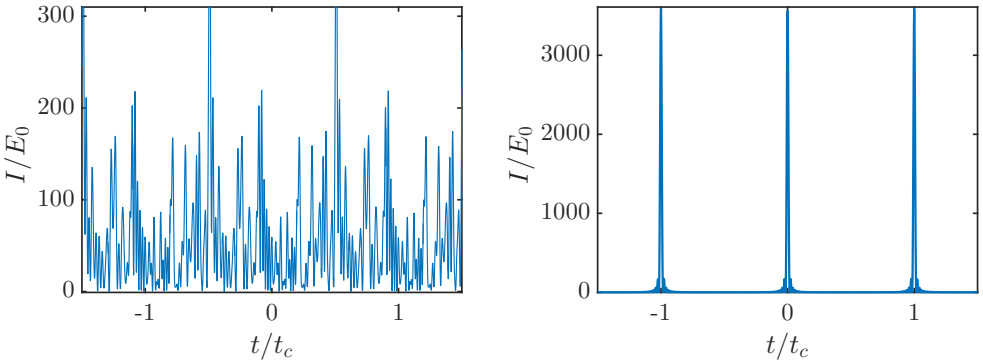

(a) *Random phase output* ***(b)*** *Modelocked output*

Figure 3.1: *Intensity of oscillator output $I(t)$ for 60 modes with (a) random phase and (b) locked phase. Fixed phase between modes leads to intensities up to N^2 times higher than individual modes.*

the cavity round trip time, as in Figure 3.1b. This situation is known as modelocking and is used in ultrashort pulse oscillators.

Different techniques for obtaining modelocking are in use and can generally be divided into active and passive methods. Most important and widely used of these is Kerr-lens modelocking.[143]

Ultrafast laser pulses

Any laser pulse is fully determined by its electric field as a function of time, $\mathcal{E}(t)$. It is mathematically more convenient to use the analytic function $E(t)$, where $\mathcal{E}(t) = 2 \cdot \Re[E(t)]$.[144] The analytic function is the one-sided inverse Fourier transform of the Fourier transform of the electric field;[145]

$$E(t) = \frac{1}{2\pi}\int_0^\infty \widetilde{E}(\omega)e^{-i\omega t}\mathrm{d}\omega; \qquad \widetilde{E}(\omega) = \int_{-\infty}^{\infty} E(t)e^{-i\omega t}\mathrm{d}t. \tag{3.3}$$

As the analytic signal is complex it can be expressed in terms of an amplitude and phase as

$$E(t) = |E(t)|\exp\left[i(\psi(t) + \psi_0 - \omega_L t)\right] + c.c., \tag{3.4}$$

where $|E(t)|$ is the time-dependent envelope, ω_L is the carrier frequency, ψ_0 is absolute phase, ψ_t is time-dependent phase and *c.c.* stands for complex conjugate. The absolute phase ψ_0 determines the position of the carrier frequency with respect to the envelope and time-dependent phase $\psi(t)$ specifies the occurrence of different frequencies at

[143] D. E. Spence *et al*, *Opt Lett* **16**, 1991.
[144] L. Cohen. *Time-Frequency analysis*. Prentice Hall, 1995.
[145] C. Iaconis *et al*, *IEEE J Quantum Elect* **35**, 1999.

different times. $|E(t)|^2$ is the temporal intensity of the pulse.

The Fourier transform of the analytic function yields the frequency representation or the spectrum of the pulse. As negative frequency components are unphysical, the spectrum is defined for positive frequencies $\omega > 0$ only and as a complex function, it can again be expressed in terms of amplitude and phase:

$$\widetilde{E}(\omega) = |\widetilde{E}(\omega)| \exp\left[i(\varphi_\omega(\omega) + \varphi_0)\right]. \tag{3.5}$$

Here $|\widetilde{E}(\omega)|$ is the spectral amplitude, φ_0 is the absolute phase and $\varphi(t)$ is known as spectral phase.

The laser pulse is completely determined by the amplitude and phase in either temporal or spectral domain. However, difficulties arise when describing short pulse propagation through media in the time domain. This is due to the transfer function being a convolution with the initial signal. Through the convolution theorem these become multiplications in the frequency domain – thus it is convenient to describe ultrashort pulses in the frequency domain.

Taylor expanding the spectral phase provides a useful tool to analyse the various effects of phase components:

$$\varphi(\omega) = \varphi_0^{(0)} + \varphi_0^{(1)}(\omega - \omega_L) + \varphi_0^{(2)}(\omega - \omega_L)^2 + \varphi_0^{(3)}(\omega - \omega_L)^3 + \ldots, \tag{3.6}$$

where $\varphi_0^{(n)} = \varphi^{(n)}(\omega_L)$ and $\varphi^{(n)} = \mathrm{d}^n\varphi/\mathrm{d}\omega^n$.[146] Of the expansion terms, the most widely know is second order phase $\varphi_0^{(2)}$, also known as chirp. Non-zero chirp results in different frequencies arriving at different times, thus increasing pulse width in the temporal domain.

As the spectral and temporal domain are related via a Fourier transform, the similarity theorem implies the widths in both domains are inversely related.[147] Hence, a wide spectrum will support a narrow pulse and vice versa. This is essentially the uncertainty principle – if a pulse is well localised in the temporal domain it will have a large uncertainty in the spectral energy domain.

The theoretical minimum of the product of pulse length and spectral width is called the time-bandwidth product (TBP),

$$\mathrm{TBP} = \Delta t \Delta\nu = \Delta t \, \frac{\Delta\omega}{2\pi}. \tag{3.7}$$

The widths Δt and $\Delta\nu$ are usually defined as Full Width Half Maximum (FWHM), an

[146] A. Monmayrant *et al*, *J Phys B-At Mol Opt* **43**, 2010.
[147] R. Bracewell. *The Fourier transform and its applications*. McGraw-Hill Higher Education, 2000.

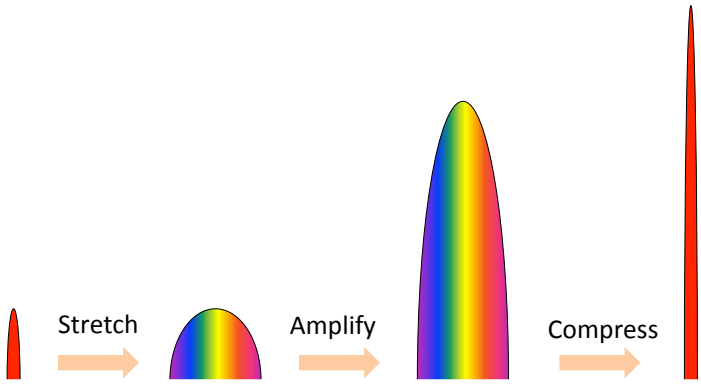

Figure 3.2: *Schematic diagram depicting the principle of chirped pulse amplification. An ultrashort pulse is first stretched, then amplified and recompressed to yield a higher power.*

easily measurable experimental quantity. TBP depends on the pulse shape; for a gaussian profile TBP = 0.441.[148] Any real pulse will have $\Delta t \Delta \nu \geq \mathrm{TBP}_{\mathrm{min}}$, with $\mathrm{TBP}_{\mathrm{min}}$ depending on the temporal profile of the pulse. Also, the shortest pulse duration can only be achieved with a flat spectral phase.[144]

Chirped pulse amplification

The increase in laser peak power had slowed considerably by the beginning of the 1980s, with the damage threshold of optical materials having been reached. As the flux could not be increased further, building lasers with larger peak powers meant increasing the beam size. This is, however, hugely cost ineffective. This hiatus in peak power increase prompted the development of chirped pulse amplification (CPA).[149]

The principle of CPA is depicted in Figure 3.2. An ultrashort pulse is passed through a stretcher. This is a dispersive system, which introduces a linear chirp to the pulse. Hence, each frequency will arrive at a different time, stretching the pulse in time. As the intensity of the pulse is reduced, it can now be safely amplified to much higher energies. The long, high energy pulse is finally passed through a compressor which counteracts the delay imposed on spectral components in the stretcher. Hence, the much higher energy pulse is temporally compressed again, yielding ultra high powers.[150]

[148] J. Diels *et al. Ultrashort Laser Pulse Phenomena.* Academic Press, 2006.
[149] D Strickland *et al*, *Opt Commun* **56**, 1985.
[150] P. Maine *et al*, *IEEE J Quantum Elect* **24**, 1988.

The Gemini laser

All of the work presented in this thesis was performed using the Gemini laser at the Central Laser Facility at Rutherford Appleton Laboratories.[151] Common to almost all high power laser systems, a master oscillator pulse is amplified using CPA. The schematic layout of the GEMINI laser is depicted in Figure 3.3.

The laser chain starts with an ultrashort oscillator, producing a 12 fs pulsetrain at 75 MHz. These short pulses are stretched in a glass block before being amplified to mJ energies in a preamplifier. A fast Pockels cell then selects pulses at 10 Hz for further amplification.

The Gemini laser provides pulses to 2 target areas. The first of these, Astra Target Area 2 (ATA2), receives pulses that have been amplified to 1 J level. Shots fired into ATA2 pass the grating based pulse stretcher only once and are stretched to 530 ps. Pulses delivered to Gemini target area are stretched to 1060 ps to allow for further amplification.

There are 3 bow-tie type power amplifiers after the stretcher, increasing the beam energy in stages up to 1 J. Pulses sent to ATA2 are then delivered to the target area where they are compressed to $\tau \simeq 40$ fs. With compressed energies of ~ 500 mJ, this represents a 10 TW scale laser system.

Double stretched pulses delivered to the Gemini target area are split after the third amplifier and then independently amplified up to 25 J. To accommodate such high energy, the beams are expanded to 150 mm before being compressed in two independent vacuum compressors. This yields two independently timeable 15 J, 30 fs, 500 TW laser pulses at a repetition rate of 20 s.[152] Up to 100 different parameters regarding each delivered shot are automatically recorded to allow for extensive data analysis.[153]

3.1.2 Laser focussing

Focussed intensities of high power laser systems, such as Gemini, can reach values in excess of 10^{22} W cm^{-2}.[154] While peak intensity is an important parameter, laser wakefield accelerators rely on a high intensity interaction for a very long propagation distance and hence beam behaviour near focus and away from it is important as well.

[151] STFC. *Astra Gemini laser system.* URL: http://www.clf.stfc.ac.uk/CLF/Facilities/Astra/12254.aspx (visited on 05/10/2016).
[152] C.J. Hooker *et al*, J. Phys. IV France **133**, 2006.
[153] E. J. Divall, Central Laser Facility Annual Report , 2008.
[154] V. Yanovsky *et al*, Opt. Express **16**, 2008.

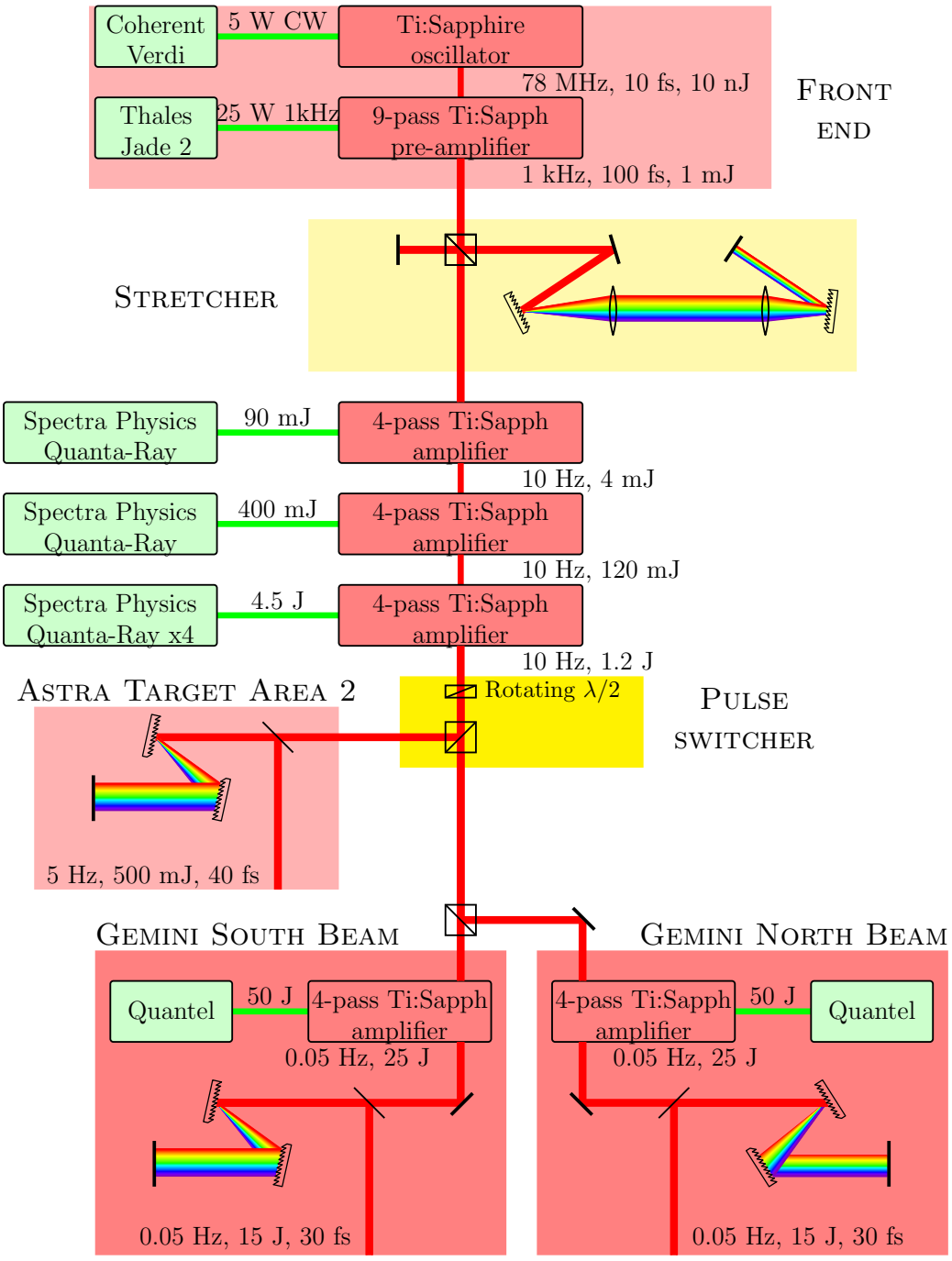

Figure 3.3: *Schematic layout of the* GEMINI *laser.*

Gaussian optics

The construction of optical cavities relies on the existence of stable transverse modes for any particular configuration. The most stable of these is formed by two concave mirrors, acting as to counteract the natural diffraction of the beam within the resonator. The modes of such a cavity are a superposition of waves propagating in the positive and negative z.[142] Each of these waves has the form of Gauss-Hermite beams, the lowest order of which has the functional form

$$E = E_0 \exp\left[i(kz - \omega t)\right] \frac{\exp\left(i\frac{kr^2}{2q}\right)}{q}. \tag{3.8}$$

This equation describes a spherical wave of amplitude E_0 with a complex radius given by $q = (z - z_0) - iz_R$, where z_R is the Rayleigh range.[3] For more clarity, Equation 3.8 can be expanded to read,

$$E = i\frac{E_0}{z_R} e^{i(kz-\omega t)} \times \frac{w_0}{w} \exp\left(-\frac{r^2}{w^2}\right) \times \exp\left(i\frac{kr^2}{2R}\right) \times \exp\left(-i\alpha\right). \tag{3.9}$$

The first term in Equation 3.9 expresses the amplitude of the wave and defines the direction of propagation towards positive z. The second term involves the spatially varying spot size,

$$w \equiv w(z) = w_0\sqrt{1 + \left(\frac{z - z_0}{z_R}\right)^2}. \tag{3.10}$$

With r being the distance from the beam axis, the exponential term signifies the gaussian shape of the beam. The transverse extent of the beam increases with propagation, with a minimum spot size $w_0 \equiv w(z_0)$ known as beam waist. This is a manifestation of natural beam diffraction. The Rayleigh range $z_R = \pi w_0^2/\lambda_L$ is the distance over which significant diffraction occurs. This is seen from Equation 3.10: after propagating a distance z_R, the beam size will have increased to $\sqrt{2}w_0$. As $I \propto w^2$, the intensity will be halved at $z = z_0 + z_R$. Both these concepts are illustrated in Figure 3.4, depicting a gaussian beam near its waist. Closely related to the concept of Rayleigh range is the beam divergence, $\theta = \lambda_L/(\pi w_0)$. This is the half-angle of beam divergence far from beam waist.

The third term in Equation 3.9 describes the shape of the wavefront of the pulse. Characterised by radius of curvature

$$R \equiv R(z) = (z - z_0) + \frac{z_R^2}{z - z_0}, \tag{3.11}$$

[3] This is also known as the confocal parameter, in which case it is usually denoted by b.

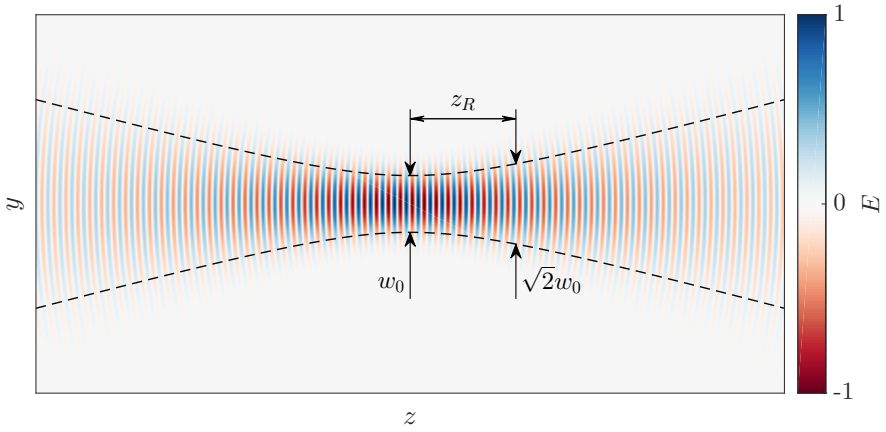

Figure 3.4: *Electric field of a focussing gaussian beam near focus. The dashed lines show evolution of spot size $w(z)$.*

this can be seen as the source term for diffraction. As energy propagates in the direction normal to the wavefront, this term creates either convergent or divergent flow of energy.

The last term in Equation 3.9 introduces a phase shift in addition to the usual kz factor. Known as Gouy phase shift it is given by $\tan\alpha = (z - z_0)/z_R$.[155] Albeit being irrelevant for long Rayleigh ranges, it is a significant factor when looking for stable modes of laser oscillators.[137]

Embedded gaussian

Not many physical laser beams propagate as perfect gaussian beams. Indeed, to extract maximal amount of energy from an amplifier crystal a top-hat beam profile is more desirable. Hence, real beams will be a superposition of many modes of Gauss-Hermite beams.

The power of gaussian beam optics can still be applied to realistic beams, though, by use of the embedded gaussian.[142] This is defined as a gaussian beam with the same divergence as the real beam, $\theta_G = \theta_R$, and a beam parameter product $w_0 \cdot \theta$ that is $M^2 \geq 1$ times larger than that of the embedded beam:

$$M^2 = \frac{w_{0R}\theta_R}{w_0\theta} \simeq \frac{\pi w_{0,R}}{\lambda_L f_n}. \tag{3.12}$$

Here use has been made of the definition of gaussian beam divergence θ and real beam divergence $\theta_R = 1/f_n$. The $f_n \equiv f/\#$ is defined as the focal length divided by beam diameter and is a useful measure of the speed of focussing of an optic system. The

[155] S Feng *et al*, *Opt Lett* **26**, 2001.

Rayleigh range for a real beam is thus defined as:

$$z_{R,R} = \frac{\pi w_{0,R}^2}{\lambda_L M^2}. \tag{3.13}$$

This value is larger than Rayleigh range for w_0, but smaller than Rayleigh range calculated for $w_{0,R}$. It is also clear that only a pure lowest order Gauss-Hermite beam has $M^2 = 1$.

As an example consider the far field of a top hat beam. The intensity distribution is the Airy disc, with $I \propto J_1^2(x)/x^2$, where J_1 is first order Bessel function of first kind and x is proportional to the distance from the beam axis.[156] The radius to first minima is given by $r = 1.22 f \lambda_L$.[4] However, measuring the $1/e^2$ radius[5] of intensity pattern, given by $0.82\lambda_L f$, yields a value of $M^2 = 0.82\pi/2 = 1.28$ for a diffraction limited Airy pattern.

Peak intensity

In order to obtain the peak intensity of a gaussian beam focus in terms of measurable quantities, we write the intensity at focus as

$$I(r,t) = I_0 e^{-(r/w_I)^2} e^{-(t/\tau_I)^2}, \tag{3.14}$$

where I_0 is the peak intensity and τ_I is the $1/e^2$ temporal duration of the pulse.[6] The total energy, which is routinely measured, is found by integrating over space and time. This is analytically possible for idealised spot shapes and temporal profiles; for experimentally measured focal spots the spatial integration is done on the image. The temporal factor can be found by either approximating a shape or measuring the pulse shape.

For a gaussian pulse given by Equation 3.14 total energy is given by:

$$\mathcal{E}_L = \int_{-\infty}^{\infty} P(t)\,\mathrm{d}t = \int_{-\infty}^{\infty}\int_S I(r,t)\,\mathrm{d}S\,\mathrm{d}t = 3.34\, I_0 w_I^2 \tau_{\mathrm{FWHM}}, \tag{3.15}$$

where τ_{FWHM} is the most often quoted FWHM temporal duration of the laser pulse. The peak intensity at focus can then be found from measured pulse energy, temporal

[156] M. Born *et al.* *Principles of Optics: Electromagnetic Theory of Propagation, Interference and Diffraction of Light.* Cambridge University Press, 1999.

[4] Cf. Appendix C

[5] This corresponds to $1/e$ value of electric field, which is the w_0 used to describe Gaussian beams.

[6] Note the that here we quote the $1/e$ value of intensity as w_I. This should not be confused with the w_0 used earlier, where it is related to the extent of the transverse electric field. As $I \propto E^2$, $w_I = w_0\sqrt{2}$.

duration and spot size:

$$I_0 = 0.299 \frac{\mathcal{E}_L}{w_I^2 \tau_{\mathrm{FWHM}}}. \tag{3.16}$$

The numerical value in Equation 3.16 is only 10% different from $1/\pi$, so calculating peak intensity intuitively viz $I_0 = \mathcal{E}_L/(S\tau_{\mathrm{FWHM}})$, where $S = \pi w_I^2$ will yield a close approximation. Additionally, when measuring the FWHM size[7] of the focal spot $d_s = \sqrt{2\ln 2} w_I$, the peak intensity is given by

$$I_0 = 0.415 \frac{\mathcal{E}_L}{{d_s}^2 \tau_{\mathrm{FWHM}}}. \tag{3.17}$$

Enclosed energy

Along with peak intensity the energy enclosed in the contour of the focal spot is a crucial parameter for determining the properties of the accelerator structure. Recent work[157,158] has shown that the final electron energy scales as the amount of energy enclosed in the FWHM contour. It is thus paramount to accurately characterise the fraction of energy within the central spot.

Figure 3.5 depicts calculated spatial profiles formed by an $f/40$ optic for a $\lambda_L = 800\,\mathrm{nm}$ laser pulse. Shown in Figure 3.5a, a perfect gaussian far field is the most widely used approximation when performing simulations. However, as mentioned earlier, in the near field most real laser beams are closer to top hat. The far field intensity distribution of a top hat beam, the Airy pattern, is shown in Figure 3.5b. Whilst the central spot is of slightly larger radius, the largest difference compared to the gaussian spot is the existence of rings around the central spot, caused by high spatial frequencies due to the sharp edge in the near field.[8]

The spot depicted in Figure 3.5b has a reasonable amount of energy displaced from the central spot. However, this calculation is for a perfectly flat spatial phase. In reality, the laser wavefront is not ideally flat and phase front errors cause more energy to be moved into the wings. Figure 3.5c depicts the far field of a top hat beam with a peak-to-valley wavefront error of $0.37\lambda_L$ and a root mean square wavefront error of $0.03\lambda_L$.

Radial profiles of intensity and energy enclosed are plotted in Figure 3.5d. The intensity profiles are normalised to their individual maxima. It is clear that the effect of wavefront distortions is to eject energy from the central spot to the wings of the pulse. Hence characterising the energy contained within the central spot is extremely

[7] Cf. Appendix C for more conversion factors between different pulse extents.
[157] S. P. D. Mangles *et al*, *Appl Phys Lett* **95**, 2009.
[158] G. Genoud *et al*, *Phys Plasmas* **20**, 2013.
[8] Cf. Appendix C for more details.

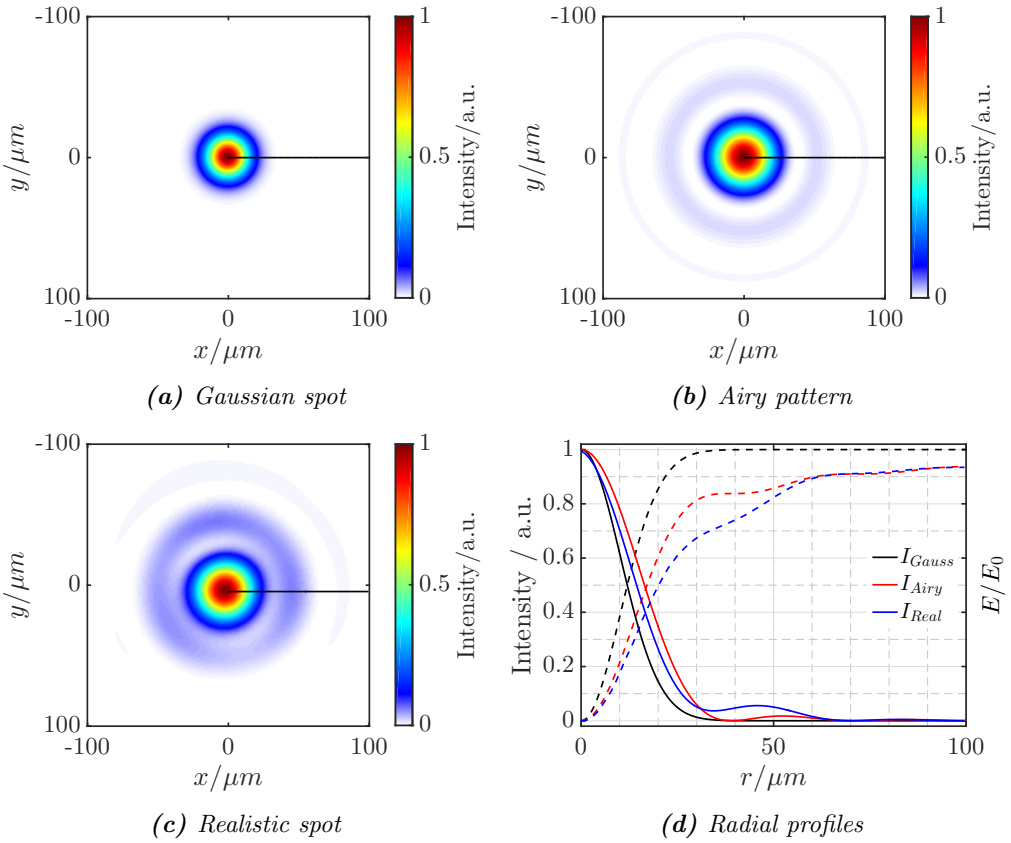

(a) *Gaussian spot* ***(b)*** *Airy pattern*

(c) *Realistic spot* ***(d)*** *Radial profiles*

Figure 3.5: *Simulated focal spot profiles for an $f/40$ optic focussing 800 nm light. Panels (a) and (b) depict the far field of Gaussian and perfect top-hat near field beams whereas panel (c) shows the intensity pattern of a top hat beam with a $0.37\lambda_L$ peak-to-valley wavefront error. Intensity and enclosed energy line-outs, taken along the black line in Panels (a), (b) and (c), are plotted in panel (d).*

important to accurately simulate the interaction.

3.2 Transmitted laser diagnostics

Since a laser pulse, propagating in a sufficiently underdense plasma, moves at almost c, it is very difficult to diagnose the wakefield structure *in situ*. Thus measuring the wake structure requires probe pulses on a single cycle timescale in order to freeze out the movement of the laser.[74,159] Hence, on a typical electron acceleration experiment a host of other parameters about the laser pulse and plasma are measured.

A fundamental suite of diagnostics used on almost all experiments is the so-called

[74] A. Sävert *et al*, *Phys Rev Lett* **115**, 2015.
[159] A. Buck *et al*, *Nat Phys* **7**, 2011.

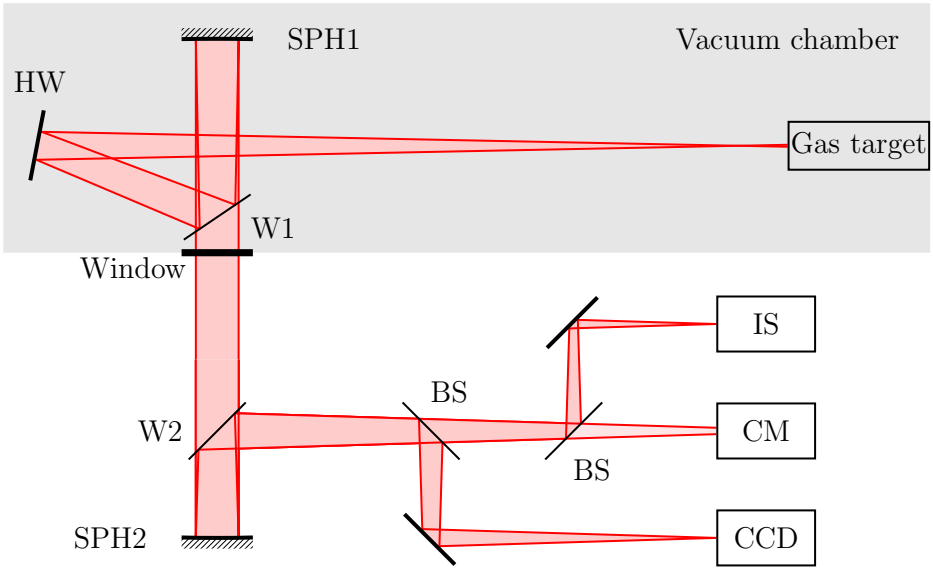

Figure 3.6: *Schematic setup for the forward line. SPH – spherical mirror, HW – holey wedge, W – wedge, BS – beam sampler, IS – imaging spectrometer, CM – calorimeter, EM – exit mode imaging.*

"forward line". The purpose of this set of diagnostics is to measure the properties of the laser pulse as it exits the plasma. This knowledge provides information about the dynamics of the laser inside the plasma. Characterising the laser exiting from the plasma is also invaluable as it provides a useful benchmark for checking whether results from PIC simulations can accurately describe experimental data.

Figure 3.6 depicts a schematic of the suite of diagnostics typically used in the forward line. As the plasma accelerator operates in vacuum, the beam needs to be transported outside the chamber to allow more flexibility in setup. Secondly, some detectors are not able to work in vacuum.

The first optic in the beam transport is usually an uncoated wedge. As the intensity here is extremely high, a dielectrically coated optic with very high damage threshold could be used. However, a spectrally flat response is required from the diagnostic line; use of an uncoated wedge provides spectrally uniform attenuation. In the experiments presented in this thesis, the first optic was a wedge with an axial hole, allowing the betatron x-ray beam to propagate to x-ray diagnostics.

A non-collimated broadband laser pulse propagating through a planar optic induces chromatic aberration. In addition, astigmatism is introduced when propagating a focussing beam through a planar optic at an angle. Hence, the next optic in the system

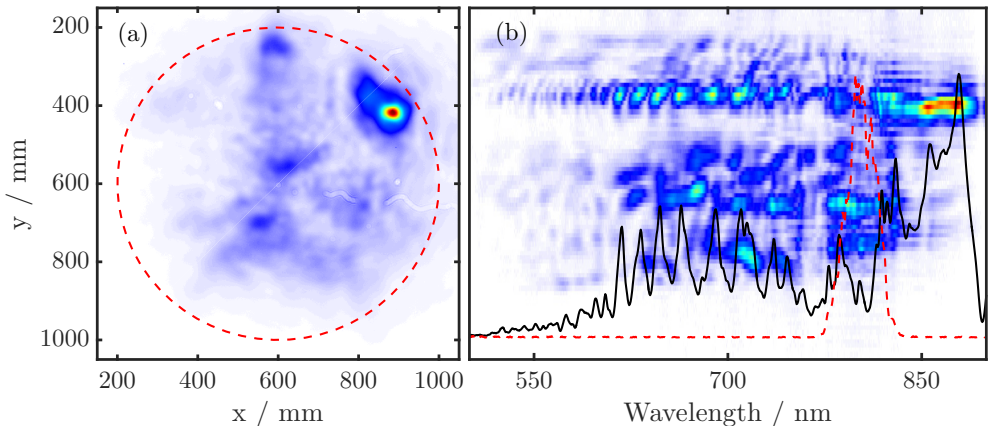

Figure 3.7: *Typical data for forward line diagnostics, (a) exit mode image and (b) 1D spatially resolved spectrum. The red dashed line in (a) is the size of the beam for vacuum propagation. The red dashed line in (b) is the vacuum spectrum of the main driver whereas the black dashed line is lineout along the guided feature.*

is a wedge, reflecting the pulse onto a long focal length spherical mirror, with the collimated beam passing through the wedge. The collimating optic is chosen to have a higher $f/\#$ than the main focussing optic in order to resolve features smaller than the incoming laser spot.

The pulse is focussed down in a reverse configuration after beam transport outside the chamber. The two focussing optics, SPH1 and SPH2 in Figure 3.6, thus form an image relay telescope. This allows the plane of the laser pulse exit from plasma to be reimaged onto diagnostics. Beam splitters or samplers are used in the focussing line to guide light onto different diagnostics.

Exit mode imaging

The use of an image relay telescope allows for the measurement of the spatial profile of the laser as it exits the plasma. This provides crucial information about the propagation of the laser through the plasma. Reflections rather than transmitted beams from splitting elements are used to ensure good image quality. Beam samplers, depicted in Figure 3.6 as BS are most commonly used.

A typical exit mode image allows to ascertain the effectiveness of guiding. Panel (a) in Figure 3.7 shows a typical exit mode image. The guided beamlet is clearly visible, against a background of an unguided halo. The total integral of the image is the amount of energy exiting the plasma, allowing for laser-plasma coupling efficiency to be determined. Furthermore, the fraction of total energy within the guided filament can be calculated, allowing for an estimate of the guided intensity of the laser. Typically,

a camera with high dynamic range is use; in this work the 16-bit Andor Ixon was employed.[160]

Forward spectrometer

In addition to measuring the guiding effectiveness, it is also imperative to understand what processes the pulse underwent during propagation in the plasma. As such, measuring the spectrum of the laser exiting the plasma is invaluable. As the laser drives the plasma wave, the photons in the pulse decrease in energy after transferring energy to the plasma. Lower energy photons appear in the spectrum as longer wavelengths, hence the bulk of the laser will undergo redshifting. However, as discussed in Section 2.4.4, the laser photons can also undergo blueshifting later on in the interaction as they slip backwards in the pulse and become trapped in a region of positive refractive index gradient.

Typically an imaging spectrometer, such as a Czerny-Turner monochromator, is used for this diagnostic. An imaging spectrometer allows one to spectrally resolve an image on its slit. The size of the slit determines the amount of light in the spectrometer – a larger slit size will yield higher signal. However, a larger slit also reduces spectral resolution as neighboring wavelengths begin to overlap on the detector. Hence, a small slit size is desirable to ensure high spectral resolution. Typically slit widths of orders of tens of microns are used. The spectrometers used in this work employed a grating with $d = 150\,\mathrm{mm}^{-1}$ and were typically blazed for 500 nm yielding spectral resolution of $\sim 1\,\mathrm{nm}$. The Andor Shamrock 303i spectrometer[161] was used for the data measured in the Gemini experiments whereas the Acton SpectraPro 2300[162] was employed in the ATA2 campaign.

However, a small slit size introduces an experimental limitation as the pointing fluctuations in the main laser are typically larger than the solid angle subtended by the aperture width. Hence, on some shots the main guided part of the image may miss the spectrometer entirely. To overcome this, a cylindrical lens was introduced before the slit. With its focussing parallel to the slit, the lens maintains an image in the direction perpendicular to the aperture. With the lens placed more than its focal length away from the spectrometer, it effectively averages the image information in the other plane. Hence, even though pointing fluctuations move the spot and the guided

[160] Andor. *Andor Ixon-Ultra 888*. URL: http://www.andor.com/scientific-cameras/ixon-emccd-camera-series/ixon-ultra-888 (visited on 12/11/2016).
[161] Andor. *Andor Shamrock 303i*. URL: http://www.andor.com/spectrograph/shamrock-spectrograph-series/shamrock-303i (visited on 12/11/2016).
[162] P. Instruments. *SpectraPro*. URL: http://www.princetoninstruments.com/products/SpectraPro (visited on 12/11/2016).

filament around, the spectrum of these components will always be measured.

A typical forward spectrometer image is depicted in Panel (b) in Figure 3.7. The image has been stretched in the imaging direction to ensure the spectrum of the guided filament is aligned with the exit mode image. A lineout of the spectrum of the guided filament is plotted as the black line, while the laser vacuum spectrum is shown as the red dashed line. Substantial redshifting of the guided filament is evident, indicating energy lost by the laser photons driving a wakefield. There is also a highly modulated blueshifted component. It is also seen that the unguided halo has not been redshifted, indicating this component of the exiting light has not been losing energy to the wake.

Exiting energy calorimeter

Another important aspect to measure about the laser plasma interaction is the amount of energy deposited in the plasma. Ideally, all of the laser energy would be coupled into the plasma wave, which can then be used to accelerate electrons. It is also important to characterise the energy transmission to confirm theoretical models about laser absorption.

As the pulse exiting the plasma contains many spectral components, it is desirable to use a calorimeter to measure the transmitted laser energy. The Gentec QE25LP-S-MB-INT was employed on some experiments described in this work.[163] One could opt to use a diode or indeed integrate the total signal on the exit mode camera. Both of these methods, however, are less reliable due to their spectrally varying quantum efficiency.

The calorimeter is least dependent on the optical quality of the image and thus can be placed anywhere in the forward line. In Figure 3.6, it is depicted as CM and deployed after transmission through two beam samplers.

Pulse length diagnostic

As the laser propagates in plasma it can often become compressed in an intricate feedback loop. The effectiveness of compression depends on plasma and laser parameters. Hence diagnosing the pulse length of the exiting pulse is important to understand the coupling between the laser pulse and plasma.

The measurement of ultrashort pulses is very difficult as the variations occur on the femtosecond timescales.[164] The most often used diagnostic to measure pulselengths is the second-order autocorrelator.[165] However, this method only provides intensity

[163] Gentec. *Energy detectors*. URL: https://www.gentec-eo.com/products/energy-detectors/QE25 (visited on 12/11/2016).
[164] I. A. Walmsley *et al*, Advances in Optics and Photonics **1**, 2009.
[165] F Salin *et al*, *Appl Optics* **26**, 1987.

information, which is insufficient to describe the actual pulse. In addition, as a second order method the result is always symmetric about zero delay, introducing further ambiguities about the shape of the pulse. The two most often used diagnostics for full measurement of ultrashort pulses, i.e. both field amplitude and phase, are variants of Frequency Resolved Optical Gating (FROG)[166,167] or Spectral Interferometry for Direct E-field Reconstruction (SPIDER).[168,169]

Implementing a pulse length diagnostic requires a specialised beam line with reflections off wedges or metallic mirrors in order to ensure flat spectral response. Secondly, the beam should propagate through as little glass as possible to maintain its short pulselength. Both these restrictions make implementation of pulse length diagnostic experimentally difficult.

3.3 Electron beam diagnostics

In order to ascertain the properties of an accelerator, one must characterise the resulting beam. It is important to know as much as possible about the accelerated beam. However, of highest importance is obviously the final energy of the particles along with how many of them reached that energy along with the quality of the resulting beam.

3.3.1 Electron spectrometer

At the heart of measuring the energies of charged particles is the fact only electric fields can do work on a charged particle, i.e. only electric fields can change the energy of a particle. This is easily seen from the equation for Lorentz force given in Equation 2.7 and the definition of work:

$$\delta W = \mathbf{F} \cdot \mathrm{d}\mathbf{s} = \mathbf{F} \cdot \mathbf{v}\, \mathrm{d}t \tag{3.18}$$

As the magnetic force term is equal to $q\mathbf{v} \times \mathbf{B}$, a dot product with $\mathbf{v}$ will be identically 0. Propagating a charged particle in a magnetic field then does not change its energy but just the ratio of its momentum components. It acts as to increase the momentum component in the direction perpendicular to both the magnetic field and the direction of particle's travel. This acceleration is proportional to the B field strength and the particle's longitudinal momentum and hence it disperses particles according to their

[166] D. J. Kane *et al*, *Opt Lett* **18**, 1993.
[167] R. Trebino *et al*, *Rev Sci Instrum* **68**, 1997.
[168] C. Iaconis *et al*, *Opt Lett* **23**, 1998.
[169] T. Witting *et al*, *Opt Lett* **36**, 2011.

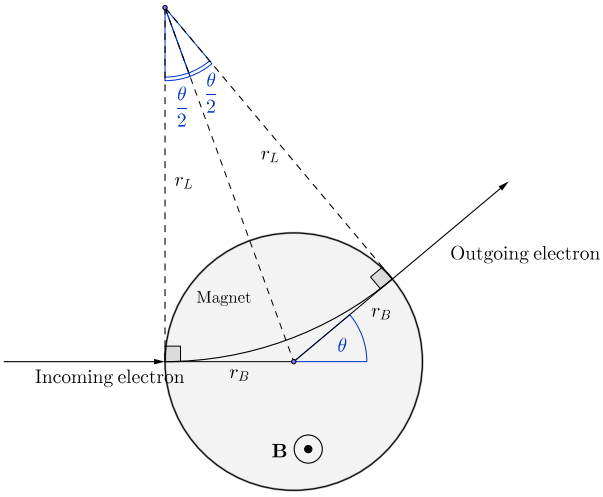

Figure 3.8: *Path of an electron through a circular uniform magnetic field pointing out of the page.*

energies.

In order to learn about the characteristics of magnetic spectrometers it is instructive to investigate the trajectory of a charged particle in a uniform circular magnetic field. Such a set up is depicted in Figure 3.8: an electron of momentum p enters a magnetic field of strength B_0. The motion of a charged particle in a uniform **B**-field is circular and has a characteristic radius called the gyroradius or Larmor radius:[170]

$$r_L = \frac{mv_\perp}{|q|B_0} \equiv \frac{p_\perp}{eB_0}. \tag{3.19}$$

The direction of gyration depends on sign of charge. With a little algebra, the deflection angle θ of the electron exiting the field is given by,

$$\theta = 2\arctan\frac{r_B}{r_L} = 2\arctan\frac{r_B eB_0}{p}, \tag{3.20}$$

where r_B is the radius of the magnetic field. Dispersion for such a spectrometer is given by

$$\frac{\partial\theta}{\partial p} = -\frac{2r_B eB_0}{p^2 + r_B^2 e^2 B_0^2}, \tag{3.21}$$

[170] F. Chen. *Introduction to Plasma Physics and Controlled Fusion.* Springer, 1984.

which for high energy electrons, or $p \to \infty$, can be expanded as

$$\frac{\partial\theta}{\partial p} = -\frac{2r_B e B_0}{p^2} + \mathcal{O}\left(\frac{1}{p^4}\right). \tag{3.22}$$

Valid for relativistic particles, Equation 3.22 shows that electron energies are more closely bunched for increasing energies. This in turn means the energy resolution decreases as electron energy increases. Dispersion can be improved by using a stronger magnetic field or a longer magnet.

The above result is valid for a circular, uniform magnetic field. However, due to space constraints a rectangular magnet is more often used. Analytic expressions can be derived for dispersion in a rectangular magnet.[60] However, having a finite extent to the magnet and a gap between the poles also means the field will have gradients near the edges. With these complications, the solution to find the deflection angle of an electron traversing a spectrometer becomes complicated and requires solving the equations of motion numerically. Usually, this tracking is done for electrons of different energies by propagating them through a precisely measured field map of the magnet.

Magnet mapping and electron tracking

New magnet mapping software was written to characterise the magnetic field maps of dipole magnets. Employing a newly built 600 mm range linear stage, the software moves a Hall probe through the magnetic field and measures its strength at user defined intervals in a 2D geometry.[9] The software was implemented with an object oriented Graphical User Interface (GUI), allowing the user to choose any linear stage controller object and a gaussmeter object. The step size can be set by the user along with the mapping ranges.

Using this software the magnetic field map of a compound magnet, consisting of three $\sim 1\,\mathrm{T}$ dipoles, used in the Gemini 2015 campaign was measured. A CAD drawing of the magnet assembly is shown in Figure 3.9a. Here, the yokes of the three individual magnets are depicted in blue, with the pole pieces shown in gray. The field map dimensions are $550 \times 150\,\mathrm{mm}$, mapped using a 1 mm step size and employing the Hirst GM08 gaussmeter.[171] Due to the slow readout of the GM08, each step took $\sim 2\,\mathrm{s}$. The total time for this measurement was about 48 h, with the software performing $\sim 83\,000$ steps.

[60] J. M. Cole. "Diagnosis and Application of Laser Wakefield Accelerators". Imperial College London, 2015.

[9] Both the 600 mm stage and magnet mapping software were designed and built by the author.

[171] H. M. Ltd. *GM08 Gaussmeter*. URL: http://www.hirst-magnetics.com/instruments/gm08_p1.shtml (visited on 06/20/2016).

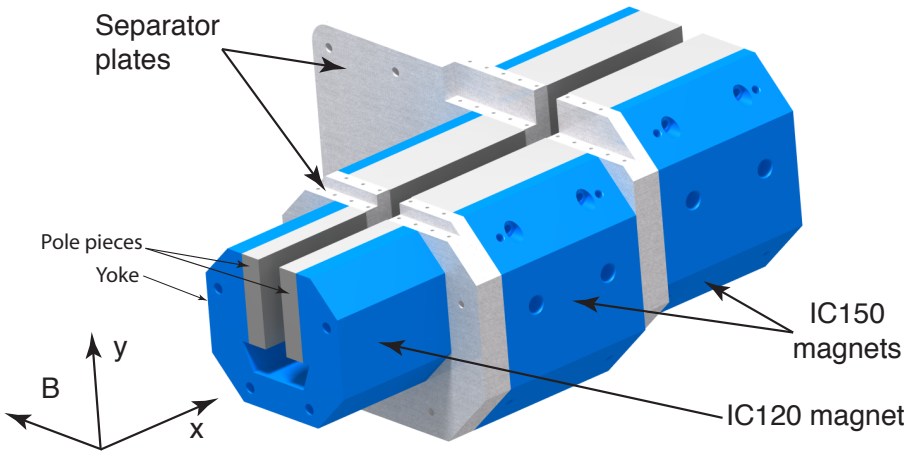

(a) CAD assembly of the compound magnet

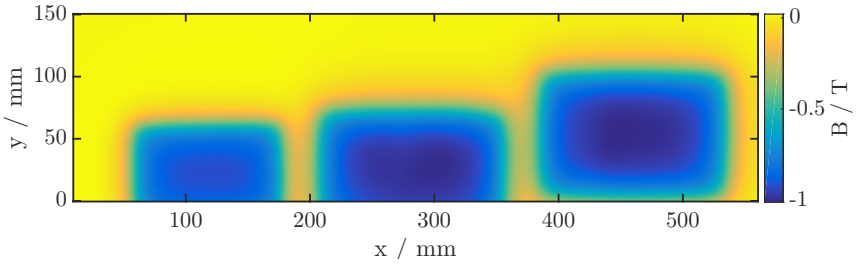

(b) Measured field map

Figure 3.9: *The compound magnet used in the Gemini 2015 experimental campaign. Panel (a) shows CAD drawing of the magnet and the measured magnetic field map is shown in Panel (b).*

The measured field map is depicted in Figure 3.9b. Although care was taken to align the Hall probe with the magnet, the resulting map is difficult to align with the physical magnet. In order to ensure correct alignment of the field with the magnet, the integral of B within a 150 by 100 mm box was maximised to find the coordinates of the centre of the third magnet.

A new GUI operated program was also written to perform electron tracking for up to three magnets and three screens. With the user defining a geometry setup and energy range for electrons, the relativistic motions of equation for the electrons are solved. This is done using the `ode45` solver in MATLAB.[172,173] In order to test the accuracy of the tracking code, electrons were propagated through an ideal circular magnet with $r_B = 50\,\text{mm}$ and $B = 1\,\text{T}$. A total of 200 electrons were tracked, with logarithmically

[172] J. Dormand *et al*, *J. Comput. Appl. Math.* **6**, 1980.
[173] L. F. Shampine *et al*, *SIAM J. Sci. Comput.* **18**, 1997.

RelTol	Time (s)	$\frac{\theta_{\text{an}}-\theta_{\text{comp}}}{\theta_{\text{an}}}$
10^{-6}	12.6	3.68^{-2}
10^{-8}	16.9	3.94^{-3}
10^{-10}	21.8	8.35^{-4}
10^{-12}	27.2	7.78^{-4}
10^{-14}	31.0	7.77^{-4}

Table 3.1: *Root mean square errors and total run times for different error tolerance settings used in the tracking code.*

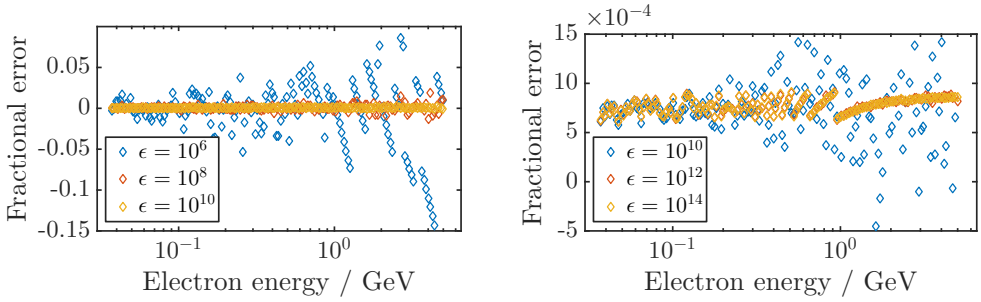

(a) *Large tolerance settings* ***(b)*** *Small tolerance settings*

Figure 3.10: *Fractional pointing angle errors $(\theta_{\text{an}} - \theta_{\text{comp}})/\theta_{\text{an}}$ for electrons tracked through an ideal circular magnet. The errors saturate above $\epsilon = 10^{-12}$ due to the inherent precision of double precision being reached.*

spaced energies between 50 and 5000 GeV. The fractional error, $E = (\theta_{\text{an}} - \theta_{\text{comp}})/\theta_{\text{an}}$, is plotted in Figure 3.10 for different `ode45` accuracy settings RelTol $\equiv \epsilon$. Errors of the order of per cent are evident for tolerance values less than 10^{-10}. No increase is seen for $\epsilon < 10^{-12}$, which is due to the inherent precision of double floating point numbers being reached. This is further illustrated in Table 3.1, showing the RMS value for the errors along with execution times. Given the flattening of the errors and required runtime, the value used in the code is 10^{-10}. Note that the relatively high value of the fractional error, of the order of 10^{-3} is arising partly due to using a finite number of grid points to express the circular magnetic field. This subsampling is the reason for the slow increase in error for electron with $p \gtrsim 1\,\text{GeV}$: all these tracks actually propagate through an equal amount of B-field.

Sample output from the electron tracking program for the magnet used on the 2015 Gemini campaign is depicted in Figure 3.11. The magnet field map is that plotted in Figure 3.9b; its nonuniformity highlights the difficulty of an analytical approach to deflection angle determination. Note the use of logarithmic spacing of electron energies

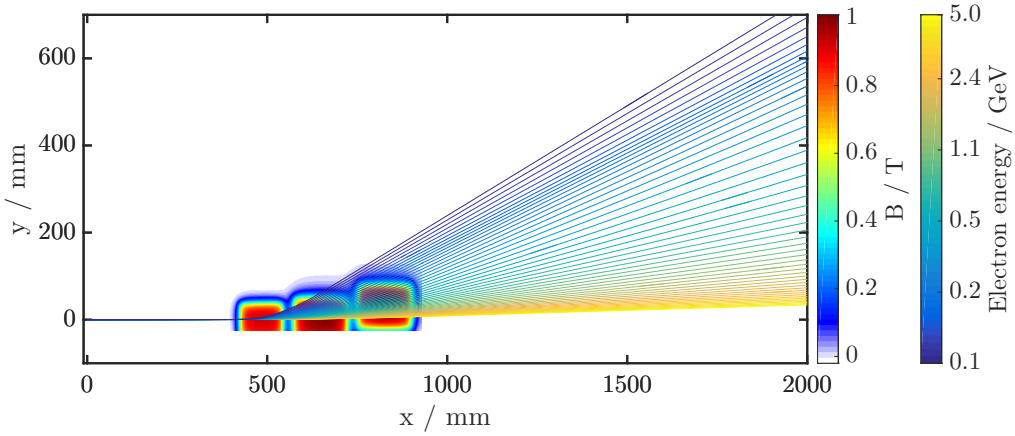

Figure 3.11: *Geometry and electron tracking for 2015 Gemini campaign.*

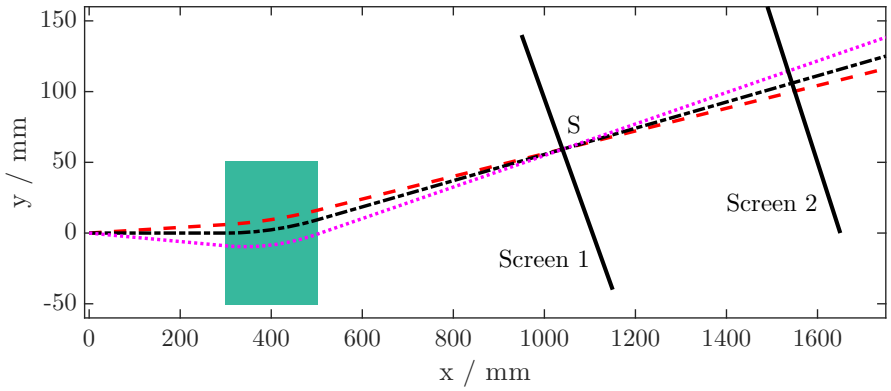

Figure 3.12: *Schematic illustrating ambiguity of electron energy measurement with only 1 detection screen. Electrons with different energies and different pointing offsets can all overlap at point S on screen 1.*

reflecting the nonlinear nature of dispersion of magnetic spectrometers.

After having been deflected by a magnetic field, the electron deviation angles need to be measured. This can be done by inserting a scintillating screen into the path of the electron beam. The light emitted when particles hit the screen can be imaged onto a CCD for real time measurements. With the position of the screen known, each point along the screen can be mapped to a deflection angle.

A complication arising in characterising laser wakefield generated beams is the pointing fluctuation of the electron beam. Electrons with higher energies pointing above the laser direction can overlap with electrons of lower energies, pointing below the laser axis. This is illustrated in Figure 3.12. The red dashed line corresponds to an

electron with $\mathcal{E} = 1000\,\mathrm{MeV}$ and pointing offset $\theta = 20\,\mathrm{mrad}$, travelling through a 1 T magnetic field. It hits the detection screen 1 at point S, overlapping with an electron of $\mathcal{E} = 650\,\mathrm{MeV}$ along the x-axis and electron with $\mathcal{E} = 426\,\mathrm{MeV}$, $\theta = -30\,\mathrm{mrad}$.

A few different solutions exist to overcome this issue. The classical approach is to use a slit before the magnet, thus only allowing electrons from a known angular spectrum to propagate. However, this method relies on the exact positioning on the pinhole; furthermore it cuts out a very large amount of the beam and thus necessitates additional measurements. Additionally, intrinsic pointing instabilities of the electron beam reduce the reliability of the diagnostic. This makes single shot measurements of the entire beam energy spectrum virtually impossible.

Another option is to insert a tracking screen before the electrons enter the magnetic field.[174] A unique angle for every part of the beam is thus measured and can be used to reconstruct the electron energy spectrum. It constitutes a single shot system, where in addition to the beam energy spectrum its profile is also measured. However, inserting material into the path of the electrons causes angular scattering and thus reduces energy resolution. Furthermore, if the beam is of very broad energy spread, low energy electrons with higher divergence angles can overwhelm the signal from high energy features. Only the average pointing of the entire beam can then be calculated, which may be different from the direction of high energy features.

A third alternative is to use two spectrometer screens,[175] as depicted in Figure 3.12. In this case, a unique line for each electron beam feature can be reconstructed and tracked back through the magnetic field. By iteratively changing electron energy until it emanates from the beam source its precise energy can be reconstructed. The electron beam will again undergo scattering in the spectrometer screen but the disruptive effect can be minimised by appropriate inter-screen distance selection.

An example showing correct energy retrieval using two spectrometer screens is shown in Figure 3.13. Panels (a) and (b) depict warped and cropped images from electron spectrometer screens 1 and 2, respectively. Similar features in the beam are denoted by the dashed vertical lines. These are chosen by the user based on visual similarities in the current software version; automatic feature recognition will be added in the future. Panel (c) in Figure 3.13 depicts the electron energy spectrum extracted from both screens. The solid lines show the backtracked and corrected energy spectrum, while the dashed lines are plotted assuming an on-axis electron beam. Tracking electrons through the spectrometer with an offset angle obtained from backtracking shifts spectra from both screens up in energy and yields excellent agreement between traces

[174] H. J. Cha *et al*, *Rev Sci Instrum* **83**, 2012.
[175] A. A. Soloviev *et al*, *Rev Sci Instrum* **82**, 2011.

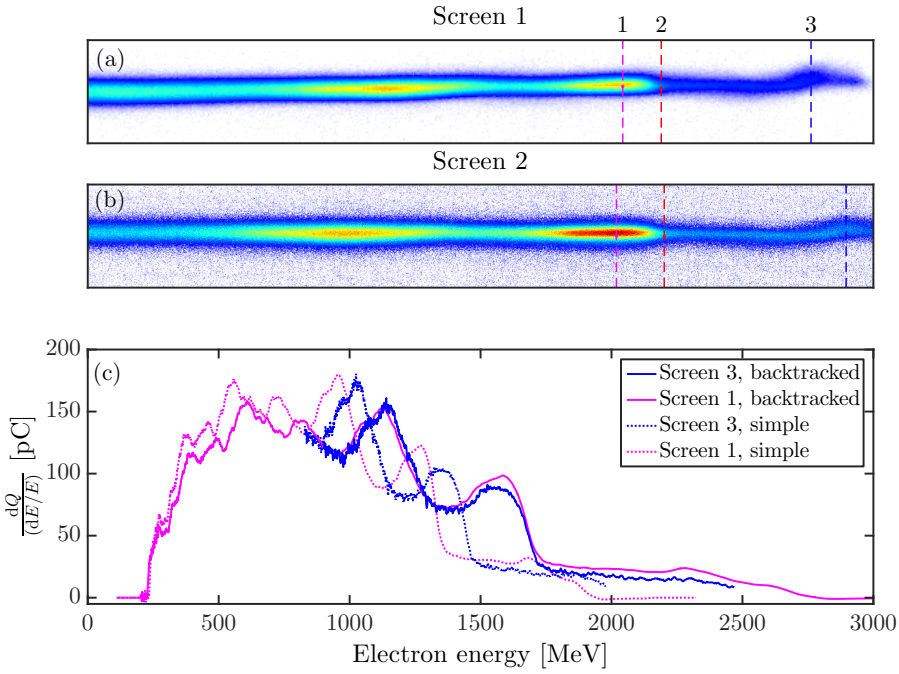

Figure 3.13: *[Two screen back tracking and accurate electron energy retrieval.] The different colour lines in Panels (a) and (b) depict common features. By backtracking each of these, an accurate offset angle can be found. Tracking electrons with this angle results in close agreement between retrieved spectra from both screens, as highlighted in Panel (c).*

Feature	θ_{offset} (mrad)	$\mathcal{E}_{\text{init}}$ (MeV)	$\mathcal{E}_{\text{corr}}$ (MeV)	$\Delta\mathcal{E}$ (MeV)
1	9.4	1278	1616	338
2	9.4	1349	1734	385
3	8.8	1716	2337	621

Table 3.2: *Backtracked electron beam angles and energies, for features identified in Panels (a) and (b) in Figure 3.13.*

from the two screens. This consistency between spectra from the different screens can thus be used as a test for the accuracy of backtracking. Hence, even though the backtracking and its accuracy relies heavily on identification of similar features in spectra, as shown in Panels (a) and (b) in Figure 3.13, the agreement between the retrieved spectra from different screens allows for incorrect feature overlap to be instantly recognised. This results in an almost unique spectrum retrieval.

Further details about backtracking performed on this data are shown in Table 3.2; the features are those identified in Figure 3.13. The retrieved pointing offset angles are

of the order of 9 mrad. Whilst being a large offset, these numbers agree with measured betatron x-ray beam offsets.[176] Also shown are the electron energies at the feature positions on the screen assuming a simple, on-axis beam, and correctly backtracked beam. As can be seen, energy errors as large as 600 MeV can occur if the electron beam exit angle is not taken into account.

3.3.2 Electron beam profile

Measuring the electron beam profile yields the distribution of charge transverse to its propagation direction. Being one of the easiest beam properties to measure, it only requires some propagation distance and a detection screen. The latter is usually a scintillating screen, imaged onto a CCD.

Whilst the electron beam profile is a very simple diagnostic, difficulties can arise when it is used in conjunction with an electron spectrometer. Due to the large mass and size of high-field dipole magnets, it is often experimentally inconvenient to cycle a vacuum chamber and remove the magnet to allow the electron beam to propagate undispersed. Hence, the magnet is usually driven out of the electron path. However, the fringe fields around the yoke of the magnet can be strong enough to deflect low energy electrons by a non-negligible amount. This will distort the beam on the screen and renders the beam profile measurement very difficult to interpret. However, this effect can be mitigated by introducing high permeability shielding structures around the electron beam path.

The beam profile monitor is of crucial importance when using only one electron spectrometer screen. The average pointing offset from the laser axis can be measured using the beam profile screen. Using this offset allows one to remove a systematic energy measurement error. Knowing the beam size and the average pointing fluctuation then allows for estimations of electron energy errors.

3.3.3 Charge calibration

The scintillator of choice for many electron accelerators is KODAK Lanex, in essence a Gd_2O_2S : Tb phosphor in a binding material. Lanex has good sensitivity to electrons and its scintillation light peaks near 550 nm, where the quantum efficiency of most CCDs reaches a maximum. Lanex has a very high dynamic range and provides a linear response to electrons over 5 orders of magnitude.[177] This means that the intensity of scintillation light is linearly proportional to incident charge density. Additionally, the energy deposited in Lanex scales very weakly with particle energy for relativistic

[176] J. C. Wood. private communication.
[177] A Buck *et al*, *Rev Sci Instrum* **81**, 2010.

electrons.[178] Saturation of Lanex Regular, employed in electron spectrometers used for this work, is found to happen above $\rho_{\mathrm{sat}} = (66 \pm 33)\,\mathrm{pC\,mm^{-2}}$.[177]

By calibrating the optical throughput of an imaging system and CCD response a calibration for charge based on intensity of scintillation can be obtained.[177,178] However, an accurate enough throughput can be very difficult to obtain in practise. This can be due to transmission through windows at oblique angles, a complicated imaging path and use of telecentric lenses. The first and latter can reduce the throughput, whilst a complicated imaging geometry makes the estimation of total collection solid angle error prone. Errors introduced by all these factors make the final calculation difficult.

An alternative is to use a long lived phosphor screen, such as imaging plate,[179] to detect the electrons at the same time as scintillation light is measured. Ionising radiation passing through imaging plate excites some molecules into a long lived metastable state. These states can then be stimulated to decay, a process called photostimulated luminescence.[180] Intensity of the emitted radiation is proportional to the number of atoms in the metastable state and thus proportional to the amount of energy stored in the image plate. Knowing the energy deposition for electrons in image plate allows for conversion from photostimulated luminescence signal to charge.[181,182]

If placed onto the opposite side of a scintillating screen, an equivalent image of charge distribution can be obtained since the charge passes through the image plate almost unaffected. A spatially dependent calibration for measured CCD signal to actual charge can thus be extracted.[183] This is illustrated in Figure 3.14, where Panel (a) shows the signal from imaging plate. The total charge on the image is 188 pC and is found using calibrations for the image plate scanner used and the image plate itself.[181,184] Note the saturation of colour scale for the imaging plate; this is an effect produced by the logarithmic conversion in the scanner and is not physical saturation.[181] Whilst scanning the image plate for a second time reduces the signal and could thus yield an unsaturated image, the decay factor has been found to be dependent on initial energy deposition and thus calculating the correct scaling becomes intangible.[176]

Whilst using image plate to calibrate a Lanex screen in a particular imaging configuration removes the necessity to precisely simulate the optical system, it can lead to inaccuracies when extracting a cross calibration. If the Lanex screen is not parallel to

[178] Y. Glinec *et al*, *Rev Sci Instrum* **77**, 2006.
[179] N. Kotera *et al*. *Method of and apparatus for reading out a radiation image recorded in a stimulable phosphor*. US Patent 4,258,264. 1981. URL: https://www.google.com/patents/US4258264.
[180] H. von Seggern *et al*, *J Appl Phys* **64**, 1988.
[181] B. Hidding *et al*, *Rev Sci Instrum* **78**, 2007.
[182] K. Zeil *et al*, *Rev Sci Instrum* **81**, 2010.
[183] S. Masuda *et al*, *Rev Sci Instrum* **79**, 2008.
[184] K. A. Tanaka *et al*, *Rev Sci Instrum* **76**, 2005.

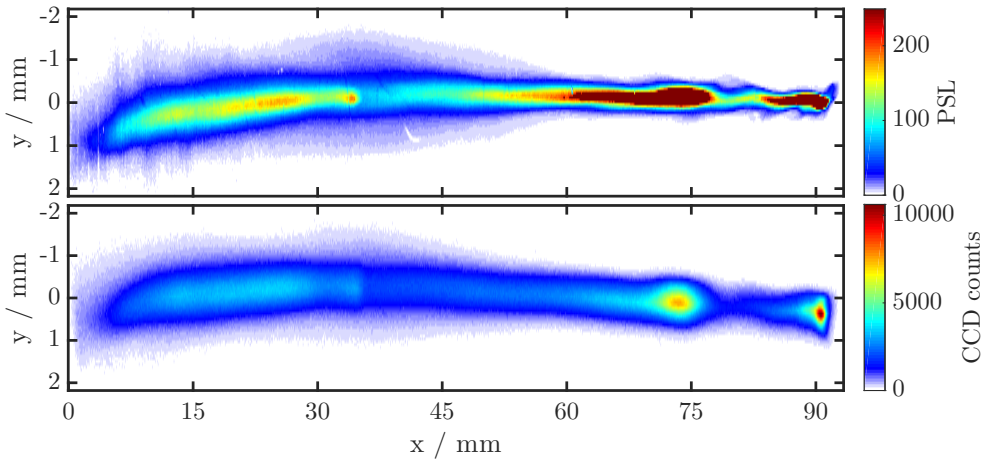

Figure 3.14: *Charge calibration using imaging plate. Panel (a) depicts photostimulated luminescence signal from an imaging plate with the Lanex signal shown in panel (b).*

the object plane of an imaging system, optical deformations arising from this can have large effects. Firstly, only a small area of the screen is in focus. Secondly, magnification will vary across the image, meaning the image will appear warped. Thus, the image of an electron beam on the image plate will not correspond to an image measured by the CCD.

A warped image on the CCD can easily be corrected by a projective transformation using MATLAB's inbuilt `fitgeotrans`. The varying focus effect across the image is a more severe issue. It renders the measured spectral density of electron beams inaccurate. However, there exists a method to correct for the defocus effect due to a tilted object with respect the lens plane. The Scheimpflug compensation[185,186] allows to have the entire image in focus. This is a purely geometrical effect with a diagram showing its principle in Figure 3.15. It involves rotating the image plane (or the CCD) and the lens about the Scheimpflug intersection point such as to introduce spatially varying object distance. In this manner the entire image can be brought to focus. Although employing the Scheimpflug compensation introduces a warping of the resulting image, this can easily be compensated with post processing.

[185] T. Scheimpflug. *Improved Method and apparatus for the Systematic Alteration or Distortion of Plane Pictures and Images by Means of Lenses and Mirrors for Photography and for other purposes.* 1904. URL: http://www.trenholm.org/hmmerk/TSBP.pdf.

[186] H. D. Zhang *et al*, *Phys Rev Spec Top-Ac* **15**, 2012.

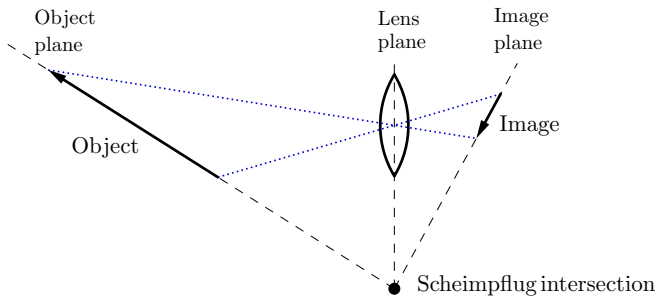

Figure 3.15: *Diagram showing the principle of the Scheimpflug compensation. A tilted object plane can be compensated for by rotating the image plane about the Scheimpflug intersection point to yield a fully in-focus image.*

3.4 Gas targets

Ultraintense laser plasma interactions generally start with a non-plasma, neutral medium. In the case of underdense plasmas, this is a volume of gas. Whilst preformed plasmas created in a discharge are sometimes used, the work presented in this thesis relied on neutral gas media, ionised by the leading edge of the laser itself.[10]

3.4.1 Gas jets

One of the easiest methods to create a gas target is by using a gas jet. In general, this is a nozzle with the purpose of creating a uniform gas flow into the medium surrounding it. Gas flow depends on the shape of the nozzle and thus varying nozzle geometries yield very different density profiles. Depending on the expansion angle and flow formation length the gas flow can be supersonic or subsonic. Nozzles with the critical cross section very close to their exit yield a non-uniform density profile with sonic flow speeds due to flow not being constricted for long enough. On the other hand, if the critical cross section is relatively far from the exit, gas flow will have time to form and can be supersonic and a flat top density profile is obtained.

Figure 3.16 shows a cross section of a supersonic nozzle. This design is based on analytic scalings that have been verified by computer simulations and parameters D_{crit}, D_{exit}, L_{opt} are optimised to yield a flat top density profile with sharp boundaries.[187] These parameters are presented in Table 3.3 for the nozzle used in the ATA2 campaign,[11]

[10] Cf. Section 2.1
[187] S. Semushin *et al*, *Rev Sci Instrum* **72**, 2001.
[11] Cf. Chapter 5

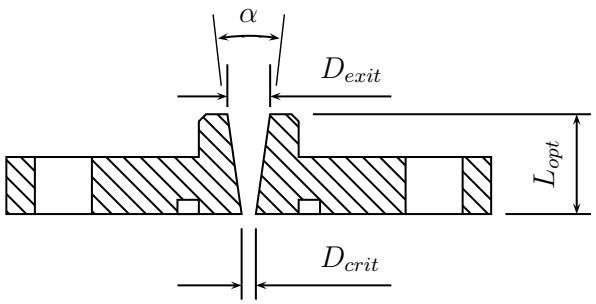

Figure 3.16: *Cross section of an optimised supersonic gas jet.*

Experimental campaign	D_{exit} (mm)	D_{crit} (mm)	L (mm)	α (°)
Gemini 2012	10	1	15	16.7
Gemini 2012	15	1	23.3	16.7
ATA2 2013	3	1	7	8.1

Table 3.3: *Parameters of different supersonic nozzles used in various experimental campaigns presented in this thesis.*

along with nozzles used in the Gemini 2012 campaign.[12] The solenoid controlling the gas flow[13] was opened 10 ms before the laser shot and closed 5 ms after the shot. Typical density profile obtained with He, for a 11.3 bar backing pressure with a 3 mm nozzle is shown in Figure 3.17. A lineout along the axis shows a density profile that can be approximated by a trapezoid. A fit of a trapezoidal profile to the axial density yields a plateau of length 2300 µm, with linear ramps of 425 microns on either side.

3.4.2 Gas cells

Whilst gas jets are the easiest experimentally realisable gas target, they do suffer disadvantages. As the flow is supersonic, any irregularities in the nozzle will strongly affect the density profile, potentially causing turbulence, and the plateau region is only approximately flat. In addition, the shot-to-shot fluctuations result in poor reproducibility of the plasma density. For all these reasons, steady state gas cells have become the targets of choice in our experiments.

Gas cells are effectively boxes with an entrance and exit hole for the laser and inlets for the gas. The cell is filled with low pressure gas tens of milliseconds before the shot

[12] Cf. Section 4.4.1
[13] Peter-Paul Series 20, model EH22, orifice 1/32"[188]

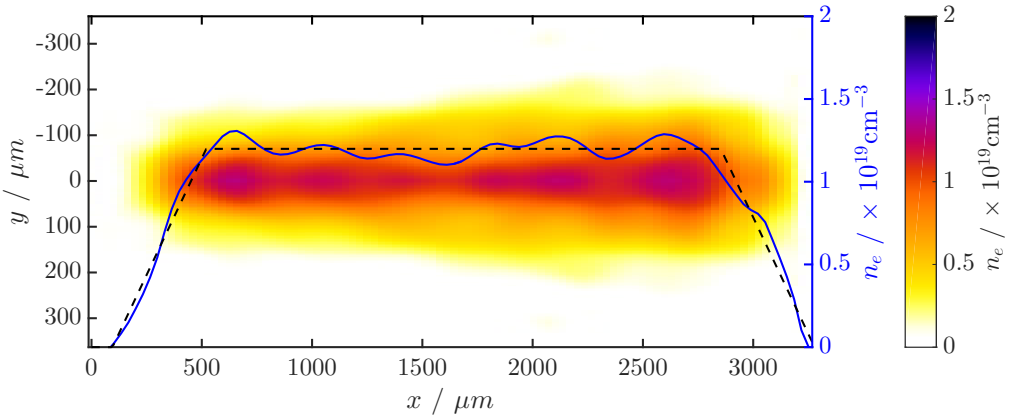

Figure 3.17: *Experimentally measured electron number density profile of a 3 mm nozzle with 11.3 bar backing pressure. The dashed line is a trapezoidal fit to the axial density profile.*

such that there is no flow when the laser arrives. This means the density profile will be reproducible and flat. Recent work has shown gas cells to be responsible for much improved electron acceleration stability.[57,189]

The gas cell used in the 2012 and 2015 Gemini campaign[14] is depicted in Figure 3.18.[15] One corner of the cell has been cut for added clarity into the structure of the cell. The gas cell consists of a solid stainless steel body, with precision machined holes that accommodate trombones. These allow the effective plasma length to be changed between shots. The trombone assemblies are moved by actuators placed on top of the cell. These are galvanically isolated from the main cell body to protect the motors from the very large EMP spikes present during our experiments.

The cell can be configured to consist of one, two or three compartments. This change is done by adding or removing separator walls. In the three section setup, the lengths of the first and third compartment are $L_1 = 1 \ldots 6$ mm and $L_3 = 2 \ldots 34$ mm whereas the length of the second compartment is determined by spacers between separator walls. Compartment 2 can be as thin as 50 µm. This setup is to allow for localised ionisation injection[190] or density downramp injection.[191]

Diagnosis of the plasma density is performed by transverse probing. This is the reason for having transparent windows as the sides of the cell. The density profile can also be inferred from measuring the pressure at the gas inlet as a function of time before the shot. Typical traces are depicted in 3.19a, showing the gas pressure increasing

[57] J. Osterhoff *et al*, *Phys Rev Lett* **101**, 2008.
[189] R. Weingartner *et al*, *Phys Rev Spec Top-Ac* **15**, 2012.
[14] Cf. Chapter 7
[15] The cell is designed by N. Carreira-Lopes and is reproduced here under his permission.
[190] A. Martinez de la Ossa *et al*, *Phys Rev Lett* **111**, 2013.
[191] A. J. Gonsalves *et al*, *Nat Phys* **7**, 2011.

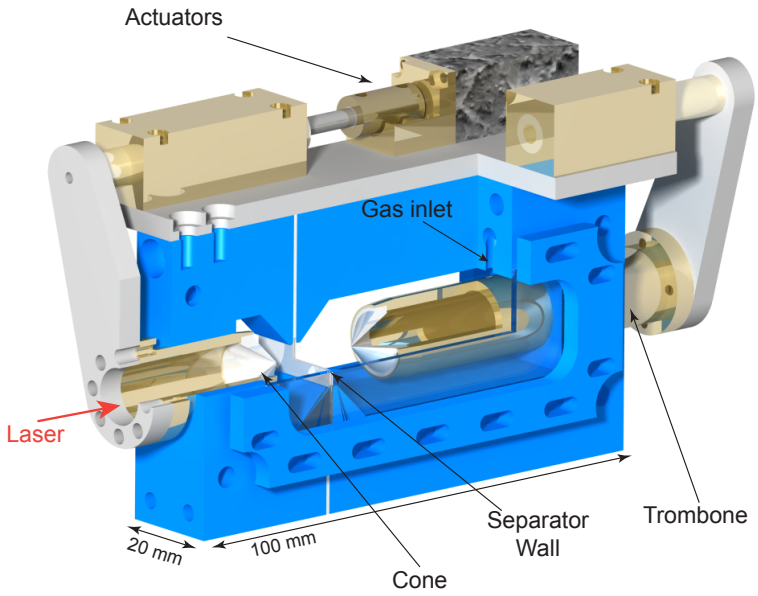

Figure 3.18: *Cutaway CAD drawing of the gas cell used in Gemini campaigns.*

initially and then reaching a steady state. The dip in the trace is from noise due to the discharge of the pump lasers for the final laser amplifier and provides a convenient marker for the shot time. Note the plasma density in Figure 3.19a is achieved by retrieving the average electron density from the interferometer and cross-calibrating this against the pressure within the gas cell at the time of the shot.

As the gas is in near steady state conditions when the laser arrives, the plasma density reproducibility in gas cells is chiefly affected by the stability of backing pressure. Employing a standard low pressure regulator provided by the laser facility had a very poor stability: consecutive shots could differ by as much as 10%. This effect is illustrated in Figure 3.19b, where the black line depicts the standard deviation of gas pressure for 100 shots. The standard deviation is about 2%, which is unacceptably high.

In order to improve the stability of the pressure in the cell, a closed loop gas control system was designed and fielded during the 2015 Gemini campaign. A schematic of the control system hardware is depicted in Figure 3.20; two independent channels were built. When executed, the control software opens the input valve V_{in} and it is kept open until pressure p in the reservoir is larger than the requested final pressure. Valves V_1 and V_2 are then toggled, releasing the volume of gas trapped between the two valves into vacuum. After each release iteration, the pressure in the reservoir is measured. If

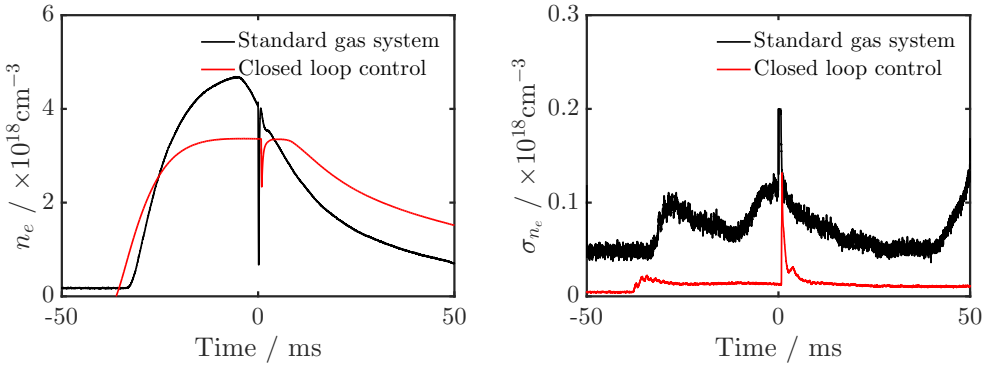

(a) Gas pressure *(b) Standard deviation of pressure*

Figure 3.19: *(a): Plasma density, derived from the pressure measured within the gas cell, as function of time in the gas cell for the standard RAL gas system and the newly developed closed loop control system. (b): Standard deviation of pressure traces, showing a far superior stability for the newly developed gas control system.*

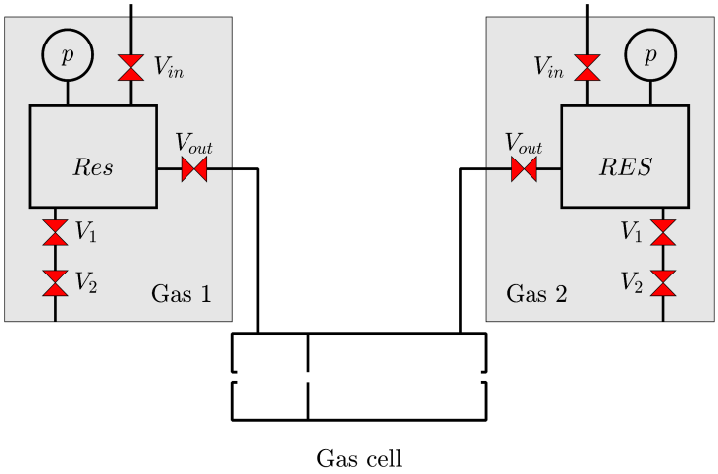

Figure 3.20: *Schematic diagram of the closed loop gas control system.*

p is within 1 mbar of the user requested pressure for more than 1 second, the loop is terminated. The red trace in Figure 3.19b is the stability of the newly implemented system, showing an almost tenfold improvement in reproducibility.

3.4.3 Gas target characterisation

The characterisation of the plasma density profile constitutes one of the most important tasks in an experiment. The mean plasma density determines the long term pulse evolution in the plasma whilst the entrance and exit ramps determine the coupling

of the laser into the plasma and the coupling of the electron beam out of the plasma. Transverse probe beams were used in the work presented in this thesis to characterise the laser plasma interaction. The probe beam was used to perform both shadowgraphy and interferometry.

Shadowgraphy

Shadowgraphy is sensitive to the second derivative of phase and hence the outline of the plasma channel is easily seen.[192] Whilst being very useful and intuitive, shadowgraphy is only a qualitative diagnostic and hence other methods are required for plasma density measurements. However, shadowgraphy images provide information about the alignment of the laser pulse in the gas target along with the direction of the laser. In this manner, it is an invaluable diagnostic to monitor the alignment of the laser.

Interferometry

Interferometry is sensitive to total phase shifts, which are detected as spatial deviations of initially straight fringes. The total phase shift $\Delta\phi$ picked up by light of wavelength λ_L along a path P is given by

$$\Delta\phi = \frac{2\pi}{\lambda_L}\int_P [1-\eta(x)]\,\mathrm{d}x, \tag{3.23}$$

where $\eta(x)$ is the refractive index of plasma. As the driving laser pulse is cylindrically symmetric,[16] Abel inversion can be used to unwrap the longitudinal phase integral.[193] Custom MATLAB software has been written for this purpose.[17]

The interferometer used in the work presented here was a version of a Mach-Zender setup, effectively working as a shearing interferometer. In a standard configuration, the plasma is placed in one arm of the interferometer with the other providing a flat phase reference. However, building a separate reference arm can often be very impractical and it is desirable for only one probe beam to propagate through the plasma. In the modified Mach-Zender case the probe beam is split into equal intensity beams after propagating through the plasma and is recombined with an offset between the beams. This allows the unperturbed part of the beam to be interfered with a region where plasma was present, yielding the same interference pattern.

[192] G. S. Settles. *Schlieren and Shadowgraph Techniques*, p. 29. 2nd ed. Springer, 2006.
[16] To first order, at least.
[193] V. Malka *et al*, *Rev Sci Instrum* **71**, 2000.
[17] Initially written by J. M. Cole,[60] modified by author.

Fluid simulations

The geometry of the exit and entrance cones of the gas cell presented in Section 3.4.2 renders direct probing of the full density profile impossible. However, to accurately simulate the laser-plasma interaction the profiles of entrance and exit density ramps are of crucial importance. Also, given the geometry of the cone tip, the gas will assume the flow pattern of a supersonic gas jet and thus there may be considerable density on-axis within the cones.

Hydrodynamic simulations of the entrance and exit cones were carried out to understand gas dynamics within the trombones. This was done using the massively parallel FLASH code.[194] FLASH employs an Adaptive Mesh Refinement (AMR) scheme to allow simulation of extremely large astrophysical phenomena without the constraints of a fixed resolution grid. The simulation is initialised with a fixed number of initial blocks (each block contains 8^D cells, where D is the dimensionality of the simulation). Blocks that require refinement are divided into either 2^D sub-blocks, depending on a user defined refinement criteria. The resulting computational grid, after the first time step of the code, is displayed in Figure 3.21a. The geometry of the simulation leading to the grid is shown in Figure 3.21b.

The hydrodynamic unit in FLASH solves Euler's equations for compressible gas dynamics.[194] The method used to solve these equations is a modified version of piecewise-parabolic method.[195] This scheme is accurate to second order in time and space and uses special algorithms to ensure shocks arising from contact discontinuities do not spread by more than one or two grid cells.

The results from the code were verified using a different geometry gas cell. In this setup, the apertures for the laser are holes in a planar ceramic end piece. Such a geometry allows for direct probing of the plasma density ramps and for quantitative comparison of the experimentally measured density profile with results from FLASH.

Figure 3.22 depicts the results from FLASH simulations for a planar, 250 micron thick gas cell end plate with a 600 micron hole. The simulation is run in cylindrical geometry and Figure 3.22a depicts the number density of He gas in the simulation volume. The red rectangle is the gas cell end wall. The main gas cell volume is below the end wall and a steady state cell fill was assumed; all simulation blocks in the gas cell were filled with a constant pressure. This allowed for much faster simulations and the flow through the hole converged to a steady flow much faster. The gas cell end plate is modelled as perfectly reflective and thus a reflected shock arises in the flow through the hole. The inset in Figure 3.22a shows this reflection in more detail. This axial

[194] B. Fryxell *et al*, The Astrophysical Journal Supplement Series **131**, 2000.
[195] P. Woodward *et al*, *J Comput Phys* **54**, 1984.

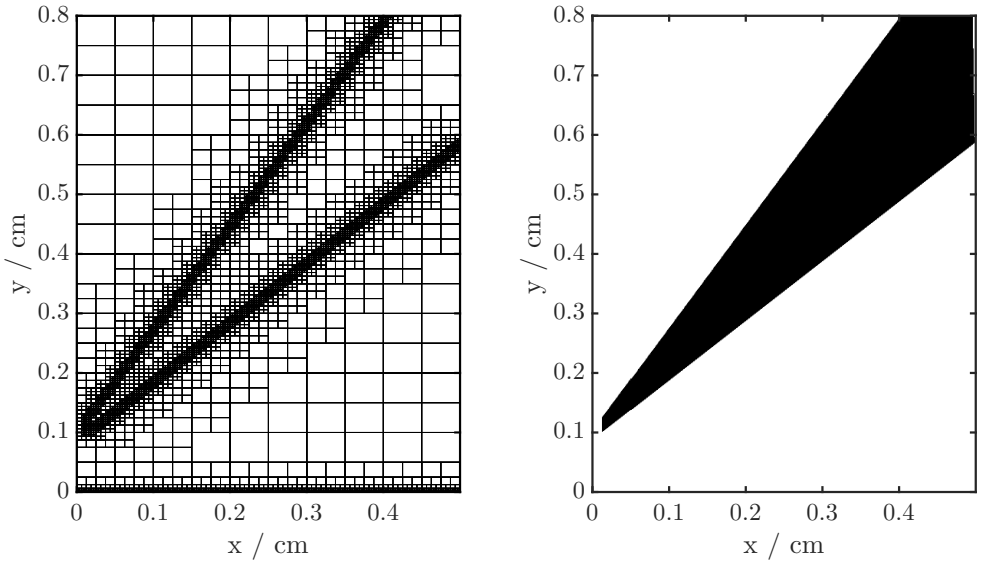

(a) AMR grid *(b) Gas cell in* FLASH

Figure 3.21: *Computational mesh, shown in panel (a) after 6 levels of adaptive mesh refinement. The initial grid consisted of 5 by 8 blocks. Panel (b) depicts the geometry used to simulate the gas cell cone, in this case for a 300 micron exit hole.*

density spike arises from the boundary conditions assigned to the perfectly rectangular cell walls; there is no evidence of this in experimentally measured density profile. This can be seen from Figure 3.22b, depicting an axial lineout, averaged radially over 50 microns, as the blue solid line. A small misalignment of the gas cell in the experiment

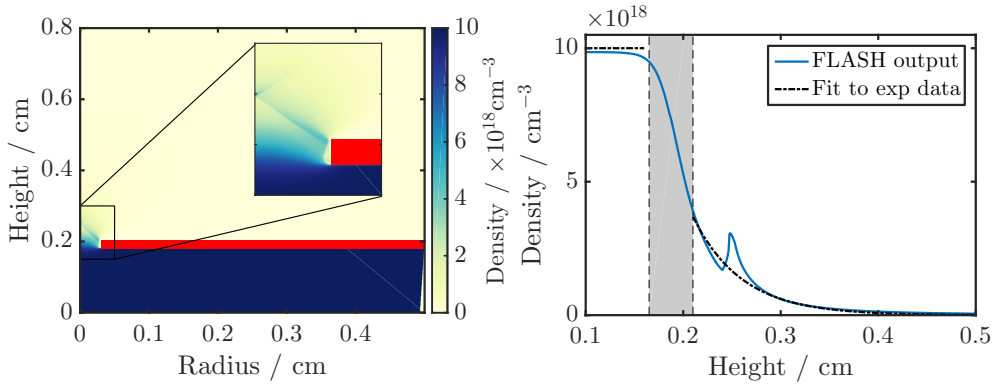

(a) Simulation output *(b) Comparison to data*

Figure 3.22: *Verification of the* FLASH *code for the gas cell simulations. Panel (a) depicts density profile in cylindrical geometry, with the inset highlighting the reflected shock in the hole arising from the obstruction. Panel (b)*

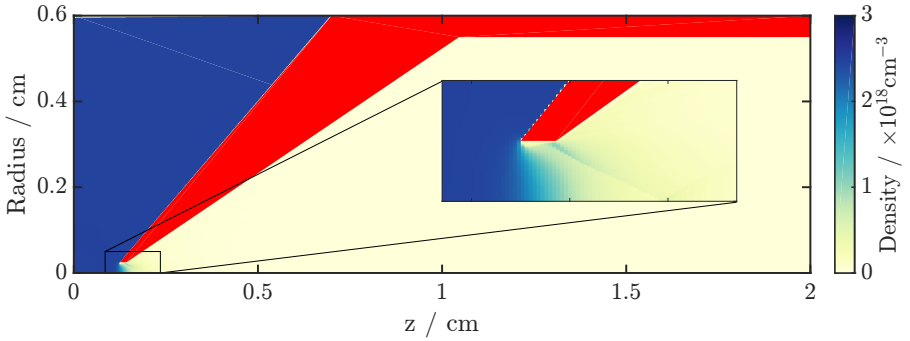

(a) Simulation output

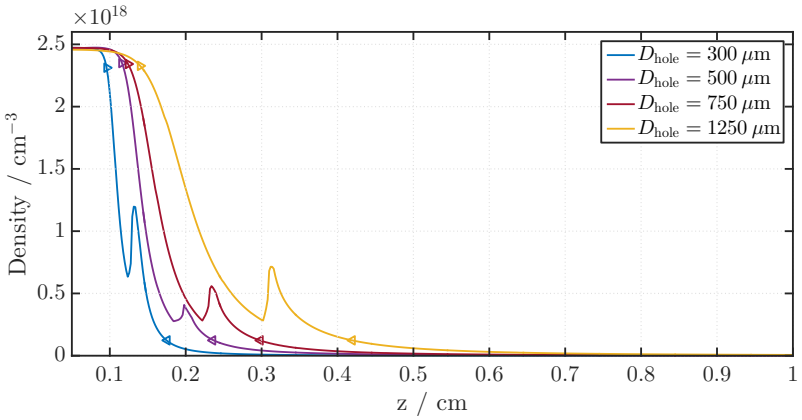

(b) Axial lineout

Figure 3.23: FLASH *simulation results characterising different entrance hole sizes for the gas cell used on the Gemini 2015 campaign. Panel (a) shows a density profile from the simulation, with a reflected shock from the cone wall highlighted in the inset. Panel (b) plots the axial density profiles for different hole sizes.*

yielded a dark area of 460 micron thickness. This is almost twice as thick as the cell wall itself and is depicted as the shaded area in Figure 3.22b. The black dash-dot line is a fit to the experimental data, yielding a 1/e scale length of ~ 0.5 mm. As can be seen, the agreement between the experimental data and simulation results is excellent.

The entrance and exit cones of the cell depicted in Figure 3.18 were simulated to provide information about the density gradients present within the regions that do not lend themselves to transverse probing. The geometry used for this simulation is shown in Figure 3.21b. Figure 3.23a depicts simulated particle density for a 300 µm hole size. All the volume outside the cone itself was filled with He gas at a constant pressure to reduce simulation time. Similarly to the flat cell end case, a reflected shock arises from the surface of the hole. Generation of this density spike is depicted in the inset in Figure 3.23a.

Hole size (micron)	95% − 5% length (mm)
300	0.80
500	1.20
750	1.74
1250	2.80

Table 3.4: *Density ramp length scales measured from* FLASH *simulations.*

Figure 3.23b depicts the axial density profiles, again averaged over a 50 micron radius column. The density profiles look very similar for all hole sizes, characterised by an exponential decay far from the hole. Inside the hole there is a smooth density drop, becoming faster for larger hole sizes. The density spike in the downramp is generated by reflection within the hole of the cone. A similar feature was observed in verification simulations performed for a flat gas cell wall, however, this spike is not present in experimental data. It is thus concluded that the density spike is a numerical artefact, caused by perfect reflection from the cone walls. Furthermore, as the laser constantly erodes the hole as shots are fired, the hole in the cone will become more rounded. Secondly, the laser blasts material off the surface of the hole. This makes the surface rough and will create very small scale turbulence. Both these realistic effects are very difficult to model, but will reduce the shock reflection from the surface of the hole.

As the density downramp is not a purely exponential fall-off, fitting the density variation becomes difficult and will be influenced by the functional dependence chosen. In order to avoid these complication, a scale length was defined as the distance between 95% and 5% levels of peak density. The 95% levels are shown as right-pointing triangles while the 5% level is marked by a left-pointing triangle in Figure 3.23b. Scale lengths measured from the simulations are collated into Table 3.4. As intuitively expected, the density ramp length scales linearly with hole size, with $L_{\mathrm{ramp}} = \kappa D_{\mathrm{hole}}$, where $\kappa = 2.4 \pm 0.2$.

3.5 Particle-in-Cell codes

Plasmas are very difficult to model theoretically due to the extremely large number of particles involved. This is particularly true for laser plasma accelerators, where the timescales in question mean the distribution function is far from equilibrium. This in turn means a fully kinetic treatment of the problem is required. For a $1\,\mathrm{cm}^{-3}$ volume of $n_e \sim 1 \times 10^{18}\,\mathrm{cm}^{-3}$ plasma this would require solving the equations of motion for more than 10^{18} particles. This is impossible, even on the latest supercomputers available

now.

An alternative approach is to use particle–in–cell (PIC) codes to simulate the dynamics of an ensemble of macroparticles, each representing a large number of plasma particles, in their self-consistent electric and magnetic fields.[196] PIC codes have proved to be of enormous use in the study of laser-plasma interactions. The seminal work by Tajima and Dawson featured simulations to verify the concept of laser plasma accelerator. PIC codes were used to predict and study phenomena inaccessible by laser powers at the time, demonstrating channelling and cavitation.[48,49] Simulations for hollow electron beams, experimentally still infeasible, have been shown to be useful for positron acceleration.[197] In addition, PIC codes are used to study the fine-scale dynamics of almost all experiments performed.

Macroparticles in PIC codes effectively represent discrete sampling points of the full 6 dimensional phase space of the species. Each macroparticle thus represents a large number of actual, physical plasma particles. Simulating the dynamics of the macroparticles follows a basic iteration, which is schematically depicted in Figure 3.24. This simple iteration forms the basis of the particle-in-cell code algorithm. Current and charge density, arising from the velocities and positions of macroparticles, are deposited onto a multidimensional grid. The current and charge density are calculated on the grid by weighing the contribution of each macroparticle according to a particle shape function. The latter can be top–hat for the simplest case, while the use of higher order polynomial particle shapes help to reduce numerical artefacts, such as numerical heating.

Next, the fields generated by the movement of the particles are calculated, along with advancing existing fields. Typically the electric and magnetic field are staggered at the grid points, with the **E**-field components defined at the cell centres (faces) and the **B**-field at the cell edges. This configuration is the Yee lattice and allows for a very robust calculation of field curl, yielding excellent stability.[198]

The macroparticles are then pushed according to the Lorentz force felt by each of them. This involves the interpolation of previously updated fields to the particle positions. Depending on the interpolation method used, the algorithm will either conserve energy or momentum (but never both). The particle push is performed by the Boris method, a robust algorithm with excellent long–term stability.[199]

[196] J. Dawson, *Rev Mod Phys* **55**, 1983.
[48] P. Mora *et al*, *Phys Rev E* **53**, 1996.
[49] A. Pukhov *et al*, *Appl Phys B-Lasers O* **74**, 2002.
[197] N. Jain *et al*, *Phys Rev Lett* **115**, 2015.
[198] Kane Yee, *IEEE T Antenn Propag* **14**, 1966.
[199] J. P. Boris. "Relativistic plasma simulation-optimization of a hybrid code". In: *Proceedings of the 4th Conference on Numerical Simulation of Plasmas*. 1970, pp. 3–67.

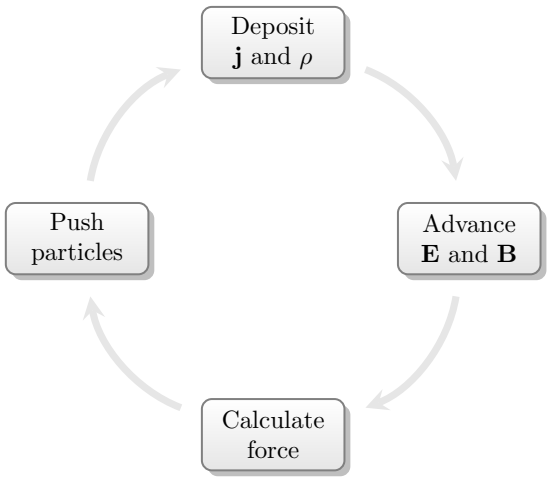

Figure 3.24: *Schematic of basic time step of a PIC code.*

As the current and charge density are inherently local quantities, the PIC algorithm lends itself well to massive parallelisation. In a simulation volume that is divided up among many processors, only the current and density at the faces of the processor subvolume interact with other CPU blocks. Thus, it is sufficient to set up guard cells at the outer faces of simulation blocks and keep these updated across different processors. Scaling up to 10^6 cores has been demonstrated with very high efficiencies.[200]

Numerical stability of PIC algorithms has been extensively researched and is subject to ensuring a sufficiently small timestep along with sufficiently high resolution. For simulations involving lasers, the smallest timestep is determined by the Courant-Friedrichs-Lewy (CFL) condition.[201] A timestep smaller than CFL limit ensures that the set of partial differential equations being solved is numerically stable. For a standard 2D finite time difference method the CFL condition for plane electromagnetic waves in vacuum becomes

$$\frac{1}{c^2\Delta t^2} < \frac{1}{\Delta x^2} + \frac{1}{\Delta y^2}. \tag{3.24}$$

In typical simulations the resolution is coarser in the transverse direction, so for laser propagation along $\mathbf{i}$, we have $\Delta x \ll \Delta y$. Equation 3.24 then reduces to $c\Delta t < \Delta x$.

Resolution of the simulation is to be chosen such that the smallest features involved are properly resolved. In the direction transverse to laser propagation, the length scale of interest is thickness of the plasma sheath or Debye length, typically much longer than the laser wavelength. As a rule of thumb a resolution of 30 cells per wavelength

[200] F. Fiuza *et al. Record simulations conducted on Lawrence Livermore supercomputer.* URL: https://www.llnl.gov/news/record-simulations-conducted-lawrence-livermore-supercomputer (visited on 06/23/2016).

[201] R. Courant *et al*, IBM Journal of Research and Development **11**, 1967.

is chosen in the laser propagation direction.

Modern PIC codes also feature modules to simulate strong field ionisation. Thus the assumption of a fully ionised plasma is no longer needed. This allows for simulation of ionisation induced effects, such as ionisation defocussing,[202] ionisation blueshift[203] or ionisation injection.[204,205]

3.5.1 EPOCH code

The open source, freely available EPOCH code[206] was used to perform simulations presented in this thesis. EPOCH is a massively-parallel, explicit, 3D, fully relativistic PIC code with support for ionisation and collisions, written in Fortran 90. Support for strong field ionisation enables the code to be used to simulate ionisation injection processes. Unlike many other PIC codes, EPOCH is written in SI units throughout, allowing for intuitive evaluation of physical phenomena being simulated. It also features a QED module[207] to allow simulation of strong field effects, such as γ-ray production.

[202] S. C. Rae, *Opt Commun* **97**, 1993.
[203] S. Wilks *et al*, *Phys Rev Lett* **61**, 1988.
[204] T. P. Rowlands-Rees *et al*, *Phys Rev Lett* **100**, 2008.
[205] C. McGuffey *et al*, *Phys Rev Lett* **104**, 2010.
[206] T. D. Arber *et al*, *Plasma Phys Contr F* **57**, 2015.
[207] C. P. Ridgers *et al*, *J Comput Phys* **260**, 2014.

CHAPTER 4
Spectral modifications to the driver pulse in laser wakefield accelerators

CHARACTERISING THE LASER PULSE after its interaction with the plasma accelerator structure can provide invaluable information about the dynamics of the process. This chapter will discuss measurements performed on the Gemini laser employing both a $f/20$ and $f/40$ focussing optic, including spectral changes and self-guiding characteristics. A simple model will be put forward to allow for an intuitive understanding of the photon acceleration dynamics. Self-guiding performance over unprecedented distances will be discussed. Finally, the ability to tailor the laser-plasma interaction by changes to the spectral phase of the driver pulse is explored.

4.1 Motivation

The interaction of short pulse lasers with plasma is extremely difficult to diagnose due to the inherently short time scales involved. Indeed, the pulse passes through a 3 mm plasma in about 10 ps. Measuring the dynamics on this time scale is challenging; the resolution of the best oscilloscopes is of the order of a picosecond, with optical streak cameras achieving resolution of the order of 100 fs.[208] Thus most measurements are resigned to characterising the integrated effects, such as the changes to the laser spectrum.

However, the measurement of total spectral changes to the driving laser pulse should not be thought of being inferior as the motivation for accurate characterisation of the driver pulse after a laser-plasma interaction is manifold. As a high intensity laser pulse traverses a tenuous plasma, energy is transferred from the laser pulse to the plasma. If the spot size and temporal duration fulfil resonance conditions, a plasma wave can

[208] P. A. Jaanimagi, *Proc. SPIE* **5194**, 2004.

be set up in the wake of the laser pulse. The energy transfer manifests itself as the redshifting of some of the photons in the laser pulse. Thus measuring the spectrum and total energy of the transmitted pulse can provide information about the plasma wave generated by the laser. Indeed, it has been shown that in the linear regime the redshift is directly proportional to plasma wave amplitude.[209–212]

As the front of the laser drives the plasma wave and undergoes redshifting, the rear of the laser occupies a phase of positive refractive index gradients. This leads to an energy increase of the photons, also known as photon acceleration.[213,214] Using additional probe beams allows one to use photon acceleration to diagnose the excited wakefield.[44,45] Photon acceleration of the driver pulse itself has also been observed and provides evidence for the existence of relativistic plasma waves.[215] Thus the spectral changes imprinted on the laser pulse as it drives a wake provide extremely useful information about its propagation and the excited plasma wave.

With demonstrations of self-guiding over distances much longer than the Rayleigh range,[72,117] it is important to explore guiding performance at even longer lengths. While external guiding structures often offer better pulse guiding, self-guided wakefield acceleration is extremely attractive due to its robustness and ease of diagnosis.[1] Most self-guiding results thus far have employed optics with focussing geometries of $f/20$ or faster, at plasma densities of few 10^{18} cm^{-3}. To realise a multi-GeV self-guided laser wakefield accelerator, plasma densities below $n_e < 1 \times 10^{18}\,\mathrm{cm}^{-3}$ need to be employed. Thus characterising self-guiding performance at even lower plasma densities provides essential input for future accelerator design in this regime. With an increase to $f/40$ providing longer Rayleigh ranges and thus potential for guiding at lower plasma densities, comparing the guiding performance with an $f/20$ and $f/40$ is valuable for better understanding of the effect of initial focussing and limitations of self-guiding.

While the shortest laser pulse length yields the highest possible intensity, it may prove useful to lengthen the pulse somewhat with adding linear chirp. The effects of non-perfectly compressed ultrashort laser pulses have been considered theoretically in

[209] N. E. Andreev *et al*, *JETP* **101**, 2005.
[210] F. Wojda *et al*, *Phys Rev E* **80**, 2009.
[211] N. E. Andreev *et al*, *New J Phys* **12**, 2010.
[212] S. Shiraishi *et al*, *Phys Plasmas* **20**, 2013.
[213] S. C. Wilks *et al*, *Phys Rev Lett* **62**, 1989.
[214] L. Silva *et al*, *IEEE T Plasma Sci* **28**, 2000.
[44] J. R. Marquès *et al*, *Phys Rev Lett* **76**, 1996.
[45] C. W. Siders *et al*, *Phys Rev Lett* **76**, 1996.
[215] C. D. Murphy *et al*, *Phys Plasmas* **13**, 2006.
[72] J. E. Ralph *et al*, *Phys Rev Lett* **102**, 2009.
[117] S. Kneip *et al*, *Phys Rev Lett* **103**, 2009.
[1] Cf. Section 7.1

	Gemini 2012	Gemini 2015	ATA2 2013
Main beam diameter [mm]	150	150	55
Focussing optic focal length [mm]	3000	6000	1000
Focussing optic $f/\#$	20	40	18
Collection optic focal length [mm]	2540	3175	762
Collection optic $f/\#$	10	12.5	10
Distance to first wedge [mm]	1800	2400	420
Intensity on first wedge $\left[10^{13}\mathrm{W\,cm^{-2}}\right]$	0.79	1.77	0.48
Wedge hole annulus ratio	0.11	0.17	0.43
Number of wedge reflections	4	4	3
Polarisation	S	S	P

Table 4.1: *Parameters characterising the exit mode setups from the Gemini 2012, Gemini 2015 and ATA2 2013 campaigns.*

previous works.[216,217] The role frequency chirp plays in generation of relativistic electron beams has also been studied.[218,219] However, previous work is divided on what the best sign of linear chirp to use is. With opposing predictions for optimum spectral phase shaping in the literature,[2] experimental work to characterise the effects of chirp on relativistic electron beam generation is undertaken.

4.2 Experimental setup

The general setup of the suite of transmitted laser diagnostic, also known as exit mode, was described in Section 3.2. All the spectral data presented in this Chapter used optical layouts conceptually similar to this; hence, we will not divulge further into the layout. As results will be presented from multiple experimental campaigns, important details and parameters characterising the optical system will be discussed.

Table 4.1 presents parameters of the optical systems employed in three different experimental campaigns: the Gemini 2012, Gemini 2015 and Astra Target Area 2 (ATA2) campaigns. One of the most important diagnostic line guidelines to adhere by is to ensure the collection optic has a higher $f/\#$ than the focussing optic. The used focal ratios clearly follow this. The second important aspect is the intensity on the first wedge, given a full power shot without any plasma. If this is too high, damage will occur to the optic, degrading the entire optical system and resulting in reduced data quality. As can be seen, although the distance to the first wedge was increased

[216] C. B. Schroeder *et al*, *Phys Plasmas* **10**, 2003.
[217] A. G. Khachatryan *et al*, *Phys Rev E* **70**, 2004.
[218] V. B. Pathak *et al*, *New J Phys* **14**, 2012.
[219] S. Y. Kalmykov *et al*, *New J Phys* **14**, 2012.
[2] Cf. Section 4.5

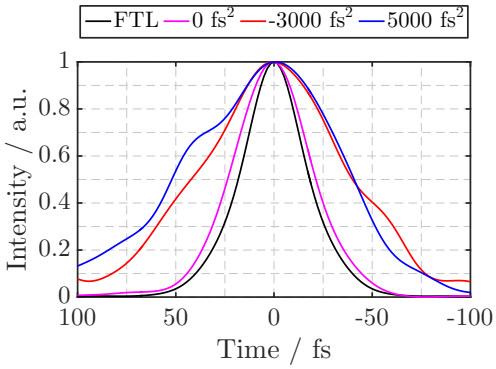

Figure 4.1: *Different pulse lengths, obtained by changing second order spectral phase with a Dazzler.*

for the Gemini 2015 campaign, a full power shot would have still been above surface damage threshold $I_{\mathrm{DT}} = 1 \times 10^{13}\,\mathrm{W\,cm^{-2}}$ for fused silica.[220] As the distance could not be further increased, the material of the optic was changed to BK7 optical glass, which has a higher damage threshold of $I_{\mathrm{DT}} = 2.8 \times 10^{13}\,\mathrm{W\,cm^{-2}}$. The first optic after the laser plasma interaction was a wedge with a central hole to allow the generated x-ray beam to be diagnosed. The ratio of the hole to the beam size on the optic, the annulus ratio, is important as it characterises the resolving power of an optical system. As is evident from Table 4.1, the hole for the ATA2 campaign was almost half the beam diameter. While an annulus increases the resolving power, this is accompanied by a decrease in total intensity and more pronounced diffraction effects.[3]

As the optical system used to image the spatial profile and spectrum of the exiting laser pulse consists of more than 10 optics with different coatings, the reflectivity of the individual optics plays a substantial role in determining the overall response of the system. Thus the spectral response of the entire system needs to be determined to extract the true spectrum at the laser interaction. This is usually achieved by measuring the throughput of the entire system with a calibrated blackbody source. If this measurement is impossible, an alternative approach is to calculate the Fresnel coefficients for all optics from the frequency dependent index of refraction.

Control over spectral phase of the main driver pulse without the need to change the stretcher or compressor positions is allowed by employing an acousto-optic programmable device in the stretched pulse.[221] Called the Dazzler, this decice allows arbitrary spectral intensity and phase to be applied to the pulse, thus allowing full

[220] D von der Linde *et al*, JOSA B **13**, 1996.
[3] Cf. Appendix C for more details.
[221] P. Tournois, *Opt Commun* **140**, 1997.

control over the compressed pulse shape. On the Gemini laser, the Dazzler has independent control over pulses sent to Gemini target area and Astra Target Area 2. The control software allows spectral phase up to the fourth order to be independently controlled. Figure 4.1 depicts pulses measured during Gemini 2015 campaign with different amounts of second order spectral phase applied by the Dazzler. The Fourier Transform limited pulse is plotted as the black line. The red and blue lines depict the pulse shapes of pulses with severe negative and positive chirp, respectively. The direction of the time axis is such that negative times correspond to the front of the pulse. Symmetric pulses with large chirp of both positive and negative sign are observed, indicating relative lack of higher order spectral phase terms.

4.3 Photon acceleration with varying plasma density

4.3.1 Experimental data

The spectral change to the driver pulse was measured as a function of plasma density during the Gemini 2012 campaign. A 15 mm supersonic nozzle was employed with pure He gas. Backing pressures up to 100 bar resulted in electron densities up to $4 \times 10^{18}\,\mathrm{cm}^{-3}$. The laser energy after compression was $\mathcal{E}_L = (13.5 \pm 0.8)\,\mathrm{J}$. The laser spot waist sizes from using an $f/20$ optic at $1/e^2$ intensity were $(17.8 \pm 0.6)\,\mu\mathrm{m}$ and $(15.8 \pm 0.5)\,\mu\mathrm{m}$ for the major and minor axes, respectively. The FWHM contour of the spot contained $(32 \pm 1)\,\%$ of the total energy. The peak intensity, found by integrating the focal spot images, is $I_{\mathrm{peak}} = (2.8 \pm 0.1) \times 10^{19}\,\mathrm{W\,cm}^{-2}$, giving a normalised peak vector potential in vacuum of $a_0 = 3.6 \pm 0.3$.

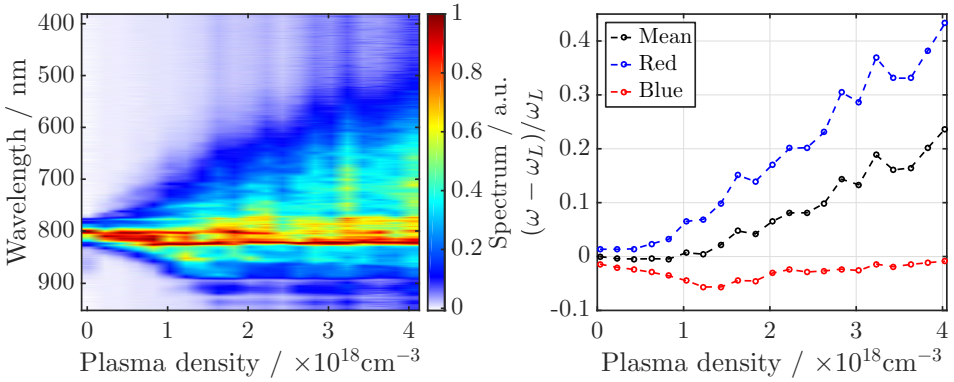

(a) Spectrometer data *(b) Spectral extents*

Figure 4.2: *Results from a plasma density scan with a* 15 mm *supersonic nozzle. Panel (a) depicts the averaged spectrum over four shots whereas the edges of the spectrum are plotted in Panel (b).*

Figure 4.2 presents results from a plasma density scan. In Figure 4.2a, the spectra integrated along the spatial axis is plotted as columns, with each shown spectrum being an average over 4 full power shots.[4] The first column, at $n_e = 0$, is a vacuum reference shot. Broadening of the bandwidth is evident, as is the asymmetrical nature of the process. The amount of blueshift detected increases with rising plasma density. There is an initial increase in redshift as well; however, the longer wavelength edge of the spectrum quickly shifts outside the detection window of the spectrometer. Note the sidebands seen for wavelengths longer than 900 nm are a relict from the diagnostic itself.

The qualitative description of the spectral changes can be converted into a quantitative measurement by measuring the shift of the edges of the spectrum. A convenient method to do this is to introduce the spectrum edge as the frequency above (below) which $e^{-2} = 13.5\%$ of the spectral energy is contained. The spectral energy is calculated by assuming $\mathcal{E}_{\text{spec}} \propto I\omega$, where I is the signal strength. Also, the mean frequency is defined as the intensity weighted average frequency, $\bar{\omega} = \int \omega \cdot \tilde{S}(\omega)\mathrm{d}\omega / \int \tilde{S}(\omega)\mathrm{d}\omega$. The spectral edges and the mean frequency calculated are plotted in Figure 4.2b for the plasma density scan shown in Figure 4.2a. An increase of the blue edge of the spectrum with plasma density is observed. The mean frequency also increases with rising plasma density. Interestingly, the red edge of the spectrum decreases initially and then stays constant. This is mainly due to instrument limits.

4.3.2 Simulations

The shift of the blue edge of the spectrum to even shorter wavelengths with increasing plasma densities can be explained by ionisation blueshift and photon acceleration. The first of these is caused by the leading edge of the laser interacting with a suddenly created plasma. The interaction with photoionised plasma leads to an upconversion of the photon frequency according to $\omega_F^2 = k_L^2 c^2 + \omega_p^2$, where ω_F is the final, upconverted frequency of the photon.[203,222] This expression is valid for so called flash ionisation, i.e. a situation in which plasma is created on the timescale of a single laser cycle. This is also the maximum possible frequency shift, as ionisation on a slower timescale will make the transition smoother and result in less blueshift.[222] The fractional frequency shift can easily be calculated and is given by $(\omega_F - \omega_L)/\omega_L \simeq n_e/(2n_c)$. Thus for the plasma densities used here, of the order of $10^{18}\,\mathrm{cm}^{-3}$, would lead to fractional frequency shifts of $\sim 10^{-4}$, clearly insufficient to explain the large blueshifts seen here. This esti-

[4] This averaging is the reason for the relatively smooth spectra; in single shots modulations are often seen, similarly to the spectra shown in Figure 4.15.

[203] S. Wilks *et al*, *Phys Rev Lett* **61**, 1988.

[222] J. Dias *et al*, *Phys Rev Lett* **78**, 1997.

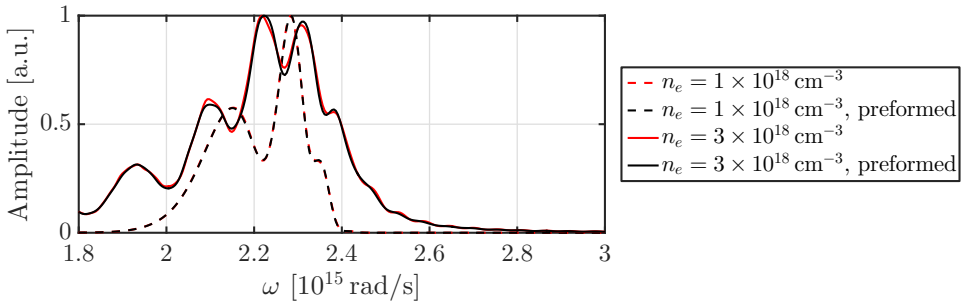

Figure 4.3: *Spectrum for a laser pulse propagating in preformed plasma (red lines) and neutral helium with ionisation enabled (black lines) for two plasma densities.*

mation agrees with implications from a previous study.[223] Confirmation of this simple estimate is provided by performing 1D simulations, with and without ionisation. Figure 4.3 shows on-axis spectra calculated from the electric field of a laser pulse propagating in a preformed plasma or neutral helium with ionisation enabled. The laser intensity is $a_0 = 3.5$ and plasma densities of $n_e = 1 \times 10^{18}\,\mathrm{cm}^{-3}$ and $n_e = 3 \times 10^{18}\,\mathrm{cm}^{-3}$ were simulated. The spectra from preformed plasma and neutral gas are extremely similar to each other at different densities, showing the measured increase in blueshift is not caused by ionisation blueshift.

As the physics of photon acceleration is predominantly one-dimensional, a large range of 1D PIC simulations were performed to study the spectral changes during the interaction. A laser of $\tau_{\mathrm{FWHM}} = 50\,\mathrm{fs}$ was propagated through a 13 mm long

[223] B. M. Penetrante *et al*, Journal of the Optical Society of America B **9**, 1992.

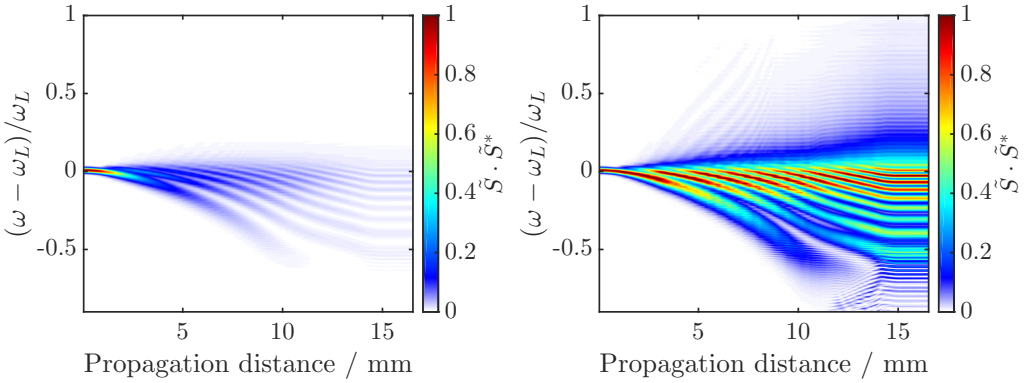

(a) *Spectral intensity* ***(b)*** *Normalised spectral intensity*

Figure 4.4: *Time evolution of laser spectrum in a 1D simulation with $a_0 = 2.5$ and $n_e = 2.5 \times 10^{18}\,\mathrm{cm}^{-3}$. Panel (a) depicts the spectral intensity whereas in Panel (b) each timepoint has been normalised to 1.*

plasma with 1 mm linear ramps at both ends. The intensities used were in the range $0.1 \leq a_0 \leq 3.9$ and plasma densities in the range $5 \times 10^{17}\,\mathrm{cm}^{-3} \leq n_e \leq 4 \times 10^{18}\,\mathrm{cm}^{-3}$ were simulated. The longitudinal resolution was set to $\Delta x k_L = 0.21$.

The evolution of the laser spectrum for $a_0 = 2.5$ and $n_e = 2.5 \times 10^{18}\,\mathrm{cm}^{-3}$ as a function of propagation distance is plotted in Figure 4.4. For each column, the spectrum $\tilde{S}$ is calculated by Fourier transforming the laser electric field and the spectral energy $\tilde{S}\tilde{S}^*\omega$ is shown. In Figure 4.4a, the redshifting and decay of the laser pulse energy is seen. Additionally, a small blueshift of the spectrum is also seen. In Figure 4.4b the spectrum for each timestep is normalised to 1, thus highlighting the change in frequencies observed. While the bulk of the laser energy is seen to redshift as the pulse does work on the plasma electrons, a sizeable fraction of energy also becomes blueshifted.

It proves instructive to examine the evolution of the laser pulse as it propagates

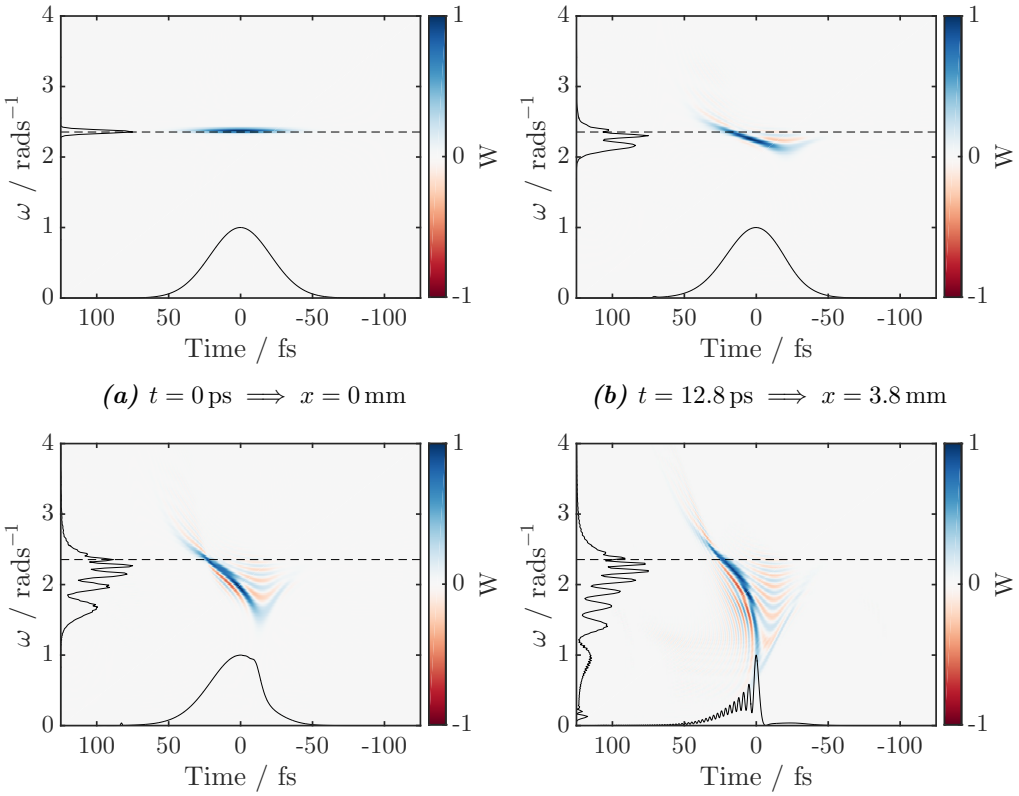

Figure 4.5: *Wigner plots of the electric field of the laser pulse at different times during the interaction. The dashed line is the central frequency of the laser in vacuum.*

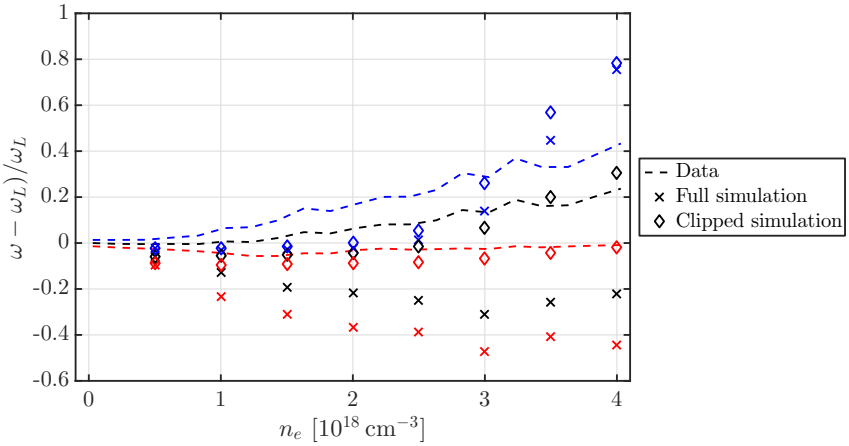

Figure 4.6: *Spectral edges calculated for a simulated density scan along with experimentally measured data: the crosses show edges of the full laser spectrum, diamonds are the edges calculated when accounting for the finite sensitivity of the spectrometer, circles are experimental data.*

through the plasma to understand the heavy modulations in the spectrum. Wigner plots,[224] effectively phase space plots of the laser pulse, are plotted for the laser at different snapshots through its propagation in Figure 4.5. The laser and plasma conditions are identical to those in Figure 4.4. Redshifting of the pulse starts from the front as the laser drives a plasma wake, growing more severe with propagation, as is evident from the spectrum marginals plotted in each of the panels in Figure 4.5. By $x = 11.3\,\text{mm}$, the depletion at the front has become severe enough for some photons to lose all their energy. Blueshifting clearly occurs at the rear of the pulse, with the amount of frequency shift also increasing with propagation distance. The spectral modulations are observed as early as $x = 3.8\,\text{mm}$ and are seen to arise from similar frequency components being present at different phases in the pulse, analogously to self-phase modulation.

Analysis to find the edges of the spectrum can be performed on the simulation data. Results from this calculation are presented in Figure 4.6, where the blue and red edge along with the mean frequency are plotted for 1D PIC simulations with $a_0 = 3.5$. The crosses of different colour represent the spectrum delimiters calculated from the simulations. A much larger redshift for the red edge is predicted, disagreeing with the experimental results. Additionally, the mean frequency is found to move to longer wavelengths as well.

However, the full spectrum available in the simulations is not equivalent to the measurements made. Thus, the spectrum obtained from simulations can be clipped to account for the sensitivity range of the spectrometer used. Spectrum edges calcu-

[224] J. Paye, *IEEE J Quantum Elect* **28**, 1992.

lated from equivalent spectra are plotted as diamonds of different colour in Figure 4.6. The agreement between measured and simulated redshifts is excellent when taking the finite field of view of the spectrometer into account. Reasonable agreement between simulation results and measured spectra edges are seen for higher plasma densities as well.

4.3.3 Simple 1D model

As discussed in Section 2.4.4, photon acceleration is the result of a comoving density gradient. Insight into the current situation can be gained by simple 1D analysis, which involves solving Equation 2.39 for various plasma densities. Figure 4.7a depicts density perturbation calculated for plasma densities in the range $0.1 \times 10^{18}\,\mathrm{cm}^{-3} \leq n_e \leq 4 \times 10^{18}\,\mathrm{cm}^{-3}$ as a function of $\xi = z - v_g t$. The laser pulse length is $\tau_{\mathrm{FWHM}} = 45\,\mathrm{fs}$ and normalised vacuum potential $a_0 = 3.5$. The gradient of refractive index $\eta^2 = 1 - \omega_p^2/(\gamma\omega_L^2)$ is shown in Figure 4.7b, where the laser field envelope is also plotted.

This simple approach helps understand the complex non-linear physical processes in a straightforward manner. Firstly, the increasing amount of redshift with plasma density is seen to arise from the increase of the density gradient near the front of the laser pulse, evident in Figure 4.7b. The plasma responds to the laser ponderomotive force and thus sets up a wake. Crucially, for higher plasma densities the plasma response is faster, thus creating larger refractive index gradients. This then leads to an increased rate of redshift. Moving away from the photon acceleration framework, higher plasma densities require more work to be done by the laser and thus lead to faster laser depletion; the latter manifests as redshifting of the spectrum.

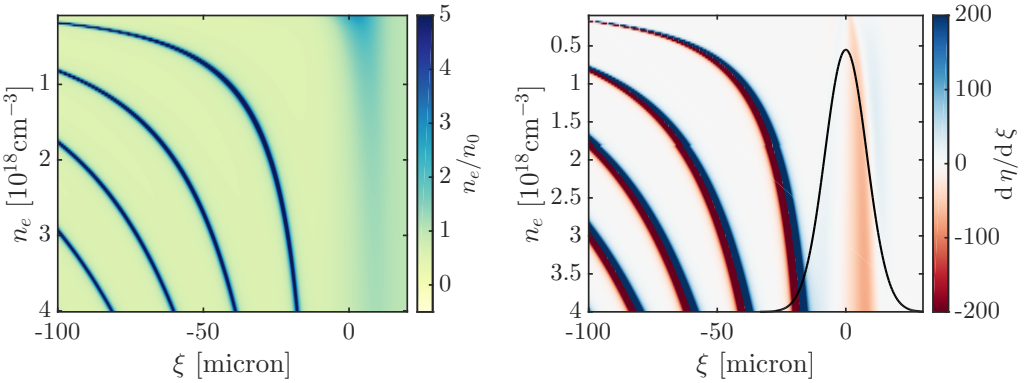

(a) Plasma wave *(b) Refractive index gradient*

Figure 4.7: *1D non-linear plasma response to a* 50 fs *laser pulse with* $a_0 = 3.5$ *for a range of plasma densities is shown in Panel (a). Panel (b) depicts the refractive index gradients in the plasma wave. The laser field envelope is also plotted as the black line in Panel (b).*

Explaining the increasing amount of blueshift follows a similar argumentation. It can be seen from Figure 4.7b that as the plasma density increases, more of the laser pulse resides in regions of positive $\mathrm{d}\eta/\mathrm{d}\xi$, with the gradient itself becoming larger as well. This increases the rate of blueshifting as the rate of photon acceleration is directly proportional to the refractive index gradient.[5] Additionally, a larger fraction of the pulse actually resides in a region of positive refractive index gradient as the plasma wavelength decreases with rising plasma density. Thus a greater amount of laser photons will feel an accelerating force, leading to an increased amount of blueshift.

4.3.4 Discussion

Albeit being simple and intuitive, the stationary 1D approach neglects pulse evolution involving self-focussing and pulse compression. These will increase the intensity of the laser and thus make the interaction more non-linear, elongating the ion cavity. Thus exact modelling of the interaction requires extensive simulations. The approach presented here allows for an understanding of the phenomena, without explicitly reproducing the experimental results.

With the physics leading to the spectral changes explored it is instructive to discuss previous work related to laser frequency modulations. The broadening observed in Figure 4.2 is symmetrical for smaller plasma densities. The red edge does not evolve further after $1.5 \times 10^{18}\,\mathrm{cm}^{-3}$. The blueshifting, however, continues and thus increases the average frequency as well. This is in contrast with recent observations from a lower intensity experiment.[158] Genoud *et al* observe the opposite effect, where the red edge of the spectrum continues to shift to lower frequencies and the blue edge remains roughly constant. In those experiments, $a_0 \simeq 1.4$ and number densities up to $3 \times 10^{19}\,\mathrm{cm}^{-3}$ are used, an order of magnitude higher than in the current study. The redshift they observe could be consistent with the amount of shift observed here, however, the evolution of the blue side is completely different. This could be attributed to much shorter interaction distances (1.8 mm vs 15 mm here) and more severe depletion, leading to smaller blueshift formation times.

For weakly relativistic pulses it has been shown that the redshift of the laser pulse is directly related to the excited wakefield amplitude.[209] This has also been observed experimentally.[210,212] Albeit the laser not being in this weak regime for the present case, this model could explain the growing redshift with the increase of density for lower n_e. The stop of the redshift would thus be interpreted as an indication of wake amplitude saturation. However, as shown in preceding sections, the observed stop of redshift is in

[5] Cf. Equation 2.65

[158] G. Genoud *et al*, *Phys Plasmas* **20**, 2013.

fact caused by diagnostic limitations.

4.4 Self-guiding over extended distances

As discussed earlier, the performance of guiding over extended lengths is critical for self-guided laser wakefield accelerators. While the plasma response provides a focussing force for $P > P_c$, the interaction itself is highly non-linear. Additionally, the very front of the laser continuously excites the plasma wave and is thus thought to not feel a focussing force, causing it to diffract away. Experimental data on the effectiveness of guiding is thus of imperative importance to correctly understand the self-guiding process of ultrashort laser pulses.

4.4.1 $f/20$ focussing geometry

The use of a variable length gas cell[6] allows the guiding performance to be easily measured at various plasma lengths. Such measurements were performed during the 2012 Gemini campaign, employing a $f/20$ focussing geometry. The laser parameters were the same as presented in Section 4.3, with spot waist sizes at $1/e^2$ intensity of $(17.8 \pm 0.6)\,\mu\text{m}$ and $(15.8 \pm 0.5)\,\mu\text{m}$. The FWHM contour of the spot was measured to contain $(32 \pm 1)\,\%$ of the total energy. The peak intensity is $I_{\text{peak}} = (2.8 \pm 0.1) \times 10^{19}\,\text{W cm}^{-2}$, yielding a normalised peak vector potential in vacuum of $a_0 = 3.6 \pm 0.3$.

A range of single shots depicting the plane of exit from the plasma are plotted in Figure 4.8. The shots presented here were chosen as the clearest examples of self-guiding at a given cell length. The parameters at which these shots were taken are presented in Table 4.2. Each of the panels in Figure 4.8 displays an area of $1 \times 1\,\text{mm}^2$. Additionally, the size of the laser nearfield for vacuum propagation over the same distance is plotted as the white dashed lines; for images where this contour is not seen, the laser would have diffracted to be larger than the area of the CCD. Note for Panels (d) and (e) the round clip limiting the unguided halo is the output aperture of the gas cell. The collection optic of the forward line was moved in unison with cell length to ensure the exit plane of the plasma was always imaged.

The Rayleigh range calculated from assuming a gaussian spot size of $w_0 = \sqrt{w_x w_y} = 16.8\,\mu\text{m}$ yields a value of $z_R = 1.1\,\text{mm}$. However, as discussed in Section 3.1.2, the spot actually deviates from pure gaussian form and thus the M^2 of the beam should be calculated. For an $f/20$ optic, a value of $M^2 = 3.3$ is found, thus giving a Rayleigh range of $z_{R,R} = 0.34\,\text{mm}$. The image in Panel (e) in Figure 4.8 was taken with a plasma

[6] Cf. Section 3.4.2

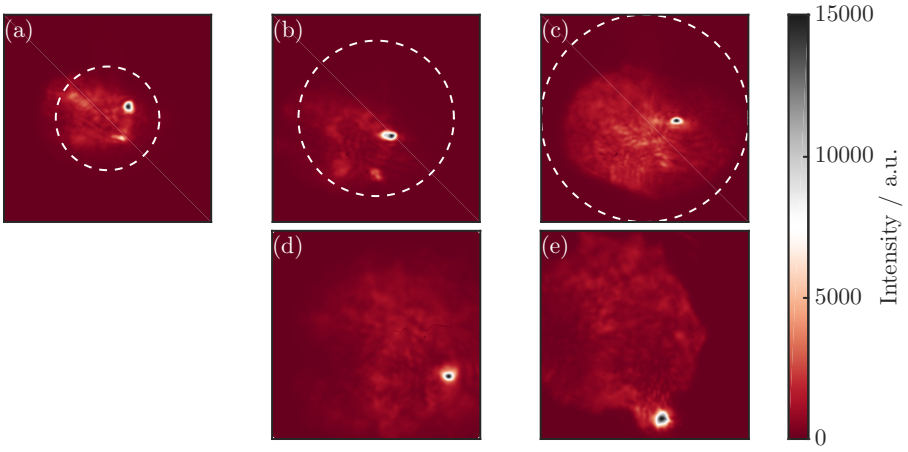

Figure 4.8: *Measured spatial modes after different propagation distances in plasma with $f/20$ focussing. The white dashed line depicts the size of the laser nearfield for vacuum propagation over the same distance. All images are normalised to a single colour table.*

Shot	L_{cell} mm	n_e $10^{18}\,\mathrm{cm}^{-3}$	P/P_c	w_{fil} µm
(a)	10	3.0	26	15.6
(b)	15	1.8	15	17.4
(c)	20	2.4	20	13.2
(d)	28	2.1	18	15.4
(e)	39	1.5	13	23.8

Table 4.2: *Experimental parameters for exit mode images presented in Figure 4.8.*

length of $L_{\mathrm{cell}} = 39\,\mathrm{mm}$. Thus, given the adjusted Rayleigh range, the shot shown in Panel (e) in Figure 4.8 shows guiding for $115 z_{\mathrm{R,R}}$. Assuming a gaussian input mode of the same size, the total guiding distance would be $35 z_{\mathrm{R}}$. In both cases, the data clearly demonstrates self-guiding over tens of Rayleigh lengths for pulses with $c\tau \sim \lambda_p$.

Previous work on self-guiding has shown that the size of the guided filament is expected to scale with the plasma wavelength.[110] However, the mode size should also be dependent on the ratio of laser power to the critical power for self-guiding.[225] The experimentally measured scaling of the exiting laser mode size with plasma density is plotted in Figure 4.9; the mode size here corresponds to the $1/e^2$ radius of intensity. The vertical error bars are standard errors in the mean; for the data point without a vertical error bar in Figure 4.9 only one shot was available. Also plotted are some theoretical predictions,[7] namely the one arising from the stationary envelope model

[110] A. G. R. Thomas *et al*, *Phys Rev Lett* **98**, 2007.
[225] E. Esarey *et al*, *IEEE J Quantum Elect* **33**, 1997.
[7] Cf. Section 2.4.3

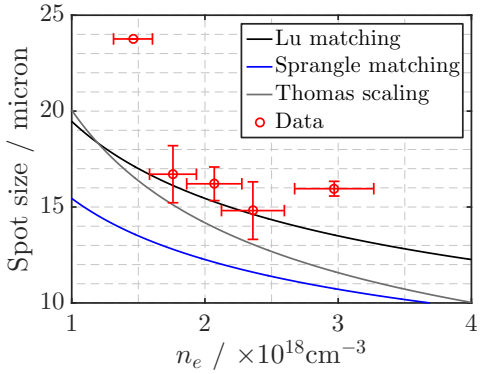

Figure 4.9: *Scaling of the measured exit mode size with plasma density, along with some theoretical predictions, for $f/20$ focussing optic.*

of Sprangle *et al*[109] and the scaling put forward by Lu *et al*.[63] Both of these scale as $w_m \propto (P/P_c)^{1/6}$ and the laser power used here is $P = \alpha P_L \simeq 140\,\text{TW}$, with α corresponding to the amount of energy contained within the $1/e^2$ radius. Additionally, the empirically observed scaling of Thomas *et al*[110] is plotted as the grey line, given by $w_{\text{FWHM}} \sim \lambda_p$.

The data points are seen to follow closest the scaling by Lu *et al.* The shots with the lowest and highest plasma density (corresponding to the longest and shortest gas cell lengths, respectively) are seen to be outliers to this trend. The reason for the spot size being much larger than the expected size can be explained by excessive depletion for the shot with the longest gas cell length. Indeed, the guiding length of 39 mm is 2.2 times longer than the depletion length, given by Equation 2.71. The pulse will guide until its power still satisfies $P > P_c$, after which slow diffraction will occur. As the pulse is still mildly relativistic when that occurs, the plasma will provide some focussing forces, but not sufficient to maintain guiding.

4.4.2 $f/40$ focussing geometry

With guiding over tens of Rayleigh lengths observed with gas cell lengths up to 42 mm, guiding performance was characterised for even longer plasmas by employing the $f/40$ optic during the 2015 Gemini campaign. The same gas cell was used, with an extension allowing for lengths up to $L_{\text{cell}} = 90\,\text{mm}$. The laser spot size at $1/e^2$ intensity was $r_{\text{minor}} = (37 \pm 2)\,\mu\text{m}$ and $r_{\text{major}} = (48 \pm 6)\,\mu\text{m}$.[8] The $1/e$ contour was found to contain $(50 \pm 5)\,\%$ of the laser energy. With a pulse duration $\tau_{\text{FWHM}} = (43 \pm 5)\,\text{fs}$ and

[109] P. Sprangle *et al*, *IEEE T Plasma Sci* **15**, 1987.
[63] W. Lu *et al*, *Phys Rev Spec Top-Ac* **10**, 2007.
[8] For detailed description of the laser focal spot see Section 7.2.1

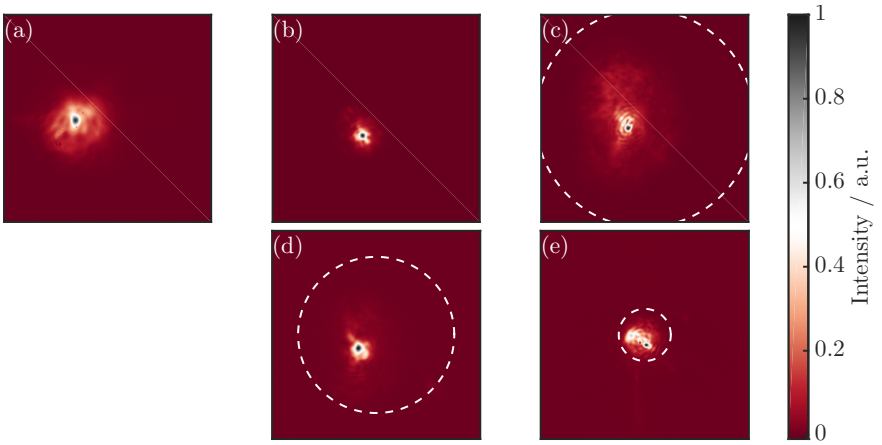

Figure 4.10: *Measured spatial modes after different propagation distances in plasma with $f/40$ focussing. The white dashed line depicts the size of the laser nearfield for vacuum propagation over the same distance. All images are normalised to their individual maxima.*

Shot	L_{cell} mm	n_e $10^{18}\,\text{cm}^{-3}$	P/P_c	w_{fil} µm
(a)	90	0.95	6.3	24.4
(b)	70	1.0	6.6	16.6
(c)	42	1.6	11	16.0
(d)	30	1.3	8.6	24.2
(e)	10	1.5	9.9	14.3

Table 4.3: *Experimental parameters for exit mode images presented in Figure 4.10.*

total energy on target of $\mathcal{E}_L = (8.6 \pm 0.4)\,\text{J}$, the peak intensity was measured to be $I = (5.7 \pm 0.8) \times 10^{18}\,\text{W}\,\text{cm}^{-2}$, yielding $a_0 = 1.6 \pm 0.1$.

Figure 4.10 depicts single shots of the exit plane of the plasma for different gas cell lengths. Details of the experimental conditions for each of the shots taken are presented in Table 4.3. The longest gas cell length used was $L_{\text{cell}} = 90\,\text{mm}$, with the exiting spatial mode shown in Panel (a) in Figure 4.10. Assuming a gaussian spot of $w_0 = \sqrt{w_x w_y} = 42\,\mu\text{m}$ yields a Rayleigh range of $z_R = 6.9\,\text{mm}$ and thus guiding over $13 z_R$ is observed. However, as discussed previously, the M^2 scaled Rayleigh range should instead be used. For an $f/40$ optic the value $M^2 = 4.1$ is obtained, yielding $z_{\text{R,R}} = 1.7\,\text{mm}$ and thus giving guiding over $53 z_{\text{R,R}}$. The plasma density for this shot was $n_e \simeq 9.5 \times 10^{17}\,\text{cm}^{-3}$, yielding an estimated depletion distance of $L_{\text{dpl}} \sim 25\,\text{mm}$. The guided filament is clearly distinguishable after propagation distance more than three times as long as the depletion length. Self-guiding is hence witnessed for distances much longer than depletion length. This result, along with other data

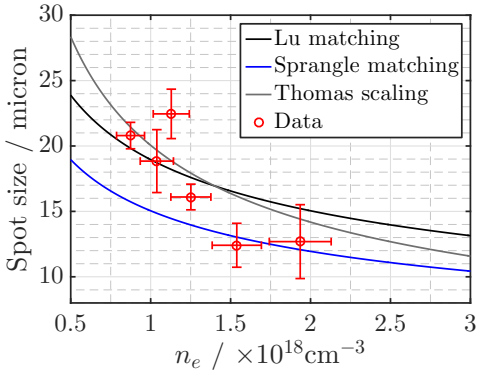

Figure 4.11: *Scaling of the measured exit mode size with plasma density, along with some theoretical predictions, for $f/40$ focussing optic with a 60 mm long gas cell.*

in Figure 4.10, shows the ability to guide ultrashort laser pulses over distances of the order of centimetres.

While single shots at different lengths are plotted in Figure 4.10, a more systematic study was performed at $L_{\text{cell}} = 60$ mm to characterise self-guiding over extremely long distances and the scaling of the guided mode with plasma density. Figure 4.11 depicts the beam waist sizes (radius at $1/e^2$ intensity) of the laser spatial mode after exiting from the plasma. The error bars are standard error in the mean. Again, scalings by Lu,[63] Sprangle[109] and Thomas[110] are plotted, with the laser power $P = \alpha P_L \simeq 120$ TW used in the former two of these. While a general trend of inverse variation with plasma density is witnessed, this does not clearly follow any of the theoretical predictions. For all plasma densities here, the depletion length is shorter than the plasma length. Thus, while self-guiding is unambiguously observed for a plasma length of 60 mm, the deviation of measured mode sizes from theoretical and empirical predictions may be caused due to laser depletion.

4.4.3 Discussion

For data obtained with the $f/20$ focussing geometry an interesting asymmetry where the guided filament emerges near the edge of the unguided halo is often observed. In fact, the location of the filament was found to be very stable for multiple shots taken at conditions similar to that in Panel (e) in Figure 4.8. This asymmetry can be explained by considering the often imperfect quasi-nearfield of the laser near the focus. In the full nearfield the spatial profile of the laser exhibits a top hat nature, where in the Fraunhofer limit in the far field a confined focal spot is observed. However, in the region close to focus, at a few Rayleigh lengths away, diffraction is governed by Fresnel

diffraction as the phase variation across the beam is now bigger. Thus any imperfections in the nearfield phase will play a large role determining the intensity pattern, leading to hotspots and very asymmetric spatial profiles. As the laser is still focussing when entering the plasma, these nearfield imperfection will affect the coupling of the laser into the plasma and can thus drive instabilities that will affect the direction of propagation of the guided filament.

This observation helps explain the prominence of filaments exiting near the edges of the unguided halo for the $f/20$ data and the lack of such observation for the $f/40$. The longer focal length leads to a larger Rayleigh length, hence reducing the degree of filamentation near the entrance of the plasma. This leads to much more centred exit position with respect to the unguided halo, as seen in Figure 4.10.

The mode sizes of self-guided beams obtained with the $f/20$ follow the scaling from Lu *et al*, $k_p w_m = 2^{3/2}(P/P_c)^{1/6}$. However, for the $f/40$ the spatial extent of the guided filaments was observed not to follow that scaling to the same extent. A reason for this deviation can be the different amount of energy coupled into the guided mode in the plasma. This variation can again be attributed to the spatial intensity profile near the focal plane. The upramp at the beginning of the gas cell can be thought of as an input coupler into a guided filament in the plasma. Clearly, with a very filamented profile at the start of the plasma ramp a lot of the energy will not be captured. A smoother quasi-nearfield profile will be advantageous in trapping more energy into the plasma cavity, thus effectively providing a higher power (as $P \equiv \alpha P_L$). Hence, with a smooth input spatial mode, different plasma densities will provide a different input coupler and can thus maximise energy capture for a particular number density. Work is ongoing to quantify this in both simulations and with a theoretical model.

Self-guiding over extremely long lengths, upwards of $100 z_{\mathrm{R,R}}$ was observed. This was deemed impossible in early work on the subject of self-guiding of short pulses with $c\tau \sim \lambda_p$.[96,97,225] Previous experimental work has clearly showed the opposite though, with self-guiding over tens of Rayleigh lengths reported by Kneip *et al*.[117] Here, these results are extended up to lengths of more than a hundred Rayleigh lengths. The main reasoning for the inability to guide ultrashort pulses was the fact the plasma does not respond quickly enough to the ponderomotive force and thus the front c/ω_p of the pulse always diffracts away.[225] From this postulate, an effective diffraction rate can be estimated by assuming c/ω_p of the pulse is lost with every z_R. Thus, the length for diffractive depletion can be estimated as $L_{\mathrm{diff}} \simeq L z_R/(c/\omega_p) = z_R \tau \omega_p$. For a $\tau = 50\,\mathrm{fs}$ pulse with $z_R = 1.1\,\mathrm{mm}$ propagating in $n_e = 1 \times 10^{18}\,\mathrm{cm}^{-3}$ the diffractive depletion

[96] P Sprangle *et al*, *Phys Rev Lett* **64**, 1990.
[97] P Sprangle *et al*, *Phys Rev A* **41**, 1990.

length is $L_{\text{diff}} \simeq 2.8\,\text{mm}$. This shows that diffraction of the front collisionless skin depth is occurring much more slowly in the experiments from this work and indeed reported in the literature before.

4.5 Effects of spectral phase on laser plasma interaction

Previous theoretical work has shown that both positively and negatively chirped pulses can yield enhancements for electron beams when compared to fully compressed pulses. Pathak *et al*[218] demonstrate that a positive chirp increases trapping rate and enhances energy coupling to the wake. It is shown that this is due to the red spectral components in the front of the pulse, lowering the phase velocity of the bubble and increasing the etching rate $\nu = c\omega_p^2/\omega_L^2$. This also increases laser energy coupling to the plasma. On the other hand, Kalmykov *et al*[219] contend that negative chirp reduces the amount of dark-current by lowering pulse front etching and thus delaying the onset of formation of a very steep laser front. The latter will cause continuous injection into the bubble which degrades bubble evolution. With polar opposite predictions for optimum spectral phase shaping in the literature, experiments were undertaken to understand the dynamics of electron acceleration and laser energy coupling into the wake.

4.5.1 Gas jet results

The amount of linear chirp applied to a pulse was varied by changing the second order phase setting in the Dazzler. While the pulse length is usually changed by de-optimising the laser compressor by varying the grating separation, such a method also introduces higher order phase effects. Notable third order spectral phase is introduced, changing the skewness of the pulse and introducing other physical effects into the interaction. Indeed, lack of change of symmetry of the laser pulse with varying amounts of chirp applied with the Dazzler is demonstrated in Figure 4.1.

The linear chirp coefficient $b \equiv \mathrm{d}^2\varphi/\mathrm{d}\omega^2$ was scanned between $-2000\,\text{fs}^2 \leq b \leq 2000\,\text{fs}^2$. The laser parameters are the same as presented in Section 4.3. The transmitted laser spectrum and energy after propagation through a 15 mm gas jet plasma target were measured. The spatially integrated spectra for different chirp settings is presented in Figure 4.12. For both panels, each row corresponds to an average of at least 4 full power shots. Additionally, to highlight the changes to the spectrum, each row has been normalised to its maximum value. Figure 4.12a depicts the transmitted spectra for $n_e = 2.3 \times 10^{18}\,\text{cm}^{-3}$ and Figure 4.12b shows data for $n_e = 3 \times 10^{18}\,\text{cm}^{-3}$. Additionally, the dashed lines show the extent of $1/e^2$ bounds of the laser spectrum

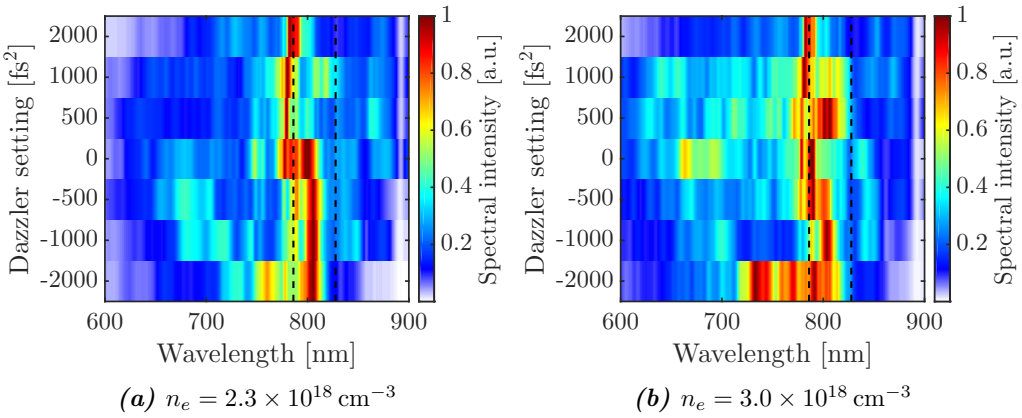

(a) $n_e = 2.3 \times 10^{18}\,\mathrm{cm}^{-3}$ ***(b)*** $n_e = 3.0 \times 10^{18}\,\mathrm{cm}^{-3}$

Figure 4.12: *Transmitted laser spectrum for different amounts of linear chirp applied with the Dazzler for (a)* $2.3 \times 10^{18}\,\mathrm{cm}^{-3}$ *and (b)* $3 \times 10^{18}\,\mathrm{cm}^{-3}$.

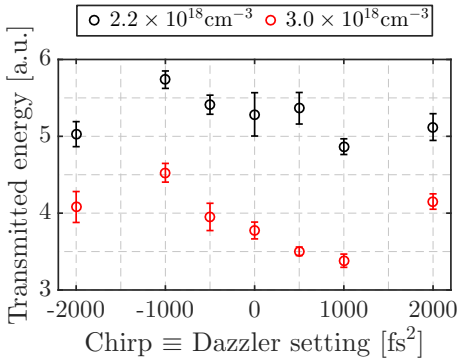

Figure 4.13: *Transmitted laser energy for different linear chirps applied to the pulse with the dazzler for two different plasma densities.*

in vacuum. There is a clear dependence in Figure 4.12a between sign of the chirp and the frequencies being transmitted through the plasma. It is seen that for positive chirps, the red part of the spectrum is depleted whereas for negative chirps the blue part is transmitted. Thus there is a correlation between the colour that comes first in the pulse and the side of the initial laser spectrum that is transmitted – the spectral components in the front of the pulse are "etched away". The same behaviour is seen for the $n_e = 3 \times 10^{18}\,\mathrm{cm}^{-3}$ data, but with more total laser energy depleted the correlation is somewhat less clear.

The effect of pulse chirp on laser energy coupling into the plasma can also be studied. Figure 4.13 depicts the measured energy throughput for two plasma densities. The transmitted energy is calculated as the integral of energy on the exit mode camera and is normalised to incident laser energy. Each datapoint is an average of at least four

shots and the error bars denote the standard error. A clear variation of transmitted energy with pulse chirp is observed. The amount of energy coupled into the plasma is seen to increase with increasing chirp, with optimum coupling observed for $b = 1000\,\mathrm{fs}^2$. The extreme values of $|b| = 2000\,\mathrm{fs}^2$ are seen to deviate from this trend and yield identical energy transmission values. This is because for these chirp values the pulse is much longer than the plasma period ($\tau_{\mathrm{FWHM}} \simeq 110\,\mathrm{fs}$ with $2\pi/\omega_p = 74\,\mathrm{fs}$ at $n_e = 2.3 \times 10^{18}\,\mathrm{cm}^{-3}$) and the coupling physics differs from the pulse front etching model. The ratio of maximum and minimum energy transmission is $r \sim 1.2$ for $n_e = 2.3 \times 10^{18}\,\mathrm{cm}^{-3}$ and $r \sim 1.3$ for $n_e = 3 \times 10^{18}\,\mathrm{cm}^{-3}$.

4.5.2 Gas cell results

The gas cell that was heavily used in the Gemini 2015 campaign[9] was first trialled during the Gemini 2012 experimental campaign. A Dazzler scan was performed with cell length set to $L_{\mathrm{cell}} = 28\,\mathrm{mm}$ and $n_e \simeq 2 \times 10^{18}\,\mathrm{cm}^{-3}$. The laser parameters were measured to be the same as presented in the preceding section.

The gas cell plasma target provided extremely stable self-guiding performance. This along with an imaging spectrometer allowed for distinction of spectrum of the guided filament and the unguided halo surrounding the spot. The difference between these is shown in Figure 4.14, where the blue line shows the spectra of the guided filament whereas the red line plots the spectrum of the surrounding halo, both normalised to 1. Also shown is the laser spectrum in vacuum. A large fraction of unshifted laser spectra is evident in the unguided spectrum whereas a redshift of the entire laser spectrum is visible for the guided filament.

Spectra of the guided filament is plotted in Figure 4.15 for a range of linear chirp

[9] Cf. Section 3.4.2

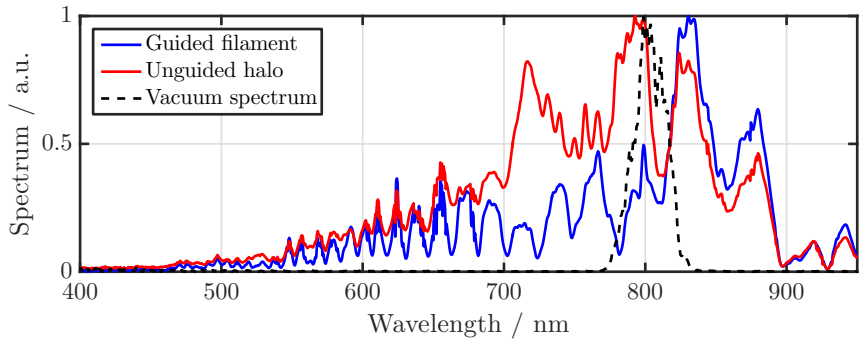

Figure 4.14: *Guided (blue line) and unguided (red line) spectrum, measured after* 28 mm *gas cell. The black dashed line shows the initial laser spectrum.*

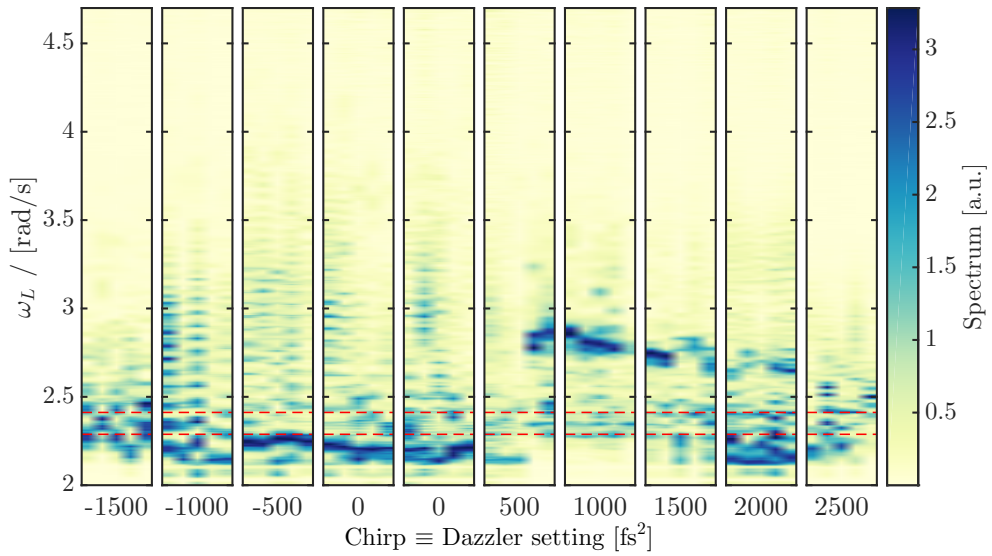

Figure 4.15: *Transmitted spectra of the guided filament for individual shots at different Dazzler linear chirp settings for $n_e = 2 \times 10^{18}\,\mathrm{cm}^{-3}$. The red dashed lines represent the width of the laser spectrum in vacuum.*

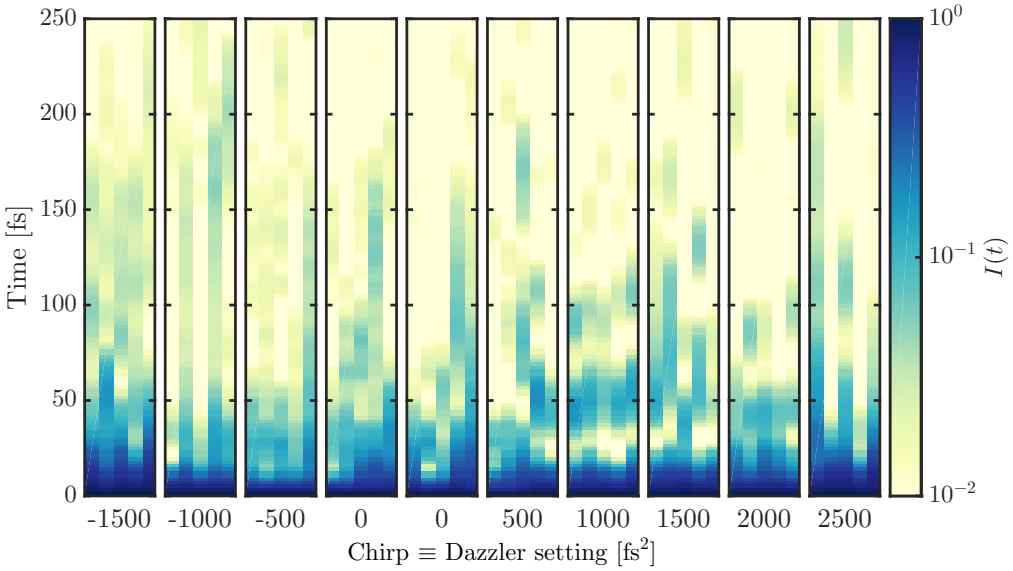

Figure 4.16: *Fourier transforms of individual transmitted spectra of the guided filament (shown in Figure 4.15) shots at different Dazzler linear chirp settings for $n_e = 2 \times 10^{18}\,\mathrm{cm}^{-3}$.*

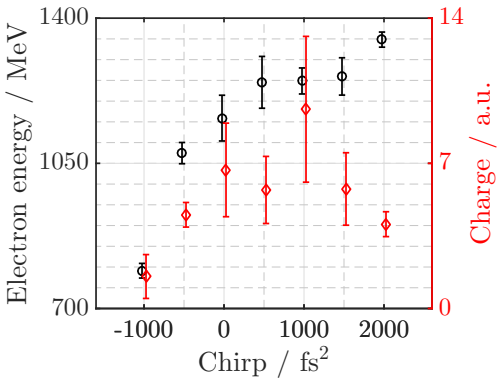

Figure 4.17: *Maximum energy and total beam charge measured with a* 28 mm *gas cell for different Dazzler settings.*

settings applied by the Dazzler. The red dashed lines show the extent of the laser spectrum in vacuum. Similarly to results seen in Figure 4.12, changing the sign of the chirp yields large effects on the guided spectrum. While negative chirps result in only slightly modified spectra, applying positive chirp increases the fraction of blueshifted spectrum hugely. Additionally, a large amount of spectral beating is observed in most of the spectra.

If the spectral beating is assumed to be due to interference from different pulselets, the spectral intensity data can be Fourier transformed to yield a map of temporal intensity. Note this is an approximation only, as the spectral phase of the pulse can not be measured with a spectrometer alone. The temporal intensity profiles arising from Fourier transforming every single-shot spectrum presented in Figure 4.15 are shown in Figure 4.16. There is a general lack of distinct, localised features corresponding to two pulse interference in the temporal profile for negative chirps. However, for positive chirps a clear second peak is often seen, with a peak at $\sim 50\,\mathrm{fs}$ very clearly observed for $b = 1000\,\mathrm{fs}^2$.

The effect of linear chirp on the generated electron beams was also studied. Figure 4.17 depicts the average cutoff electron energy (black circles) along with the total beam charge (red diamonds). Due to experimental constraints the pointing offset is not known for these shots; also the cross calibration to absolute charge was not performed. Thus the charge measurement provides information about the relative change only. Also, arising from lack of detailed pointing information on-axis electron beams are assumed for all Dazzler settings. The cut-off beam energy is seen to increase with a more positive chirp parameter b. Interestingly, some increase is even seen for the longest pulse with $b = 2000\,\mathrm{fs}^2$. A clear optimum chirp is observed for beam charge at $b \simeq 1000\,\mathrm{fs}^2$. For the highest amounts of positive chirp, the total charge is seen to reduce again.

4.5.3 Discussion

The transmitted spectra measurements performed with gas jet targets allow the dominant energy depletion mechanism to be determined. There are two main processes for energy loss in the operation regime here, the so called Decker model[113] and diffraction loss. The Decker model describes energy depletion of the laser pulse as a slow etching of the pulse, at a rate of $\nu = c\omega_p^2/\omega_L^2$. The laser energy is also depleted via diffraction losses as the front c/ω_p of an ultrashort pulse that is not guided.[97] Assuming the characteristic length of diffraction is Rayleigh range, the pulse front moves back in the boosted frame at a rate of $c/(\omega_p z_R)$. Hence, pulse front etching dominates over diffraction losses if the laser spot size w_0 satisfies $w_0^2 > 2(\omega_L/\omega_p)(c^2/\omega_p^2)$. This simple scaling implies that for densities of the Dazzler scans reported here, pulse front erosion is the dominant energy loss mechanism. The spectral transmission results from the gas jet measurements indeed provide unambiguous evidence that the energy loss is well described by the Decker model.

Intuitively it would be expected from the pulse erosion model that the smallest amount of energy is transmitted for the shortest pulse. This is in contradiction to the data presented in Figure 4.13, where optimised laser energy coupling was observed for moderate positive chirp. The reason for this is twofold. On the one hand, etching rate is increased for positively chirped pulses, meaning faster pulse erosion with $\nu_{\text{etch}} = c\omega_p^2/\omega_L^2$. At the same time, non-linear wake excitation means the rear of the bubble resides in an ion cavity, where it moves at the speed of light. Thus the rear of the pulse catches up with the front, leading to pulse compression with a rate of $\nu_{\text{comp}} = c\omega_p^2/(2\omega_L^2)$.[106] Thus the pulse is etched from the front, losing energy to the wake, and the rear of the pulse continuously moves forward, providing energy compression into a shorter pulse. Both of these phenomena are enhanced for longer wavelengths, thus explaining why the rate of energy loss is increased with positively chirped pulses.

The spectra of the guided filament presented in Figure 4.15 exhibits clear spectral beating for a majority of shots. The Fourier transforms of these spectral show clear features at $\sim 50\,\text{fs}$. This could be taken as an indication of interference between pulses separated by 50 fs. The fact that such strong features become more prominent with positive chirp could be explained by the prominence of red frequencies at the front of the pulse becoming extremely redshifted earlier in the interaction. This radiation then falls back in the bubble and is blueshifted at the rear of the bubble, in the presence of a positive refractive index gradient. Such pulselets would be be separated by $\sim \tau_p$, the plasma period; the plasma period $\tau_p = 2\pi/\omega_p$ is $\tau_p = 79\,\text{fs}$ at $n_e = 2 \times 10^{18}\,\text{cm}^{-3}$,

[113] C. D. Decker *et al*, *Phys Plasmas* **3**, 1996.
[106] J. Schreiber *et al*, *Phys Rev Lett* **105**, 2010.

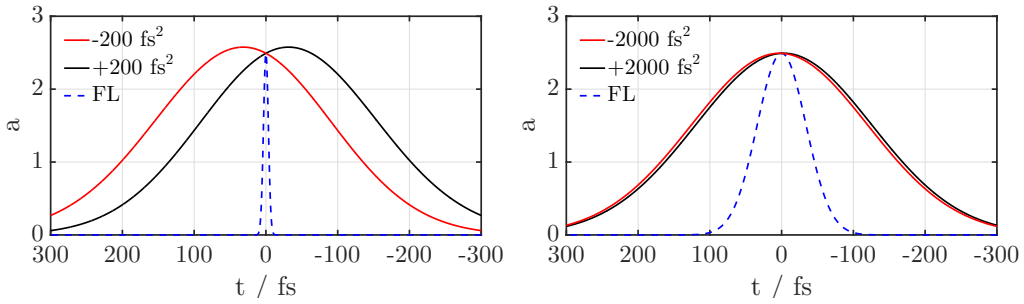

(a) *Fourier limited* $\tau = 4\,\mathrm{fs}$ **(b)** *Fourier limited* $\tau = 40\,\mathrm{fs}$

Figure 4.18: *Transform limited pulses of duration* 4 fs *(Panel (a)) and* 40 fs *(Panel (b)) stretched by* 200 fs^2 *(Panel (a)) and* 2000 fs^2 *(Panel (b)) of positive and negative chirp, highlighting the asymmetry in* $a(t)$ *due to instantaneous frequency chirp. Negative times corresponds to earlier in the pulse.*

longer than the separation between the peaks.

The increase of maximum electron energy with chirp is interesting as it contradicts some previous work. Pathak *et al*[218] suggest that negatively chirped lasers yield higher peak energies as the phase velocity of the bubble is higher, the opposite to the current study. This can be explained by noting that injection threshold is proportional to the wake phase velocity. Thus negatively chirped pulses incur a higher self-injection threshold, leading to shorter acceleration distances and thereby reducing the electron beam energy. At the same time, positively chirped pulses compress at a faster rate than pulses with negative chirp, thus increasing the laser power. This leads to a larger blowout, which will reduce the injection threshold and increase total available energy gain. The increased self-injection threshold also explains the total beam charge asymmetry about the shortest pulse seen in Figure 4.17.

A similar asymmetry of accelerated charge with pulse asymmetry was reported by Leemans *et al*.[226] However, in that work the predominant reason for increased charge is found to be the pulse skew, as chirp was created by deoptimising the pulse compressor. Indeed, the authors explicitly mention that frequency chirp is of minimal importance. More recent work employing compressor length changes observed a reverse effect, showing decrease of total charge with positive chirp.[227] In this work the observed changes are attributed to a frequency chirp along with an asymmetric intensity profile.

Varying chirp of the pulse with pulse compressor changes always introduces higher order phase terms as well. Most notably, third order spectral phase is added to the pulse, changing its skewness. Using the Dazzler negates this addition of third order phase; indeed the measurement of the pulse at different chirp parameters reveals a

[226] W. P. Leemans *et al*, *Phys Rev Lett* **89**, 2002.
[227] T. Z. Zhao *et al*, *Plasma Phys Contr F* **58**, 2016.

symmetrical pulse at all settings as shown in Figure 4.1. However, the temporal profile $E(t)$ of the laser is not what drives the plasma wave, but rather the quantity $a = eE/(m_e c\omega_L)$ is. Introducing a frequency chirp also makes $a(t)$ asymmetrical about the centre as the instantaneous frequency $\omega_{\text{inst}} = \omega_0 - \mathrm{d}\varphi/\mathrm{d}t$ becomes a function of time.[228] Figure 4.18 shows $a(t)$ calculated for a $\tau_{\text{FL}} = 4\,\text{fs}$ and $\tau_{\text{FL}} = 40\,\text{fs}$ Fourier limited pulses of amplitude $E_0 = 1 \times 10^{13}\,\text{V}\,\text{m}^{-1}$, stretched by chirps of $|b| = 200\,\text{fs}^2$ and $|b| = 2000\,\text{fs}^2$ in Panels (a) and (b), respectively. As can be seen, for extremely short pulses the frequency chirp introduces a significant asymmetry into $a(t)$. However, for bandwidth limited pulses of the order of 40 fs the asymmetry is small. Thus in this work the change in electron beam properties is indeed caused by the frequency chirp itself, rather than pulse asymmetry, making it the first such measurement.

4.6 Conclusion

The spectral modifications undergone by the laser pulse driving a highly relativistic plasma wave were characterised. Simultaneous red and blueshifting were observed as different parts of the laser pulse reside in varying refractive index gradients. A simple and intuitive model describing the photon acceleration dynamics was put forward and good agreement between 1D PIC simulations and measured data was observed when accounting for the finite field of view of the spectrometer. This allows for quick identification of the features in the spectra to intuitively understand the laser interaction dynamics.

Self-guiding over hundreds of Rayleigh ranges was experimentally measured when using an $f/20$ focussing optic. The scaling of the size of the guided filament was found to closely match theoretical predictions based on the 3D non-linear theory by Lu *et al*.[63] Self-guiding over distances up to 90 mm was experimentally measured with an $f/40$ focussing geometry. The extended guiding at plasma densities of $n_e \simeq 9.5 \times 10^{17}\,\text{cm}^{-3}$ extends the self-guiding regime to previously uncharted number densities, paving the way for multi-GeV electron acceleration in the self-guided regime with densities $n_e < 1 \times 10^{18}\,\text{cm}^{-3}$.

Experimental measurements of wakefield acceleration driven by positively and negatively chirped laser pulses were performed. An improved coupling of the laser energy to the plasma was observed with moderate positive chirp. The spectral signatures of the initial chirp were characterised, with an increased stability of generating very blueshifted spectral peaks with positive chirp. Additionally, varying chirp allowed for unambiguous identification of pulse front etching as the predominant laser energy loss

[228] S. De Silvestri *et al*, *IEEE J Quantum Elect* **20**, 1984.

mechanism. Increasing positive chirp was also measured to increase electron beam energy, with total beam charge reaching an optimum for moderate positive chirps. Understanding the changes caused by different signs of linear chirp provides further options for controlling laser wakefield accelerators.

CHAPTER 5
Suppression of self-injection in laser wakefield accelerators

THIS CHAPTER PRESENTS EXPERIMENTAL and theoretical work on the topic of inhibiting self-injection. Experimental evidence for suppression of the self-injection process was observed during a campaign at ATA2. Further work provided a model to explain the physics of the process. It is found that beam loading from the initially injected bunch changes the transverse momentum of sheath electrons returning to axis and thus increase the threshold for self-injection.

5.1 Motivation

Many advanced laser plasma accelerator concepts rely on controlled injection and stable acceleration of the electron bunch. In order to achieve the former, the normalised laser potential a_0 is kept below ~ 2 to operate in the so called quasi-linear regime. One of the main reasons for doing so is the necessity to avoid self-injection of electrons. Whilst being of utmost importance in some scenarios, self-injected electrons typically possess many unwanted characteristics such as large emittance and spot size. This means that self-injected electrons would degrade the beam quality of the witness bunch. The solution thus far has been to operate the accelerator in a quasi-linear regime, with $a_0 \sim 1 - 2$. Using a matched density should ensure that no significant intensity amplification will happen and thus self-injection will not occur.

However, from the scalings in the 3D non-linear regime[63] it is evident that single stage energy gain $\Delta W \propto a_0$. Thus operating at higher laser intensities leads to increased energy gains. Secondly, as dephasing length and depletion length scale the same in this regime, 3D non-linear regime yields maximum efficiency for transferring energy from

[63] W. Lu *et al*, *Phys Rev Spec Top-Ac* **10**, 2007.

the laser to the electron beam. In addition to this, operating in a fully non-linear regime with $a_0 \gtrsim 2$ results in full cavitation of the bubble. Hence focussing fields inside the bubble will vary linearly with radial distance which in turn is a requisite to conserve emittance. The latter is a crucial parameter characterising particle beams and their focussability. Operating in the quasi-linear regime has been analysed before,[229] showing that it is indeed possible to induce linear transverse fields within the wake by proper tailoring of the laser spot size. However, being so intimately linked to laser focal spot shape will reduce reliability due to jitter issues, additionally the accelerating field varies radially as well. In the 3D non-linear regime these restrictions are not present. Thus the relative robustness of the bubble regime makes it desirable to operate in the 3D non-linear regime.

In this chapter we present experimental evidence of suppression of self-injection due to beamloading effects from preinjected charge. In our experiment, the preinjection is achieved by employing ionisation induced injection. Injecting charge externally would also have the same effect and thus enables staging of laser wakefield accelerators operating in 3D non-linear regime.

5.2 Experimental setup

The experiment was conducted in Astra Target Area 2 (ATA2). The layout of the experimental chamber is shown in Figure 5.1. The main laser beam diameter is 55 mm and it enters the interaction chamber through a window in a gatevalve, which allows the compressor chamber to stay under vacuum even when the target chamber is at atmosphere. For full power shots the gate valve is opened to avoid B-integral issues in the window. Polarisation of the main beam at focus is horizontal along the x-axis, as defined in Figure 5.1.

The beam is reflected off two high reflectivity dielectric mirror, M1 and M2. A 632 nm alignment beam, highlighted in Figure 5.1, is injected through M2. This allows most of the alignment to be done without using the 800 nm main beam. In order to allow for alignment with visible beams, mirrors M3 and M5 have protected silver coatings. The off-axis angle of the gold coated $f/16$ parabola is $\theta_{\text{off}} = 7.97°$, allowing the beam to pass M3 and be folded with M5. The positions of the parabola and M5 were chosen to keep the intensity on M5 as low as possible. However, the mirror did suffer laser damage every few days and was replaced regularly.

The optical setup for the transmitted laser diagnostics is also shown in Figure 5.1 as the blue beamline. The first optic after the plasma interaction is a holey wedge (cf

[229] T. Mehrling *et al*, *Phys Rev Spec Top-Ac* **15**, 2012.

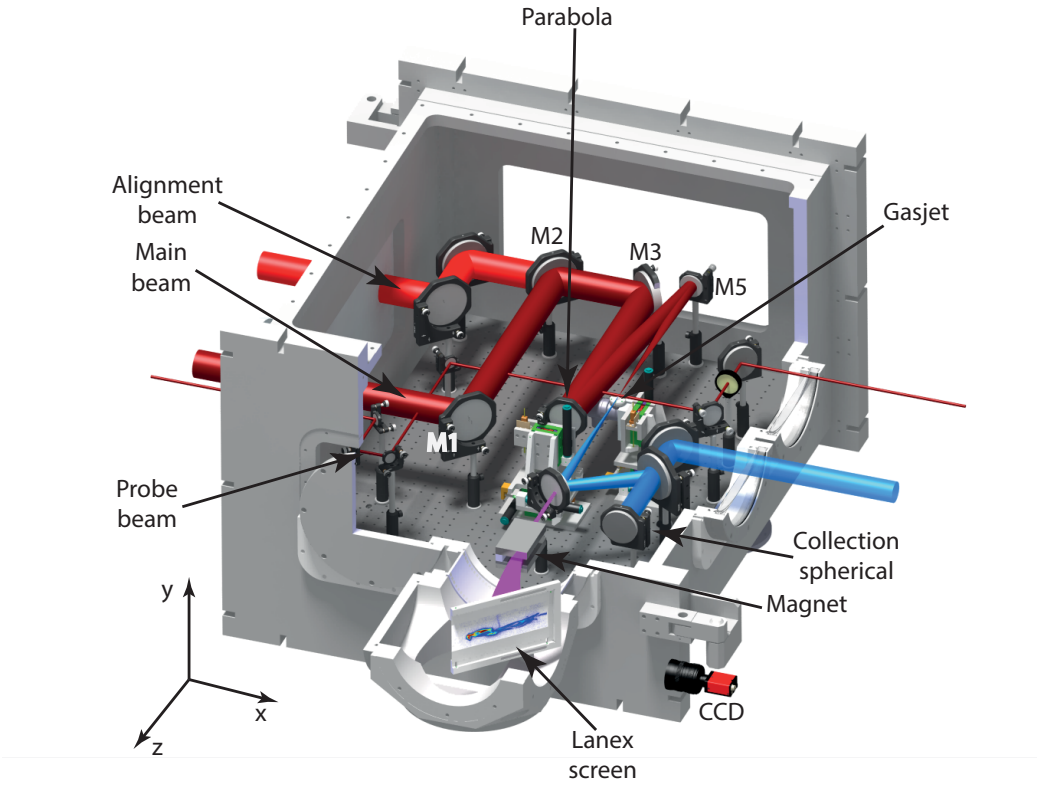

Figure 5.1: *Cutaway CAD drawing showing the layout of the ATA2 2012 experiment.*

Section 3.2). The beam is reflected off another wedge and collimated by a 3 inch diameter, 762 mm focal length spherical mirror. The collimated beam is then transported out of the vacuum chamber as shown in Figure 5.1.

The hole in the wedge allows the electron beam to pass through undeterred. The electron energies are diagnosed using a permanent dipole magnet spectrometer with an average field strength of $B = 0.7\,\mathrm{T}$ over 119 mm. A scintillating screen (Lanex Regular) is placed at 45° to characterise the deflection angles of the electron beam. The resolution of the spectrometer is plotted in Figure 5.2. The dashed lines show the errors in measured energy due to a 1 mm misalignment of the screen whereas the solid lines are the errors arising from beam divergence, taken as $\theta_{\mathrm{half}} = 3.3\,\mathrm{mrad}$. Evidently the measurement error is dominated by the divergence of the beam. Scintillation light emitted at 546 nm is imaged onto a 14-bit charge-coupled device (AVT Stingray F-033[230]). There is an interference filter before the CCD chip to block out any residual

[230] Allied Vision Technologies. *Stingray F-033 documentation*. URL: https://www.alliedvision.com/en/products/cameras/detail/Stingray/F-033.html (visited on 05/10/2016).

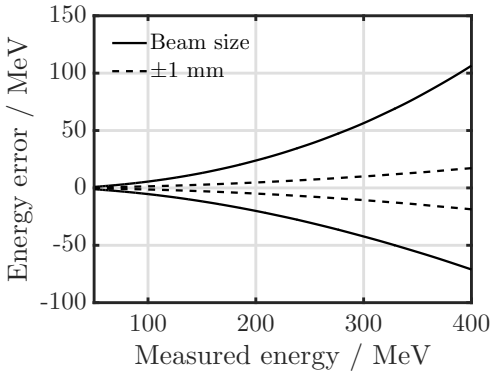

Figure 5.2: *Spectrometer resolution with errors in measured energy arising from 1 mm misalignment of screen end, dashed lines, and errors arising from beam divergence, solid lines.*

laser light.

The holey wedge was replaced with a 100 mm diameter scintillating screen to perform beam profile measurements. This screen was placed at 45° to the main beam axis and scintillation light was imaged onto a CCD (AVT Stingray F-033). This diagnostic enabled measurement of the average beam pointing offset and the beam divergence.

The laser-plasma interaction was diagnosed using transverse probing. A low energy, independently compressed 12 mm diameter beam enters the interaction chamber spatially offset from the main beam, as shown in Figure 5.1. It is then folded and passes through the interaction perpendicular to the main laser. The plane of the driver laser is imaged with a two lens image relay system onto shadowgraphy and interferometry diagnostics.

5.2.1 Focal spot and laser characteristics

Before commencing full shots multiple images of the focal spot at best conditions were recorded. This is crucial for enabling simulations after the experiment. The focal spot diagnostic comprised of an apochromatic, infinity corrected, high numeric aperture and long working distance 10× microscope objective,[231] coupled to a 14-bit CCD. The spatial calibration of the image was performed with a $d = 7$ mm period grating, placed in the near field of the beam. The focal plane was determined by scanning the z-position of the objective and was nominally set to the edge of the nozzle. Focal scans were performed by moving the z position of the parabola such that the focal plane moved further into the gas jet or further out. The definitions of focussing further into or out of the jet are sketched in Figure 5.3. Also shown is a sketch of the plasma

[231] Edmund Optics. *Mitutoyo 10x NIR*. URL: http://www.edmundoptics.co.uk/microscopy/infinity-corrected-objectives/mitutoyo-nir-nuv-uv-infinity-corrected-objectives/46403/ (visited on 05/10/2016).

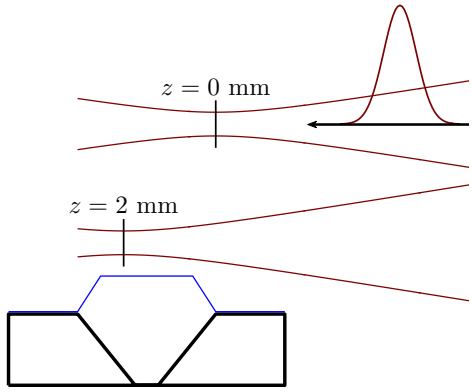

Figure 5.3: *The definition of focussing planes in the nozzle. The laser moves from right to left, with $z = 0$ plane coinciding with the edge of the nozzle. The plasma density profile is sketched as the blue line. Focussing further into the nozzle corresponds to focussing further to the left.*

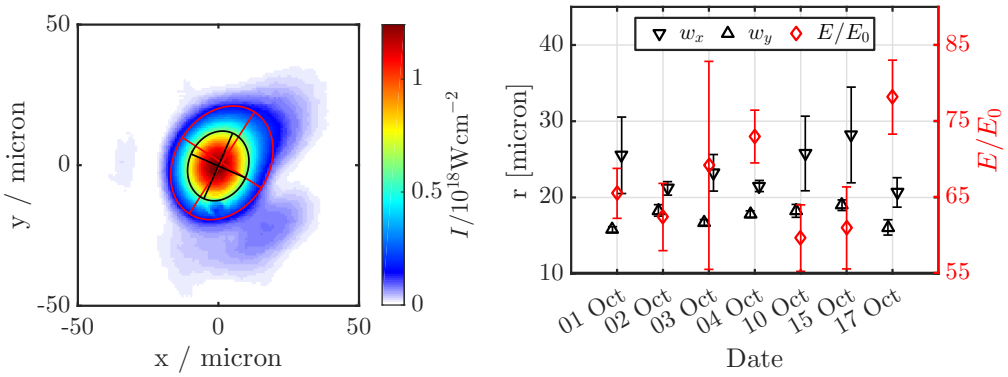

(a) *Typical focal spot* ***(b)*** *Focal spot data*

Figure 5.4: *Characteristics of measured focal spots. Panel (a) depicts a single spot image whereas panel (b) collates spot parameters from different days.*

density profile, which was found to be close to trapezoidal with linear 0.5 mm ramps at the edges of a 2 mm plateau. The focal position corresponding to the beginning of the density plateau is $z = 0.5$ mm.

Figure 5.4 summarises the focal spot characteristics. A typical single shot focal spot, measured by attenuating the fully amplified ASTRA beam with wedges and neutral density filters, is depicted in Figure 5.4a. The black line in the same image shows the extent of the full-width-half-maximum contour, whereas the red line is the outline of $1/e^2$ level. Figure 5.4b shows the beam waist sizes for different days of the experiment. The fraction of energy within the $1/e^2$ contour is also plotted. Good stability and day-to-day reproducibility is evident and justifies comparing data taken on different days.

The achieved focal spot was elliptical with beam waists ($1/e^2$ intensity radius) of $w_x = (24.0 \pm 4.8)\,\mu\text{m}$ and $w_y = (17.3 \pm 1.3)\,\mu\text{m}$, respectively; the errors quoted are the standard deviation. The diffraction limit for the focussing geometry is 15 microns, thus the best focus was 1.6 times diffraction limited. On average, the $1/e^2$ contour of the spot contained $(66.9 \pm 9.7)\,\%$ of the total energy. However, as the images were saved in 8-bit format, this is an overestimate due to the dynamic range of the data being restricted.

The amount of energy delivered to target was implied from a calibrated near field camera before the compressor by measuring the total throughput from before the compressor to target. On average, the energy on target was $(419 \pm 38)\,\text{mJ}$. The pulse duration was measured to be $\tau_{\text{FWHM}} = (37 \pm 3)\,\text{fs}$. With the pulse parameters and the enclosed energy, the peak intensity on target was $(1.1 \pm 0.3) \times 10^{18}\,\text{W cm}^{-2}$, corresponding to a normalised vacuum potential of $a_0 = 0.71 \pm 0.08$.

The target used was a 3 mm diameter supersonic nozzle, with a solenoid valve kept open for 15 ms and opened 10 ms before the shot. Backing pressures were measured using an absolutely calibrated pressure transducer before each shot. Backing pressures in the range $p = 0 \ldots 25$ bar were used, resulting in plasma densities up to $3 \times 10^{19}\,\text{cm}^{-3}$. Pure helium and helium with 5% CO_2 impurity were used.

5.3 Experimental results

5.3.1 Electron beam profile for pure helium

An electron beam profile measurement with pure helium was performed at $n_e = 1 \times 10^{19}\,\text{cm}^{-3}$ whilst keeping all controlled variables constant. Individual shots of this stability run are plotted in Figure 5.5a, where all images have been normalised to their respective maxima. Calibration of the laser axis position on the profile screen was not performed on this day and hence the zero position on the axes is arbitrarily chosen as the middle of the image.

Pointing of the beam was measured by calculating an intensity weighted centroid for each image. Divergence is measured by fitting an ellipse to the FWHM contour of the electron beam for shots 4, 5, 10, 13, 14 and 15. For all other shots, the beam is not smooth enough for this method. Instead, the image is summed either vertically or horizontally. For the resulting line, the boundaries of a central region containing 50 % of the total energy are found, such that there is 25 % of total energy to either side. For two dimensional gaussian, this is equivalent to finding the FWHM widths in each direction.

A summary of the divergence and pointing measurements for this dataset is collated

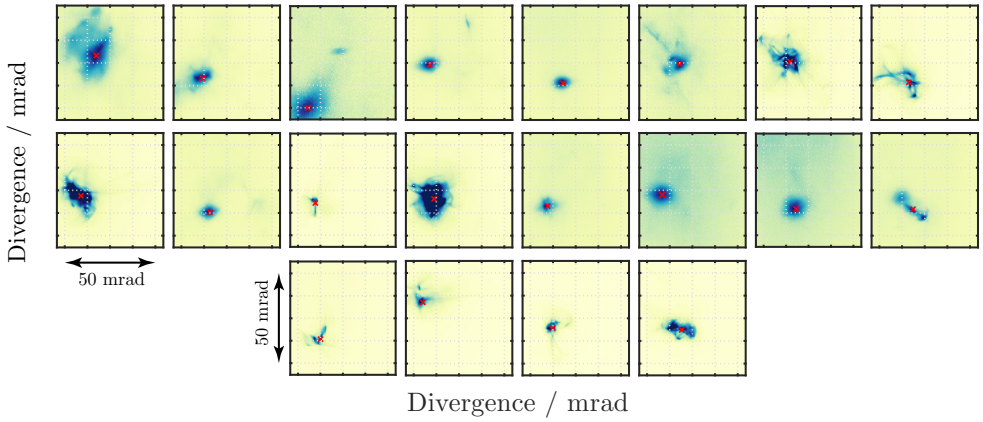

(a) Individual shots

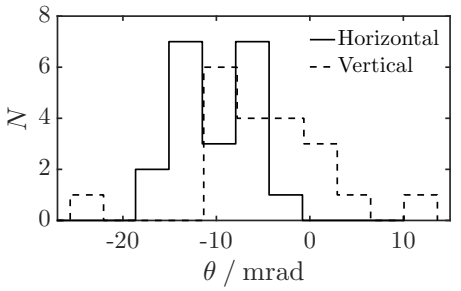

(b) Beam pointing

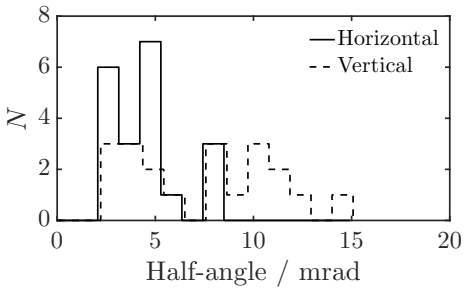

(c) Beam divergence

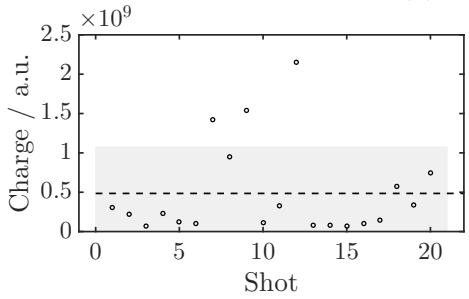

(d) Total charge

Figure 5.5: *Results from beam pointing stability run for self-injected electron beams with* $n_e = 1.0 \times 10^{19}$ cm^{-3}. *Panel (a) depicts single shots, with the red cross marking the extracted pointing direction. Panels (b) and (c) plot statistics of beam pointing and divergence, respectively, while the total integrated charge is shown in Panel (d).*

	Pointing (mrad)	Divergence (mrad)
Horizontal	-12.0 ± 4.5	4.1 ± 1.8
Vertical	-6.2 ± 7.2	6.9 ± 3.6

Table 5.1: *Summary of electron beam pointing results for pure helium.*

in Table 5.1, where quoted errors are the standard deviation. Reference for the pointing direction is arbitrary, as mentioned before. However, large variations about the mean direction are clearly observed. Histograms of vertical and horizontal beam pointing are shown in Figure 5.5b. The error in the vertical direction is dominated by a few shots with extremely large pointing offsets. The large fluctuations can be caused by the imperfect spatial profile of the laser before focus, as for this dataset the vacuum focus was placed $z = 2.5\,\mathrm{mm}$ into the nozzle.[1]

The divergence of the beam also exhibits very large variability, as illustrated in Figure 5.5c. The mean FWHM divergence of the beam ellipse is $(4.1 \pm 1.8)\,\mathrm{mrad}$ by $(6.9 \pm 3.6)\,\mathrm{mrad}$, with the best opening angle as small as $\theta_{\mathrm{maj}} = 2.3\,\mathrm{mrad}$ and $\theta_{\mathrm{min}} = 2.2\,\mathrm{mrad}$. The average vertical and horizontal beam divergences yield an eccentricity of $\epsilon = 1.7$. Note the beam is elongated in the direction perpendicular to laser polarisation. However, in most shots the beam consists of many beamlets and thus the divergence measurement is that of the entire envelope.

The integrated charge on the beam profile screen is plotted in Figure 5.5d. An absolute calibration of the imaging setup was not performed for the electron profile diagnostic in this configuration, so all the data is in units of total signal. Again a large variability is clear, with the bulk of shots having less charge than the average. A few very bright shots dominate, with charge varying by more than an order of magnitude between the highest and lowest charge. Additionally, no clear correlation between beam divergence and beam charge are observed.

5.3.2 Electron beam profile for mixed gas

The electron beam profile and its stability was measured for $n_e = 0.94 \times 10^{19}\,\mathrm{cm}^{-3}$, using a mixture of He and 5% CO_2. A total of 50 shots were taken, keeping all user variable parameters constant. An electron beam was observed on the beam profile monitor for every shot taken. The first 20 shots of this scan are plotted in Figure 5.6a. Again, all images are normalised to their respective maxima. The spatial scale of the image is identical to those in Figure 5.5a.

Both the centroid of the electron beam and its divergence were found by fitting an ellipse to the FWHM contour of the electron beam. For this data, the precise direction of the laser axis was referenced and hence pointing angles are measured with respect to the laser axis. Histograms showing the beam pointing stability and beam size are plotted in Figures 5.6b and 5.6c, respectively.

A summary of the pointing and divergence data is presented in Table 5.2. The electron beam has a large horizontal offset angle for most shots, whereas in the vertical

[1] For more details about the near field effects, cf Sections 4.4.3 and 6.2.2.

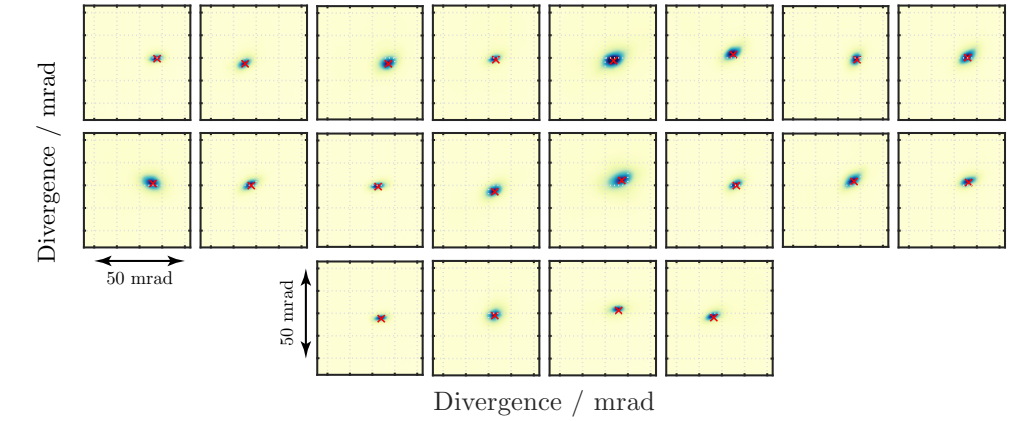

(a) Individual shots

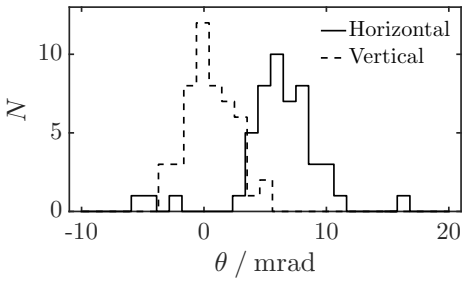

(b) Beam pointing

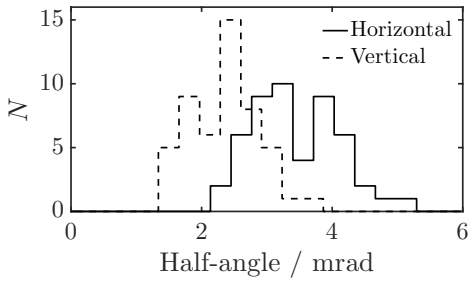

(c) beam divergence

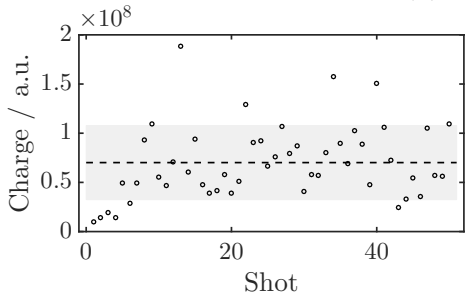

(d) Total charge

Figure 5.6: *Results from beam pointing stability run for ionisation injected electron beams with* $n_e = 0.94 \times 10^{19}\,\mathrm{cm}^{-3}$*. Panel (a) depicts single shots, with the red crosses corresponding to beam pointing direction. Panels (b) and (c) plot statistics of beam pointing and divergence, respectively, while the total integrated charge is shown in Panel (d).*

	Pointing (mrad)	Divergence (mrad)
Horizontal	5.7 ± 3.4	3.3 ± 0.6
Vertical	-0.1 ± 2.0	2.1 ± 0.5

Table 5.2: *Summary of electron beam pointing results for gas with 5%* CO_2 *impurity.*

plane it follows the laser direction. The beam is slightly elongated along the x-axis, which corresponds to the laser polarisation direction. The ellipticity of the beam is inferred from the average measured divergences, yielding a value of $\epsilon = 1.6 \pm 0.3$.

The total charge obtained by integrating the images is plotted in Figure 5.6d. The dashed line is an average of all 50 shots and the gray area shows the standard deviation of the dataset. Small fluctuations about the average are present, however, an electron beam is generated on every shot. A quantitative comparison of total beam charge between self-injection and ionisation injection is not possible due to different camera gain and telecentric lens aperture settings. However, the stability of injection can be estimated by calculating the ratio of standard deviation to the mean value of integrated signal. For self-injection, $\sigma_Q/\langle Q\rangle = 1.2$ whereas for ionisation injection we obtain a value of 0.57. Thus ionisation injection leads to enhanced injection stability.

The differences between ionisation injected and self-injected beams are also seen in beam divergence. The average beam divergence angle is $\theta_{\mathrm{hor}} = (3.3 \pm 0.6)\,\mathrm{mrad}$ and $\theta_{\mathrm{ver}} = (2.1 \pm 0.5)\,\mathrm{mrad}$ for ionisation injection, whereas the average values for self-injected beams are $\theta_{\mathrm{hor}} = (4.1 \pm 1.8)\,\mathrm{mrad}$ and $\theta_{\mathrm{ver}} = (6.9 \pm 3.6)\,\mathrm{mrad}$. This shows the ionisation injected electron beams have superior collimation. Moreover, the stability of the beam, expressed as $\zeta \equiv \sigma_\theta/\langle\theta\rangle$ is much smaller for ionisation injection. For the horizontal axis we obtain $\zeta_{\mathrm{II}} = 0.18$ and $\zeta_{\mathrm{SI}} = 0.44$ whereas in the vertical plane we have $\zeta_{\mathrm{II}} = 0.24$ and $\zeta_{\mathrm{SI}} = 0.52$. These values are similar to the stability of injected charge, showing a twofold improvement for ionisation injection compared to self-injection.

5.3.3 Electron energy spectra for pure helium

Electron spectra were measured for a range of plasma densities at different focal positions in the nozzle. The density scan was performed by filling a reservoir to $\sim 25\,\mathrm{bar}$ and closing the regulator, thus providing a logarithmic pressure scan. Raw data for all shots taken in plasma density range $0.9 \times 10^{19} < n_e < 1.3 \times 10^{19}\,\mathrm{cm}^{-3}$ with different focus positions within the nozzle is shown in Figure 5.7. Here, $z = 0$ corresponds to the focal plane being on the front edge of the nozzle and increasing numbers correspond to focussing further into the nozzle, as defined in Figure 5.3. The laser was focussed at a height 1 mm above the nozzle. The data is binned into $0.1 \times 10^{19}\,\mathrm{cm}^{-3}$ bins.

Clearly at these laser conditions self injection is a highly variable method for electron beam generation[2] Observed beams exhibit large variability in charge. The highest amount of charge measured was 78 pC; however, averaging all the shots where an electron beam was observed (defined as $Q > 5\,\mathrm{pC}$) yields $Q_{av} = (32 \pm 22)\,\mathrm{pC}$. Another notable feature of all the beams is the large degree of filamentation, also observed in

[2] For stability analysis of self-injected electrons at higher laser powers, cf Section 7.5.

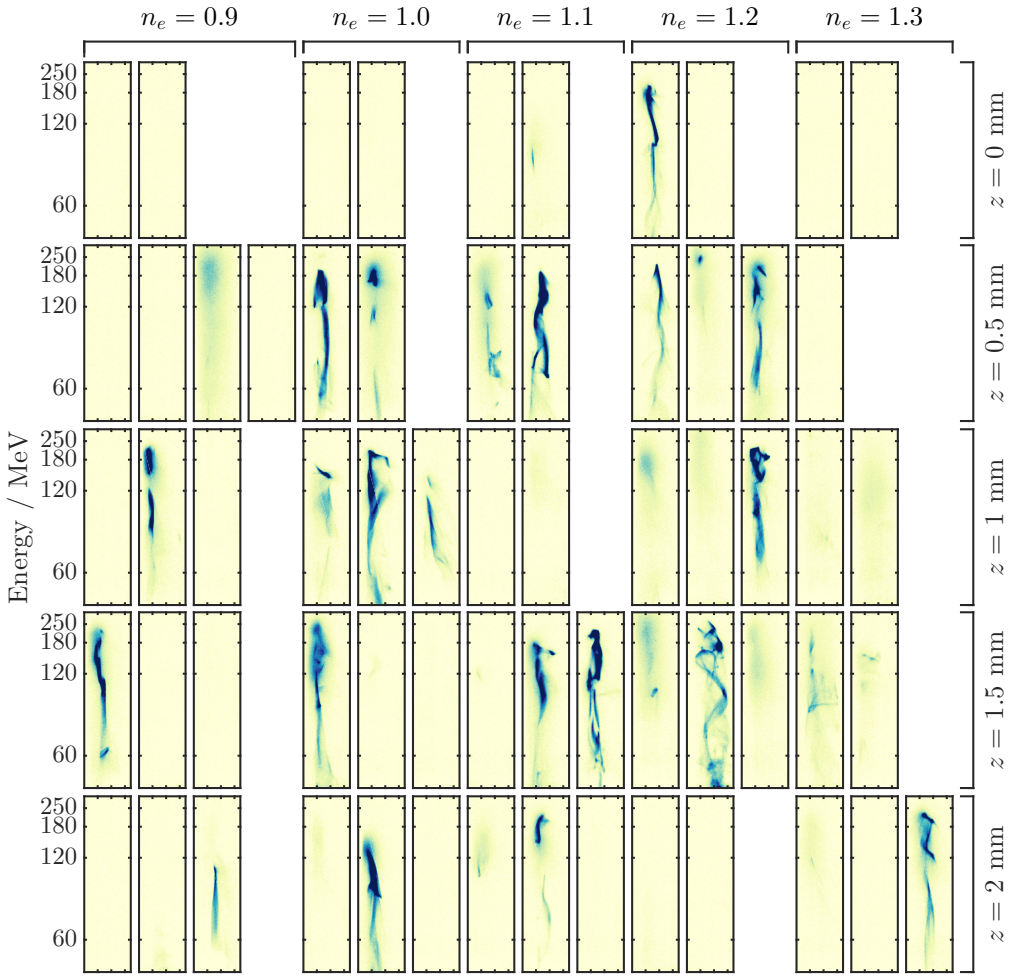

Figure 5.7: *Raw electron spectra obtained with pure helium as a function of plasma density and focal plane position. All images are plotted on the same color scale.*

the beam profiles in Figure 5.5a, and lack of transverse momentum correlation. That is to say there is a large variation in transverse momentum across the beam both in the directions perpendicular and parallel to dispersion.

The extreme positions for focus, right at the edge of the nozzle and 2 mm into it, are least reliable for electron beam generation. However, there is still a large uncertainty as to whether a beam is generated when the laser focus is initially set between these positions. This is a result of the highly non-linear nature of self-injection, relying very heavily on pulse self-focussing and compression to drive the wake amplitude to breaking.

The peak energy was characterised using cut-off energies. This is defined as a point

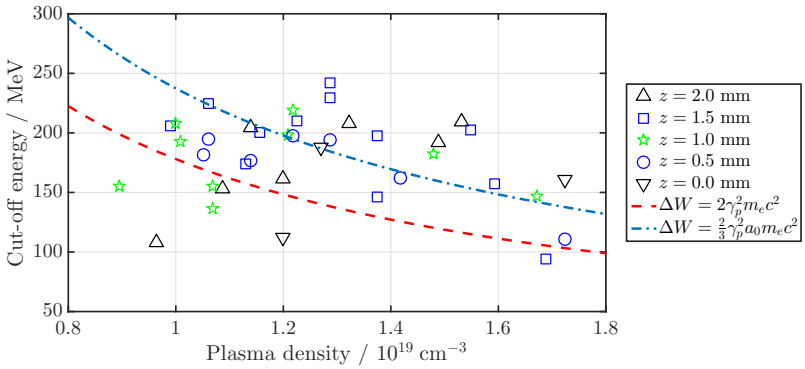

(a) Retrieved cut-off energies

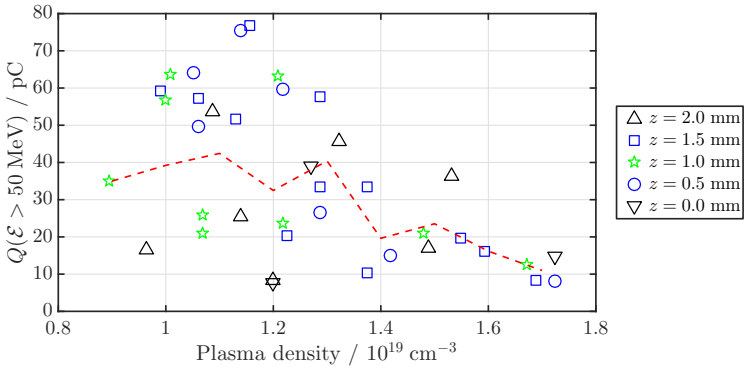

(b) Total charge

Figure 5.8: *Retrieved cut-off energy and charge above 50 MeV as a function of plasma density for self-injected beams at different focal plane positions, plotted in Panels (a) and (b), respectively. The red dashed line Panel (a) is the linear single stage energy gain and the blue dash-dot line is the 3D non-linear energy gain with $a_0 = 4$. The red dashed line Panel (b) is average charge calculated for plasma density bins of 0.1×10^{19} cm^{-3} width.*

in the spectrum where the signal rises to a threshold value above noise level. The threshold was set at 5 times the standard deviation of the background; all maximum energies were found from traces integrated along the divergence axis. Relying on peaks in electron spectra as a characterisation tool is unreliable as some beams lack a distinct peak in the spectrum. In order to account for beam divergence effects in deducing the cut-off energy, a rudimentary instrument function was used. This involved setting the cut-off point to correspond to the trajectory of an electron with pointing $-\theta/2$ to the beam axis. Such a trajectory effectively defines the divergence cone of the beam.

In order to accurately measure the peak electron energy the pointing offset of the beam is required. While ideally this would be measured for each individual shot, an average offset can also be used. However, no such measurement was performed for this dataset and thus on-axis pointing is assumed.

Retrieved cut-off energies for self-injected electron beams are plotted in Figure 5.8a. The cut-off energies are of similar absolute values to the linear energy gain. The general trend of energy scaling with plasma density, however, does not follow the linear energy scaling. This can be explained by the highly non-linear nature of the interaction. The laser will compress in time and also self-focus and the amount of energy captured will depend on the focal plane intensity distribution of the particular shot. As the electrons will be accelerated in the 3D non-linear regime, the total energy gain depends linearly on the self-focussed a_0. As the latter will depend on both self-focussing and pulse compression, it is very difficult to predict the maximum energy gain. It is known, however, that self-injection requires $a_0 \simeq 4$. Assuming that $a_0 \simeq 4$ will be maintained for the acceleration distance, the scaling shown as the blue dash-dot line in Figure 5.8a is obtained. Due to the large scatter, the agreement with peak energies is difficult to ascertain. However, the scalings do not seem to contradict the data.

The dependence of cut-off energy on the focal plane position also exhibits some interesting trends. It is evident that the extreme values of 0 and 2 mm yield poor beams. The highest energy electron beams are generated when focussed 1.5 mm into the gas jet.

The dependence of accelerated charge above 50 MeV on plasma density is plotted in Figure 5.8b, again for different focal planes. No beams were observed for $n_e < 9 \times 10^{18}\,\mathrm{cm}^{-3}$. The extreme focus positions yield lower charges than other focus positions, with the highest charge being measured with almost equal probability in the intermediate planes.

5.3.4 Electron energy spectra for mixed gas

Similarly to the pure helium case, electron beam energy spectra was measured as a function of plasma density and focus position within the nozzle. Again a reservoir was filled to ~ 25 bar pressure and shots taken until electron beams were not observed any more. Raw electron spectrometer spectra for all shots within the density range $0.8 \times 10^{19} \leq n_e \leq 1.2 \times 10^{19}\,\mathrm{cm}^{-3}$ are plotted in Figure 5.9. All images have the same colour scale.

Similarly to the pure helium case, focussing at $z = 0$ mm results in highly variable injection and very poor stability. Interestingly, higher plasma densities yield higher electron energies at this focus position. Focussing further into the nozzle improves the stability of beam generation greatly. Again resembling the pure helium case, focussing 2 mm into the nozzle reduces the total charge of the beams, whilst resulting in rather stable injection.

Cut-off energies were used to characterise the electron acceleration in a similar

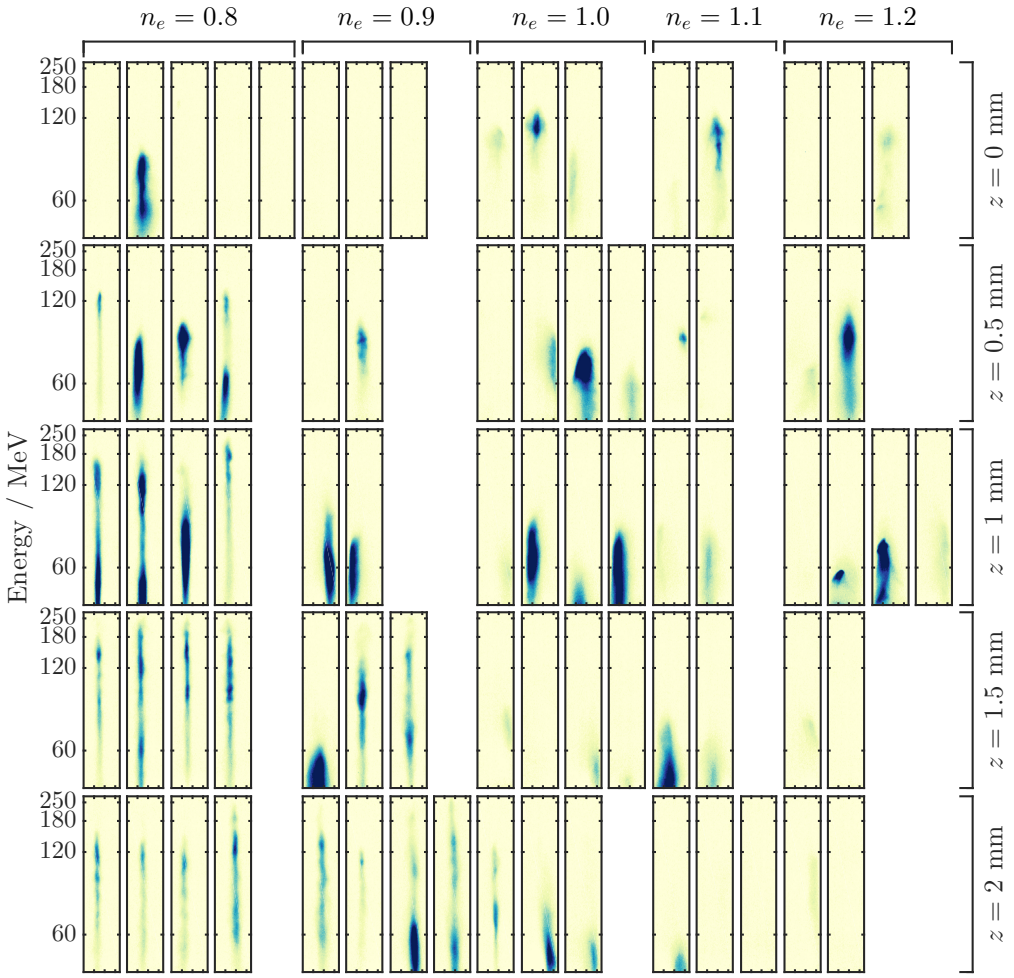

Figure 5.9: *Raw electron spectra obtained using helium with 5% CO_2 impurity as a function of plasma density and focal plane position. All images are plotted on the same colour scale.*

manner to the self-injection case. However, the average absolute pointing direction was measured for electron beams generated with ionisation impurity[3] and this offset was used for the electron tracking. The cut-off energies obtained using He with 5% CO_2 impurity are plotted in Figure 5.10a as a function of plasma density and focus position in the nozzle. The solid red line is the average energy and the shaded area represents the standard deviation, calculated for plasma density bins of $0.05 \times 10^{19}\,\mathrm{cm}^{-3}$ width. Higher peak energies are obtained at lower plasma densities, as intuitively expected from the ${n_e}^{-1/2}$ scaling, plotted as the dashed magenta line in Figure 5.10a. However,

[3] Cf. Table 5.2

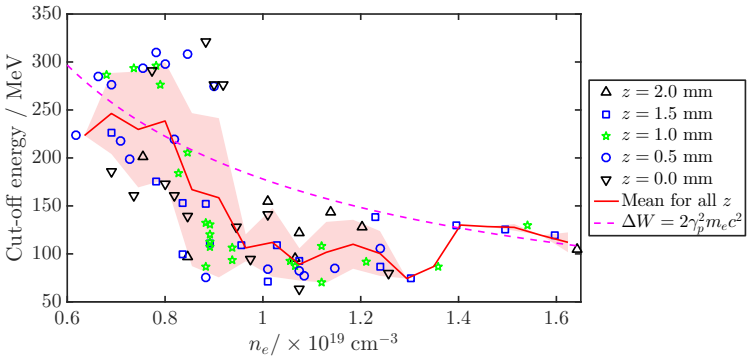

(a) *Retrieved cut-off energies*

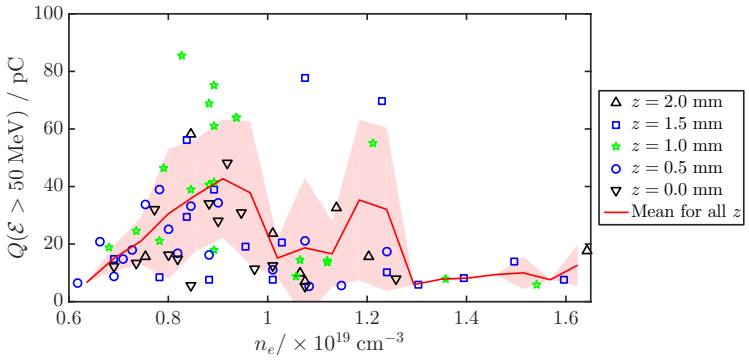

(b) *Total charge*

Figure 5.10: *Retrieved cut-off energy and charge above 50 MeV as a function of plasma density for ionisation-injected beams at different focal plane positions, plotted in Panels (a) and (b), respectively. The solid red line both plots is the average and the shaded area corresponds to the standard deviation, calculated for density bins of* $0.05 \times 10^{19}\,\mathrm{cm}^{-3}$ *width. The dashed magenta line in Panel (a) depicts the linear energy scaling.*

while there seems to be little variation to the cut-off energy above $n_e = 1 \times 10^{19}\,\mathrm{cm}^{-3}$, below this density a steep increase in beam energy is observed. Another turnaround is seen at $n_e \sim 0.7 \times 10^{19}\,\mathrm{cm}^{-3}$ with beam energies starting to decrease with decreasing plasma density.

The dependence of peak energy on the focal plane position exhibits some interesting features. For high plasma densities $n_e > 1.3 \times 10^{19}\,\mathrm{cm}^{-3}$ focussing deep into the nozzle is required to produce an electron beam. This contrasts with behaviour for $n_e < 0.9 \times 10^{19}\,\mathrm{cm}^{-3}$, where the highest energies at a given plasma density are obtained by focussing up to 1 mm into the nozzle.

The total charge of electrons above 50 MeV is plotted in Figure 5.10b, as a function of plasma density and focal plane position. Across all observed beams the average charge is $Q = (19 \pm 12)\,\mathrm{pC}$. Gradual increase in charge with plasma density is observed

with a peak at $n_e = 0.9 \times 10^{19}\,\mathrm{cm}^{-3}$. The highest charges were obtained when focussing 1 mm into the nozzle whereas focussing at the extremes of 0 mm and 2 mm generally yielded lower charge beams.

5.3.5 Suppression of self-injection: comparing electron beams

Electron beam with different behaviour were obtained by changing the gas from pure helium to one with 5% impurity. Firstly, electron beams were observed for plasma densities $n_e > 0.6 \times 10^{19}\,\mathrm{cm}^{-3}$ with ionisation induced injection, whereas for self-injection the threshold was $n_e > 0.9 \times 10^{19}\,\mathrm{cm}^{-3}$. Additionally, in the density region where self-injection was observed, the electron beam cut-off energies were found to be much lower with ionisation injection. This implies that an injection mechanism other than self-injection, even in the density span where self-injection was previously observed.

The ionisation injected electron beams are observed to have superior beam quality compared to the self-injected beams. This is firstly evident from Figures 5.7 and 5.9, depicting the raw electron spectrometer images for self-injection and ionisation injection, respectively. The ionisation induced electron beams have better collimation across the beam and little transverse filamentation is observed. To emphasise this fact, the transverse position of maximum charge was calculated for slices across the energy spectrum. This method is illustrated in Figure 5.11, depicting a typical self-injected and ionisation injected beam. The location of the maximum of the slice lineout is found for every energy along the dispersion direction. For each shot a variance of the peak positions is then calculated; this value is a measure of beam quality as it reflects the amount of variation in transverse direction. The mean of this value is calculated for all

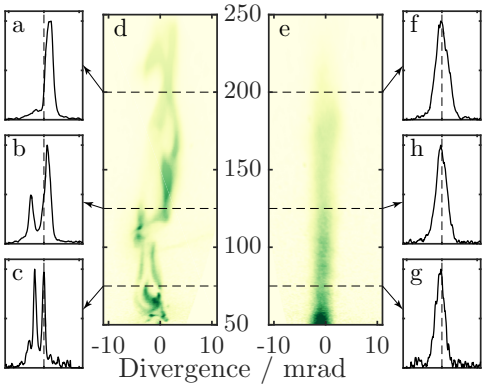

Figure 5.11: *Slice lineouts, in Panels (a), (b) and (c), for self-injected beam depicted in Panel (d); Panels (f), (g) and (h) similarly depict lineouts at same energies for ionisation injection beam plotted in Panel (e).*

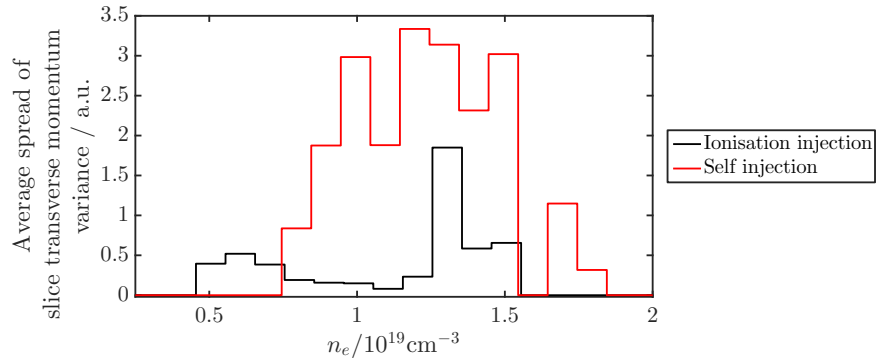

Figure 5.12: *Mean variance of transverse slice peak charge location as a function of plasma density for self and ionisation injected beams.*

shots, with $0.1 \times 10^{19}\,\mathrm{cm}^{-3}$ wide bins, for both self-injection and ionisation injection. This data is plotted in Figure 5.12. Superior beam quality is observed for ionisation injected electron beams in all density regions.

The measured beam divergences, presented in Sections 5.3.1 and 5.3.1 for self and ionisation-injected beams, respectively, corroborates the above analysis. Ionisation injected beams were found to have a lower average beam divergence. The mean beam divergence angle is $\theta_{\mathrm{hor}} = (3.3 \pm 0.6)\,\mathrm{mrad}$ and $\theta_{\mathrm{ver}} = (2.1 \pm 0.5)\,\mathrm{mrad}$ for ionisation injection, whereas the average values for self-injected beams are $\theta_{\mathrm{hor}} = (4.1 \pm 1.8)\,\mathrm{mrad}$ and $\theta_{\mathrm{ver}} = (6.9 \pm 3.6)\,\mathrm{mrad}$. This yields an improvement of $\theta_{\mathrm{h,SI}}/\theta_{\mathrm{h,II}} = 1.2$ and $\theta_{\mathrm{v,SI}}/\theta_{\mathrm{v,II}} = 3.3$.

All the above evidence suggests that the use of ionisation injection suppresses self-injection. The fact that the total charge measured is very similar, of order of tens of picocoulombs, means that the very different electron beam properties cannot be explained by ionisation injected beams overwhelming all detectors. Instead, similar charge is measured, meaning the behaviour of the wakefield is quite different in the two cases.

5.4 Simulation results

Theoretical modelling of experiments described in the previous sections is extremely complicated due to scale of nonlinearities involved. Instead, particle-in-cell simulations were performed to understand the physics of the self injection suppression process.

5.4.1 Simulation parameters

The simulations were carried out using the 3D version of the EPOCH code.[4] Whilst 2D simulations are often used, there are profound differences which require the use of 3D code. In 3D the quantity $a_0^2 w^2$ is conserved, whereas in 2D only $a_0^2 w$ is conserved. This leads to very different self-focussing behaviour. Additionally, the transverse electric field arising from a beam load varies differently with distance from the load in 2D slab and 3D geometry.

Simulations were performed with a resolution of $k_L \Delta x = 0.21$, or 30 points per laser wavelength in the longitudinal direction and $k_p \Delta y = k_p \Delta z = 0.17$, or 37 points per plasma wavelength in the transverse directions. The simulated density profile was a 2 mm long plateau of $n_e = 1.1 \times 10^{19}\,\mathrm{cm}^{-3}$ with 500 micron linear ramps. For self-injection simulations 2 particles per cell were used.

Ionisation injection simulations were performed assuming all He electrons, the outer 4 electrons from carbon and the outer 6 electrons from oxygen should already be ionised. Thus C^{4+} and O^{6+} ions were used. The gas mixture ratio was found to be by mass, i.e. 95% of the total mass was He atoms and 5% was CO_2 atoms. The number density of an ideal gas is given by

$$n = \frac{N_A}{V}\frac{m}{M}, \tag{5.1}$$

where N_A is Avogadro's number and M is the molar mass of the gas. Thus we can find the ration of number densities of He and CO_2 occupying the same volume, given the mass fractions f_{He} and $f_{\mathrm{CO_2}} = 1 - f_{\mathrm{He}}$:

$$R_n \equiv \frac{n_{\mathrm{He}}}{n_{\mathrm{CO_2}}} = \frac{m_{\mathrm{He}} M_{\mathrm{CO_2}}}{m_{\mathrm{CO_2}} M_{\mathrm{He}}} = \frac{f_{\mathrm{He}} M_{\mathrm{CO_2}}}{(1 - f_{\mathrm{He}}) M_{\mathrm{He}}}. \tag{5.2}$$

Given that each He atom will contribute 2 electrons and each CO_2 molecule will give 16 electrons to the background electron density, we find the total electron density as

$$n_e = 2 \cdot n_{\mathrm{He}} + 16 \cdot n_{\mathrm{CO_2}} = 2R_n \cdot n_{\mathrm{CO_2}} + 16 \cdot n_{\mathrm{CO_2}}, \tag{5.3}$$

which yields an equation to calculate the fraction of impurity molecules:

$$n_{\mathrm{CO_2}} = \frac{n_e}{2R_n + 16}. \tag{5.4}$$

The total number of carbon atoms is then $n_{\mathrm{CO_2}}/3$ and the number of oxygen atoms is $2n_{\mathrm{CO_2}}/3$.

The laser transverse intensity profile was modelled as a 2D gaussian spot in the sim-

[4] Cf. Section 3.5.1

Simulation	a_0	f_{CO_2}
A	0.9	0
B	1.0	0
C	1.0	0.05
D	1.0	0.35

Table 5.3: *Intensities and impurity fractions for simulation scan.*

ulations. This is an approximation and numerous studies have highlighted the necessity to use the full spatial profile along with the spatial phase.[232–234] While measuring the spatial intensity profile is trivial (cf Figure 5.4a), reliably measuring the spatial phase front is more complicated. Thus this data was not measured, rendering the exact simulation of the interaction impossible. We instead focus on simulating a spot of similar spatial extent and temporal duration to capture the physics of the suppression dynamics.

The laser spot used in the simulations was a 2D gaussian with a spot size of $w_0 = 19\,\mu\text{m}$, where w_0 is the $1/e$ extent of the electric field. The temporal profile was modelled as a gaussian with $\tau = 37\,\text{fs}$, where τ is the FWHM width of the intensity profile. A moving box is used, with the motion along the x-axis. The window moves at the group velocity of the laser, $v_g \simeq \eta c$, with η given by Equation 2.43.

A range of different simulations were performed to understand the physics of suppression of self-injection. All the simulations performed used the same spot size and background plasma density. Table 5.3 summarises the critical parameters of the four simulations performed. Simulations A and B both probe self-injection, with the lower intensity in A allowing understanding of the threshold for injection. Simulations C and D look into the suppression of self-injection, with C using an impurity fraction very close to that of the experiment. Run D is using an impurity fraction that is much larger in order to understand the dynamics of injection for heavy beam loads.

5.4.2 Simulation results

To understand the suppression physics, the location of injection in the interaction is first found. To this end, Figure 5.13 depicts the total number of injected electrons for different simulations in the scan. Electrons are defined as injected if their longitudinal momentum is $p_x > 15\,\text{MeV}$. As intuitively expected, self-injection occurs earlier in the higher intensity simulation B, depicted as the black line in Figure 5.13. Self-injection

[232] Z.-H. He *et al*, *Nat Comms* **6**, 2015.
[233] J. Ferri *et al*, *Sci Rep* **6**, 2016.
[234] B. Beaurepaire *et al*, *Phys Rev X* **5**, 2015.

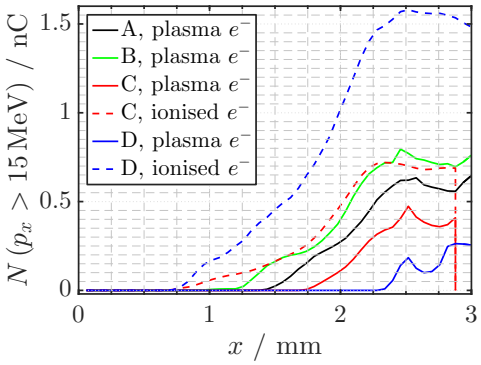

Figure 5.13: *Total injected charge as a function of distance for the simulation scan. For simulations C and D both the number of electrons from the background plasma and impurity species are plotted.*

is observed to happen at $x \simeq 1.5\,\mathrm{mm}$ and $x \simeq 1.25\,\mathrm{mm}$ for simulations A and B, respectively. The physics of self-injection and the threshold will be discussed later on.

For the simulations with impurity species, charge from both self-injection and ionisation injected electrons are plotted as the solid and dashed lines, respectively. Electrons ionised from the inner shells of C and O are injected early on in the interactions, as soon as a coherent bubble structure is formed and the trapping condition is fulfilled.[5] The very heavy beam load simulation D results in total injected charge that is ~ 2.5 larger than the total in simulation C. The ionisation injected charge in simulation C, though, is very similar to self-injected charge for the same intensity. This agrees with experimental data exhibiting similar magnitudes of injected charge for self and ionisation injection. For simulation C, with the same a_0 as B, self-injection is clearly suppressed at $x \simeq 1.25\,\mathrm{mm}$. Some background plasma electrons are, however, injected later on in the interaction, $x \simeq 1.75\,\mathrm{mm}$. Interestingly, the rate of increase of impurity electrons also rises at the same point, indicating a change in bubble potential. For the heavily beamloaded simulation D, no plasma electrons are injected until very late in the interaction, whereas the rate of injection of dopant electrons is approximately constant. We note that while the ratio of charge between ionisation injection and self-injection is similar in simulations and in the experimental data presented earlier, the absolute values differ greatly. The simulations overestimate the amount of injected charge, similarly to previous studies.[99,235]

To understand the injection process and its suppression further, snapshots of the plasma density are plotted in Figure 5.14. The columns in Figure 5.14 show the shape

[5] Cf Section 2.5.6 and Equation 2.84.
[99] F. S. Tsung *et al*, *Phys Rev Lett* **93**, 2004.
[235] F. S. Tsung *et al*, *Phys Plasmas* **13**, 2006.

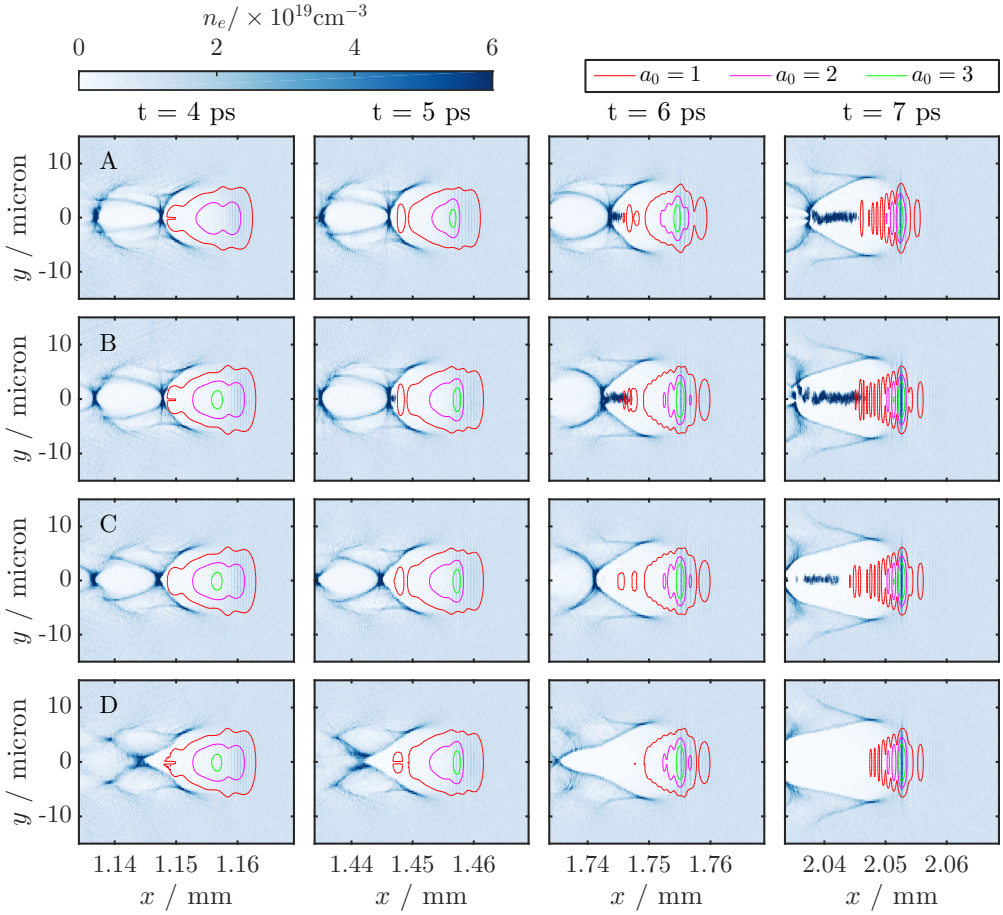

Figure 5.14: *Plasma density snapshots at different propagation times for different simulations. The columns show density plots from different times with simulations A, B, C and D (as defined in Table 5.3) in rows. The solid lines depict isocontours of the normalised vector potential of the laser.*

of the accelerator cavity at different times whereas the rows depict the self-injection simulations along with low and high beam loading runs. The effect of beamloading is evident as early as $t = 4\,\mathrm{ps}$, where for simulations C and D the rear of the bubble is elongated. Whilst this elongation is subtle for the low beamload used in simulation C, the large amount of injected charge in simulation D causes a very large lengthening of the bubble.

At $t = 5\,\mathrm{ps}$ the self-injected bunch in simulation B is visible. Simulation A has undergone injection by $t = 6\,\mathrm{ps}$. Due to the later injection and lower initial a_0, the bubble expansion is slower for simulation A. By this time the cavity has undergone large elongation for simulations C and D as well. The expansion of the bubble, due to the

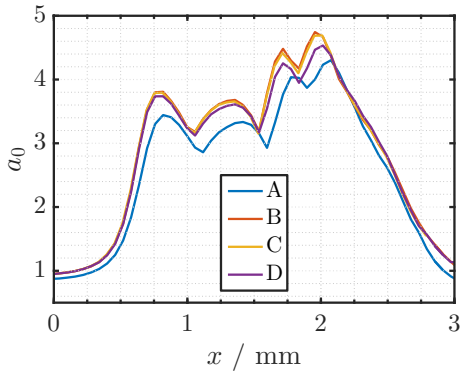

Figure 5.15: *Evolution of peak normalised vector potential in simulations A, B, C and D. A constant wavelength of* $\lambda_L = 800\,\text{nm}$ *is assumed.*

combined effects of laser amplification and beam load result in injection of background electrons in simulation C by $t = 7\,\text{ps}$, much later than in the corresponding pure helium simulation in B.

The solid lines are isocontours of the laser normalised vector potential, at the $a_0 = [1, 2, 3]$ levels. Here the value of a_0 has been calculated by not accounting for redshifting, using $\lambda_L = 800\,\text{nm}$. Albeit starting off with a lower intensity, by $t = 5\,\text{ps}$ the profile of the laser intensity in simulation A looks similar to the other three. Evidently the laser evolution is very similar in simulations B, C and D; this is to be expected as the beam load is behind the laser and no information from the misshaped bubble can affect it. Additionally, the ionisation impurity fractions are very small and thus very little ionisation induced defocussing or energy loss to ionisation will occur. This is illustrated in Figure 5.15, showing peak normalised vacuum potential throughout the interaction simulations A, B, C and D.

The effect of lengthening of the cavity can be further analysed to understand the injection dynamics. The axial electron density plotted as a function of propagation distance x is shown in Figure 5.16. As the window moves at $v_{\text{box}} < c$, the injected electrons appear to move forward. Lengthening of the bubble due to self-injected charge is clear for simulations A and B. A similar longitudinal expansion is evident for simulation C as well. In the case of simulation D, however, the bubble is heavily loaded from very early on and a sharp sheath near the back of the cavity is never formed.

The speed of the back of the bubble plays an important role in injection, as this velocity determines the minimal longitudinal momentum required for trapping. Figure 5.17 shows the gamma-factor of the rear of the bubble, as defined by the red line in Figure 5.16, for simulations A, B and C. Also shown are the linear bubble phase

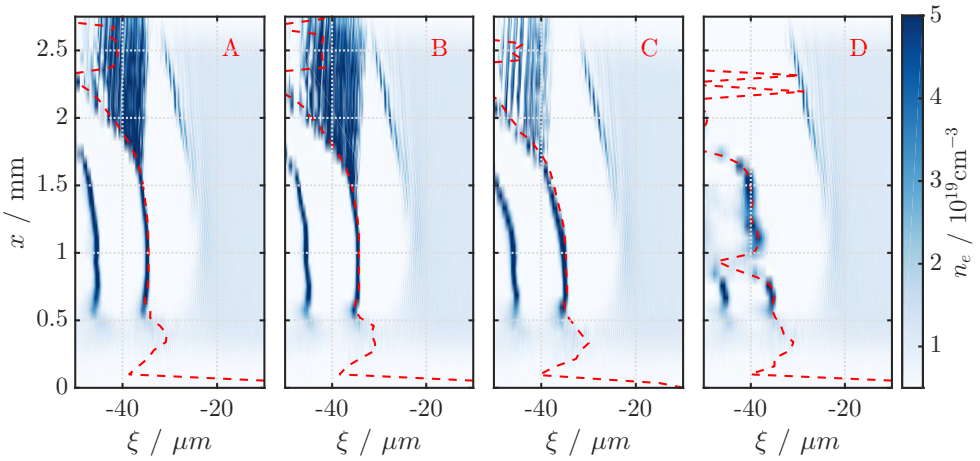

Figure 5.16: *Axial plasma density as a function of propagation distance for all simulations. The red line tracks the rear of the bubble.*

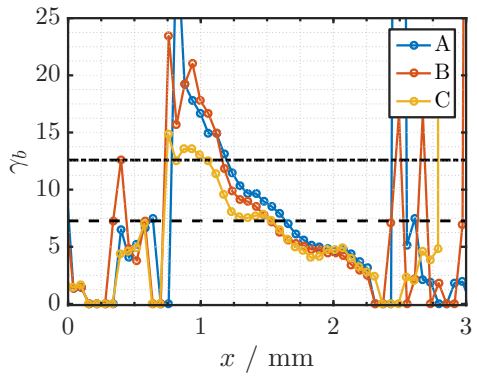

Figure 5.17: *Gamma-factor of the rear of the bubble for simulations A, B and C. The black dash-dot line corresponds to the linear phase velocity whereas the black dashed line is the phase velocity of the bubble accounting for laser depletion.*

velocity, $\gamma_p = \omega_L/\omega_p$ as the dash-dot line and the non-linear phase velocity for the bubble, $\gamma_p = \omega_L/(\sqrt{3}\omega_p)$, as the dashed line. The bubble speeds are rather different at times of injection in the different simulations: in A, $\gamma_{\text{inj}} \simeq 8.5$; in B, $\gamma_{\text{inj}} \simeq 9.5$ and in C, $\gamma_{\text{inj}} \simeq 4.7$. From here it is thus clear that the speed of the back of the bubble cannot explain self-injection on its own.

It is also known that while the back of the cavity plays an important role in injection, the expanding bubble model entails the change of size of the entire ion sphere. Indeed it is the transverse expansion that plays a crucial role in capturing electrons in this theory, allowing the hamiltonian of electrons with large impact factors to reduce. This

expansion can result from plasma density transitions[236] or intensity amplification.[74] However, the laser evolution in the simulations presented here is nearly identical, as shown in Figure 5.15. Hence the suppression of self-injection cannot be the result of a change of bubble expansion rate driven by laser amplification.

The pseudopotential Ψ (cf Section 2.3.3) at the rear of the bubble can be calculated from the electric and magnetic field diagnostics. Remembering that $E_x = -\partial\Psi/\partial\xi$ and $E_y - cB_\theta = -\partial\Psi/\partial y$, the electric field and magnetic fields can be integrated to yield the pseudopotential Ψ. The value of Ψ at the rear of the bubble, as defined by the positions in Figure 5.16, is plotted in Figure 5.18a.

As can be seen from Figure 5.18a, the pseudopotential at the rear of the bubble starts to decrease as the bubble is formed and charge pileup at the sheath crossing point develops. This decrease in pseudopotential is very similar in simulations A, B and C, with Ψ starting to increase very quickly in simulation D due to the very high beam load. The lowest pseudopotential is reached at $x \simeq 0.95\,\mathrm{mm}$, after which Ψ starts to slowly increase in simulations A and B. For simulation C, though, the behaviour of Ψ diverges at $x \simeq 0.8\,\mathrm{mm}$. This is due to ionisation injected charge in the cavity, reducing the pseudopotential at the back of the bubble.

As the behaviour of the pseudopotential is seen to differ in simulation C due to ionisation injected electrons, we can calculate the threshold value of Ψ required to self-inject to study the suppression effect. With initial electron energy $H = 1$, we find

$$\Psi_c = -1 + \frac{\sqrt{1 + p_\perp^2}}{\gamma_b}, \tag{5.5}$$

where Ψ_c is the pseudopotential threshold for self-injection.[122,124] The value for Ψ_c can be estimated by making use of the measured values of γ_b from Figure 5.17; for $p_\perp$ we can use[119] $p_\perp = \pi a_0/4$ by employing the measured values of a_0 depicted in Figure 5.15. The evolution of both Ψ and Ψ_c between $x = 1\,\mathrm{mm}$ and $x = 2\,\mathrm{mm}$ is plotted in Figure 5.18b as the solid and dashed lines, respectively. Self-injection is predicted to occur once $\Psi < \Psi_c$. We see that for simulation B, the injection condition is met at $x \simeq 1.3\,\mathrm{mm}$ and for simulation A $\Psi < \Psi_c$ is met at $x \simeq 1.4\,\mathrm{mm}$. These agree well with the injection positions observed from Figure 5.13. However, while the injection condition is reached at $x \simeq 1.35\,\mathrm{mm}$ for simulation C, no self-injection occurs. Self-injection is suppressed, until further laser evolution leads to some background electron

[236] S. A. Yi *et al*, *Phys Plasmas* **20**, 2013.
[74] A. Sävert *et al*, *Phys Rev Lett* **115**, 2015.
[122] M. R. Islam *et al*, *New J Phys* **17**, 2015.
[124] A. Pak *et al*, *Phys Rev Lett* **104**, 2010.
[119] A. G. R. Thomas, *Phys Plasmas* **17**, 2010.

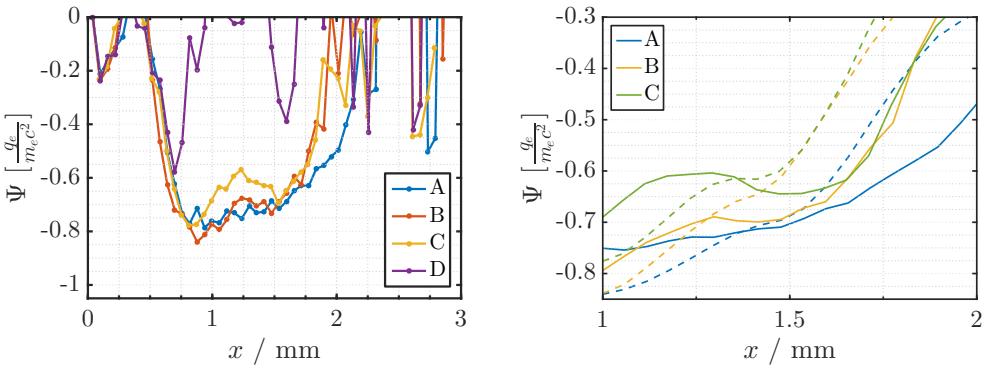

(a) Ψ ***(b)*** Ψ *along with* Ψ_c

Figure 5.18: *The pseudopotential at the rear of the bubble (a) along with a zoom (b) between 1 and 2 mm, also showing the critical potential required for self-injection.*

being injected at $x \simeq 1.75\,\mathrm{mm}$.

The fact that self-injection is not observed at the predicted location in the interaction when a beam load is present signifies the suppression of self-injection. As the model in Equation 5.5 is reasonably accurate in predicting self-injection for the other simulations, one is to conclude one of the assumptions made in calculating the value for Ψ_c is not valid any more. The physically relevant parameter is the transverse momentum, previously taken as $p_\perp = \pi a_0/4$. This expression was indeed derived without accounting for beamloading. As the load provides a repulsive force to sheath electrons, these return to axis with less transverse momentum. With $\Psi_c \propto p_\perp$, this reduces the critical pseudopotential for self-injection, meaning the wake pseudopotential needs to be deeper for self-injection to occur.

5.5 Conclusion

Experimental data obtained with pure helium and helium with a 5% CO_2 impurity was presented, showing that self-injection from the background plasma can be suppressed due to beamloading from ionisation injected electrons. Electrons that are ionisation injected into the accelerator cavity early on in the interaction reduce the absolute value of the pseudopotential at the rear of the bubble. Additionally, the beam load provides a repulsive force to sheath electrons returning to axis, thus reducing their transverse momentum. This leads to no self-injection of background injection for identical laser conditions.

Whilst demonstrated here with the use of ionisation injection, the suppression effect arises from the beam load and is thus independent of the injection technique used. This

opens up the possibility of staging laser wakefield accelerators employing the highly non-linear bubble regime. Previous staging concepts have all made use of the quasi-linear regime, where full cavitation of the bubble does not occur.[75,237] One of the reasons for this design is self-injection, which produces beams of low and unpredictable quality. The fully non-linear regime has desirable properties, however, amongst which are fully linear focussing fields within the bubble and transverse invariance of accelerating field. This allows for acceleration of flat electron beams, where the spot size is much larger in one plane. Furthermore, high single-stage energy gains are possible with higher laser intensities, reducing the amount of stages required to achieve a final energy. Finally, as described in Section 2.5.7, the 3D non-linear regime allows for much higher laser to electron efficiencies.

[75] W. P. Leemans *et al*, *Phys Today* **62**, 2009.
[237] K. Nakajima *et al*, *Phys Rev Spec Top-Ac* **14**, 2011.

CHAPTER 6
On the differences between ionisation injection and self-injection

ONE OF THE MOST IMPORTANT factors affecting the accelerated beam is the method of injection used. In this chapter a direct comparison between the two most frequently used injection methods in laser wakefield acceleration is undertaken. Experimental data comparing electron beams generated by employing ionisation injection and self-injection is presented, showing a smaller initial transverse momentum for ionisation injection. Injection dynamics affecting the maximum energy gain for ionisation injected beams are discussed. Spectral signatures of different injection methods are presented.

6.1 Motivation

Ionisation induced injection has been seeing widespread use as an injection method with very simple experimental implementation. Apart from changing the gas medium to include an ionisation impurity, the only constraint is a minimum intensity, given by $a_0 \geq 1.7$.[1] As such, ionisation injection has seen widespread employment in different experiments. However, there exists a lack of thorough comparisons between electron beams obtained with self-injection and ionisation injection. McGuffey *et al*[205] discuss the increased charge and present individual spectra, noting that the maximum electron beam energy is similar for self and ionisation injection but the total amount of charge is much larger. Pak *et al*[124] show an increase in peak energy for ionisation induced beams with increase in laser intensity, but do not provide comparisons between self-injected and ionisation injected beams. Clayton *et al*[55] report acceleration up to 1.45 GeV, but

[1] Cf. Section 2.5.6
[205] C. McGuffey *et al*, *Phys Rev Lett* **104**, 2010.
[124] A. Pak *et al*, *Phys Rev Lett* **104**, 2010.
[55] C. E. Clayton *et al*, *Phys Rev Lett* **105**, 2010.

with only tens of picocoulombs of charge in the beam; the high energy electron beam is obtained below the observed self-injection threshold of $n_{\text{th}} \simeq 3 \times 10^{18}\,\text{cm}^{-3}$. Other work[238–240] has evidenced at least a twofold increase in injected charge for ionisation injection, all employing plasma densities in excess of $7 \times 10^{18}\,\text{cm}^{-3}$. Xia *et al* also provide empirical energy and charge scalings with laser intensity.[240] The theoretical model by Chen *et al*[123] does not give a scaling for peak energy or injected charge either. Thus a quantitative comparison between the two injection methods has not been undertaken before. Indeed, if ionisation injection is to become a viable injection method allowing controlled multi-GeV scale electron acceleration, its parameters and scalings need to be better understood.

As shown in Chapter 4, spectral characterisation of the driver pulse after the interaction can provide information about the wakefield. In the low impurity case it can be shown that the pulse loses negligible energy to ionisation of the dopant gas,[2] implying that the redshifting of the pulse should be similar between self-injection and ionisation injection. However, a large amount of charge can be trapped in the wakefield early in the interaction, thus modifying the wake structure. This in turn can severely alter the refractive index gradients seen by the laser and thus yield very different blueshifting. Thus spectral characterisation of the laser driving an accelerator employing ionisation injections can reveal further information about injection location and the fields within the wake.

6.2 Signatures of injection method on laser spectra

While it has been shown that employing an impurity species can drastically change the generated electron beam properties, less work has been done to characterise the effect on the laser pulse. An added gas with higher ionisation potentials will require more energy from the laser to ionise, further, local ionisation can potentially lead to more significant ionisation blueshift due to fast changing plasma density.[203]

6.2.1 Experimental results

A comparison between spectra obtained with both pure helium and helium with 5% CO_2 impurity was performed employing the ASTRA laser. The elliptical spot was

[238] M. Z. Mo *et al*, *Appl Phys Lett* **102**, 2013.
[239] F. G. Desforges *et al*, *Phys Plasmas* **21**, 2014.
[240] C. Xia *et al*, *Phys Plasmas* **18**, 2011.
[123] M. Chen *et al*, *Phys Plasmas* **19**, 2012.
[2] Cf Section 5.4
[203] S. Wilks *et al*, *Phys Rev Lett* **61**, 1988.

measured to have waist ($1/e^2$ intensity) sizes of $(24.0 \pm 4.8)\,\mu m$ and $(17.3 \pm 1.3)\,\mu m$.[3] The $1/e^2$ contour was measured to contain $(66.9 \pm 9.7)\,\%$ of the total energy on target, measured to be $(419 \pm 38)\,mJ$. With a pulse duration of $(37 \pm 3)\,fs$, the peak intensity is calculated to be $(1.1 \pm 0.3) \times 10^{18}\,W\,cm^{-2}$. A 3 mm gas jet was used, with backing pressures $< 25\,bar$ yielding electron number densities up to $\sim 2.3 \times 10^{19}\,cm^{-3}$.

Figure 6.1 depicts transmitted laser spectra measured at varying plasma densities and focal plane positions. The focal plane location relative to the gas jet is described in Figure 5.3. For all data presented here the spectral sensitivity has not been accounted for as such measurements were unavailable. Panels (a)-(e) in Figure 6.1 depict plasma density scans with pure helium whereas collections of spectra from ionisation induced injection are plotted in Panels (f)-(j). Each column in the panels depicts the transmitted spectrum of a single full power shot and has been normalised to its maxima.

The difference between the spectra measured with different gases is striking. For self injection, an increasing blueshift with plasma density is seen for focal planes $z = 0\,mm$ and $z = 0.5\,mm$. Prominent redshift is also observed. For focal planes further in the gas jet, a very clear, broad spectral peak at much higher frequencies is observed. Additionally, the centroid of this feature is blueshifted less with focussing further into the gas jet. Very strong laser depletion is also observed, with the pump laser spectrum entirely diminished in transmission for a number of shots at $z = 1.5\,mm$. Finally, a density dependence of the wavelength of the blue peak is observed, with higher number densities causing more blueshift.

For ionisation injection, a markedly different behaviour is seen to emerge. For all focus positions and nearly all plasma densities, a very prominent blueshifted feature is observed near 560 nm. Some number density dependence of the blueshift centroid wavelength is observed at $z = 0\,mm$, with similarities of the central wavelength of the feature to self-injection scan at $z = 1.5\,mm$. For other focal planes the most notable feature is the low density behaviour for all number densities. A rapid increase in frequency of blueshifted peak with rising plasma density is witnessed. This rapid change is seen to occur at $n_e \simeq 6 \times 10^{18}\,cm^{-3}$.

The blueshifting can be analysed by calculating the intensity weighted mean frequency of each single-shot spectrum for the density scan at each focal plane. To exclude laser wavelengths, only radiation with wavelengths shorter than 760 nm is included. Figure 6.2 depicts the results from this analysis, plotting the mean wavelength of blueshifted light as a function of plasma density. The results from self-injection are shown in Figure 6.2a with ionisation injection data in Figure 6.2b. The relative stability of the mean wavelength with plasma density is clearly observed for self-

[3] Full details characterising the laser are presented in Section 5.2.1

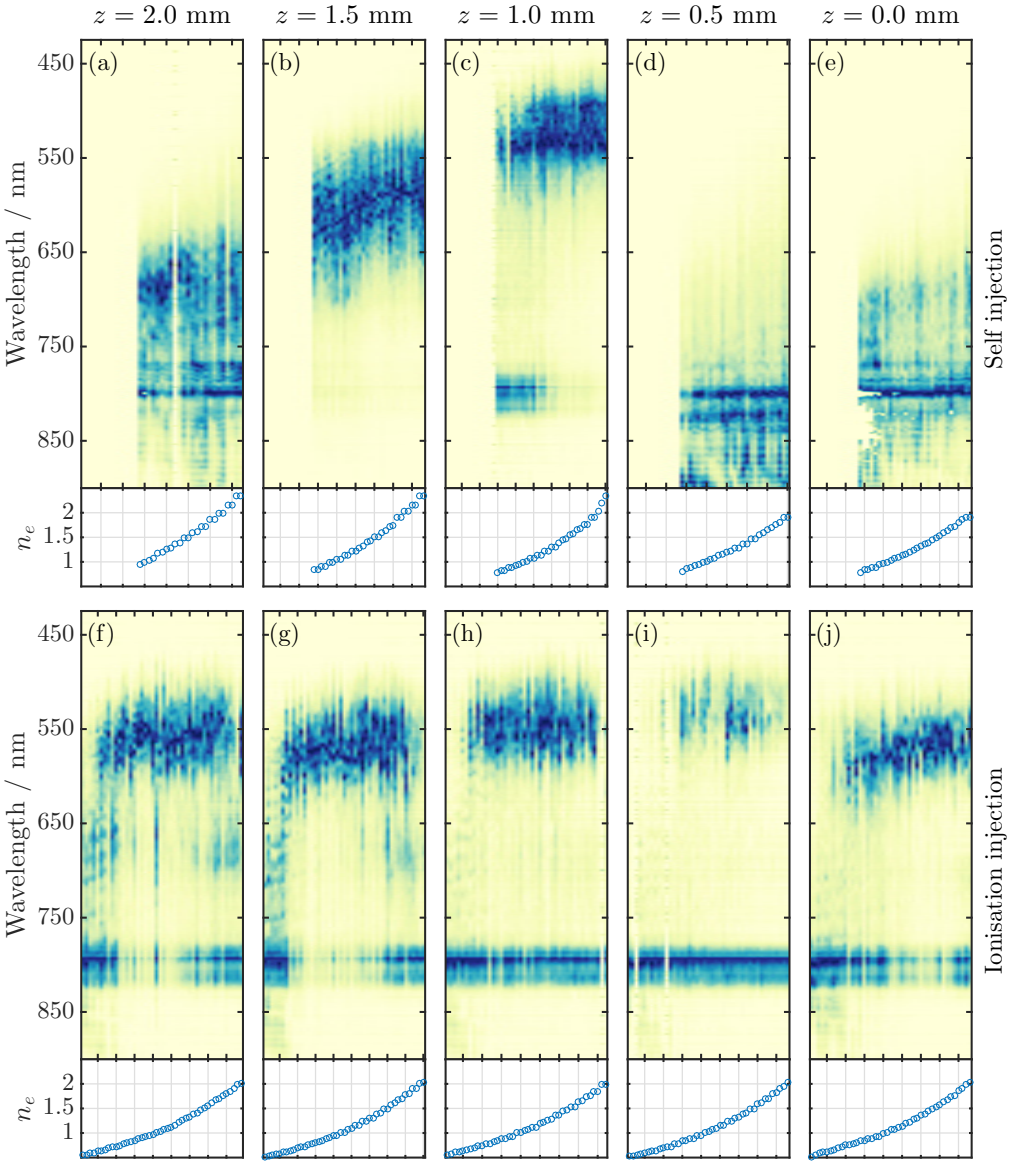

Figure 6.1: *Single shot spectra for self injection (Panels (a)-(e)) and ionisation injection (Panels (f)-(j)) as a function of plasma density and focal plane in the gas jet. The plasma density $n_e[10^{19}\,\mathrm{cm}^{-3}]$ is plotted as the circular marker for each spectra in the panel underneath it. All spectra are normalised to their individual maxima.*

injection. While the former is broadly true, a slow monotonic increase with plasma wavelength is also witnessed. For ionisation injection, a fast rise with number density for $n_e \leq 8 \times 10^{18}\,\mathrm{cm}^{-3}$ is seen at all focus positions, whereas a slow decrease of the

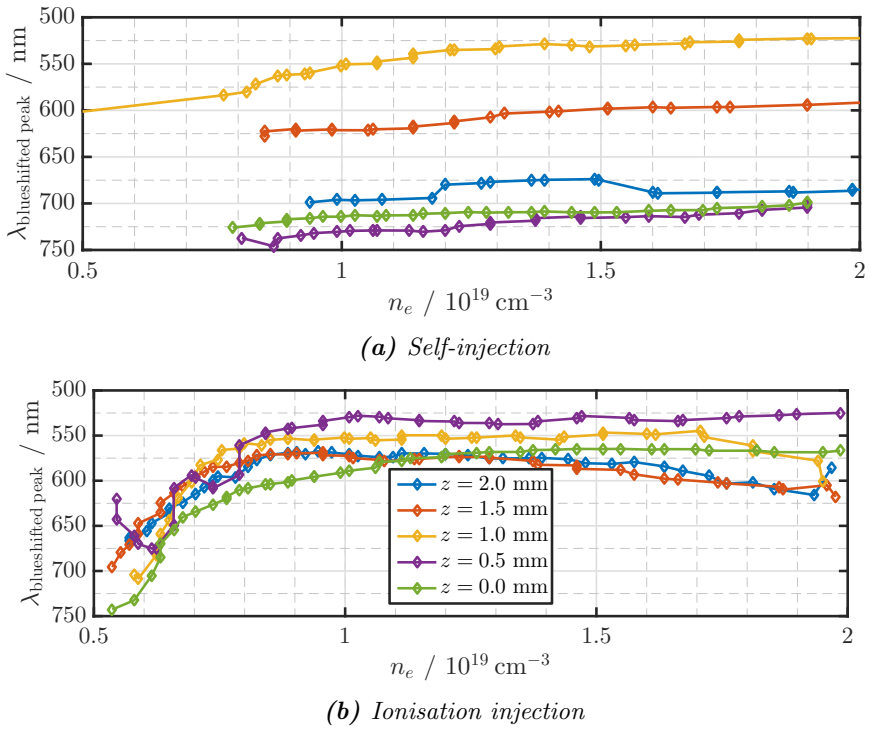

(a) *Self-injection*

(b) *Ionisation injection*

Figure 6.2: *Intensity weighted mean wavelength of the blueshifted peak for different focal planes as a function of plasma density for (a) self-injection and (b) ionisation injection. The legend for both panels is shown in Panel (b).*

central frequency is observed for densities above $1.5 \times 10^{19}\,\text{cm}^{-3}$.

6.2.2 Discussion

The first thing to consider for the relatively constant blueshifted features observed with ionisation injection is whether these are caused by recombination of the carbon and oxygen ions. However, this is extremely unlikely to be the case. Firstly, the broad nature of the feature would indicate reasonably high ion temperatures, if the spectral lines were to be broadened to such an extent. As the ions gain almost no energy from the passing laser, velocities to yield this level of broadening can not be achieved. Indeed, to observe spectral broadening of $\Delta\lambda = 30\,\text{nm}$ at $\lambda_0 = 550\,\text{nm}$, the temperature of carbon ions needs to be $k_B T \simeq 6\,\text{MeV}$.[241] Another possible mechanism for large blueshifts is ionisation blueshift. However, this depends heavily on the background plasma density and thus can not yield a constant blueshift with number density. Finally, the relative invariance of the blueshift with plasma density also rules out Raman

[241] H. R. Griem. *Principles of Plasma Spectroscopy:* Cambridge University Press, 1997.

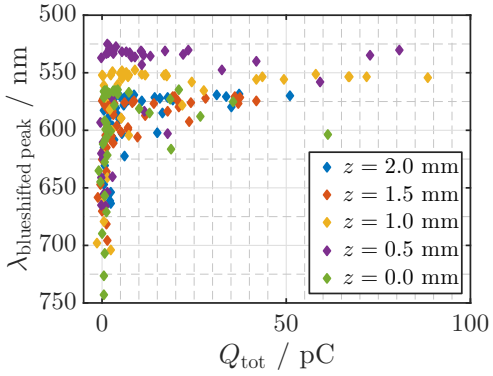

Figure 6.3: *The correlation between observed spectral blueshift and measured beam charge for ionisation injection.*

scattering. Additionally, to observe an anti-Stokes line at 560 nm a plasma density at least an order of magnitude larger than used here is required.

The behaviour observed for ionisation injection at low plasma densities is interesting as a number of implications can be drawn. Firstly, for very low plasma densities the blueshift is seen to not be as severe, with almost no light observed around 550 nm. Seeing this increase with plasma density implies that the higher rate of self-focussing is playing a role. Indeed, the blueshift is seen to saturate at $n_e \sim 8 \times 10^{18}\,\text{cm}^{-3}$. This can also be interpreted as a threshold density for this blueshift feature. It is well known that ionisation injection requires intensities of $a_0 > 1.6$. With a vacuum normalised vector potential ~ 0.7, it is a reasonable assumption that the onset of the highly reproducible blueshifted feature corresponds to the the ionisation injection intensity threshold having been reached. This would imply that for every shot, a large amount of electrons are trapped by the wake. Indeed, for number densities $n_e > 6 \times 10^{18}\,\text{cm}^{-3}$ relativistic electron beams are measured for ionisation injection.[4] The correlation between observed blueshift and injected charge is emphasised in Figure 6.3, depicting the average wavelength of the blueshifted peak and the total charge for $\mathcal{E} \gtrsim 50\,\text{MeV}$. It is evident that for shots where significant charge is seen a blueshift is also evident. Thus the stable blueshifted spectral feature is linked to the trapping of ionised electrons within the bubble.

The same cannot be said about spectra measured with pure helium. In this case, the shift of the blueshifted spectral peak is seen to strongly depend on the position of the focal plane. Additionally, electron beams were occasionally generated at all positions. However, as discussed in Section 4.4.3, a few Rayleigh ranges before the focus the laser spot is very often not smooth, but instead heavily filamented. For

[4] For more details on electron beams from ionisation injection, cf. Section 5.3.4

the laser spot size used here, the value for $M^2 = 3.6$, and thus the realistic Rayleigh range is $z_{\mathrm{R,R}} \simeq 300\,\mu\mathrm{m}$. This is shorter than the 500 µm steps of the focal plane scan. Thus, a very different laser profile will couple into the plasma at varying focal planes. This will change the amount of energy captured by the guided filament and result in different laser evolution. Higher amounts of guided laser energy lead to higher self-focussed intensities in the early interaction, when the pulse is still long enough to have a sizeable fraction residing in the positive refractive index gradients present at the rear of the bubble. Thus a larger amplitude plasma wave is set up, with higher refractive index gradients leading to larger blueshifts.

6.3 Experimental comparison of ionisation and self injection

During the Gemini 2015 experimental campaign a direct comparison between self injection and ionisation injection was undertaken by collecting datasets with pure helium and a mixed gas. The impurity species used was CO_2 at a mass concentration of 10%. The laser spot[5] was measured to be elliptical with $r_{\mathrm{minor}} = (37 \pm 2)\,\mu\mathrm{m}$ and $r_{\mathrm{major}} = (48 \pm 6)\,\mu\mathrm{m}$; these values correspond to the $1/e^2$ radius of intensity (or $1/e$ extent of the electric field). The average energy within the $1/e$ contour of the spot is $(50 \pm 5)\,\%$. With a pulse duration of $\tau_{\mathrm{FWHM}} = (43 \pm 5)\,\mathrm{fs}$, the peak intensity on target was measured to be $I = (5.6 \pm 0.8) \times 10^{18}\,\mathrm{W\,cm^{-2}}$, yielding $a_0 = 1.6 \pm 0.1$.

A plasma density scan was performed with a fixed 20 mm gas cell length with the average laser energy on target being $\mathcal{E}_L = (8.2 \pm 0.5)\,\mathrm{J}$ amounting to a power of $P_L \simeq 180\,\mathrm{TW}$. Elucidating the motivation for this work, we note that a single result regarding ionisation injection has been published in the current plasma density ($n_e < 3 \times 10^{18}\,\mathrm{cm^{-3}}$) and laser power ($P > 150\,\mathrm{TW}$) regimes.[55] Further, no direct comparisons between self-injection and ionisation injection have been put forward.

6.3.1 Maximum electron energy

Figure 6.4 depicts the measured maximum electron beam energies as a function of plasma density for self-injection and ionisation injection. Also plotted is the linear energy gain, $\Delta\mathcal{E} = 2\gamma_p^2 m_e c^2$, as the solid magenta line. As can be seen, the peak energy gain scales dissimilarly with plasma density for the different injection methods. For the case of self-injection, as discussed in Section 7.4.1, the maximum energy gain exceeds the linear scaling and an initial increase of cut-off energy is seen with plasma density.

[5] More details regarding the laser are presented in Section 7.2.1

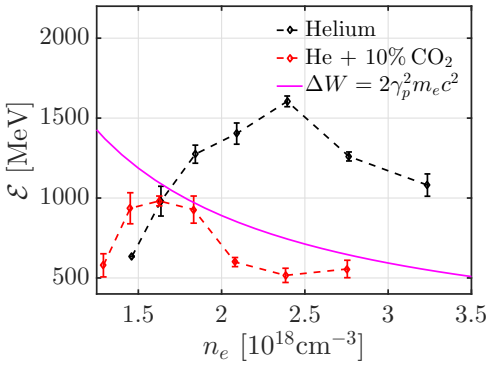

Figure 6.4: *The dependence of cut-off energy of self-injected and ionisation-injected electron beams on plasma density with a* 20 mm *gas cell and* $\mathcal{E} = (8.2 \pm 0.5)$ J *on target.*

Whilst a somewhat similar general behaviour is witnessed for the ionisation-injected beams, the highest measured electron energy is far lower than that for self-injection. Additionally, for plasma densities $n_e \geq 1.6 \times 10^{18}\,\mathrm{cm}^{-3}$, the maximum beam energy can be seen to broadly resemble the linear scaling.

The injection thresholds are also seen to be different for self-injection and ionisation injection. This has been observed previously,[205,238] and is due to the minimum intensity requirement for ionisation induced trapping being much smaller than for self-injection. At lower plasma densities the rate of self-focussing is lower and thus the necessary conditions for ionisation injection are reached later in the interaction. The lower plasma density also results in a reduced accelerating field and with a limited plasma length this results in lower electron beam energies.

Figure 6.5 depicts a length scan for ionisation injected electron beams at different

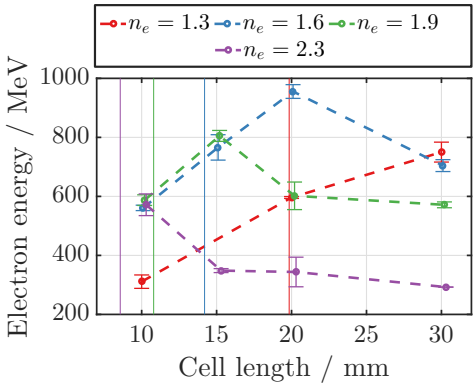

Figure 6.5: *The dependence of ionisation-injected electron beam cut-off energy on plasma density and cell length with* $\mathcal{E} = (9.9 \pm 0.2)$ J *of laser energy on target.*

plasma densities with $\mathcal{E}_l = (9.9 \pm 0.2)\,\mathrm{J}$ on target. The expected $\mathcal{E} \propto n_e^{-1}$ scaling with plasma density is observed, with lower plasma densities yielding higher beam energies. Additionally, an inverse scaling with plasma density is observed for dephasing length: higher plasma densities reach the maximum energy with shorter distances. The numeric values for the linear dephasing length are plotted as the thin vertical lines in Figure 6.5. While there is qualitative agreement in the acceleration length scaling, as discussed above, the quantitative match is not excellent. It is observed that maximum energy gain is always reached for distances longer than the calculated dephasing length. However, there is some evolution distance in the plasma before the bubble, and thus the accelerator cavity, is fully formed. This could explain for the discrepancy in the simple estimate and the measured values. We note that the data from this scan agrees with the data presented in Figure 6.4, with a peak energy of $\mathcal{E} \simeq 1000\,\mathrm{MeV}$ obtained with $L_{\mathrm{cell}} = 20\,\mathrm{mm}$ at $n_e = 1.6 \times 10^{18}\,\mathrm{cm}^{-3}$.

In order to explain the reduced energy gains with ionisation injection, we recall the trapping condition for an electron ionised by the laser field within the wake:[6]

$$1 + \phi_{\mathrm{min}} - \phi(\psi_i) \leq \frac{\sqrt{1 + \frac{a^2(\psi_i)}{2}}}{\gamma_p}. \tag{6.1}$$

Assuming that the electrons are liberated at the phase peak of the laser, i.e. where $a_0(\psi) = 0$, we obtain:

$$\phi_{\mathrm{tr}} - \phi_{\mathrm{min}} \leq 1 - \frac{1}{\gamma_p}. \tag{6.2}$$

For tenuous plasmas, where $\gamma_p \gg 1$, we thus see that if the trapping condition is fulfilled, the effective potential difference an ionised electron will experience is $\Delta\phi_{\mathrm{II}} = \phi_{\mathrm{max}} - \phi_{\mathrm{tr}} + 1$. With the trapping condition fulfilled, this can be rearranged to yield $\Delta\phi_{\mathrm{II}} \leq \phi_{\mathrm{max}} - \phi_{\mathrm{min}}$. For self-injected electrons the maximum available energy gain is $\Delta\phi_{\mathrm{SI}} = \phi_{\mathrm{max}} - \phi_{\mathrm{min}}$. We thus see that for ionisation injected electrons, the maximum available energy gain is always smaller than that for self-injected electrons as $\Delta\mathcal{E} = (1 + \beta_p)\gamma_p^2 \Delta\phi\, m_e c^2$.

This concept is illustrated in Figure 6.6 showing the wake calculated by solving Equation 2.39 for a plasma density $n_e = 1.9 \times 10^{18}\,\mathrm{cm}^{-3}$ and laser with $a_0 = 2$ and $\tau_{\mathrm{FWHM}} = 45\,\mathrm{fs}$. Panel (b) plots the wake potential as the blue line and the laser intensity as the red line. The effective potential difference felt by an electron ionised at different phases of the wake are sketched as the set of black and green lines. For an electron ionised at the peak of the laser pulse, a smaller total potential difference for energy gain is available when compared to the case of ionisation earlier in the pulse.

[6] Cf. Section 2.5.6

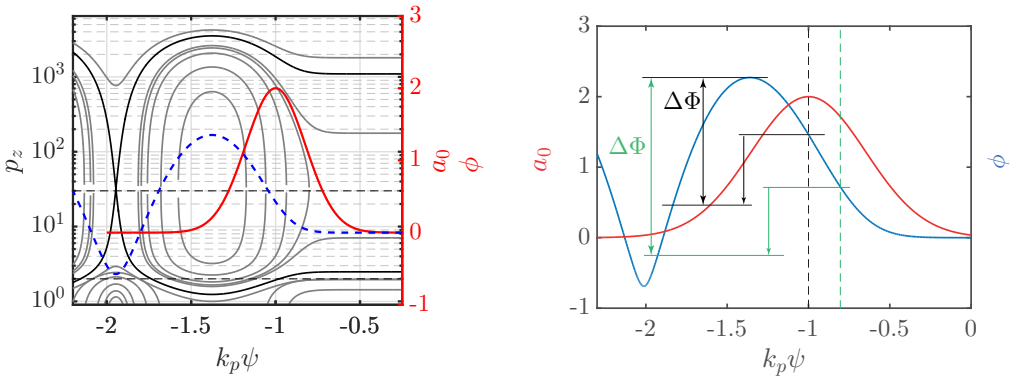

(a) Phase space trajectories *(b) Sketch of available energy gains*

Figure 6.6: *Physics of ionisation induced trapping for electron ionised at different phases within the wake for $n_e = 1.9 \times 10^{18}\,\mathrm{cm}^{-3}$, $a_0 = 2$ and $\tau = 45\,\mathrm{fs}$. Panel (a) depicts different γ-ψ phase space trajectories, with the black line being the separatrix. Electrons ionised closed to the intensity peak of the laser pulse will be trapped on a more deeply trapped trajectory, resulting in lowered energy gain. Panel (b) depicts the mechanism of lowered energy gain with different ionisation phases. Electron ionised at the peak of the laser feel a lower maximum potential difference as they are turned around in the wake potential earlier.*

Panel (a) in Figure 6.6a depicts the γ-ϕ phase space trajectories in the wake potential, where the potential is also drawn with the blue dashed line and the laser intensity profile is shown by the red line. This diagram allows us to analyse the trajectories of electrons ionised within the wake. An ionised electron will have $H_i = 1 - \psi(\phi_{\mathrm{ion}})$ and thus electrons ionised later in the wake will have a lower hamiltonian value. This means these orbits are more deeply trapped, corresponding to the innermost trajectories in Panel (a) in Figure 6.6a. Hence Figure 6.6 shows that electron ionised closer to the intensity peak of the laser will have a smaller available energy gain.[242] We note that in the limit of electron ionised at the peak of the wake potential, the energy gain available corresponds to that of the linear scaling $\Delta\mathcal{E} = 2{\gamma_p}^2 m_e c^2$.

The preceding analysis shows that ionisation injected electron will always have energy gains smaller than self-injected electrons. However, this effect alone cannot account for the energy scaling of ionisation induced electrons observed in Figure 6.4, as the theory always predicts larger energy gains than $2{\gamma_p}^2 m_e c^2$. In later chapters we see that even for self-injection, the energy gain is actually limited by bubble evolution induced dephasing, where bubble expansion renders electrons close to the midpoint of the bubble into a decelerating phase.[7] Additionally, if the laser intensity increases to values where impurity electrons are ionised before the trapping conditions in Equation 6.2 is met, the ionised electrons will not be trapped and instead execute open orbits in

[242] J. Faure, CERN Yellow Reports **1**, 2016.
[7] Cf. Sections 7.3.4 and 7.4.3

phase space. This mechanism has been identified as the physical reason for the so-called self truncated ionisation injection.[243,244] Thus, we see that the limited beam energies for ionisation-injected electrons are the combination of bubble evolution and ionisation injection truncation.

6.3.2 Injected charge

In Figure 6.7, the beam charge for $\mathcal{E} \gtrsim 200\,\mathrm{MeV}$ is plotted for self-injected and ionisation-injected electron beams, with $\mathcal{E} = (8.2 \pm 0.5)\,\mathrm{J}$ of laser energy on $L_{\mathrm{cell}} = 20\,\mathrm{mm}$ target. The measured total beam charge is very similar for both injection methods, apart from at $n_e = 2.4 \times 10^{18}\,\mathrm{cm}^{-3}$. For low plasma densities, the electron beams from ionisation injection exhibit higher charge. At plasma densities where the energy of self-injected electrons is higher than ionisation injected beams, the total accelerated charge scales very similarly. The outlier to this trend is $n_e = 2.4 \times 10^{18}\,\mathrm{cm}^{-3}$ where ionisation induced beams were measured to have much higher beam charge. The data at this density exhibits unusually large variability, also evidenced by the large error bar, implying some irregularity in the system. The general observed trend for both injection methods is a slow, linear increase of injected charge with plasma density.

The scaling of ionisation injected charge above 200 MeV as a function of total plasma length is plotted in Figure 6.8 for different plasma densities with $\mathcal{E}_L = (9.9 \pm 0.2)\,\mathrm{J}$ on target. For almost all lengths, an increase of charge with plasma density is witnessed. It should be noted that the peak in charge or $n_e = 2.3 \times 10^{18}\,\mathrm{cm}^{-3}$ at $L_{\mathrm{cell}} = 20\,\mathrm{mm}$ corresponds to the conditions where unusually large beam charge was observed in Fig-

[243] M. Zeng *et al*, *Phys Plasmas* **21**, 2014.
[244] M Mirzaie *et al*, *Sci Rep* **5**, 2015.

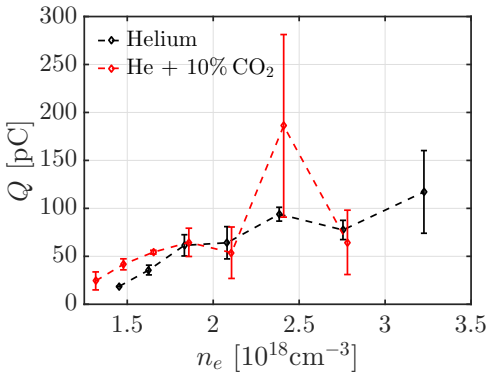

Figure 6.7: *The dependence of beam charge of self-injected and ionisation-injected electron beams on plasma density with a* 20 mm *gas cell and* $\mathcal{E} = (8.2 \pm 0.5)\,\mathrm{J}$ *on target.*

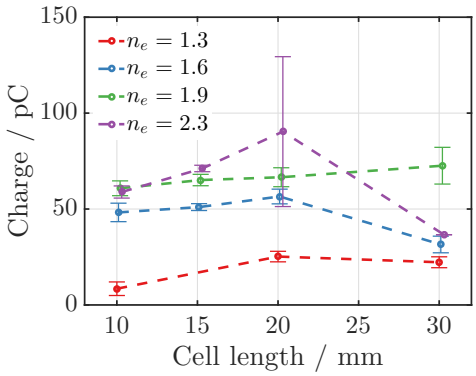

Figure 6.8: *The dependence of ionisation-injected electron beam charge on plasma density and cell length with* $\mathcal{E} = (9.9 \pm 0.2)$ J *of laser energy on target.*

ure 6.7. Thus these conditions may in fact correspond to some interesting resonance. However, it is observed that for the longest cell lengths the charge again drops (apart from at one density). This decrease in charge with length implies, along with the observed continuous energy spread, that a large amount of electrons have been decelerated below the detection threshold.

The fact that the total charge is similar for ionisation injected and self-injected electron beams seems to be in contradiction to previous studies. However, almost all previous results, where much higher charge is reported, were conducted with lower laser powers and higher plasma densities. In fact, most results are very similar in terms of absolute charge. This is somewhat surprising, as the total injected charge is a non-linear interplay between self-focussing and plasma response, the first determining the ionisation locations and the second providing the potential structure. As such, it is very difficult to model and the total injected charge is not understood for both ionisation injection and self injection.

6.3.3 Divergence

Having demonstrated the extremely similar scaling for total charge, we look at the divergence of the measured electron beams. In Figure 6.9 the energy resolved divergence for both self and ionisation-injected beams is plotted as the dotted line of black and red colour, respectively. These shots are from the dataset presented in Figures 6.4 and 6.7. The divergence is measured along the direction of the laser polarisation. In the same plot, the perpendicular momentum at a given energy, calculated by $p_\perp = p_\parallel \cdot \theta_{\mathrm{FWHM}}$ and $p_\parallel = \mathcal{E}$, is shown as the solid line of different colours. The shots with the highest energy gain for the injection methods are shown, with plasma densities given in the

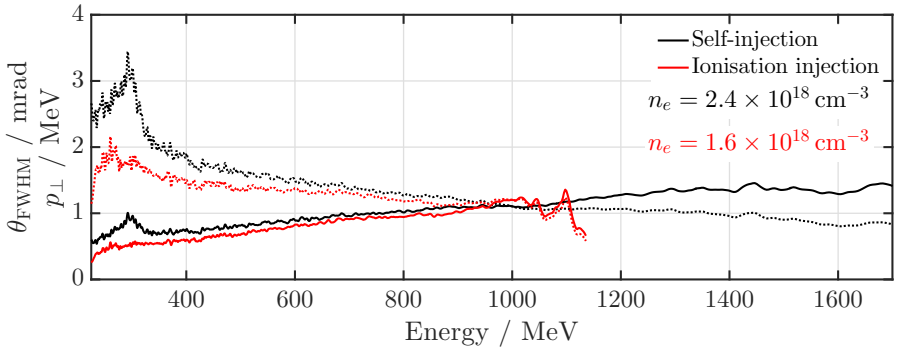

Figure 6.9: *Energy dependent divergence (dotted line) and transverse momentum (solid line) for electrons with self-injected (black) and ionisation injected (red) beams.*

figure.

The divergence of the self-injected beam is larger than that of the ionisation injected beam for nearly all beam energies. The difference can be as large as 25% for energies below 400 MeV. As energy increases, though, the difference in divergence reduces. In both injection methods the transverse momentum is seen to increase with longitudinal momentum. This implies a coupling between the transverse and longitudinal momenta. Indeed, analysis of this effect in the linear regime[245] shows that the transverse momentum varies as

$$\frac{p_\perp}{p_{\perp 0}} = \left(\frac{\gamma_f}{\gamma_i}\right)^P, \tag{6.3}$$

with $P = 1/4$. This highlights the direct coupling between longitudinal and transverse momentum. Analysis for the non-linear bubble regime also gives a similar scaling.[118,119]

The counter-intuitive increase of transverse momentum with increasing longitudinal momentum can also be examined heuristically by employing Liouville's theorem.[82] As an electron is injected off-axis, it has a finite transverse momentum. An ensemble of particles with different initial positions and momenta occupy a finite volume in the transverse phase space, the area of which is also known as emittance. As the electron is accelerated, its transverse excursion distance decreases as its longitudinal momentum increases. Hence, by Liouville's theorem, stating conservation of phase space volume, the transverse momenta of particles must increase.

The data presented in Figure 6.9 facilitates fitting Equation 6.3 to the measured

[245] A. J. W. Reitsma *et al*, *Laser Part Beams* **22**, 2004.
[118] I. Kostyukov *et al*, *Phys Plasmas* **11**, 2004.
[119] A. G. R. Thomas, *Phys Plasmas* **17**, 2010.
[82] T. Kibble *et al*. *Classical Mechanics*. Imperial College Press, 2004.

data. Such a fitting a power law to the calculated transverse momenta results in values for the power P as $P_{SI} = 0.41$ and $P_{II} = 0.63$. Hence different beam dynamics are observed. Also, initial transverse momenta can be calculated from these fits assuming $\gamma_i = \gamma_p$, resulting in $p_{\perp 0,SI} = 0.19\,\mathrm{MeV}$ and $p_{\perp 0,II} = 0.08\,\mathrm{MeV}$. The non-linear theory by Thomas[119] gives initial transverse momentum as $p_{\perp 0} = (\pi/4)a_0 m_e c$, yielding a value of $p_{\perp 0} = 0.8\,\mathrm{MeV}$ for $a_0 = 2$. The observed value is of lower value for the self-injection case, with the discrepancy potentially arising from the assumption of full blowout or by the lack of datapoints for the fit below 200 MeV. Additionally, this analysis relies on a linear energy chirp, mapping out the betatron phase into distinct longitudinal momentum. For an evolving bubble, caused by self-focussing or compression, this assumption may cease to be valid and phase mixing can occur.

Finally, the fits allow us to compare the initial transverse momenta of self and ionisation injection. The ratio of the predicted initial transverse momenta for the two injection methods predicts cooler beams for ionisation injection, with self-injected electrons predicted to have a transverse momentum 2.2 times larger.

6.3.4 Discussion

A direct comparison between ionisation injection and self injection revealed interesting features. The maximum beam cut-off energies were found to scale very differently between self-injection and ionisation injection, with self-injected beams reaching much higher peak energies. A detailed analysis of the ionisation injection trapping physics revealed that ionisation injected beams always obey such scaling and the energy gain achieved will always be less than that available for self-injected beams. It was observed that the phase in which the impurity electrons are ionised affects strongly the energy gain available, implying that the maximum available energy gain can be tuned for a given laser intensity by changing the impurity species alone. This opens the possibility of changing the beam energy of a LWFA injector with varying the impurity species alone and not affecting any laser dynamics.

The total charge was found to be extremely similar between self-injection and ionisation injection. It was found that near the threshold for self-injection, ionisation injection produces beams with higher charge. However, in a regime where self-injection was optimised, the total charge in the beam scaled in a very similar manner. This implies that when in a regime of optimised self-injection, ionisation induced injection does not improve on the total charge. This can be seen as a natural consequence of beam loading, if the amount of charge injected is limited by the beam load itself. Indeed, the very similar scaling of total charge at plasma densities where the measured charge was the same suggests an underlying limit for total accelerated charge.

From similar amount of charge for the two injection methods and higher electron energies for self-injection it is easily seen that the overall laser energy to electron beam energy conversion efficiency is higher for self-injection. While this is certainly true for the current work, changing the impurity species may lead to higher electron energies and thus increase the overall efficiency. However, with self-injection working in an optimised manner, the combination of high electron energies and high beam charge means the overall efficiency is expected to still be higher.

The comparison between the divergence scaling with energy reveals a smaller initial transverse momentum for ionisation injection. This in turn means that the geometrical emittance of ionisation injected beams is smaller than for self-injection, as $\epsilon_g = \sqrt{\langle x^2 \rangle \langle x'^2 \rangle - \langle x x' \rangle^2}$. Indeed, the reduced divergence was also reported by McGuffey *et al*,[205] implying a smaller transverse emittance given the same source size. However, the current work represents a more detailed measurement, without the ambiguity of a beam profile monitor, where high charge, low energy electron signal often dominates.

The divergence measurements and the associated calculation of the initial transverse momentum revealed a smaller initial value of $p_\perp$ for self-injection than predicted by theory.[119] This is an indication that the self-injection observed here is not the usually seen transverse wavebreaking. This implies that the collection volume for self-injection is smaller than expected for self-injection, signifying an interesting regime of self-trapping.[8]

6.4 Conclusion

Spectral signatures of employing ionisation injection imparted on the driver laser were measured. Over a range of focal planes, the transmitted laser spectrum was measured to contain a prominent blueshifted feature when a gas mix was used; the blueshift was seen to be constant for plasma densities above $n_e \geq 8 \times 10^{18}\,\mathrm{cm}^{-3}$. The onset of the blueshifted feature is seen to occur at the same plasma density as the threshold for high energy electron beam generation. This observation provides means for empirical assertions of ionisation induced injection, without explicitly measuring the electron beams, providing extra control and understanding over the acceleration interaction.

A direct comparison was performed between self-injection and ionisation induced injection. Such work has not previously been done for laser powers in the 200 TW regime. It was found that self-injection consistently leads to higher electron energies.

[8] See also the results presented in Sections 7.3 and 7.4.

While ionisation injection allowed for electron beam generation at lower plasma densities, the peak energy was observed to not scale as in the self-injection case. It was found by analysing the trapping physics of ionisation injected electrons that this is a general feature and that the maximum energy reduces as trapping occurs closer to the peak intensity of the laser. This could allow for customisation of maximum energy gain in future LWFA based injectors, with the peak energy of the bunch easily tunable with only a change of the impurity gas.

The total beam charge was found to scale similarly over a broad range of plasma densities, with ionisation injected electron beams delivering higher beam charges than self-injected beams at low values of n_e. Analysis of the energy resolved beam divergence revealed that the initial transverse momentum is more than two times smaller for beams generated with ionisation injection. This means that ionisation injected electron beams are injected with a smaller transverse emittance, in agreement with predictions from previous work.[205]

CHAPTER 7
Multi-GeV scale electron acceleration

THIS CHAPTER PRESENTS experimental results detailing electron acceleration beyond 2 GeV employing laser wakefield accelerators in the self-guided, self-injected regime. This was made possible by using a longer focal length focussing optic; doubling the focal length extends the characteristic diffraction length by a factor of four. This allows longer interaction lengths and was found to yield higher electron beam energies along with high laser energy to electron beam energy efficiencies. Finally, aspects relevant to stable long-term operation of laser wakefield accelerators in the self-injection regime were explored.

7.1 Motivation

The simplest laser wakefield accelerator comprises of a gas jet and a laser pulse focussed into it. Due to the very high intensities involved, the laser will self-guide and drive a wakefield for distances longer than the Rayleigh length. The plasma wave can also be driven to amplitudes high enough for the coherent structure to break and some electrons self-inject into the cavity. This is the self-guided, self-injecting regime of laser wakefield accelerators. Maximum electron energies nearing gigaelectronvolts, employing a 200 TW laser, have been demonstrated.[117]

As the self-guided regime relies on self-focussing, the laser will propagate at the matched spot size. For $P > P_c$, where P_c is the critical power for self-focussing, and for propagation at the matched spot size w_0, the energy gain will be given by[1]

$$\Delta\mathcal{E} = \frac{\omega_L^2}{6c^2} w_0^2 m_e c^2. \tag{7.1}$$

Thus, for a constant laser power, increasing the focal spot size by a factor of two should

[117] S. Kneip *et al*, *Phys Rev Lett* **103**, 2009.
[1] Cf. Equation 2.77 and discussion there

deliver a fourfold boost in final electron energy. Secondly, the characteristic scale for diffraction, the Rayleigh range, also scales as the square of the focal spot size. As plasma responds to the ponderomotive force of a laser driver within a timescale of the order of plasma frequency, the very front of the laser will always propagate in the quiescent plasma. Employing a pulse with a longer Rayleigh length thus allows the energy of the very front of the pulse to be beneficial in driving the plasma wave for longer. Further, a longer Rayleigh length results in more stable propagation and less envelope oscillations, as shown in Figure 2.9.

External guiding structures can be used to extend the high intensity interaction length; by employing a capillary discharge single stage electron energy gain of 4.2 GeV with a 300 TW laser has been shown.[53] However, the use of preformed plasma channels greatly increases the sensitivity of the nonlinear laser interaction to input pointing fluctuations. Further, large pointing offsets often result in partial destruction of the capillary itself.[2] Finally, the structure of the capillary means that it is not possible to perform direct optical probing of the plasma, which means the highly nonlinear propagation dynamics can only be inferred from computer simulations. Thus, while in principle being advantageous, the added experimental complications may in fact be detrimental to the overall reliability of the accelerator. Hence, achieving the highest possible energy gains in the self-guiding regime is of considerable interest in the long term development of reliable laser plasma based accelerators.

Since the first demonstration of GeV energy gains in the self-guided regime, the energy frontier has been pushed to 2 GeV by increasing the laser power to 1 PW.[56] However, building larger lasers is not the optimum way to higher energy gains. The preferred option would be to reach similar energy gains without such dramatic increase in laser power or the extra experimental complications that arise from capillary discharges. With this in mind, and being guided by the scaling in Equation 7.1, the effect of increasing the focal length by a factor of two and thus doubling the focal spot size on single stage electron energy gain was experimentally studied as a means to increasing the peak electron energies with a constant ~ 250 TW laser power.

The unique characteristics of laser wakefield accelerated electrons have made these beams attractive for many applications. Nonlinear relativistic Thomson scattering,[246] neutral lepton plasma production[247] and betatron imaging of biological samples[248]

[53] W. P. Leemans *et al*, *Phys Rev Lett* **113**, 2014.

[2] Note this is true for gas cells as well. However, in gas cells, the sensitive part is only the entrance or exit of the cell. In capillaries, damage affects the bulk density profile.

[56] X. Wang *et al*, *Nat Comms* **4**, 2013.

[246] G. Sarri *et al*, *Phys Rev Lett* **113**, 2014.

[247] G. Sarri *et al*, *Nat Comms* **6**, 2015.

[248] J. M. Cole *et al*, *Sci Rep* **5**, 2015.

or high-energy-density physics[249] are among a few of these. With a proliferation of utilisation of wakefield generated electron beams, a secondary aim of the experimental campaign was to establish a regime of stable long term operation.

7.2 Experimental setup

The experimental setup is shown in Figure 7.1. In the Gemini target area, the laser beams enter the bunker from the compressor area, situated above. Thus, the first mirror M1 in the target chamber reflects the beam such that it becomes parallel to the breadboard. This optic is a HR coated dielectric, allowing a fraction of the beam energy to pass through. Monitoring the leakage then allows for additional on shot pointing and energy measurements. The laser is polarised along the x-axis (as defined in Figure 7.1) as it enters the chamber; due to flipping the polarisation on M1 the polarisation at focus is along the y-axis.

The next optic is a deformable mirror, DM in Figure 7.1, inserted into the beamline to correct for spatial phase aberrations arising from the laser system. As the $f/40$ focussing optic used is a spherical mirror, the deformable mirror is also used to compensate for astigmatism and spherical aberration arising from using the mirror off-axis. The deformable mirror is coated with a high reflectivity dielectric coating. The beam reflects off the DM onto mirror 3, M3 in Figure 7.1. The incidence angle is kept as low as possible to ensure correct behaviour of the deformable mirror. The unusual angle of incidence on M3 necessitates the use of a silver coated optic.

After being reflected off the 6 m spherical mirror, SPH in Figure 7.1, the focussing beam is folded with a high damage-threshold dielectric mirror M5. The fluence on this optic is the largest, as the focussing beam has halved its diameter and thus near-field intensity is four times higher. Due to poor coatings, many mirrors were actually destroyed by the laser and the total energy delivered to target was thus limited. Higher quality mirrors were employed later in the campaign, allowing the full available laser energy to be used. The transmission through the folding mirror was measured by imaging a scattering screen placed behind it; this was a diagnostic to allow the reflectivity of the mirror to be monitored. A large increase in signal behind the mirror indicated failure of the optic. The total energy throughput from the first optic to target was measured to be 0.9. Combined with the measured compressor throughput of 0.67, the total energy on target is $0.6E_{\mathrm{amp}}$, where E_{amp} is the laser energy measured after the amplifier, before entering the compressor.

As the wavefront from the laser is non-prefect and additional aberrations are in-

[249] J. C. Wood *et al*, *CLF Ann Rep* , 2015.

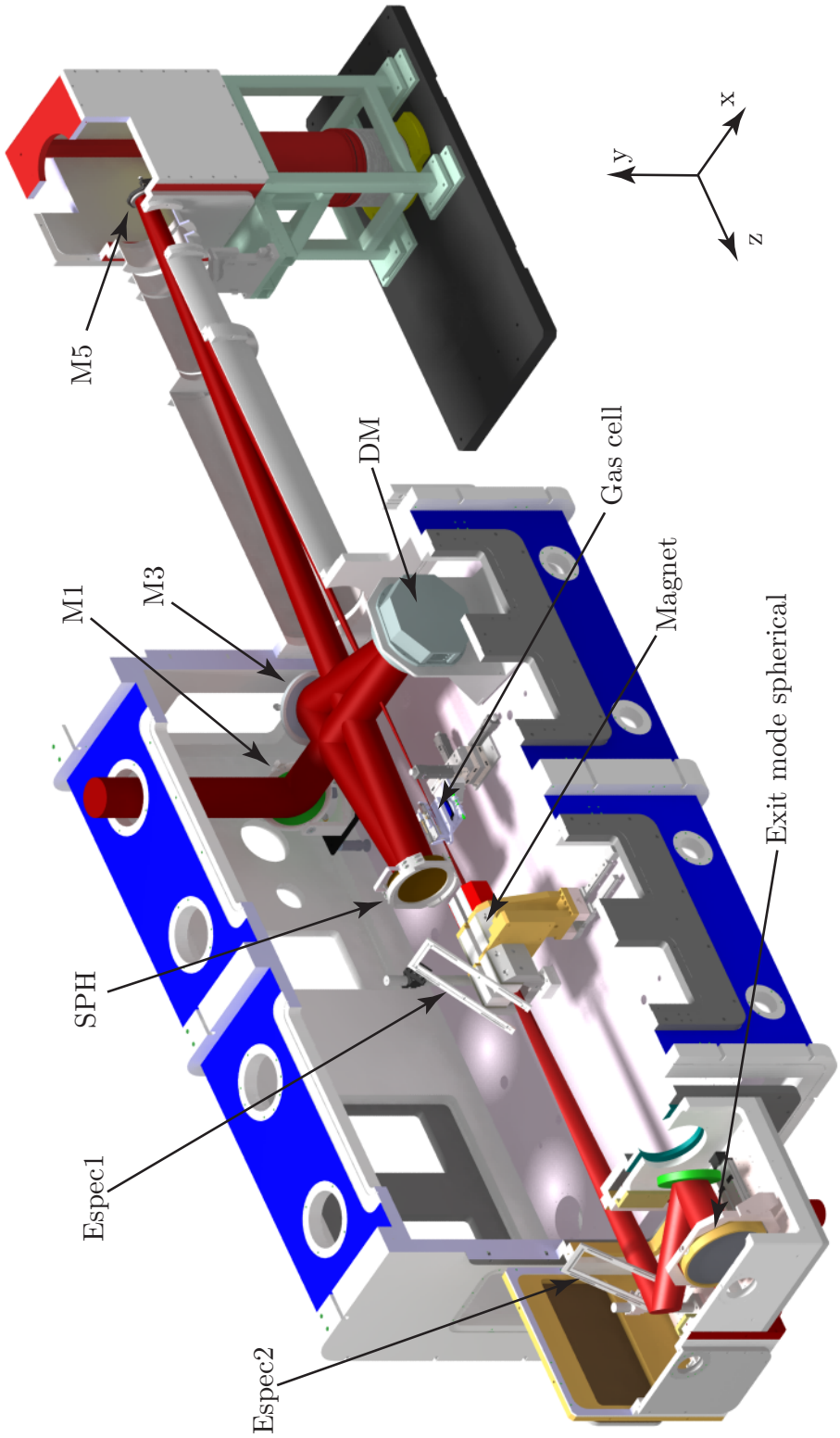

Figure 7.1: *Cutaway CAD drawing of Gemini 2015 campaign, showing the main components of the experiment, including the main beamline optics, gas cell and magnetic spectrometer.*

troduced in the beam transport optics in the vacuum chamber, a closed loop adaptive optic was employed to optimise the spatial phase. The deformable mirror used for this, DM in Figure 7.1, is a commercial product from Imagine Optic.[250] It consists of 64 mechanically driven actuators bonded to a dielectrically coated reflecting surface. The wavefront was measured after the folding mirror by sliding in an uncoated wedge, reflecting the beam upwards. It was then transported out of the vacuum chamber where a $f = 200\,\mathrm{mm}$ lens was used to collimate the beam. Along with the main focussing optic SPH, this lens forms an imaging system, allowing the plane of the deformable mirror to be imaged onto the wavefront sensor. The closed loop algorithm then attempted to minimise all Zernike polynomials apart from tilts and defocus. A typical optimised wavefront had an RMS error of $\sigma_\lambda \sim 0.03\,\mu\mathrm{m}$. The focal spot was then imaged and often manual corrections were added in open loop mode to ensure the correct focal plane and most symmetrical spot shape.

The gas cell used in this campaign is described in Section 3.4.2, along with the newly commissioned gas delivery system. The plasma density was measured on every shot by using Moiré interferometry. A trace of the pressure in the gas cell was saved on every shot as well. The peak pressure at the time of the shot arrival was calibrated against retrieved plasma density from the interferometric measurement.

7.2.1 Focal spot parameters

The optimised focal spot was measured on a daily basis, right after the optimisation process. The focal spot diagnostic comprised of an apochromatic, infinity corrected, high numeric aperture and long working distance $10\times$ microscope objective,[231] coupled to a 14 bit CCD. The spatial calibration of the image was performed with a $d = 7\,\mathrm{mm}$ period grating, placed in the near field of the laser. Typically, a few hundred single shot images of the attenuated short pulse were saved. Recent work by the staff of the laser facility showed that the spot measured in low power mode is identical to that in full shot mode.

Each focal spot was analysed by fitting an ellipse to different intensity contours. This allowed a consistent measurement of the focal spot size. In addition, the amount of energy enclosed within different intensity contours was calculated. Finally, the peak fluence was calculated by integrating the total background subtracted signal and scaling that to be equal to the amount of laser energy delivered. This was then converted into intensity by using the average value for the duration of the pulse, $\tau = (43 \pm 5)\,\mathrm{fs}$. The

[250] Imagine Optic. *ILAO deformable mirror*. URL: http://www.imagine-optic.com/en/product/ilao (visited on 08/09/2016).

[231] Edmund Optics. *Mitutoyo 10x NIR*. URL: http://www.edmundoptics.co.uk/microscopy/infinity-corrected-objectives/mitutoyo-nir-nuv-uv-infinity-corrected-objectives/46403/ (visited on 05/10/2016).

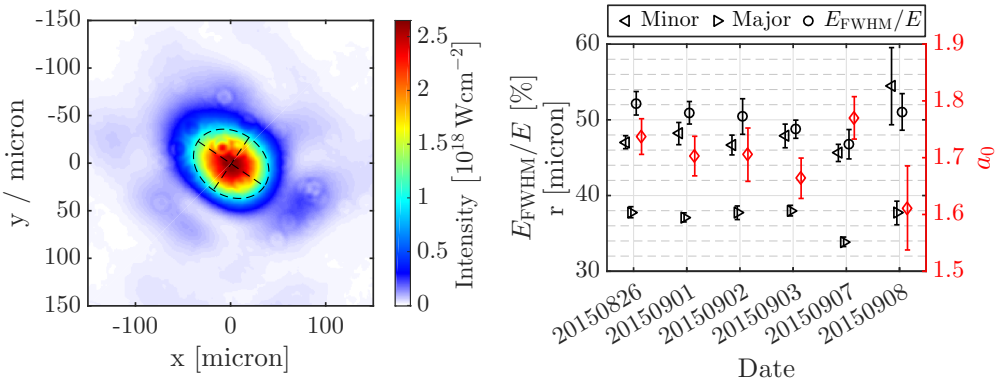

(a) *Low power focal spot* ***(b)*** *Focus data*

Figure 7.2: *Panel (a) shows a single shot focal spot image measured during the Gemini 2015 campaign; the black dashed line is fitted to the $1/e$ intensity contour. In Panel (b) the focal spot data from different days is shown. The minor and major axis of an ellipse fitted to the $1/e^2$ contour of the focal spot are plotted as the triangles, along with the energy enclosed in the $1/e$ contour. The measured normalised vector potential is plotted as the red diamonds. All errors are standard deviations.*

latter was measured using a SEA-SPIDER[169,251] in the target chamber, after reflection off all the beam delivery optics.

A single shot image of the low power focal spot is depicted in Figure 7.2a. The colour axis has been converted to full power intensity, assuming a total laser energy of 10 J. The black dashed line is an ellipse that was fitted to the I_{peak}/e contour. Data characterising the focal spot from multiple days of the experiment is plotted in Figure 7.2b. The minor and major axis of the fitted ellipse are plotted as left and right pointing triangles, respectively. The error bars for all quantities in this plot are the standard deviation of the measured quantity. Average values of the spot size are given by $r_{\text{minor}} = (37 \pm 2)\,\mu\text{m}$ and $r_{\text{major}} = (48 \pm 6)\,\mu\text{m}$, with these values corresponding to the $1/e^2$ radius of intensity (or $1/e$ extent of the electric field). The average energy within the $1/e$ contour of the spot is $(50 \pm 5)\,\%$; the data for encircled energy is plotted as circles in Figure 7.2b. The peak normalised vector potential is calculated by integrating each image and scaling the peak such that the total energy in the image is equal to 10 J. The average value for the normalised vector potential across days is $a_0 = 1.7 \pm 0.1$. For runs where energy was limited, the normalised vector potential scales as $a_0 = 1.7 \cdot (\mathcal{E}_{\text{laser}}/10)^{1/2}$.

[169] T. Witting *et al*, *Opt Lett* **36**, 2011.
[251] A. S. Wyatt *et al*, *Opt Lett* **31**, 2006.

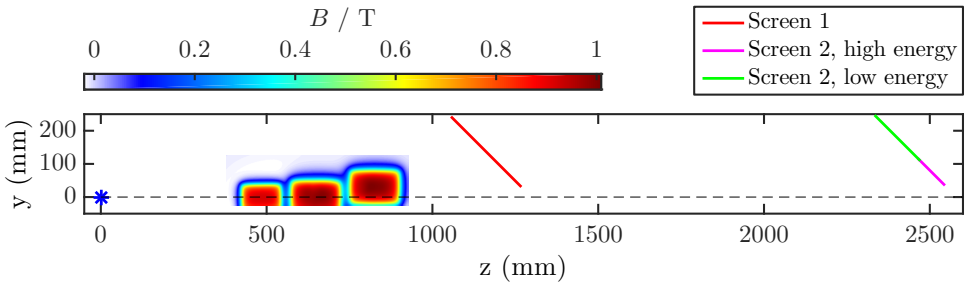

Figure 7.3: *Layout of the electron spectrometer. The blue star denotes the focal plane of the laser. The regions of the Lanex screens imaged by the three cameras are highlighted as different colour lines.*

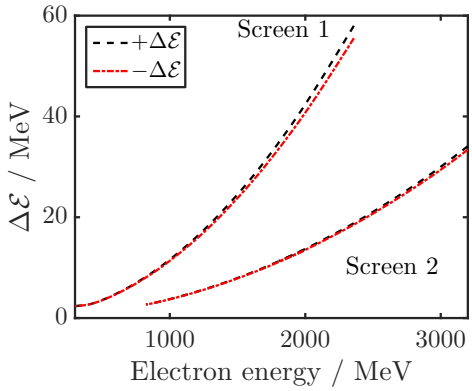

Figure 7.4: *Errors arising from an inaccuracy of 1 mm in measuring the position of electron spectrometer screens.*

7.2.2 Magnetic spectrometer

The magnetic spectrometer used to characterise electron beams consisted of a 42 cm long, $\langle B \rangle = 0.95\,\mathrm{T}$ dipole magnet and two spectrometer screens, as shown in Figure 7.1. A detailed measurement of the magnetic field of the dipole is presented in Figure 3.9. The physical layout of the spectrometer, including the positions of the scintillating screens, is shown in Figure 7.3. In this setup, only electrons with energies $\mathcal{E}_{\mathrm{min}} \simeq 950\,\mathrm{MeV}$ are detected on Screen 2. For Screen 1, the low energy cut-off is $\mathcal{E}_{\mathrm{min}} \simeq 130\,\mathrm{MeV}$. However, an obstruction in the vacuum chamber increased the low energy detection limit to $\mathcal{E}_{\mathrm{min}} \simeq 200\,\mathrm{MeV}$ on screen 1.

Errors arising from poor imaging or misread positions on screen can be evaluated by calculating the difference between actual and measured energy. Such errors arising for a measurement offset of 1 mm, a reasonable value in accuracy of determining screen position, are plotted in Figure 7.4. For screen 2, the error is always below 1%.

7.3 Gas cell length scans

The design of the gas cell used allows the plasma length to be changed remotely. This in turn enables the study of electron acceleration and injection dynamics as a function of plasma length. A wealth of physics to study is thus uncovered, allowing direct measurement of accelerating electric field, characterisation of the evolution of transverse focussing fields, estimates for dephasing and depletion lengths and clear determination of injection position in the plasma.

7.3.1 Low laser energy scans

Data from a typical length scan is plotted in Figure 7.5, conducted at a fixed plasma density of $n_e = (2.3 \pm 0.3) \times 10^{18}\,\mathrm{cm}^{-3}$ and laser energy of $(5.7 \pm 0.4)\,\mathrm{J}$, yielding a laser power of $P \sim 125\,\mathrm{TW}$. This is about half of the total laser energy available, meaning the normalised vector potential on target is $a_0 \simeq 1.3$. Each panel in Figure 7.5 shows all the shots taken at a given length, with the length of the gas cell given at the bottom of the panel. The dispersion of the magntic spectrometer results in the non-linear energy increase along the vertical axis; the horizontal axis is proportional to divergence. The colour scale is common for all shots. For each shot, the warping introduced by Scheimpflug compensation is corrected and a background subtraction is performed.

An electron beam has been injected and accelerated to $\sim 700\,\mathrm{MeV}$ energy for cell lengths as short as 3 mm. This means that injection into the wakefield has happened in the first few millimetres of the interaction. These low charge beams have a narrow divergence of $\lesssim 2\,\mathrm{mrad}$ and gain energy rapidly with increasing plasma lengths. On average, the beams have doubled their energy within the next 3 mm, reaching 1.4 GeV in an acceleration distance of a mere 6 mm. The total beam charge seems to be increasing with accelerator distance, implying continuous injection into the wake. The peak energy of the electron bunch increases until a maximum energy is reached at $L \simeq 9\,\mathrm{mm}$. After this length, the peak energy of the electron beam starts to gradually decrease, indicating dephasing has been reached.

A secondary injection event is observed at cell length $L = 12\,\mathrm{mm}$. This secondary bunch contains up to three times more charge than the previously accelerated beam. The maximum energy of this secondary injection bunch similarly increases rapidly with plasma length. However, the second, higher charge beam reaches a peak energy for plasma length $L = 16\,\mathrm{mm}$, after which no significant energy gain or loss is observed. This would imply the laser has depleted all its energy; this hypothesis is supported by the relative stability of the cutoff energy of the high energy, lower charge bunch.

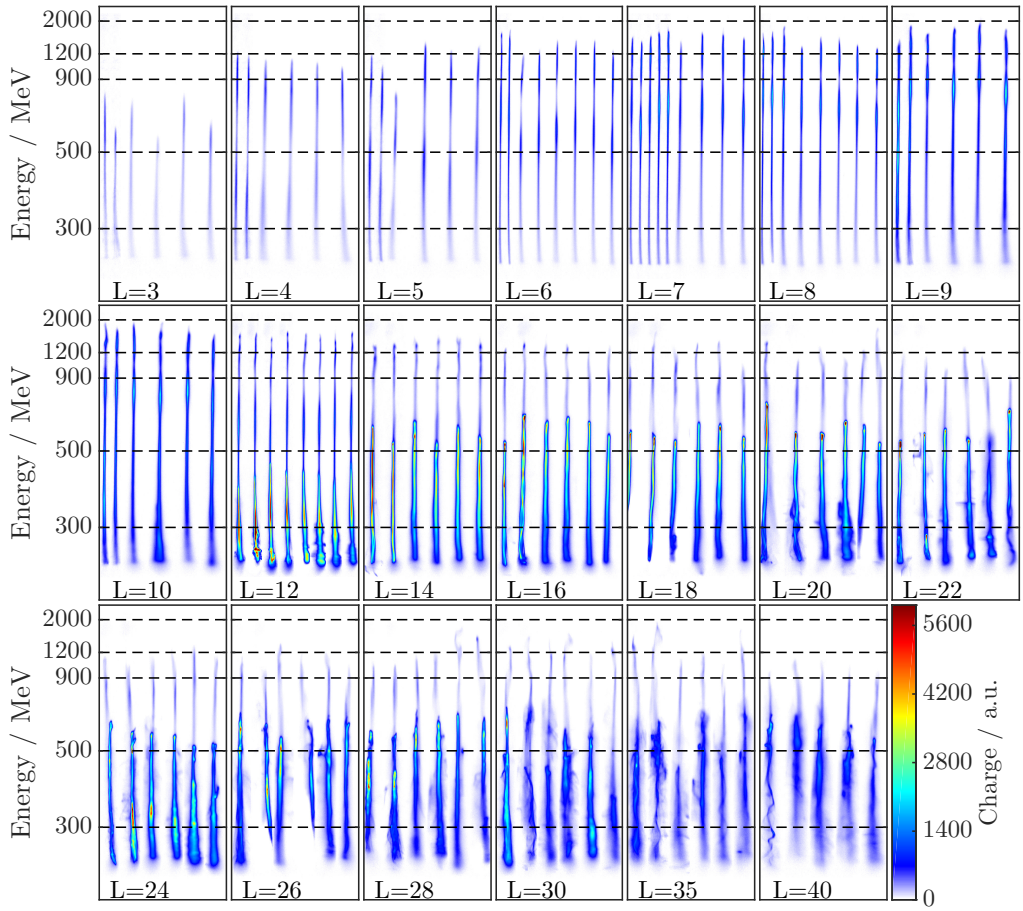

Figure 7.5: *Montage of raw data from a typical length scan, showing all shots taken for a given length. For each panel, the electron energy increases in the vertical direction in a non-linear fashion due to the dispersion of the magnetic spectrometer; the horizontal axis is proportional to beam divergence. All images are normalised to a common colour scale.*

In order to highlight the acceleration and secondary injection, single-shot spectra from some gas cell lengths are plotted in Figure 7.6. The spectrum from the shortest cell length, $L = 3\,\mathrm{mm}$, shows a flat energy spectrum with a cut-off of $\sim 700\,\mathrm{MeV}$. As length of the cell is increased, the electron beam energy is seen to increase as well, with nearly 2 GeV energies reached at $L = 9\,\mathrm{mm}$. Secondary injection and the acceleration of that bunch is clearly seen for cell lengths of $L = 12\,\mathrm{mm}$ and $18\,\mathrm{mm}$. The highly charged beam acceleration progresses much more slowly. Continuous injection is also witnessed in Figure 7.6, with the charge increasing for all lengths up to the secondary injection point.

The pointing fluctuations of the beams shown in Figure 7.5, leading to electron en-

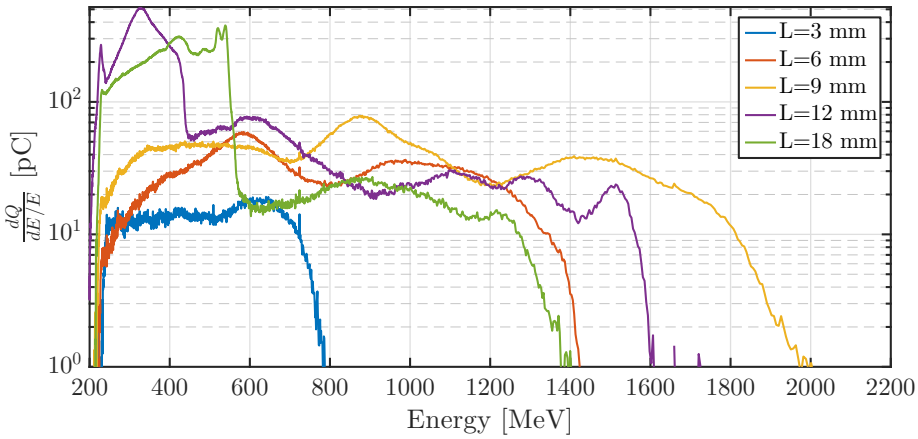

Figure 7.6: *Sample single-shot spectra measured with different length gas cells, for data scan plotted in Figure 7.5. Acceleration up to* $L = 9\,\mathrm{mm}$ *is seen, as is the secondary injection at* $L = 12\,\mathrm{mm}$.

ergy misreadings, were corrected by performing backtracking of similar beam features.[3] Due to distinct peaks not being present in all spectra, a cut-off energy was defined instead. This is taken as the point in the electron spectrum where the signal rises to a level of $5\sigma_n$ above the background; σ_n is the standard deviations of the noise at the highest energy end of the spectrometer. Further, to account for beam divergence, this cut-off was taken as the trajectory of an electron with an angle $-1\,\mathrm{mrad}$ to the backtracked pointing direction. This trajectory effectively defines the edge of the beam cone. In addition, the maximum energy of the secondary peak, where applicable secondary injection is seen, is calculated. Both of these are plotted as open circles of different colour in Panel (a) of Figure 7.7. Points that have been excluded from further analysis are plotted as red points.[4] The total beam charge, measured for $\mathcal{E} \gtrsim 200\,\mathrm{MeV}$, is plotted in Panel (b) and the high energy charge for electron energies $\mathcal{E} \gtrsim 950\,\mathrm{MeV}$ is depicted in Panel (c) of Figure 7.7.

The rapid increase in electron energy up to $L \simeq 10\,\mathrm{mm}$ is clearly evident, with the rate of acceleration seen to decrease with increasing length. Further, the total injected charge, plotted in Panel (b) in Figure 7.7, is increasing almost linearly with length up to $L \simeq 10\,\mathrm{mm}$, implying continuous injection into the wake. This fact is also clearly visible from the raw spectra shown in Figure 7.5. The integrated charge on spectrometer screen 2, plotted in Panel (c) in Figure 7.7, is also linearly increasing. The rate of injection can be estimated by performing a linear fit to the range of linear

[3] Cf. Section 3.3.1

[4] In general, shots where an electron beam was not produced, the laser energy was outside its expectation value or the gas pressure was wrong, are excluded from further analysis.

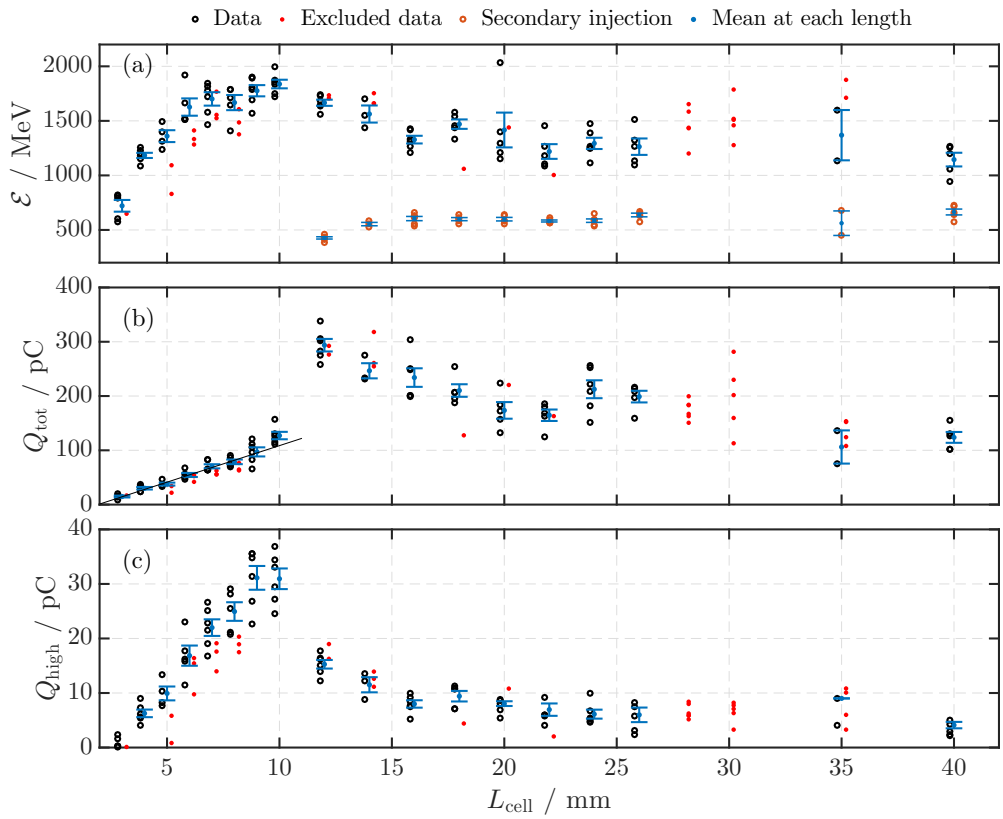

Figure 7.7: *Cuttoff energies and beam charge for the length scan shown in Figure 7.5. Panel (a) shows the cut-off energies, with the cut discussed in the main text; Panel (b) shows the total charge in the electron beam for energies $\mathcal{E} \gtrsim 200\,\mathrm{MeV}$ with the black line a linear fit to $L \leq 9\,\mathrm{mm}$; Panel (c) depicts the charge seen on the high energy spectrometer, with a cut of $\mathcal{E} \gtrsim 950\,\mathrm{MeV}$.*

charge increase, as shown by the black line in Figure 7.7. This yields a rate of injection of $\nu_i = (13.5 \pm 0.5)\,\mathrm{pC\,mm^{-1}}$ or $\nu_i = (8.4 \pm 0.3) \times 10^{10}\,\mathrm{m^{-1}}$. Thus 1.7×10^6 electrons are injected in a distance equal to one plasma wavelength. This is 2×10^{-5} of the total number of electrons in a volume of $\lambda_p w_0^2$. The fit also allows a calculation of the cell length where charge first reaches beyond 200 MeV as $L_i = (1.9 \pm 0.3)\,\mathrm{mm}$. Albeit not being the true injection position, with the rate of acceleration witnessed from Panel (a) in Figure 7.7, this still provides a good indication of injection location.

Secondary injection is observed at $L = 12\,\mathrm{mm}$, at much lower initial energies than the first bunch. The charge in the secondary bunch is as much as three times higher than in the first injected bunch. This electron bunch does not accelerate to high energies, though, and its maximum energy is capped with $\mathcal{E} \sim 600\,\mathrm{MeV}$. However, the energy of the first bunch stays relatively constant with distance for cell lengths longer than 16 mm, implying that no more acceleration is taking place. This is an indication of

pump depletion.

Interestingly, while the onset of secondary injection is seen to increase the total beam charge, it is also seen to reduce the amount of charge at highest energies. This sudden drop is witnessed in Panel (c) in Figure 7.7, with charge in the high energy part of the electron beam dropping by a factor of two. This is intriguing as just before secondary injection the rate of acceleration is seen to reduce slightly. However, with the previous dynamics being relatively smooth, this discontinuity is a sign of a sudden change of the bubble cavity.

It should also be emphasised here that this length scan was performed with about half of the total laser energy available, corresponding to a laser power of $\sim 125\,\mathrm{TW}$. This is less than half the power used in previous studies on this laser system, however, from Figure 7.7 it is clear that the electron energies are already greatly enhanced and reach as high as 2 GeV. Hence, employing a longer focussing optic has enabled the electron energies to be extended into the multi-GeV regime with a $P \simeq 125\,\mathrm{TW}$ laser.

The preceding data presentation and discussion shows the wealth of injection and acceleration dynamics observed from this length scan; these insights are all but lost for plasma density scans at a fixed plasma length. Further, the plasma upramp and laser power remain very much the same for all shots. This allows for the interpretation of the beam dynamics to be relatively straightforward.

Peak accelerating field measurements

The measurement of the maximum energy of electrons at multiple points during acceleration allows the accelerating electric field to be measured. In the 3D non-linear regime, the longitudinal field is linear with distance in the bubble:[5]

$$E(l) = E_p \left(1 - \frac{l}{L_{\mathrm{dph}}}\right), \quad 0 \leq l \leq 2L_{\mathrm{dph}}, \tag{7.2}$$

where E_p is the peak accelerating gradient at the rear of the bubble and L_{dph} is the dephasing length. Equation 7.2 assumes a longitudinally symmetric, fully cavitated bubble. As an electron gains energy in the bubble, its energy as a function of plasma length L is given by

$$\mathcal{E}(L) = \int_0^{L_a} E(l)\,\mathrm{d}l + \mathcal{E}_0, \tag{7.3}$$

where $\mathcal{E}_0$ is the initial energy of an electron, injected at the very back of the bubble. Here, $L_a \equiv L - x_{\mathrm{inj}}$ is the total acceleration length; it is assumed the electron is injected at a distance x_{inj} from the beginning of the plasma. Equation 7.2 along with Equation

[5] Cf. Section 2.5.1

7.3 implies that the electron achieves its peak energy after accelerating for a distance equal to $L_{\rm dph}$ and starts to lose energy with further propagation. Thus, for a given acceleration length L_a, the electron energy is given by[252]

$$\mathcal{E}_l = -\frac{E_p}{2L_{\rm dph}}L_a^2 + E_p L_a + \mathcal{E}_0. \tag{7.4}$$

As the injection point within the plasma is not exactly known, Equation 7.4 should be expressed in terms of plasma length L. We then obtain a quadratic equation

$$\mathcal{E}_l = aL^2 + bL + c, \tag{7.5}$$

where

$$a = -\frac{E_p}{2L_{\rm dph}}; \qquad b = E_p\left(1 + \frac{x_{\rm inj}}{L_{\rm dph}}\right); \qquad c = \mathcal{E}_0 - x_{\rm inj}E_p\left(1 + \frac{x_{\rm inj}}{2L_{\rm dph}}\right). \tag{7.6}$$

The coefficients a, b, c can be obtained from a quadratic fit to a dataset similar to that presented in Figure 7.7, Panel (a). As electron energies obtained here are of order of hundreds of megaelectronvolts, the injection energy $\mathcal{E}_0 \simeq \sqrt{n_c/n_e}m_e c^2 \sim \mathcal{O}(10\,\mathrm{MeV})$ can be neglected. With this assumption, the peak accelerating field, dephasing length and injection length can be found from the fit coefficients as

$$E_p = \left(b^2 - 4ac\right)^{1/2} \tag{7.7}$$

$$L_{\rm dph} = \frac{b - \left(b^2 - 4ac\right)^{1/2}}{2a} - \frac{b}{2a} \tag{7.8}$$

$$x_{\rm inj} = \frac{b - \left(b^2 - 4ac\right)^{1/2}}{2a} \tag{7.9}$$

Hence, by measuring the peak electron energy in a length scan and fitting a parabola to that data, the dephasing length, the peak accelerating field and the injection position can be obtained.

Different parabolic fits to the the dataset shown in Figure 7.5 are plotted in Figure 7.8. The datapoints are the average cut-off energy at each cell length, with the error-bars representing the standard error. The solid red line is a fit to both acceleration and deceleration parts of the length scan, i.e. using all data for cell lengths $L < 16\,\mathrm{mm}$. However, the bubble field is linear only up to an extent in the front half of the bubble. This is because cavitation does not occur instantaneously. Secondly, continuous injection into the wake means that even after dephasing has been reached by the highest energy electrons, there is a continuum of electrons with lower energies that have just

[252] D. E. Cardenas *et al*, *arXiv* , 2015.

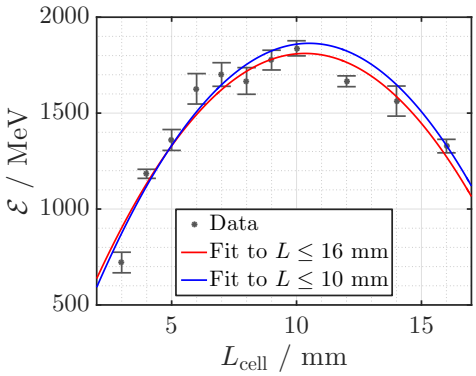

Figure 7.8: *Parabolic fit to maximum electron energy variation with gas cell length. The red line shows a fit to both accelerating and decelerating points on the graph whereas the blue is line fitted to points up to the peak energy.*

reached dephasing and so will accelerate up to the same maximum energy. This would then mean that instead of seeing a decline in maximum beam energy, a plateau should be observed. Hence, physically the data should observe a parabolic dependence on distance only up to the length where maximum beam energy is observed. With this in mind, fits were also performed by utilising data from cell lengths up to maximum energy gain, $L = 10\,\text{mm}$ for the dataset presented in Figure 7.7. This fit is plotted as the blue line in Figure 7.8.

Fitting was performed for multiple length scans, encompassing a range of plasma densities and laser intensities. A summary of the calculated peak electric fields, dephasing lengths and injection positions is presented in Table 7.1. Shown here are the results from fits to all of the datapoints and data for the acceleration portion only, which is physically relevant. Results from the former are presented for comparison reasons only. Peak electric fields of hundreds of $\text{GV}\,\text{m}^{-1}$ are measured for all scans, with the highest value of $E_z = (570 \pm 190)\,\text{GV}\,\text{m}^{-1}$ measured.

a_0	n_e $10^{18}\,\text{cm}^{-3}$	E_{peak} GV/m		L_{dph} mm		x_{inj} mm	
		Acc only	All	Acc only	All	Acc only	All
1.8	1.6	113 ± 4	124 ± 15	34.4 ± 1.6	30.0 ± 5.6	1.6 ± 3.1	2.3 ± 11.0
1.4	2.3	362 ± 27	349 ± 39	10.3 ± 1.0	10.4 ± 1.7	0.2 ± 2.0	0.0 ± 3.2
1.4	2.6	339 ± 49	336 ± 62	9.7 ± 1.9	9.6 ± 2.4	-0.2 ± 3.6	-0.4 ± 4.7
1.8	2.6	299 ± 15	284 ± 24	12.0 ± 0.8	12.6 ± 1.6	1.0 ± 1.5	0.9 ± 3.2
1.4	3.2	570 ± 190	540 ± 200	5.6 ± 2.4	5.8 ± 2.7	0.9 ± 4.3	0.6 ± 5.1

Table 7.1: *Summary of the calculated peak electric field, dephasing length and injection position for five different length scans. The errors quoted here are 1σ confidence bounds.*

The errors quoted in Table 7.1 are for the 1σ confidence bound. The calculated errors for the injection position x_{inj} are seen to be extremely large. The source for such large errors for x_{inj} is that the lowest electron maximum energy used in the fit is $\sim 600\,\mathrm{MeV}$, meaning there are no points to constrain the fit near the lower energies. This leads to large uncertainties in the value for the injection location. Indeed, injection $200\,\mu\mathrm{m}$ before the start of the plasma is calculated for one dataset. In most cases, though, injection is predicted to happen very close to the start of the plasma.

The peak electric fields and dephasing lengths calculated from the fits up to the maximum energy are plotted against plasma density in Figures 7.9a and 7.9b, respectively. Also plotted in Figure 7.9a as the red dashed line is the cold wavebreaking field, given by Equation 2.29. Larger peak fields are observed with increasing plasma density, as intuitively expected. Also, the peak electric field is measured to be larger than the cold wavebreaking field, as suggested by 3D non-linear theory. The dashed red line in

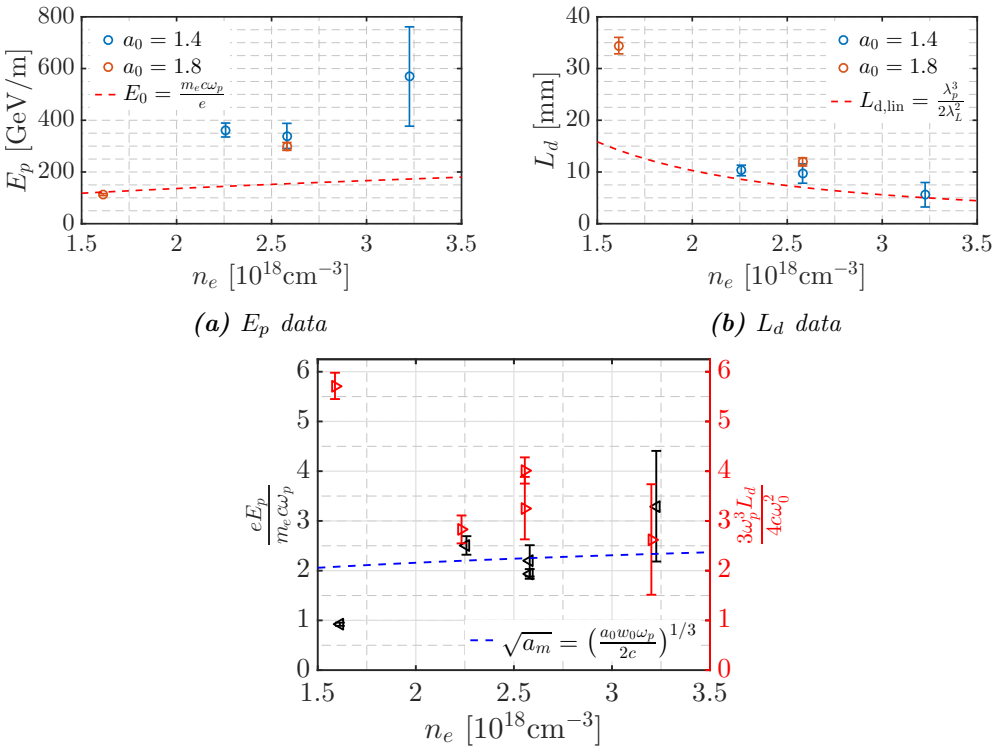

(a) E_p *data*

(b) L_d *data*

(c) Data normalised to yield $\sqrt{a_0}$

Figure 7.9: *The calculated values of peak electric field, Panel (a), and dephasing length, Panel (b), as a function of plasma density. Panel (c) show the values of* $\sqrt{a_0}$*, as obtained from the peak accelerating field and dephasing data by rearranging the respective expressions in the 3D non-linear regime, along with 3D scaling for the matched* a_0*.*

Figure 7.9b is the linear dephasing length. Again, the qualitative behaviour of the data follows the general inverse plasma density scaling.

In the 3D non-linear regime, the peak accelerating field scales as $E_p = \sqrt{a_0}E_0$ and the dephasing length is given by

$$L_D = \frac{4c\omega_L^2}{3\omega_p^3}\sqrt{a_0}. \tag{7.10}$$

Both of these expressions can be rearranged to yield an "expected" value of $\sqrt{a_0}$ from the experimental data. The measured peak electric field and dephasing data, normalised by the aforementioned equations, are plotted in Figure 7.9c. Also shown is the 3D non-linear scaling for a_0 with a matched spot size, given by Equation 2.76, calculated assuming $a_0 = 1.8$ and $w_0 = 42\,\mu\text{m}$.

The first thing to note is that the results from the length scan performed at the lowest plasma density of $n_e = 1.5 \times 10^{18}\,\text{cm}^{-3}$ exhibit large disparity from other data-points. The electric field measurement predicts $a_0 \sim 1$, whereas the dephasing length is much longer then predicted, yielding $\sqrt{a_0} \simeq 5.5$. The measured electric field value implies much less intensity amplification, thus putting into question the validity of the 3D non-linear regime treatment. This implies that the physics differs from a quasi-static bubble in the fully cavitated regime, with electron rephasing or quasi-linear mode of operation perhaps resulting in extended interaction lengths.

The other scans predict focussed intensities that are in excess of the matched scaling. However, the scaling ignores self-compression and thus higher values for a_0 should in fact be observed. On average, the data suggests a self-focussed normalised vector potential of $a_0 \simeq 9$. The literature suggests a minimum of $a_0 \simeq 4$ for self-injection to occur; indeed Equation 2.82 yields $a_0 > 5.3$ for $n_e = 2.3 \times 10^{18}\,\text{cm}^{-3}$. The measured values for $\sqrt{a_0}$ are clearly in excess of these threshold suggesting self-injection must indeed be seen. The value of $\sqrt{a_0}$ obtained from the experimental data also shows a general trend of slow increase with plasma density, once again in agreement with increased self-focussing rates at higher number densities.

7.3.2 High laser energy length scan

A length scan was also performed at a lower plasma density with higher laser energy. The plasma density was measured to be $n_e = 1.8 \times 10^{18}\,\text{cm}^{-3}$ with the laser energy delivered on target $E_L = (9.8 \pm 0.2)\,\text{J}$, where the error bars are standard deviations. These laser energies yield a normalised vector potential of $a_0 = 1.8$ and a laser power of $P_L \simeq 215\,\text{TW}$. The cell length was varied in steps of 4 mm between 12 mm and 40 mm.

Figure 7.10 depicts the results from this length scan. Each panel depicts the three

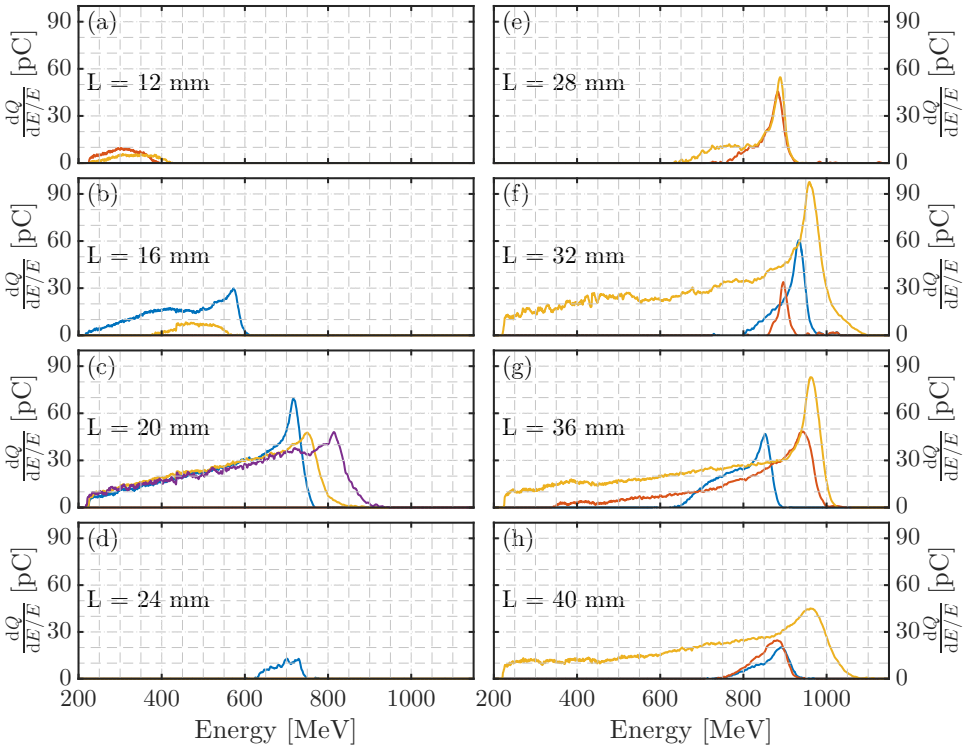

Figure 7.10: *Single shot spectra taken at different gas cell lengths with increased laser energy and* $n_e = 1.8 \times 10^{18}\,\mathrm{cm}^{-3}$. *Each panel shows all shots taken at a particular gas cell length; the y axis limits are common to all panels.*

shots that were taken at each gas cell length. For gas cell lengths shorter than $L = 12\,\mathrm{mm}$ no electron beam was observed. The electron beam energy is seen to increase with cell length up to $L = 32\,\mathrm{mm}$, after which no further energy gain is seen. However, the most striking feature of the scan is the production of quasi-monoenergetic electron beams. The energy spectrum is seen to become more peaked as cell length is increased, reducing the absolute energy spread. In most cases a low energy tail, so called "dark-current", is also observed, even for longer gas cell lengths. However, some shots exhibit no such features and yield a purely monoenergetic energy spectrum.

This is further illustrated in Figure 7.11 showing the measured energy of the peak in the spectrum, the relative energy spread $\Delta\mathcal{E}/\mathcal{E}$ and the total beam charge. The errors in the peak energy are of the order of 1% and thus not plotted for clarity. The dashed lines are visual guides highlighting the change of peak energy and relative energy spread and are not fits to the data. The energy spread $\Delta\mathcal{E}$ is the full-width-half-maximum. An increase of peak energy with gas cell length is witnessed, with maximum energy of $\mathcal{E} \simeq 900\,\mathrm{MeV}$ reached for $L > 30\,\mathrm{mm}$. The evolution of the relative energy spread

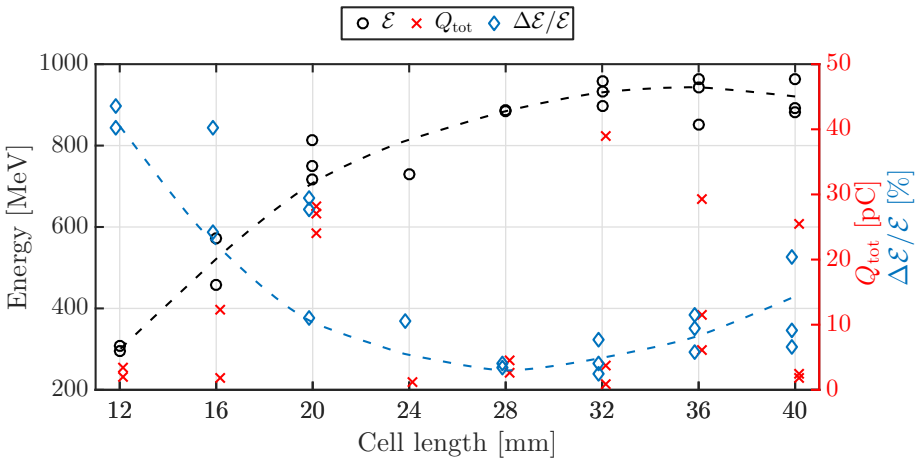

Figure 7.11: *The peak energy, beam charge and relative energy spread as a function of gas cell length for* $n_e = 1.7 \times 10^{18}\,\text{cm}^{-3}$. *The dashed lines are visual guides and not fits to the data.*

is seen to exhibit a steady decrease with cell length. A minimum in energy spread is reached at $L \simeq 30\,\text{mm}$. The narrowing of the energy spread is consistent with phase space rotation of a broader energy spread beam. This is a process whereby an initially large energy spread narrows as the electrons in the front of the bunch reach dephasing and start to lose energy. With the tail of the bunch still gaining energy, the bunch becomes compressed and the energy spread is reduced. Crucially, the monoenergetic beams clearly result from one injection event, in start contrast to results presented in the previous section where large energy spreads implying continuous were seen. The physics leading to this difference is discussed later on.

The narrowest energy spread is measured for shot 3 at $L = 32\,\text{mm}$, with a central energy of $\mathcal{E} = (896 \pm 10)\,\text{MeV}$ and an energy spread of $\Delta\mathcal{E} = 22\,\text{MeV}$; this gives a relative energy spread of $\Delta\mathcal{E}/\mathcal{E} = 2.4\%$. We also see that at $L = 28\,\text{mm}$, two shots yield a spectra with a quasi-monoenergetic spectrum, with an energy spread of 3% and average charge 3.6 pC. The average beam charge for shots with $\Delta\mathcal{E}/\mathcal{E} < 10\%$ is $\langle Q \rangle = (8.3 \pm 4.0)\,\text{pC}$.

7.3.3 Simulations

The length scans presented earlier uncover a wealth of acceleration and injection dynamics. Most of the observed trends and phenomena can be explained by invoking descriptions of dephasing and laser evolution, thus providing a qualitative understanding of the accelerator. In order to further understand the physics involved, a large scale simulation campaign is currently under way. However, as the spatial wavefront of the laser is not known, exactly reproducing the experiment in simulations is very

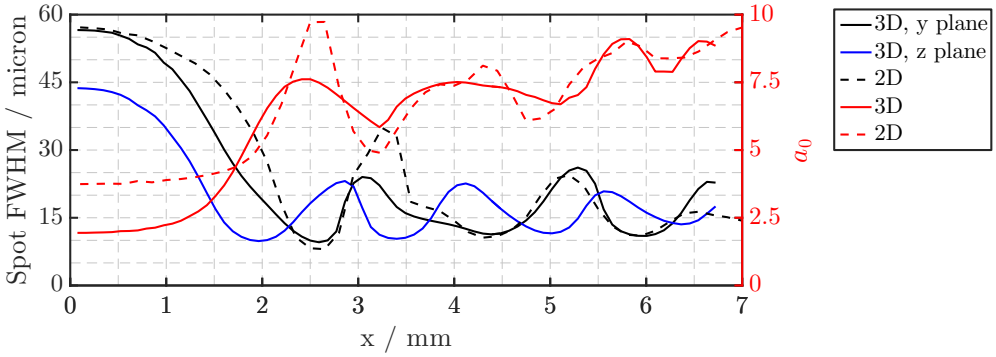

Figure 7.12: *Laser evolution in 3D simulation, showing the asymmetric self-focussing of the laser pulse. Also shown are scaled 2D simulations, yielding agreement with 3D laser dynamics.*

difficult. As such, the simulation campaign is focussing on reproducing and studying the phenomenology of the interaction, employing 2D and 3D simulations.

Figure 7.12 presents results from a 3D simulation, performed with number density $n_e = 3 \times 10^{18}\,\mathrm{cm}^{-3}$, $a_0 = 2$, $\tau_{\mathrm{FWHM}} = 45\,\mathrm{fs}$, $w_{0,y} = 48\,\mu\mathrm{m}$ and $w_{0,z} = 36\,\mu\mathrm{m}$. The density profile consisted of a 0.5 mm linear ramp followed by a plateau region. The resolution was $k_L \Delta x = 0.21$ and $k_p \Delta y = k_p \Delta z = 0.13$. Figure 7.12 depicts the evolution of the laser spot size in transverse planes along with the intensity evolution. The spot size is found by integrating along the time axis in the y and z planes. The initial focal spot asymmetry is seen to persist throughout the laser evolution, with self-focussing occurring in anti-phase between the planes. This leads to very asymmetric evolution of the plasma cavity as well. Interestingly, the laser spot size oscillations being almost $\pi/2$ out of phase mean that the laser intensity is seen to stay relatively constant, even as the spot size in either plane varies. This interesting phenomenon could potentially be diagnosed in future experiments by employing a short enough probe pulse.[74]

The laser intensity is seen to undergo severe self-focussing, reaching intensities as high as $a_0 \sim 7.5$ after 2.5 mm of propagation and $a_0 \sim 9$ by $x = 6.5\,\mathrm{mm}$. Note the value of a_0 quoted here is using a fixed value of $\lambda_L = 800\,\mathrm{nm}$, thus not accounting for spectral changes to the laser. The self-focussed values of a_0 seen in the simulations are in reasonable agreement with experimentally measured values for $\sqrt{a_0} \simeq 3$.

It is well known that self-focussing behaviour in 2D and 3D simulations is fundamentally different, as in 2D the total laser power is proportional to $a_0^2 w_0$ whereas in 3D it scales as $a_0^2 w_0^2$.[235] Thus starting from the same laser spot size and intensity equivalent results can not be obtained. However, if we require the same initial spot size in a 2D simulation to yield the same self-focussed intensity and spot size as in 3D, a simple

[74] A. Sävert *et al*, *Phys Rev Lett* **115**, 2015.
[235] F. S. Tsung *et al*, *Phys Plasmas* **13**, 2006.

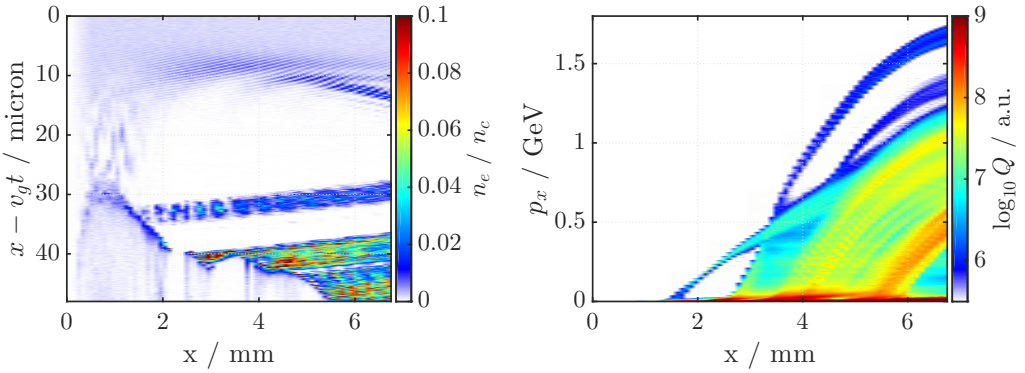

(a) Bubble evolution *(b) Electron energy evolution*

Figure 7.13: *Bubble evolution and electron beam energy evolution in the 3D simulation. Panel (a) shows the evolution of the axial plasma density while the spectrum of accelerated electrons as a function of propagation distance is plotted in Panel (b).*

scaling to increase the initial intensity (and thus power) can be found. Rearranging the equations for laser power in 2D and 3D yields the $a_0^{\mathrm{2D}} = a_f^{\mathrm{2D}}(a_0^{\mathrm{3D}}/a_f^{\mathrm{3D}})^{1/2}$. Thus, requiring an initial $a_0 = 2$ to self-focus to $a_f = 7$ gives $a_0^{\mathrm{2D}} = 3.74$. Results from a 2D simulation with this a_0 and $w_{\mathrm{FWHM}} = 58\,\mu\mathrm{m}$ are plotted as the dashed lines in Figure 7.12. The imposed restriction of the 2D simulation to match intensity of the 3D run is seen to occur at $x \simeq 2.4\,\mathrm{mm}$, with the spot sizes being of equal size at that distance as well. Additionally, remarkably similar evolution of the 2D spot size is seen when comparing to one plane of the 3D simulation, with the self-focussing oscillations accurately reproduced. The laser intensity is seen to evolve similarly as well.

The plasma response and electron beam evolution is presented in Figure 7.13. Figure 7.13a depicts the axial plasma density as a function of propagation distance x, highlighting the bubble evolution. Almost immediately after full cavitation an injection event is seen. This is seen to occur during the initial self-focussing of the laser and the associated bubble expansion. This initial trapping is followed by more bubble elongation. At $x \simeq 3\,\mathrm{mm}$ a secondary, continuous injection is seen to begin. A small fraction of electrons injected here accelerate to very high energies of nearly 2 GeV, as evidenced from Figure 7.13b. After this a short bubble contraction is seen, with the bubble starting to again elongate after $x \simeq 3.5\,\mathrm{mm}$. An asymmetry in the electron spectrum is also evident, with much more charge concentrated in the low energies.

The simulation data allows to probe the injection physics by studying the correlation between injected charge, bubble size and laser intensity. These three curves are plotted in Figure 7.14, with the laser intensity shown as the red line, the phase velocity of the back of the bubble γ_b as the black circles and the injected charge is the blue line. The

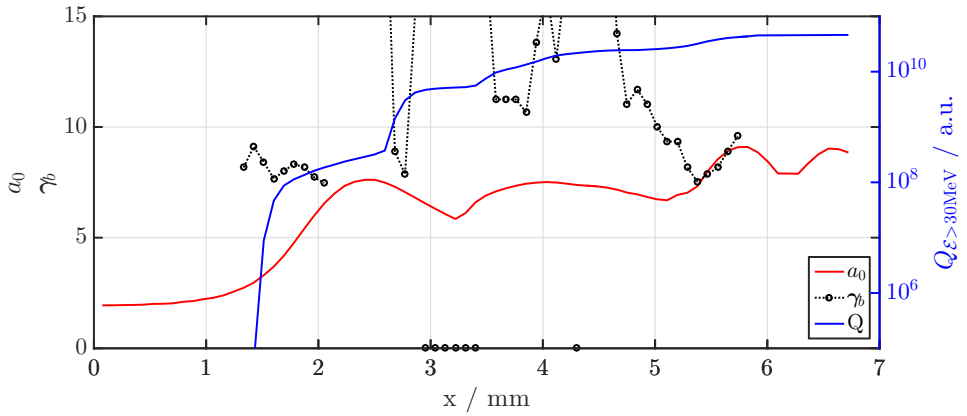

Figure 7.14: *Results from the 3D simulation, showing the laser intensity a_0, total injected bunch charge Q and the gamma factor of the phase velocity of the rear of the bubble γ_b.*

data for γ_b is noisy due to difficulties in determining the position of the rear of the bubble. Electrons are deemed injected if their longitudinal momentum is $p_x > 30\,\mathrm{MeV}$. As can be seen, the first injection event occurs at $x \simeq 1.5\,\mathrm{mm}$. This in the initial self-focussing region of the laser. The bubble is also observed to expand over this period and the change of rate of bubble expansion is seen to terminate the injection. This leads to localised injection, as evidenced in Figure 7.13b.

The second injection event is observed at $x \simeq 2.7\,\mathrm{mm}$. Here, the laser intensity is somewhat decreasing but the rear of the bubble is seen to be slowing, signifying bubble expansion. The expansion terminates very quickly, as seen from Figure 7.14 and also from Figure 7.13a, and leads to injection stopping. The laser intensity is seen to start increasing again after $x \simeq 3.3\,\mathrm{mm}$. A third injection event, the start of continuous injection, is observed at $x \simeq 3.5\,\mathrm{mm}$, almost immediately after the start of laser intensity increase. The bubble is still quite transient, with the rear of the bubble seen to contract somewhat in Figure 7.13a before starting to expand continuously. This is accompanied by the laser intensity staying relatively constant.

While the 3D simulation discussed above is performed at a plasma density that is higher than the scan yielding monoenergetic electron beams,[6] the isolated injection event occurring at $x \simeq 1.5\,\mathrm{mm}$ is still relevant in explaining the narrow energy spread beams. The limited phase space volume of the injected bunch means that phase space rotation can yield very narrow energy spreads. These results can thus only be obtained if the subsequent injection events are suppressed. With a lowered plasma density, the self-focussing and self-compression evolution is slower, which can lead to suppression

[6] Cf. Section 7.3.2

of the later injection events.

7.3.4 Discussion

More simulations are currently being performed to extend the study up to longer plasma lengths, along with enabling explicit tracking of injected electrons to determine their initial positions. The laser energy depletion will be studied to understand how this affects the final phases of acceleration. Additionally, simulations with lower plasma densities will be performed to understand the generation of monoenergetic electron beams.[7]

With more conclusive verification of acceleration and injection dynamics still to be performed, qualitative explanations for the observed behaviour can be put forward. Due to continuous injection into the wake, the maximum energy of the beam should plateau with increasing length after dephasing has been reached. The fact this is not observed in experiments indicates that the rollover in maximum electron energy is caused by another effect. It is known that to achieve self-injection the pulse must self-focus and compress. It is also observed from simulations that severe bubble elongation occurs at the same time as self-injection. As the bubble elongates, the point at which the longitudinal electric field reverses sign moves further towards the bubble rear. Thus, with a bunch of electrons residing in a phase close to dephasing, bubble elongation causes all those electrons to find themselves in a decelerating field. This would suddenly reduce the charge of electrons with highest energies, and also reduce the total available energy gain. The concurrence of secondary injection and maximum energy rollover seen in Figure 7.7 lends support to this hypothesis, as secondary injection is often caused by bubble elongation. This is further supported by the fact that a large sudden decrease in high energy charge is seen at the same gas lengths as secondary injection.

The generation of electron beams with nearly 2 GeV peak energy marks a new record for 125 TW lasers.[8] However, the fact that self-injection is observed for lasers with $a_0 \sim 1.4$ in only 3 mm of $n_e \sim 2 \times 10^{18}\,\mathrm{cm}^{-3}$ plasma does not fit with previous work. A successful semi-empirical model put forward by Mangles *et al*[120] allows the minimum energy in the central spot required for self-injection to be calculated. This model requires a minimum of 9 J in the central FWHM of the spot to guarantee self-trapping in 3 mm at $n_e = 2.3 \times 10^{18}\,\mathrm{cm}^{-3}$. This is greatly exceeding the total energy delivered on target. The failure of this model in the present case arises from the fact that it explicitly relies on a power threshold, thus neglecting self-focussing and only

[7] Cf Section 7.3.2 and Figure 7.11

[8] Cf. Discussion in Section 7.4 on page 211

[120] S. P. D. Mangles *et al*, *Phys Rev Spec Top-Ac* **15**, 2012.

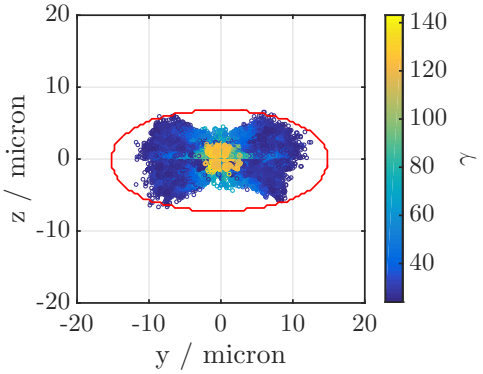

Figure 7.15: *Initial positions of particles injected in the first injection event. The colour bar corresponds to the particle energy; the red contour if the FWHM outline of the laser transverse intensity profile.*

accounting for self-compression.

A different injection mechanism to the most often observed transverse wave breaking is so-called longitudinal injection. Observed in simulations and then experimentally,[253] this trapping differs significantly from transverse self-injection. Longitudinal injection is seen to occur very early in the interaction, when a grossly mismatched laser spot is still very large and electrons near the laser axis feel a reduced ponderomotive force, thus streaming through the laser pulse. These are then trapped near the rear of a rapidly forming bubble and accelerated. Secondary, transverse self-injection is observed later in the interaction, after the pulse has sufficiently self-focussed and compressed. However, transverse self-injection is measured to produce more than an order of magnitude more charge than longitudinal injection. Additionally, longitudinal injection is very quickly terminated as it relies on a very large spot being mismatched to the plasma wave. Thus, this method is not seen to describe the initial injection seen in the data.

The latter claim also agrees with simulation results. Presented in Figure 7.15 are the transverse positions of electrons with $\gamma > \gamma_p$. These electrons are trapped, with the colour axis representing their total energy. A large degree of asymmetry is seen, with most trapped electrons being injected along the y-plane. This asymmetry closely follows the shape of the laser, the red contour showing the FWHM extent of the transverse intensity profile. This shows that the electrons have large transverse positions at injection, thus not having streamed through the bubble as predicted by longitudinal injection.

The generation of quasi-monoenergetic electron beams was observed at a lowered plasma density and increased laser power. It is observed from Figure 7.11 that the

[253] S Corde *et al*, *Nat Comms* **4**, 2013.

monoenergetic beamlet initially has a much larger energy spread and $\Delta\mathcal{E}/\mathcal{E}$ reduces with increased plasma lengths. This kind of behaviour implies phase space rotation. Additionally, though, the fact that such a monoenergetic beam can be produced means that injection into the wake must be a localised event. Indeed, from Figure 7.10 it is clear that even at shorter plasma lengths the energy spectrum is not continuous.

From the simulations presented above, and particularly from Figure 7.13b, we observe a very localised injection event early in the interaction. This can be seen to be the source of the monoenergetic beams. However, the limited energy spread also means that the subsequent injection events have been suppressed. This can be seen as a consequence of operating at lowered plasma densities, where self-focussing and self-compression occur at slower rates.

The peak energy of the monoenergetic beams never exceeds 1 GeV, meaning that a lower energy gain is observed with higher laser powers. Whilst perplexing, the simulation results presented in Figure 7.13a provide an explanation for this. Namely, after the first injection event early in the interaction the bubble is seen to continuously expand. In the lowered plasma density case, this proceeds slowly enough as to not lead to more injection events. It does mean, however, that the initially injected bunch finds itself in a phase of the wake that is much closer to the centre of the bubble where the longitudinal field vanishes. Hence, the bubble evolution effectively dephases the electron bunch and thus reduces the available energy gain. It should be noted that such a rephasing of the bunch also creates the necessary conditions for phase space rotation as it places the electron beam near the position where the accelerating field reverses sign.

The 3D simulations are seen to predict a peak intensity of $a_0 \simeq 8$ and that it stays relatively constant throughout the interaction, as seen from Figure 7.12. This value is in reasonable agreement with the value for $\sqrt{a_0}$ derived from the experimentally measured electric fields and dephasing lengths presented in Figure 7.9. A slow increase of a_0 with plasma density is observed from the data, which will be confirmed with further 3D simulations at different plasma densities.

Finally, from the above regarding the generation of monoenergetic electron beams and the discussion about secondary injection we see that bubble evolution plays an extremely important role in explaining the observed phenomena. The detailed length scans performed at a fixed plasma density provide a unique opportunity to examine the dynamics of electron beam acceleration and injection and allowed for the identification of the bubble evolution features, with the findings being supported by PIC modelling.

7.4 Plasma density scans

7.4.1 High laser energy scans

The two crucial parameters determining the properties of an accelerated electron beam in laser wakefield accelerators are the plasma density and length. Scans with varying accelerator distance were presented in the preceding section, with $\sim 125\,\mathrm{TW}$ laser enabling acceleration up to nearly $2\,\mathrm{GeV}$ and monoenergetic electron beams observed at lower plasma densities and higher laser energies. However, most of these scans performed at fixed plasma density and it is important to optimise the plasma density as well.

Plasma density was scanned under the optimum laser parameters, delivering a peak energy of $11\,\mathrm{J}$ on target. This was the highest intensity achieved during the experimental campaign, corresponding to a peak normalised vector potential of $a_0 = 1.8$ and a laser power of $P_L \simeq 240\,\mathrm{TW}$. Plasma density was varied in the range of $1.6 \times 10^{18}\,\mathrm{cm}^{-3} < n_e < 3.3 \times 10^{18}\,\mathrm{cm}^{-3}$. Raw electron spectrometer data taken at different plasma densities is shown in Figure 7.16. Electron beam energy increases vertically; the non-linear dispersion arising from the magnetic spectrometer again causes bunching near the higher energies. The horizontal dimension is proportional to beam

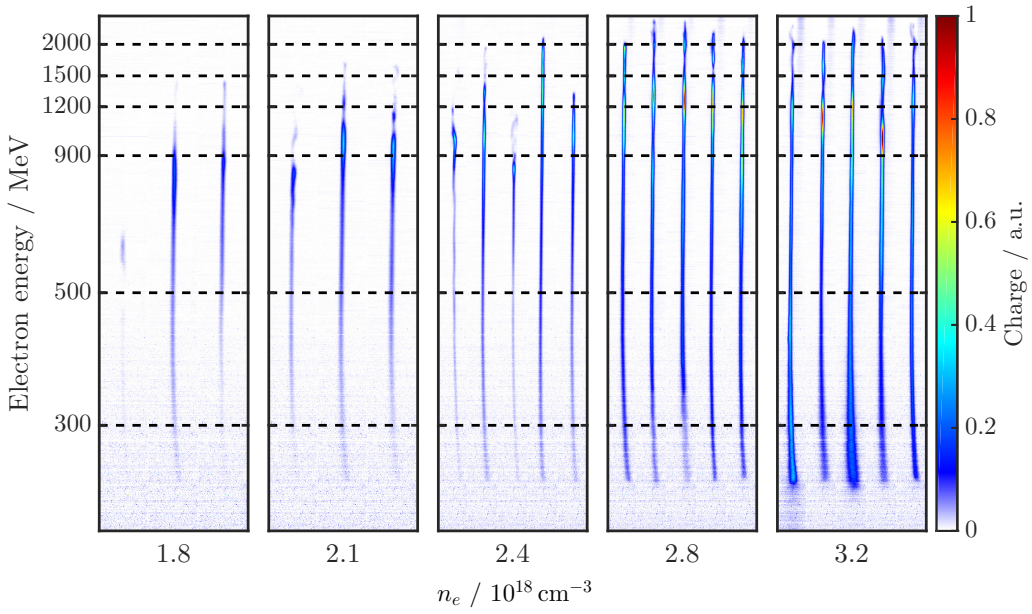

Figure 7.16: *Raw electron spectrometer data for the high laser energy pressure scan with gas cell length of 20 mm.*

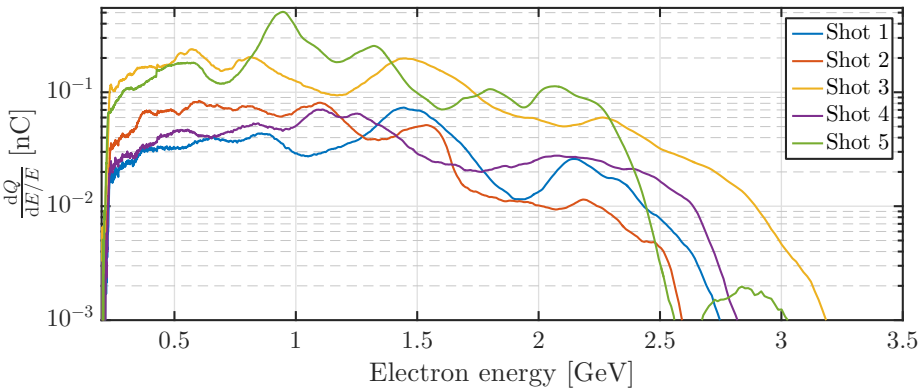

Figure 7.17: *Single shot electron spectra for the highest electron energies obtained.*

Shot	$\mathcal{E}_L$ J	Beam charge pC			Beam energy mJ		
		> 2 GeV	> 1 GeV	> 0.25 GeV	> 2 GeV	> 1 GeV	> 0.25 GeV
1	11.29	4.4	31.0	77.5	9.9	47.5	73.6
2	11.31	2.0	31.5	122.2	4.5	42.8	93.4
3	11.42	14.9	98.9	343.4	34.8	154.2	286.3
4	11.31	6.4	35.7	92.1	14.6	53.6	85.7
5	11.31	15.2	127.8	373.9	33.0	182.1	335.1

Table 7.2: *Beam parameters for shots presented in Figure 7.17, showing the beam charge and energy in different electron energy bins.*

divergence. An increase in maximum energy is evident with rising plasma density, up to a maximum at $n_e = 2.8 \times 10^{18}\,\mathrm{cm}^{-3}$. After that the electron beam energy stops its increase and instead a much larger divergence beam at lower energies is observed. A greater amount of charge is observed with increased plasma density as well. Interestingly, at the lowest plasma densities a low charge quasi-monoenergetic electron beam is observed. The conditions leading to this were discussed in the preceding sections.[9]

The variation of peak energy with plasma density witnessed in Figure 7.16 is counter-intuitive. Instead of a ${n_e}^{-1}$ scaling the cut-off energy raises with increasing plasma density. The maximum electron energy peaks at $n_e \simeq 3 \times 10^{18}\,\mathrm{cm}^{-3}$ and rolls over for higher densities. The initial rise of electron energy with plasma density is caused by two effects. Firstly, injection will be occurring earlier in the interaction as the plasma density increases, due to faster self-focussing and compression of the pulse. Secondly, at lower plasma densities the accelerating field will be smaller. The reason

[9] Cf. Section 7.3.2 and Section 7.3.3

for this is twofold: a_0 will be smaller at a lower plasma density supporting a larger matched spot size and the electric field scales as $E_z \propto \sqrt{a_0 n_e}$. Thus, the total energy gain is limited as the target length is fixed.

Spectra for single shots taken at the conditions yielding the highest energy electron beams are plotted in Figure 7.17. All these shots have been backtracked to correct for pointing variations of the electron beam. A large shot-to-shot variability is evident, however, the beams always reach multi-GeV energies. The amount of charge and energy above 2 GeV, 1 GeV and 0.25 GeV are shown in Table 7.2. As can be seen, a significant fraction of the beam charge is in electrons with energies beyond 2 GeV, with up to a tenth of the total beam energy in that part of the spectrum. Thus these results represent a truly multi-gigaelectronvolt laser wakefield accelerator. Also, these beam energies represent the highest recorded electron energies in the self-guided, self-injection regime of laser wakefield accelerators for laser power below 1 PW.

7.4.2 Low laser energy scans

Datasets were taken with a slightly reduced laser energy by scanning plasma density for three gas cell lengths. The energy delivered on target was $\mathcal{E}_L = (9.5 \pm 0.3)$ J and the gas cell lengths used for density scans were 10 mm, 15 mm and 30 mm. By exploring the dynamics of electron beams with varying plasma densities at different gas cell lengths more can be learned about acceleration limitations and injection.

Plotted in Figure 7.18 are the results for this dataset: the total beam charge ($\mathcal{E} \gtrsim 200$ MeV) is shown in Panel (a), the high energy charge for energies $\mathcal{E} \gtrsim 900$ MeV is depicted in Panel (b) and finally the cut-off energies are shown in Panel (c). All errors shown are standard errors in the mean. As evidenced from the total injected charge shown in Figure 7.18a, self-injection occurs at the same plasma density for all gas cell lengths. This is in agreement with the intuitive and indeed quantitative picture, as self-focussing and compression are functions of plasma density only. Additionally, this observation demonstrates unambiguously the threshold plasma density for injection, $n_{th} = 1.6 \times 10^{18}\,\mathrm{cm}^{-3}$. This is because if further pulse evolution were to lead to trapping, self-injection at lower plasma densities would be observed for $L_{\mathrm{cell}} = 30$ mm than for $L_{\mathrm{cell}} = 10$ mm. As plasma density is increased beyond $4.5 \times 10^{18}\,\mathrm{cm}^{-3}$, a rollover in total charge is seen, with total beam charge reducing. For highest plasma densities an increase of total charge is observed; however the electron beams observed at these densities are severely modulated and very filamented. Similarly to data presented in previous sections, charge is seen to initially increase with increasing plasma density.[10] Multiple density scans at various cell lengths all imply continuous injection.

[10] Cf Section 7.3.

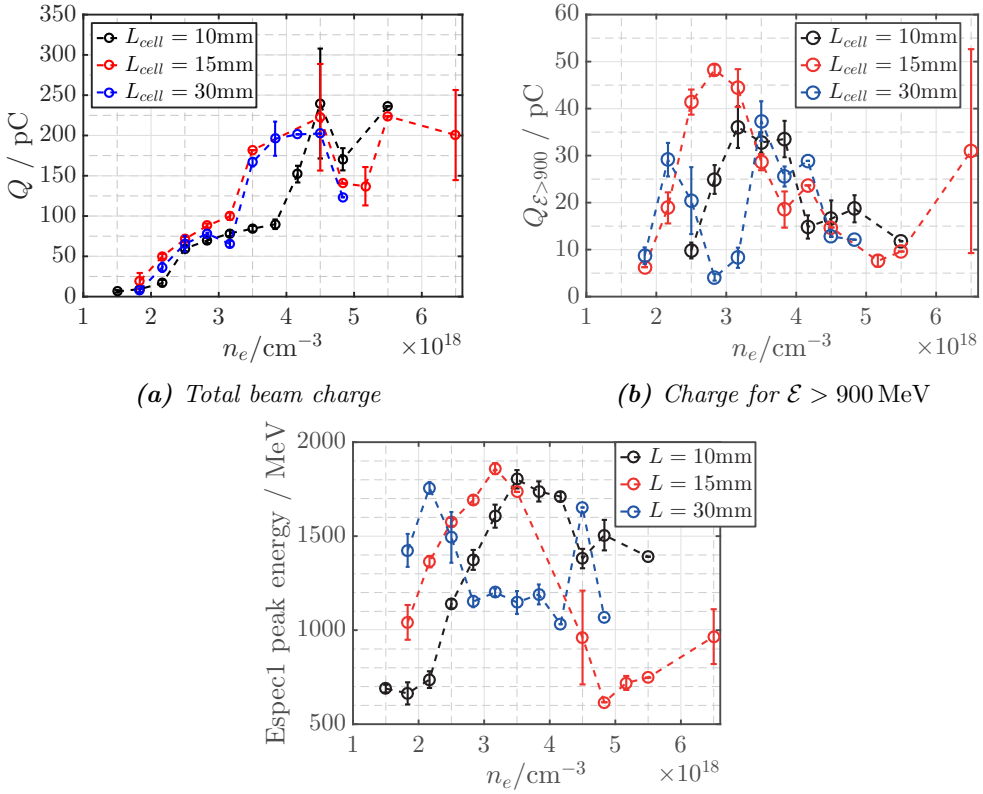

(a) Total beam charge

(b) Charge for $\mathcal{E} > 900$ MeV

(c) Maximum electron energies

Figure 7.18: *Results from plasma density scans at different gas cell lengths: (a) shows the total beam charge for electrons with energies $\mathcal{E} \gtrsim 200$ MeV; (b) shows the charge above $\mathcal{E} > 900 MeV$; (c) depicts the electron beam cut-off energies.*

A rapid rise in injected charge is seen for the longer cell lengths in Figure 7.18a, once plasma density increases beyond $3.2 \times 10^{18}\,\mathrm{cm}^{-3}$. This signifies the occurrence of secondary injection, discussed previously in Section 7.3.1. The fact that the shortest gas cell deviates from this trend is important, as it implies that the extra charge injection happens at a length $10\,\mathrm{mm} < L_i < 15\,\mathrm{mm}$. Indeed, the extra injection event is eventually seen for the 10 mm gas cell length as well, but only when plasma density is increased to $n_e \gtrsim 4 \times 10^{18}\,\mathrm{cm}^{-3}$. This agrees with data presented in Figure 7.7, showing secondary injection having happened at $L = 12\,\mathrm{mm}$. Additionally, it is observed that for all length scans performed with $2.3 \times 10^{18}\,\mathrm{cm}^{-3} \leq n_e \leq 3.3 \times 10^{18}\,\mathrm{cm}^{-3}$, secondary injection is always observed at $L \simeq 12\,\mathrm{mm}$.[254] Additionally, for $L_{\mathrm{cell}} = 10\,\mathrm{mm}$ the total injected charge is seen to stay relatively constant for $n_e \gtrsim 3 \times 10^{18}\,\mathrm{cm}^{-3}$. This means

[254] J. C. Wood. "Betatron radiation from laser wakefield accelerators and its applications". Imperial College London, 2016.

that injection rate has slowed considerably.

The secondary injection observations allow one to ascertain two things. Firstly, the observation of secondary injection with cell length $L_{\text{cell}} = 15\,\text{mm}$ at $n_e \simeq 3.2 \times 10^{18}\,\text{cm}^{-3}$ and no secondary injection for $L_{\text{cell}} = 10\,\text{mm}$ at the same plasma density means that secondary injection occurs between 10 mm and 15 mm. Secondly, a lower limit of $L_{\text{dpl}} \gtrsim 15\,\text{mm}$ can be set to pump depletion length at $n_e = 3.3 \times 10^{18}\,\text{cm}^{-3}$, as the secondary injection event seen at this density is caused by laser evolution. By following the same argumentation, it allows to set a lower limit of $L_{\text{dpl}} \gtrsim 10\,\text{mm}$ for the pump depletion length at $n_e \simeq 4 \times 10^{18}\,\text{cm}^{-3}$. This is again because secondary injection, driven by laser evolution, is observed at $n_e \simeq 4 \times 10^{18}\,\text{cm}^{-3}$ for $L_{\text{cell}} = 10\,\text{mm}$. The theoretical values for pump depletion, given by Equation 2.71 for a $\tau = 45\,\text{fs}$ pulse, are $L_{\text{dpl}} = 7.1\,\text{mm}$ at $n_e \simeq 3.3 \times 10^{18}\,\text{cm}^{-3}$ and $L_{\text{dpl}} = 5.9\,\text{mm}$ at $n_e \simeq 4 \times 10^{18}\,\text{cm}^{-3}$. Thus the theoretical values for the pump depletion length are seen to be underestimates.

The total amount of high energy charge, plotted in Figure 7.18b, is seen to initially increase linearly for all gas cell lengths. However, higher plasma densities are required to gain energies in excess of 1 GeV for $L_{\text{cell}} = 10\,\text{mm}$ than for the longer cell lengths. This is somewhat expected as for a given plasma density, injection will occur later in the interaction for lower plasma densities. Thus with a limited acceleration length, shorter cell length will yield lower maximum energies. The late injection at lower plasma densities is compounded by lower accelerating fields as $E_{\text{peak}} \propto n_e^{1/2}$.

Finally, Figure 7.18c shows the measured maximum electron energy as a function of plasma distance for the three gas lengths. The rise of maximum electron energy with increasing plasma density is interesting as it opposes the intuitive n_e^{-1} scaling.[11] This is a manifestation of the rate of self-focussing and pulse compression increasing with plasma density, thus leading to self-injection earlier in the interaction. Additionally, the fact that the plasma length is fixed changes the scaling as lower plasma densities support a lower accelerating field and a longer dephasing length. Thus at lower plasma densities the shorter plasma length is a smaller fraction of dephasing length. This is discussed in more detail later on.[12]

The peak electron beam cut-off energies shown in Figure 7.18c are observed to reach a maximum at different number densities for different gas cell lengths. The longest gas cell length requires the lowest plasma density to reach a maximum beam energy; the shortest gas cell necessitates the use of the highest number density for optimal beam energy. With a plasma density increase beyond the optimum, a decrease in beam energies is seen. This rollover is very sharp for the longer cell lengths of 15 mm and

[11] Cf. Section 7.4.1 for similar results.
[12] Cf. Section 7.4.3 and Figure 7.22.

30 mm; a somewhat smoother decrease is witnessed for $L_{\text{cell}} = 10\,\text{mm}$. Interestingly, for cell lengths $L_{\text{cell}} = 10\,\text{mm}$ and $L_{\text{cell}} = 15\,\text{mm}$, the rollover of maximum energy coincides with the density where secondary injection is observed in Figure 7.18a. This implies similar physics to that observed in length scans, where the reduction of cut-off energies of continuously injected beams was seen to be due to bubble evolution.

The most interesting feature shown in Figure 7.18c is the fact that maximum electron energy achieved is relatively constant at $\mathcal{E}_{\text{max}} \simeq 1800\,\text{MeV}$ at different plasma lengths and densities. The peak energy gain is achieved for $L_{\text{cell}} = 10\,\text{mm}$ at $n_e = 3.5 \times 10^{18}\,\text{cm}^{-3}$, a plasma density 1.7 times higher than the $n_e = 2.1 \times 10^{18}\,\text{cm}^{-3}$ for $L_{\text{cell}} = 30\,\text{mm}$. Thus a saturated regime of acceleration is observed. From the preceding discussion, we recall that depletion length at $4 \times 10^{18}\,\text{cm}^{-3}$ is longer than at 10 mm, thus meaning that the energy gain at $L_{\text{cell}} = 10\,\text{mm}$ is not laser energy depletion limited. The same can be said about the 15 mm long cell, as further injection into the wake is seen for higher plasma densities than the optimum $n_e \simeq 3.6 \times 10^{18}\,\text{cm}^{-3}$ for maximum electron beam energy. Thus the limiting factor must be dephasing. However, the fact that secondary injection is seen to occur at the density at which optimum electron energy is seen implies that the limitation to the beam energy is dephasing due to bubble evolution. This will be discussed in further detail in the following section.

7.4.3 Discussion

Record electron energies in the self-guided, self-injecting regime employing a 240 TW laser were measured. However, the densities at which these beams were accelerated do not follow the general scalings. Using Equations 2.76 and 2.75 at $n_e = 2.9 \times 10^{18}\,\text{cm}^{-3}$ yields $\Delta W = 1\,\text{GeV}$. This value, accounting for fixed power self-focussing, is already much higher than the linear energy gain of $\Delta W = 0.6\,\text{GeV}$. The error in plasma density measurement is not large enough to yield agreement between experimental results and this value. Thus the laser intensity must be amplified to higher values or the phase velocity of the wake is larger than theoretically assumed. The latter can occur for non-gaussian pulse shapes, affecting the erosion of the pulse and thus the wake velocity.[255] Figure 7.19 depicts results from 2D simulations designed to study phase velocity of the wake and the effect of modelling a realistic pulse shape. The simulation was performed at $n_e = 2 \times 10^{18}\,\text{cm}^{-3}$ and $a_0 = 2$ with $w_0 = 45\,\mu\text{m}$. The phase velocity of the wake was measured by tracking the point within the bubble where the longitudinal field vanishes.[256] Very similar behaviour is seen for both pulse shapes, with the

[255] M. J. V. Streeter. "Ultrafast Dynamics of Relativistic Laser Plasma Interactions". Imperial College London, 2013.

[256] C. Benedetti *et al*, *Phys Plasmas* **20**, 2013.

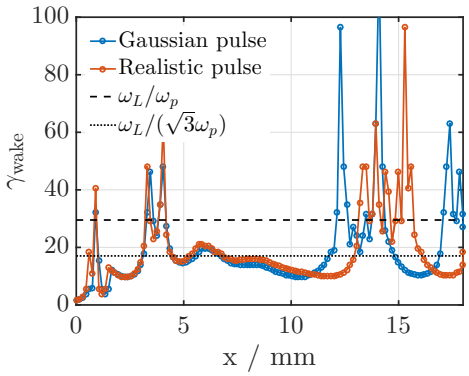

Figure 7.19: *Measured gamma factors γ_{wake} for a gaussian shaped ideal pulse and a realistic pulse, based on the measured pulse shape. The dashed black line is the linear wake velocity and the dotted black line corresponds to the non-linear wake velocity accounting for laser depletion.*

largest difference being in late time evolution. Notably, the gamma factor of the wake follows the non-linear model accounting for pulse erosion, $\gamma_{\mathrm{wake}} = \omega_L/(\sqrt{3}\omega_p)$, plotted as the dotted line in Figure 7.19. While these findings need further verification with 3D simulation, we can preliminarily conclude the very high electron energies are not caused by a largely increased wake velocity.

Assuming correct modelling of the phase velocity, the final value of a_0 required to obtain $\mathcal{E} = 2.8\,\mathrm{GeV}$ is calculated from Equation 2.75 as $a_0 = 9.2$. This value is very close to the self-focussed intensities seen in 3D simulations presented in Figure 7.12. The calculated value of $a_0 = 9.2$ also agrees with the values for $\sqrt{a_0}$ measured from dephasing lengths and peak electric fields, as shown in Figure 7.9c. Calculating the matched a_0 from Equation 2.76 with $a_0 = 1.8$ and $w_m = 42\,\mu\mathrm{m}$ yields $a_m = 5.2$. This is about 1.75 times lower than the value required for the measured energy gain. This shows that self-compression plays an important role in determining the final intensity.

As the modelling of the laser matches with higher initial intensities, we can instead postulate that the increased energy gains are due to better coupling of laser energy into the wake. This assumption can be corroborated by studying the scaling of previously obtained peak electron energies with plasma density. Figure 7.20a shows a collection of published experimental results from the last decade, with measured maximum electron energy plotted against laser power.[257] A clear trend of increasing electron energy with increasing power is evident. The obtained electron beams are plotted according to the particular experimental technique used: the black stars denote self-injection results, red stars denote ionisation injection, magenta diamonds denote capillary guided experiments, green upwards triangles denote staged experiments and cyan downwards

[257] S. P. D. Mangles, CERN Yellow Reports **1**, 2016.

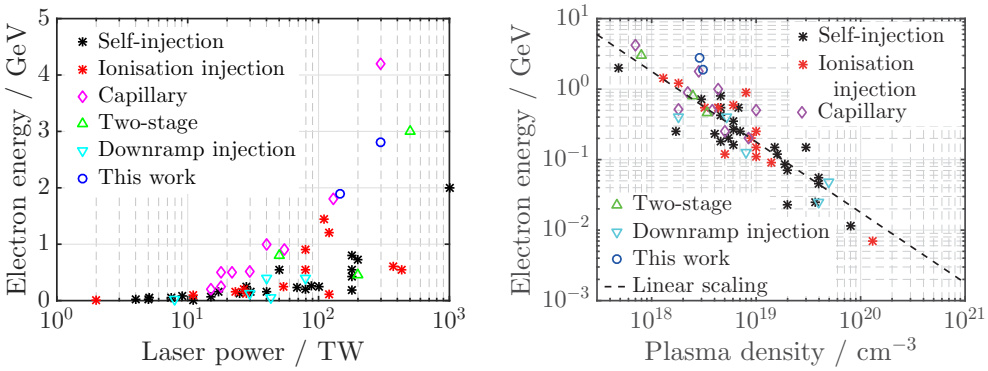

(a) Scaling with laser power *(b) Scaling with plasma density*

Figure 7.20: *Collection of previously published electron acceleration results, highlighting the scaling of achieved electron energy with laser power, Panel (a), and plasma density, Panel (b).*

triangles represent downramp injected beams. The highest electron beam energies have been achieved by employing external guiding structures and employing staging. Results from current work, plotted as blue circles in Figure 7.20a, lie far above previous results in the self-guided, self-injected regime, demonstrating enhanced electron energies at a given laser power.

Figure 7.20b shows the scaling of measured electron energies with plasma density for the same collection of results.[257] Also plotted as the black dashed line is the linear energy scaling, $\Delta W = 2{\gamma_p}^2 m_e c^2$. A general trend following the linear scaling is seen, with a large amount of results lying above this line. Assuming that both plasma density and electron energy have been measured correctly, the extra energy gain is achieved via the non-linear lengthening of the bubble and from the amplification of the accelerating field, i.e. the a_0 term. For the results presented in this thesis, the maximum measured electron energy is always found to lie far above the linear scaling, meaning that intensity amplification plays an extremely significant role in determining the final energy. Additionally, the lack of results with similar energy gains at the given density and laser power again suggests an enhanced coupling of the laser energy into the wake, compared to previous work.

The reasons for this enhanced coupling are not yet fully understood. It is, however, clear that compared to the previously employed $f/20$ focussing optic the maximum energy gain has been more than doubled by doubling the focal length. This increases the focal spot size by at least a factor of two, thus quadrupling the Rayleigh range. Hence the rate of diffraction is reduced and laser propagation becomes more smooth. This is illustrated in Figure 7.21, showing the solutions to Equation 2.61 for $P/P_c = 61$ and $n_e = 3 \times 10^{18}\,\mathrm{cm}^{-3}$. The oscillation wavelength of the spot size is seen to increase

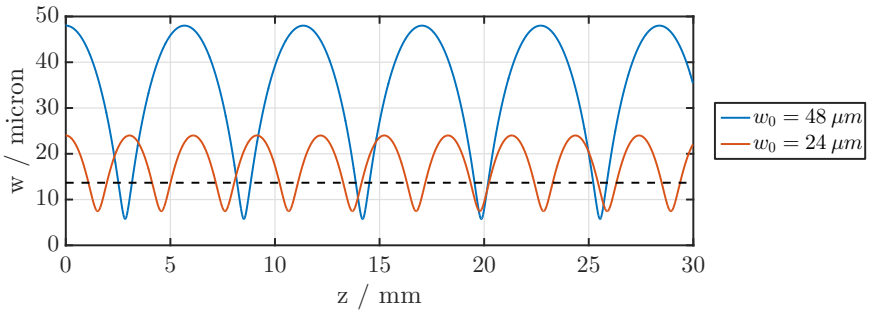

Figure 7.21: *Solutions to the envelope Equation 2.61 for* $P/P_c = 61$ *and* $n_e = 3 \times 10^{18}\,\mathrm{cm}^{-3}$ *and approximate spot sizes obatined with* $f/40$ *and* $f/20$ *focussing optics.*

proportionally to the initial spot size. Thus, in the stationary envelope model longer focal lengths result in less spot size oscillations. This in turn reduces bubble evolution and yields more stable acceleration. There may also be beneficial properties from the shape of the density ramp at the entrance of the plasma, enhancing focussing for energy on the periphery of the spot and thus allowing the bubble to capture it.

The increase of electron energies with increasing plasma density before peaking and starting to reduce again is an interest aspect. As mentioned in the previous section, this is mainly due to the rate of self-focussing affecting the injection location and the reduced electric field at lower plasma densities; combined with a fixed plasma length a lower energy gain is observed at lowered number densities. These factors also affect the plasma density required to reach a maximum energy gain, with experimental data presented in Figure 7.18c. A very simplistic model can be compiled, by integrating Equation 7.3 from 0 to a limiting length, which is the shortest of plasma length and pump depletion length. Results from such a model are plotted in Figure 7.22 for the plasma lengths used in the experimental study,[13] $L = 10\,\mathrm{mm}$, $L = 15\,\mathrm{mm}$ and $L = 30\,\mathrm{mm}$. The solid lines show scaling for a fixed intensity of $a_0 = 2$ whereas for the dashed lines a matched intensity is used, given by Equation 2.76. This model neglects any injection threshold, thus the increase in electron energy with increasing plasma density is only due to the scaling of the electric field. The peak energy corresponds to dephasing limited energy gain, after which electrons will lose energy. Fully dephased electrons will lose all their energy and thus result in null energy.

Peak energies are reached at lower plasma densities for longer lengths, as in Figure 7.18c. This means that the peak energy is observed for the case where the dephasing length matches the plasma length. It is also seen that accounting for self-focussing increases the energy and pushes the optimum plasma density to higher values. If

[13] Cf. Section 7.4.2

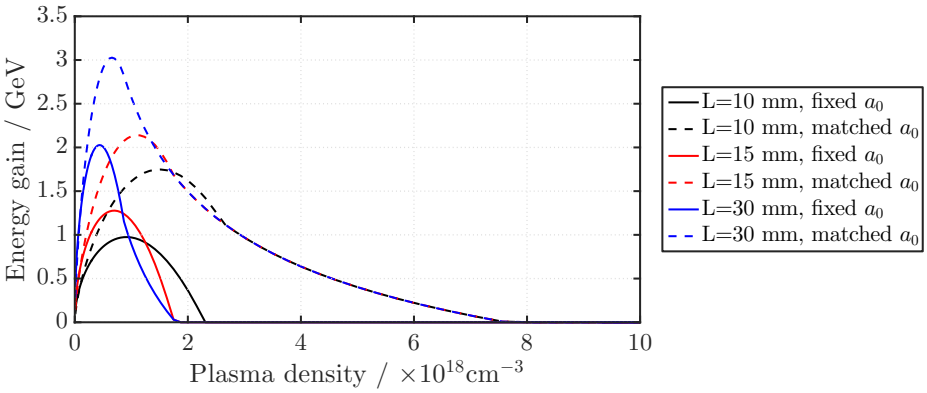

Figure 7.22: *A very simple model to describe the scaling of peak electron energy as a function of plasma density for a fixed length plasma.*

Equation 7.2 is expanded by substituting in the 3D non-linear expression for peak electric field and dephasing length,[14] it is found that $\mathcal{E} \propto n_e^2 L^2 + \sqrt{a_0 n_e} L$ and indeed a predominantly parabolic dependence of energy with plasma density is observed in Figure 7.22. The deviation from this at high plasma densities signifies depletion, where electron energy gain is limited by pump depletion length. This is because in the model, no further energy loss will occur once the depletion length is reached, thus resulting in the deviation from parabolic energy dependence on n_e. The electron density where the peak energy is obtained is not correctly predicted by this model as it neglects injection thresholds, however, it provides instructive and useful to study the qualitative behaviour.

The simple model neglects all dynamical effects affecting the bubble during actual acceleration. However, laser and bubble evolution play very important roles in determining the final electron beam energy. From Figures 7.18a and 7.18c, we recall observing that for cell lengths 10 mm and 15 mm the peak electron energy is obtained at the same plasma density where secondary injection into the wake is seen. It was also observed from simulations that the secondary and tertiary injection events are accompanied by bubble expansion. Secondary injection was seen to limit the maximum electron beam energy in Figure 7.7 and this observation can be extended into the current set of data to explain the saturated energy gain in Figure 7.18c. We thus see that the independence of maximum electron beam energy of plasma density is due to bubble evolution induced dephasing. In the observed plasma density range, at some point laser evolution will lead to a secondary injection event, which is closely related to bubble elongation. This results in a set of electrons at the highest energies suddenly

[14] Cf Equations 2.66 and 2.70.

becoming rephased into a region of decelerating field. This effectively reduces the peak energy gain.

Finally the threshold for self-injection into the wake needs to be discussed. For trapping to occur at $n_e = 1.6 \times 10^{18}\,\mathrm{cm}^{-3}$ in a plasma 10 mm long, the self-injection threshold model by Mangles *et al*[120] yields a minimum of 12.2 J of energy to be contained in the FWHM of the spot. This is in excess of the total energy delivered to target and thus this model clearly does not explain injection in this study. A similar conclusion was reached in Section 7.3.4. A small discontinuity in plasma density is seen to lead to self-trapping in simulations; however the scope of plasma lengths and densities over which self-injection has been consistently observed rules any such irregularities out. Injection from an impurity gas can also not explain the consistent injection as ionisation injected beams have very different properties.[15] With other possibilities ruled out, we conclude that injection is driven by laser pulse evolution, as trapping is also observed with decreased laser energies, with an initial normalised vector potential $a_0 \sim 1.4$, for plasma lengths as short as 3 mm.[16]

7.5 On stability of self-guided, self injected LWFA

During the 2015 experimental campaign the success of tomographic imaging employing betatron x-ray sources[248] was extended by performing a scan of a prenatal mouse embryo. In order to further increase the resolution of the tomogram, it is necessary to increase the number of projections taken at different angles. The latest scan was thus performed with 360 projections over 180°. In order for this imaging to be performed, an x-ray source with high stability was required. By extension, this also means that the electron acceleration is to be of highest stability. In order to perform this scan, a total of 533 full power laser shots were taken over a span of nearly 4 hours. This data set can be analysed as a stability test, to draw information on the parameters affecting the reproducibility of laser wakefield accelerators.

Raw data from the electron spectrometer, summed along the non-dispersion axis, is plotted for all shots in Figure 7.23. An electron beam was observed on every shot where the laser fired. Additionally, maximum energies above a gigaelectronvolt were measured for all but one shot; laser failure was behind this. However, a long term trend of increasing peak energy is clearly observed. Additionally, the maximum on the secondary-injection bunch is seen to steadily rise as well.

The slow, long-term energy increase is further illustrated in Figure 7.24a, plotting the shot-to-shot fluctuations of the measured cut-off energy and beam charge. Due

[15] Cf. Section 6.3
[16] Cf. Section 7.3

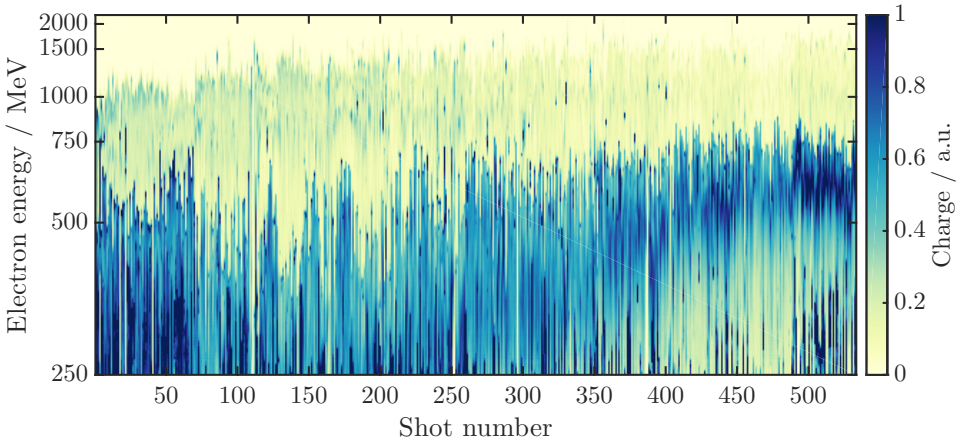

Figure 7.23: *Raw spectra for all shots in the long time stability run. Each column shows spectrometer data that has been integrated along the non-dispersive axis; all shots are plotted using the same colour table.*

to experimental constraints and equipment malfunction, the camera imaging the low energy part of screen 2 (as shown in Figure 7.3) was unable to save images. Hence, backtracking was performed on the very few images where the electron beam energy was high enough to be visible on the camera imaging the high energy part of screen 2. The maximum electron energies in Figure 7.24 thus inherently feature more scatter as the shot-to-shot fluctuations have not been accounted for in all shots. In order to calculate the maximum energies taking into account the electron beam pointing offset, the average electron beam angle of the backtracked shots was used for all other images.

Figures 7.24b and 7.24c depict histograms of maximum electron beam energy and beam charge, respectively. A large spread of more than a gigaelectronvolt is evident in the electron beam energies. However, multi-GeV beams are obtained on all shots, with a total of 14% of the shots having maximum energies exceeding 2 GeV. The largest fraction, 58% of shots have a maximum energy between 1.5 GeV and 2 GeV and 28% of all shots yield cut-off energies below 1.5 GeV. Only 2% of all shots produce less then 100 pC of charge in energies above 200 MeV. The largest amount of shots, 60%, yield charge between 100 pC and 200 pC. High charge shots with more than 300 pC of charge account for 38% of the shots.

Clearly the large scatter in maximum beam energies is non-ideal and needs to be addressed. In the scope of current analysis, the electron energy dependence on plasma density and laser energy can be investigated.[17] Figure 7.25a plots the plasma density

[17] As mentioned before, the fact that for most shots performing backtracking was not possible also increases the scatter in maximum beam energies.

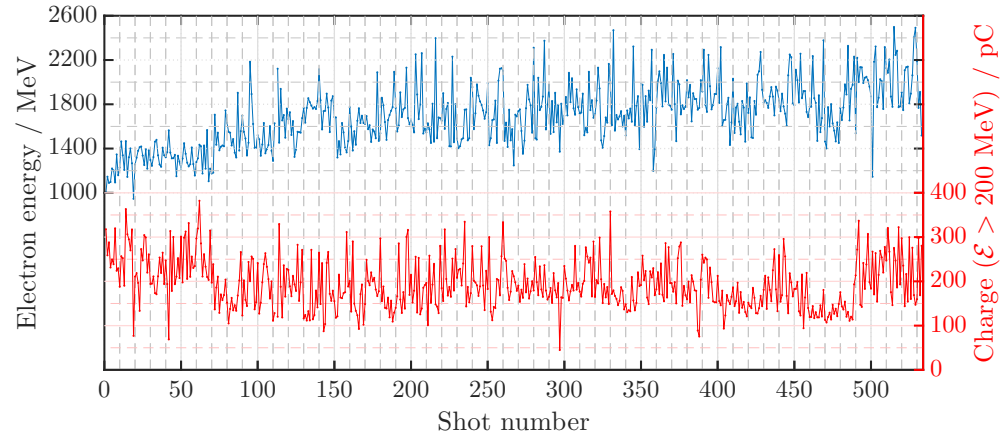

(a) Shot-to-shot variation

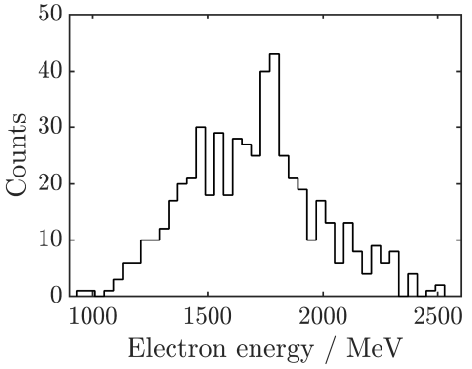

(b) Histogram of electron energies

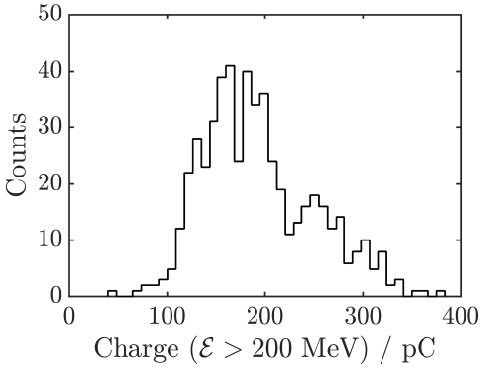

(c) Histogram of beam charge

Figure 7.24: *Maximum electron energies along with integrated beam charge for $\mathcal{E} > 200\,\mathrm{MeV}$ for all shots taken. Panel (a) shows the shot-to shot variation whereas panel (b) and (c) depict histograms of maximum energy and beam charge, respectively.*

on each shot as measured by the gas pressure diagnostic. Clearly there are large jumps in the plasma density, occurring when the x-ray beam quality was deemed insufficient and thus the plasma density was changed. Most of the scan was performed with the gas delivery system set to a pressure of 85 mbar, with occasional increments of 5 mbar either way.

Figure 7.25b plots the dependence of measured cut-off energy on the measured plasma density. It reveals the maximum electron energy to be almost independent of n_e, at least within the plasma density range scanned. Indeed, maximum beam energies are measured to be almost identical for plasma densities as different as $1.9 \times 10^{18}\,\mathrm{cm}^{-3}$ and $3.1 \times 10^{18}\,\mathrm{cm}^{-3}$. Beam charge, depicted along the colour scale in Figure 7.25b, is seen to exhibit almost no shot-to-shot correlation with plasma density. It is, however,

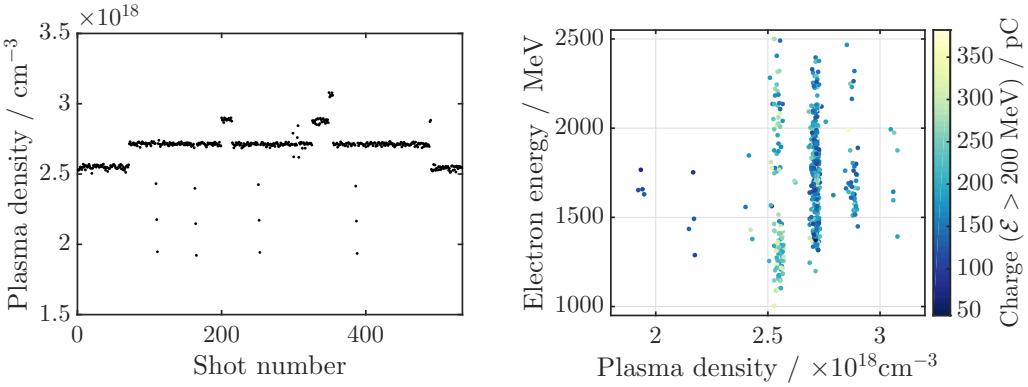

(a) Shot-to-shot plasma densities *(b) $\mathcal{E}_{\max}$ and $Q_{\mathcal{E}>200\,\mathrm{MeV}}$ vs plasma density*

Figure 7.25: *Variation of the plasma density during the stability run and the dependence of maximum electron energy and beam charge on the plasma density.*

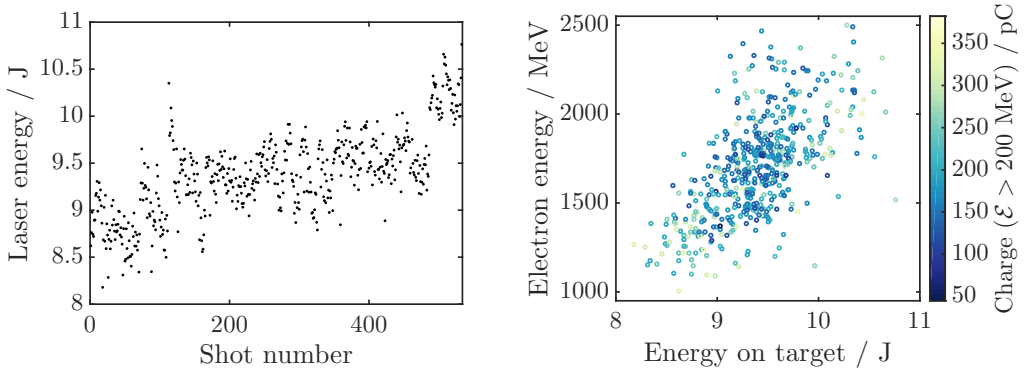

(a) Shot-to-shot laser energy *(b) $\mathcal{E}_{\max}$ and $Q_{\mathcal{E}>200\,\mathrm{MeV}}$ vs laser energy*

Figure 7.26: *Variation of laser energy delivered to target during the stability run and the dependence of maximum electron energy and beam charge on laser energy.*

clear that lowest plasma densities yield lower charge beams. Additionally, the highest beam charges seem to be generated with plasma densities $n_e \simeq 2.6 \times 10^{18}\,\mathrm{cm}^{-3}$.

The next parameter that can affect the maximum beam energy is the laser energy on target. Logged on every shot and adjusted for compressor and beam optics throughput, the variation of laser energy delivered on target is plotted in Figure 7.26a. There is qualitative similarities between the trend here to that in Figure 7.24a, with a slow upwards trend and a step for the last ~ 30 shots. Figure 7.26b shows the dependence of maximum beam energy with laser energy, with charge additionally plotted on the colour axis. A clear correlation is evident, with cut-off energy linearly increasing with rising laser energy. Again the beam charge appears to have no clear dependence on the laser energy.

	E_{laser}	n_e	$\mathcal{E}_{\text{peak}}$	Q_{beam}
E_{laser}	1.000	0.079	0.634	-0.061
n_e		1.000	0.182	-0.136
$\mathcal{E}_{\text{peak}}$			1.000	-0.133
Q_{beam}				1.000

Table 7.3: *Correlation coefficients between measured beam energy, beam charge, laser energy on target and plasma density.*

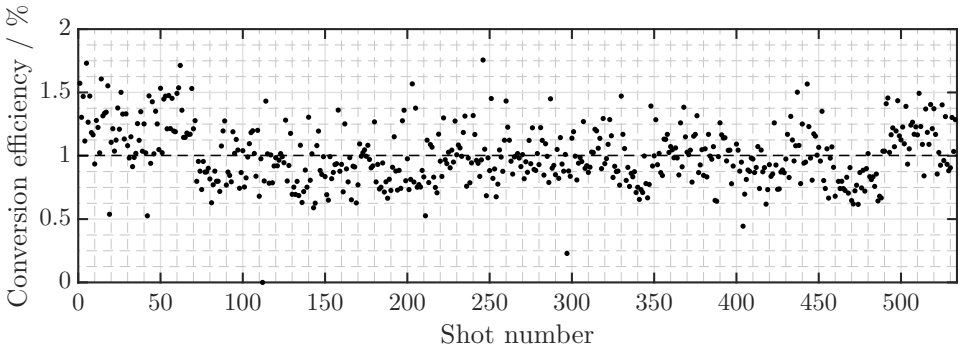

Figure 7.27: *Measured shot-to-shot conversion efficiency from laser energy to electron beam energy. The black dashed line is the average across the run.*

Table 7.3 gathers calculated correlation coefficients between the measured electron energies, beam charge, laser energy and plasma density. As mentioned before, there is a strong correlation between on-target laser energy and maximum electron beam energy, with $r = 0.634$. However, there does not seem to be a clear correlation between any of the other quantities; indeed, the correlation coefficient between laser energy and plasma density is higher than between laser energy and beam charge.

Finally, the conversion efficiency η from laser energy delivered onto the plasma to electron beam energy can be calculated.[18] The shot-to-shot variation of η is plotted in Figure 7.27. There is clearly a large variation in the efficiency, with the average value of $\eta = (1.00 \pm 0.01)\,\%$ plotted as the black dashed line. The error quoted here is the standard error of the mean.

Discussion and implications

Whilst there is a clear correlation between the amount of laser energy delivered on target and the maximum beam energy, there still exists a large amount of scatter for each laser energy. This implies that while laser energy is important, the spot

[18] Cf Section 7.6 for more analysis of efficiency.

quality will also play a significant role. For each shot, the far-field of the laser after compression was saved and can be analysed to yield further information about the focal spot quality. However, as the focal spot is only measured during low-power operation, when the compressor far-field diagnostic is not operating, only partial information can be extracted as the correlation between spot quality on the laser diagnostic and on target is unknown. A further complication in this analysis is the very poor quality of the compressed far-field diagnostic. For some full power shots the laser on target was diagnosed using the exit mode diagnostic; the focal spot in the target chamber was deemed reproducible and very good quality whereas the diagnostic in the laser produced highly varying and poor quality spots.

Due to the very poor images, direct characterisation of the full power laser focal spots was impossible. Instead, the length of the FWHM contour of the intensity pattern along with the ratio of the integral of signal with values higher than the half-maximum to the total energy were calculated. However, including these parameters in the analysis was found to significantly increase the scatter in laser quality parameter and reduce the degree of correlation between laser spot quality and electron beam energy. This is somewhat expected as the diagnostic is greatly influenced by non-linear phase errors inherent to the diagnostic. Thus, with the data available from the experiment, it is impossible to further characterise the dependence of electron beam qualities on the laser parameters.

The electron beam peak energy was observed to be insensitive to plasma density, as evidenced by a correlation coefficient of -0.14. This is very interesting as it implies a regime of acceleration saturation. Indeed, the maximum electron beam energy was observed to be a function of laser energy. Thus, the accelerator was operated in a regime where the main limitation to the energy gain was the laser energy. From previous sections,[19] we know that the even at different pressures, the electron energy was mainly limited by laser evolution driven dephasing. Operation of the acceleration at lengths greater than the secondary injection length thus ensures a saturated energy gain, where large changes of plasma density have small effects on the final energy. This does, however, imply that in the saturated regime, a truly stable laser wakefield accelerator can only exist in conjunction with a highly reproducible laser.

[19] Cf Section 7.4.2

7.6 On the efficiency of self-guided, self-injected LFWA

While the maximum energy of an accelerator is an important metric, in the design of large scale colliders the efficiency of the system is of equal, if not higher, importance. Efficiency encompasses the different losses along the system in converting power from the grid into beam energy. Indeed, for largest proposed colliders such as CLIC, the total power consumption is estimated to be 582 MW, with an RF-to-beam efficiency as high as 28.2 % and a total wall-plug to electron beam efficiency of 4.8 %.[5] Hence, for future laser wakefield accelerator based collider designs the efficiency of laser power to beam energy conversion is of utmost importance.

The total beam energy can be easily found by integrating over all energies:

$$\mathcal{E}_{\text{beam}} = \int \frac{\mathrm{d}Q}{\mathrm{d}\mathcal{E}/\mathcal{E}} \mathrm{d}\mathcal{E}. \tag{7.11}$$

The efficiency η is then simply found by calculating the ratio of the beam energy $\mathcal{E}_{\text{beam}}$ and the total laser delivered on target. Efficiencies calculated in such manner are presented in Figures 7.28 and 7.29. It is important to note that experimental conditions limited the measurement of electron energies to a range with $\mathcal{E} \leq 200\,\text{MeV}$. Thus, the total beam energies calculated here are underestimates and hence the values of η presented here are lower estimates.

The shot-to-shot efficiency for length scans performed at a constant plasma density[20] are shown in Figure 7.28, with experimental parameters presented in Table 7.4. While shots were taken at longer gas cell lengths than the η data is plotted for in Figure 7.28, these were not included in this analysis. This is a result of imposing a beam quality restraint on the data to be used; shots, where a beam with filaments or indications of other instabilites is produced are deemed to operate in an unwanted regime. We note in passing that these shots sometimes produced very large amount of charge, yielding high values for η.

Datasets with higher plasma densities are seen to reach the peak efficiency at shorter gas cell lengths. This is due to the laser depletion length being close to the gas cell lengths. Peak efficiencies as high as 2.5% are reached. It is also of interest that the highest values of η are reached with the lowest laser energies used. This suggests that beamloading may be limiting the total amount of charge injected. Secondly, beams with similar peak energies are observed with both low and high laser energies, implying

[5] *A Multi-TeV Linear Collider based on CLIC Technology: CLIC Conceptual Design Report*. Tech. rep. CERN-2012-007. CERN, Jan. 2012. URL: http://project-clic-cdr.web.cern.ch/project-CLIC-CDR/CDR_Volume1.pdf.

[20] The length scans analysed here for efficiency are the same as presented in Section 7.3.

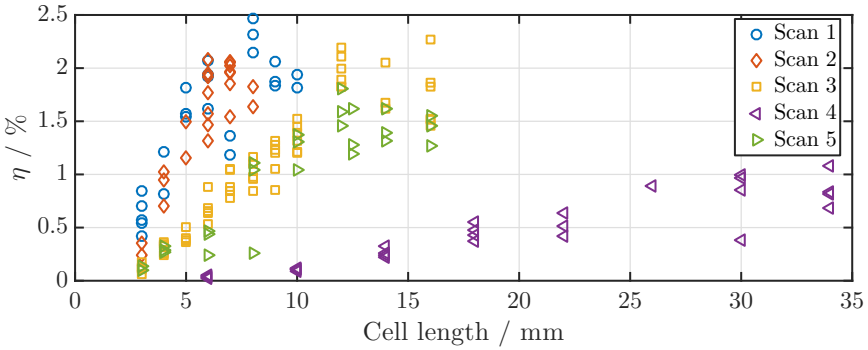

Figure 7.28: *Experimentally measured single-shot efficiencies for length scans performed at constant plasma density.*

Scan	n_e $10^{18}\,\mathrm{cm}^{-3}$	$\mathcal{E}_L$ J	η_{peak} %
Scan 1	2.6	5.6	2.5
Scan 2	3.2	5.6	2.1
Scan 3	2.3	5.7	2.3
Scan 4	1.6	11.3	1.1
Scan 5	2.6	11.0	1.8

Table 7.4: *Experimental parameters of the length scans presented in Figure 7.28.*

that the peak electric field is not increased by a significant factor with increased laser energy. This agrees with results presented in Section 7.3, in Table 7.1 and Figure 7.7. Finally, we note that for monoenergetic electron beams presented in Section 7.3.2 the highest conversion efficiency was $\eta = 0.24\%$.

Efficiencies obtained from datasets where the plasma density was varied at a fixed gas cell length are plotted in Figure 7.29, with experimental parameters for the different scans presented in Table 7.5. Scans 2, 3 and 4 are also presented in Section 7.4.2, while the data from Scan 6 is analysed in Section 7.4.1. Again shots where severe beam breakup was observed have been omitted. A peak efficiency of nearly 3% is observed for one shot. Additionally, for some shots η is seen to reach values as high as 2%. In general, though, the efficiency is limited to $\eta < 1\%$. Similarly to the length scans, efficiency is maximised for plasma densities nearing $3 \times 10^{18}\,\mathrm{cm}^{-3}$ and cell lengths between 10 and 20 mm. Additionally, it is seen that scans with the highest laser energy (Scans 1 and 6) results in the highest efficiencies.

Evidently, efficiencies as high as a few percent can be maintained in a stable manner. This primarily depends on the mode of operation chosen, i.e. whether the accelerator is optimised for optimum energy gain or highest amount of charge. For the highest energy,

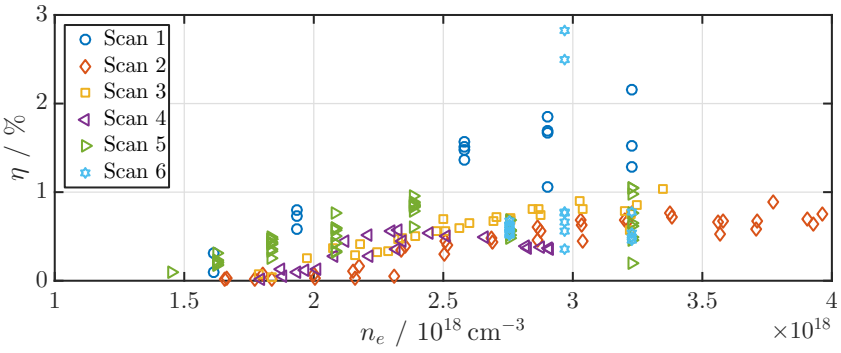

Figure 7.29: *Experimentally measured single-shot efficiencies for plasma density scans at different gas cell lengths.*

Scan	L_{cell} mm	$\mathcal{E}_L$ J	η_{peak} %
Scan 1	12.5	11.2	2.2
Scan 2	10.0	9.6	0.9
Scan 3	15.0	9.7	1.0
Scan 4	30.0	9.6	0.6
Scan 5	20.0	8.3	1.1
Scan 6	20.0	10.9	2.8

Table 7.5: *Experimental parameters of the plasma density scans presented in Figure 7.29.*

very early injection leads to high beam energies with limited charge. For the highest charge, some electrons have already dephased, meaning they have returned some of the energy they gained from the accelerator structure. Some of this energy can then be recycled to accelerate other electrons, but obviously the efficiency will suffer.

It is instructive to compare the laser to electron beam energy efficiency achieved in the current work to other reports. In Figure 7.30, the efficiency as a function of laser power is plotted for a collection of published experiments.[257] Most papers do not explicitly report total beam energy. In this case the reported charge and the achieved electron energy are used to calculate an estimate for $\mathcal{E}_{\text{beam}}$. For reports where integrating current transformers were used for charge measurement, the total charge has been reduced by an empirical factor published by Glinec *et al*.[178] The quoted value for total laser energy has been used.

As can be seen, the highest overall efficiency to date has been achieved by employing a capillary to guide the pulse.[54] The large majority of experiments, however, are

[178] Y. Glinec *et al*, *Rev Sci Instrum* **77**, 2006.
[54] W. P. Leemans *et al*, *Nat Phys* **2**, 2006.

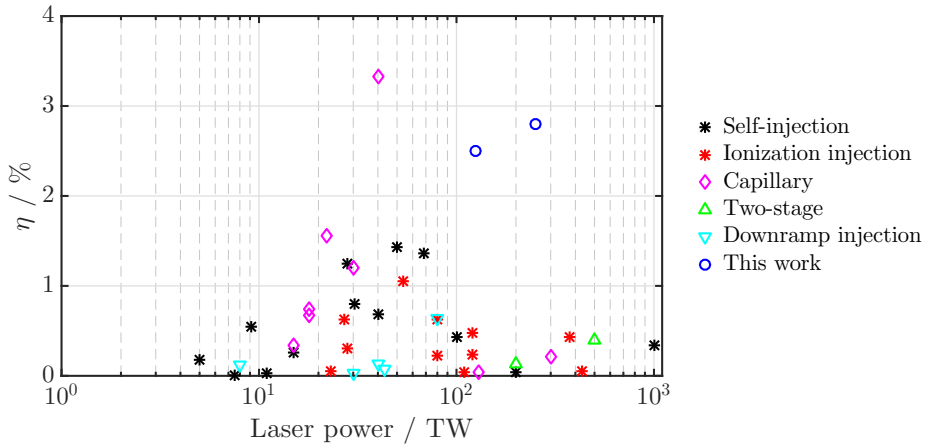

Figure 7.30: *Laser energy to electron beam energy conversion efficiency for a collection of reported experiments, along with values obtained within this work.*

limited to conversion efficiencies that are below 1%. The peak laser energy to electron energy conversion efficiencies achieved during this work are plotted as the blue circles in Figure 7.30 and are clearly much higher valued than previous results (par one). Additionally, for laser powers in excess of 100 TW, the current results are 5 times higher than previous peak efficiencies. While single shot efficiencies may perhaps not be the most representative, the average value of η achieved in this work over hundreds of shots[21] was 1%; this value is twice as high as the average from previous published results. In all, this comparison provides further support to the enhanced laser coupling hypothesis.

With the efficiency goals of large scale colliders in mind, the current modes of operation of laser plasma accelerators still prove to be insufficient. More efficient coupling, as evidenced in the current work, provides small steps towards higher efficiencies. Much more work needs to be done to further understand the intricacies of laser coupling in the bubble regime. Direct probing of the laser-plasma interaction is required in addition to performing PIC simulations. Additionally, laser energy coupling can be further increased by tailoring focal spots to ensure more energy is contained within the central spot. Finally, tailoring the bunch profiles to make full use of field structure within the nonlinear bubble needs to be explored. The physics of heavily loaded bubbles[258] needs to be explored more thoroughly to understand regimes of stable high efficiency operation.

[21] Cf. Section 7.5, page 220.
[258] E. Guillaume *et al*, *Phys Rev Lett* **115**, 2015.

7.7 Conclusion

Electron acceleration in self-guided laser wakefield accelerators was experimentally studied, with the aim to extend the energy frontier into the multi-gigaelectronvolt regime by doubling the focal length of the main focussing optic. This was hypothesised to allow matched propagation at lower plasma densities, thus allowing for larger energy gains. Higher than previously reported electron energies in the self-guiding, self-injecting regime were subsequently measured, with a substantial amount of beam energy above 2 GeV. The electron beams were, however, generated at plasma densities much higher than expected from theoretical scaling. This discrepancy is attributed to the increased self-focussing efficiency, with evidence for very efficient coupling of laser energy into the wake.

A large collection of plasma length scans facilitated the acceleration and injection dynamics of an electron beam to be measured. These allowed the measurement of the accelerating field within the bubble. With theoretical scaling suggesting fields of several hundreds of gigavolts per metre, the highest experimentally measured value was $E_{\mathrm{acc}} = (570 \pm 190)\,\mathrm{GV\,m^{-1}}$. These extremely high electric fields enabled acceleration of electron beams with peak energies beyond 1 GeV, in a plasma length of mere 5 mm and laser power of $P \sim 125\,\mathrm{TW}$.

Very stable self-injection at plasma densities and plasma lengths below those suggested by an empirical model was witnessed. The self-trapping occurred within the first millimetres of the interaction for plasma densities of $n_e \sim 2.5 \times 10^{18}\,\mathrm{cm^{-3}}$. Self-injection was also seen for a plasma density as low as $n_e = 1.6 \times 10^{18}\,\mathrm{cm^{-3}}$ in a 10 mm plasma. With a large-scale simulation campaign still under way, there is already evidence that the mechanism behind this trapping is the evolution of the laser pulse intensity, allowing electrons to become dephased from the forming bubble.

The increased electron energies and charge was seen to increase the x-ray yield, allowing for more successful tomographic imaging of biological samples. During this run, 533 shots were taken and an electron beam was observed on all shots. The stability of the electron energy and charge was analysed, revealing a regime of operation where energy gain was saturated and did not depend on plasma density. The electron beam energy was found to correlate with the laser energy, though, meaning that the stability of the electron beam is directly dependent on the reproducibility of the laser.

The efficiency of conversion from laser energy to electron beam energy was calculated for a range of different accelerator parameters. A peak value of $\eta = 2.8\%$ was obtained, with efficiencies above 2% routinely measured. Comparing this to reports from the literature reveals it to be the highest conversion efficiency from laser to

electron beam energy for self-guided, self-injected LWFA.

CHAPTER 8
Conclusion and outlook

THIS THESIS presented work performed on characterising self-guided laser wakefield accelerators in the multi-gigaelectronvolt regime. Many aspects of the accelerator were examined, including spectral changes, self-injection dynamics and suppression, ionisation injection, effects of an extended focal length, laser to electron energy conversion efficiency and electron beam generation stability.

8.1 Discussion of results

8.1.1 Spectral changes to LWFA driver

Section 4.3 presented results from plasma density scans looking at the spectral changes to the laser pulse itself as it drives the plasma accelerator. The spectral modifications were found to strongly depend on the plasma density, with very strong blueshifting of the spectrum observed. The redshift of the laser, previously shown to be correlated to plasma wave amplitude,[209,212] was found to remain relatively stable. This was found to be a measurement artefact due to the limited detection range of the diagnostic. As the spectral shifting is a result of highly non-linear feedback loops between the laser and the plasma wave, a simple 1D stationary model was conceived to explain the phenomenology intuitively. It was shown the redshifting is indeed caused by the work the laser pulse does to drive the plasma wave. Further, the blueshifting is observed to arise from the plasma wave itself, providing regions of positive refractive index gradients suitable for photon acceleration. A range of 1D particle-in-cell simulations were performed confirming these observations.

[209] N. E. Andreev *et al*, *JETP* **101**, 2005.
[212] S. Shiraishi *et al*, *Phys Plasmas* **20**, 2013.

8.1.2 Extended self-guiding

The performance of self-guiding over extended distances was evaluated in Section 4.4 with $f/20$ and $f/40$ focussing geometries. Guiding over 39 mm or more than 100 Rayleigh ranges was observed with the $f/20$ optic at $n_e = 1.5 \times 10^{18}\,\mathrm{cm}^{-3}$. Analysis of guiding performance found that the extent of the exiting laser spatial mode closely followed the matched spot size proposed by Lu *et al*.[63] Self-guiding with an $f/40$ optic was also characterised, with guided modes observed for a plasma length of 90 mm and a plasma density of $n_e = 9.5 \times 10^{17}\,\mathrm{cm}^{-3}$. This corresponds to self-guided propagation over 53 Rayleigh ranges and is similar to distances obtained with capillary guiding.[53]

8.1.3 Effect of linear chirp on LWFA

The use of an acousto-optic programmable device such as the Dazzler allowed the isolated effect of second order spectral phase on laser wakefield accelerators to be studied. Detailed in Section 4.5 through an extensive experimental dataset it was found that moderate positive chirps, where the red frequencies in the pulse precede the blue ones, allows for increased laser energy coupling into the plasma. Further, varying the sign of the chirp provided unambiguous support for the pulse front etching model.[113] This assertion arises from the transmission of spectral components that were entering the plasma in the tail part of the pulse; the frequencies in the front of the pulse were not transmitted. The effect of linear chirp on electron beam properties was also characterised. It was found that increasing positive chirp increased the electron beam energy by more than 300 MeV and that the total beam charge peaked at moderate positive chirps. This constitutes the first such measurement in the multi-GeV regime. Additionally, it was shown that the obtained effect of chirp is solely due to the frequency changes and not the pulse symmetry, as in previous work.[226,227]

8.1.4 Suppression of self-injection in the bubble regime

Chapter 5 presents experimental and modelling work demonstrating the suppression of self-injection with the use of ionisation injection. It is thought that self-injection is an inevitable process occurring if the laser intensity is high enough.[61,119] Through comparing electron beams obtained with both self-injection and ionisation injection it

[63] W. Lu *et al*, *Phys Rev Spec Top-Ac* **10**, 2007.
[53] W. P. Leemans *et al*, *Phys Rev Lett* **113**, 2014.
[113] C. D. Decker *et al*, *Phys Plasmas* **3**, 1996.
[226] W. P. Leemans *et al*, *Phys Rev Lett* **89**, 2002.
[227] T. Z. Zhao *et al*, *Plasma Phys Contr F* **58**, 2016.
[61] I. Kostyukov *et al*, *Phys Rev Lett* **103**, 2009.
[119] A. G. R. Thomas, *Phys Plasmas* **17**, 2010.

was found that the beam properties are fundamentally different. With increased beam quality for the ionisation injection case at similar plasma densities, it was concluded that self-injection had been suppressed through the preloading of the wake. 3D particle-in-cell simulations were performed to understand the self-injection physics and study the suppression mechanism. It was found that for extremely heavy beamloads, the cavity is very modified and no self-injection can occur due to the bubble shape changes. In the moderate beam load case, it was observed that self-injection was suppressed by reducing the transverse momentum of the sheath electrons returning onto the laser axis. This increases the threshold for self-injection and suppresses trapping of sheath electrons.

8.1.5 Comparing ionisation injection and self-injection

Owing to the lack of quantitative results highlighting the differences between ionisation injected and self-injected electron beam energies, such a direct comparison was undertaken and is presented in Chapter 6. Contrary to previous work it was found that the total beam charge scales very similarly with plasma density in both self-injection and ionisation injection cases for $P_L = 180\,\mathrm{TW}$. Additionally, it was observed that for ionisation injection the maximum energy gain was always much smaller than in the case of self-injection. This is attributed to bubble evolution, leading to both truncation of injection and limiting the energy gain of already injected electrons. In agreement with previous predictions it was found that the initial transverse momentum of ionisation injected electron beams was smaller than for self-injection by a factor of two. Given similar electron beam source sizes this means a smaller emittance for ionisation injected electron beams. The spectral signatures of ionisation injection employing a $P_L = 10\,\mathrm{TW}$ laser were characterised, showing a consistent blueshifted peak. This was associated with early injection yielding stable photon acceleration for a portion of the pulse.

8.1.6 Multi-GeV electron acceleration

Section 7.4.1 presents results showing multi-GeV electron beam energies obtained with a self-guided, self-injecting 250 TW laser. The key change compared to previous experiments at the same laser was the twofold increase of the focal length of the main optic. The longer focal length resulted in a much larger focal spot and a longer Rayleigh range. Record electron beam energies, with more than 10% of the polychromatic beam energy above 2 GeV, represent the highest results from the self-guided, self-injected regime for these laser powers and were obtained at $n_e = 2.8 \times 10^{18}\,\mathrm{cm}^{-3}$. Such high plasma densities are not in line with the scaling laws, predicting $\mathcal{E} \propto n_e^{-1}$ scaling with

plasma density. Through 3D particle-in-cell simulations it was shown that the record energies arise due to intensity amplification of the laser, both via self-focussing and self-compression. The self-focussing dynamics in particular play a very important role, resulting in self-injection very early in the interaction.

Through a series of plasma density scans at different gas cell lengths a regime of saturated energy gain was found. It was observed that regardless of cell length or plasma density, at the optimum conditions an energy gain of $\mathcal{E} \simeq 1800\,\mathrm{MeV}$ was obtained. This is again attributed to bubble evolution and the dephasing of highest energy electrons with cavity size changes.

8.1.7 Accelerating field measurements

The design of the plasma target allowed for the plasma length to be changed dynamically, facilitating the measurement of electron beam dynamics with increasing plasma length. Scans performed at reduced laser energies, with only half of the nominal energy on target, yielded electron beams with cut-off energies of 1.8 GeV from plasmas only 9 mm long. These electron beam energies are already much higher than obtained with $f/20$ focussing optic with twice as much laser energy. The length scans allowed for the direct measurement of accelerating electric field, with the highest result obtained being $E_{\mathrm{peak}} = (570 \pm 170)\,\mathrm{GV\,m^{-1}}$. Interesting injection dynamics were observed, with a late stage secondary injection event occurring after 12 mm of propagation. Containing up three times more charge, the secondary injected beam accelerated to energies of $\sim 600\,\mathrm{MeV}$ before laser depletion. It was also observed that the bubble elongation accompanying the secondary injection event limited the energy of the first, high energy bunch via bubble evolution induced dephasing.

8.1.8 Efficiency of self-guided, self-injecting LWFA

The efficiency of laser energy to electron beam energy is seldom quoted or investigated yet remains one of the most important aspects of future large scale accelerator designs. The efficiency was analysed for data taken with laser powers up $P_L = 250\,\mathrm{TW}$ for length and plasma density scans. Peak efficiency of $\eta = 2.9\%$ was found with values beyond 2% routinely measured. With a lack of previously reported values, estimates of η were compiled for a range of previously published results and it was found that the efficiencies measured in the current work represent the highest recorded values for laser wakefield accelerators in the self-guided and self-injected regime. It was also found that ionisation injected beams typically yield lower overall conversion efficiencies.

8.1.9 Stability of self-guided, self-injecting LWFA

In order to perform tomographic imaging of a prenatal mouse embryo the accelerator was operated in a regime of high stability yielding 533 consecutive shots with multi-GeV electron beams. The reproducibility and stability of electron acceleration was analysed to reveal underlying reasons affecting stability of operation. It was found the accelerator was operated in a saturated energy gain regime, where changes to plasma density were not correlated with cut-off energy. A significant correlation was observed between laser energy on target and the peak electron energy. The total beam charge was observed to not depend on either laser energy or plasma density.

8.2 Outlook and further work

The self-guiding performance characterised in this work showed guiding over unprecedented distances. However, in most cases it was found that the guiding distance is much longer than the laser depletion distance. Thus it would prove instructive to investigate self-guiding with lasers with similar power, but longer pulse lengths. A pulse length with duration $\sim 90\,\mathrm{fs}$ should theoretically yield a depletion distance twice of that measured in the current work. This could allow even longer self-guiding at low, $n_e \lesssim 1 \times 10^{18}\,\mathrm{cm}^{-3}$ plasma densities, potentially resulting in even larger energy gains.

The experimental demonstration of the advantageous effects of linear chirp is important as it provides future accelerator designers with another option to fine-tune the acceleration performance. It was shown that varying the chirp allows the amount of energy transferred to the plasma wave to be changed and thus yields more beam charge and higher electron beam energies. Having such control over electron beam properties in the blowout regime is extremely useful, potentially allowing energy gain tuning to correctly match later stage beam optics. In R&D fields, this can be extremely useful when testing scientific equipment or characterising the response of detectors.

The length scans performed within this work provide extremely detailed information about electron beam dynamics during acceleration with details about the injection dynamics also revealed. This data has highlighted the importance of laser evolution on the resulting electron beam energy gains. Such insights enable future accelerator designs to properly account for these effects and thus avoid deleterious effects arising from bubble evolution induced dephasing. Additionally, such detailed measurements allow for realistic benchmarking of particle-in-cell codes.

Measurements of highest reported values of self-guided, self-injected electron beams with sub-petawatt lasers was reported in the current work. This is an exciting result, showing more than a twofold increase in electron beam energy with a simple change of

focussing optic focal length. Such a result is thought to stem from the much smoother laser propagation as the Rayleigh range is quadrupled with the doubling of the focal length. This makes the accelerator much less sensitive to exact plane of focus of the laser. Additionally, it is thought that the smoother spatial profile before vacuum focus can lead to increased energy capture into the wake. This could be understood by thinking of the plasma density ramp as a fibre input coupler with a given numerical aperture. Matching the laser focus to that allows for the largest coupling efficiency into the supported guiding mode. This is on going work, with a simulation campaign under way to understand the capture efficiency of different plasma ramp lengths. Additionally, theoretical work in understanding coupling physics into a longitudinally varying focal distance coupler is also ongoing.

The observed suppression of self-injection opens the prospect to operate laser wakefield accelerators in the bubble regime while avoiding self-injection and thus degrading the injected beam quality. The advantages of the fully non-linear bubble regime are the linear and spatially independent accelerating and focussing fields; linear focussing forces lead to conservation of emittance. This allows for acceleration of elliptical beams and accurate energy spread control with chirped electron beams and load shape tailoring. While it has been shown that one of the advantages of the quasi-linear regime is the fact that transverse fields take the form $F_\perp \propto \nabla_\perp a_0^2$ and thus allow for tailoring of the focussing gradients,[259] we also recall that the laser profile will not stay static during the interaction.[260] The evolution of the laser spatial profile can thus lead to focussing properties that severely degrade the bunch quality. As the forces mainly arise from the ion column in the blowout regime, this effect is largely avoided.

Further work is to be done on fully characterising the suppression physics of self-injection. Crucially, the dependence of suppression on injected beam charge and load shape needs to be investigated to allow for the development of optimised acceleration. This can be studied with particle-in-cell simulations encompassing large parameter spaces. The effect of the initial density ramp needs to be considered and the emittance evolution of the electron bunch will be monitored to ensure no beam degradation. This modelling work is envisaged to lead to proof-of-principle experiments demonstrating explicitly emittance conservation and large energy gains in staged laser wakefield modules in the near future.

The demonstration of multi-gigaelectronvolt energy gains in a single self-guided stage also proves central to research into staging multiple laser wakefield accelerator modules. Ultrafast probing allowing *in situ* observation of beam dynamics[74] can prove

[259] C. B. Schroeder *et al*, *Phys Rev Spec Top-Ac* **13**, 2010.
[260] J Vieira *et al*, *Plasma Phys Contr F* **54**, 2012.
[74] A. Sävert *et al*, *Phys Rev Lett* **115**, 2015.

invaluable in properly understanding the matching of the electron bunch beta function into the accelerator stage. The large electron energy gains can then allow for work to be done on the extraction as well. The advantage compared to externally guided laser wakefield accelerators is tremendous here, as both the plasma and beam dynamics can be directly probed and compared to simulation results to verify the latter.

The efficiency of laser driven wakefield accelerators is an area that has seemingly seen relatively little interest devoted to it. Indeed, there is an extremely scant number of publications explicitly quoting laser energy conversion efficiencies. With so much work devoted to pushing the energy frontier this seems like a slight oversight; more work should be done to characterise this aspect of the accelerator. A detailed experimental study, beyond the matter of fact measurements presented in the current body of work, is envisaged to be undertaken in the near future to understand the experimental limitations on laser energy conversion efficiency. Again, the non-linear regime has been shown to have beneficial properties with increased beam loads when compared to linear regime. Such theoretical predictions need experimental verifications, though.

The field of laser wakefield accelerators is seeing a continual increase in institutions and people dedicated to it and progress is happening at an ever-increasing rate. This results in the wealth of understanding of the complex femtosecond interactions occurring during the interaction becoming better and better. The results presented in this thesis carry on this and have expanded the understanding of laser wakefield modules in the self-guided regime. Whilst some parameters of the generated beam are not suitable for laser wakefield accelerators to be employed as modules of a large-scale collider at the moment, these accelerators are proving invaluable with continual use in other applications. More work on the staging of independent modules and understanding the physics of electron beam coupling into complicated plasma ramps will allow the staging to be pushed forward. Meanwhile, much research into the optimisation of the beams from single plasma accelerator modules is underway as well. Such continual exploration of the physics of laser wakefield accelerators will allow the field to prosper and lead the way to a laser driven particle collider.

APPENDIX A
Symbols and constants

A.1 Frequently used symbols

List of frequently used symbols along with their meanings is in Table A.1.

a_0	normalised vector potential
Z	Nuclear charge of an atom
λ_L	laser wavelength in vacuum
k_L	laser wave vector
ω_L	angular frequency of laser
ω_p	electron plasma frequency
$\hat{\mathbf{i}}, \hat{\mathbf{j}}, \hat{\mathbf{k}}$	unit vectors along the x, y, z axis, respectively
E	Electric field
$\mathcal{E}$	Energy of a particle
n_e	Plasma electron density
φ	Spectral phase

Table A.1: *Frequently used symbols.*

A.2 Normalisations used in plasma physics

Plasma physics exhibits many self-similar solutions. Secondly, it is often easier to work in natural units. Normalisations used in plasma physics are shown below in Equation A.1. In addition to these, time is normalised to plasma frequency $t = t\omega_p$ and lengths are normalised to skin depth $k_p = \omega_p/c$, $x = xk_p$.

$$\begin{aligned} \mathbf{a} &= \frac{e\mathbf{A}}{m_e c^2} & \mathbf{v} &= \frac{\mathbf{v}}{c} \\ \phi &= \frac{e\phi}{m_e c^2} & \mathbf{p} &= \frac{\mathbf{p}}{mc} \end{aligned} \tag{A.1}$$

A.3 Fundamental constants

The values for fundamental physical constant used throughout this thesis are given in Table A.2.

Symbol	Name	Quantity	Unit
e	elementary charge	1.602×10^{-19}	C
m_e	rest mass of an electron	9.11×10^{-31}	kg
m_p	rest mass of a proton	1.67×10^{-27}	kg
$m_e c^2$	electron rest mass energy equivalent	511.1	keV
ϵ_0	permittivity of free space	8.85×10^{-12}	Fm^{-1}
μ_0	permeability of free space	$4\pi \times 10^{-7}$	Hm^{-1}
c	speed of light in vacuum	299 792 458	ms^{-1}
k_B	Boltzmann's constant	1.38×10^{-23}	JK^{-1}
h	Planck's constant	6.62×10^{-34}	Js

Table A.2: *Fundamental constants.*

APPENDIX B
Derivations

B.1 Maxwell's equations

Maxwell's equation are a set of differential equations governing the behaviour of electromagnetic fields:

$$\nabla \cdot \mathbf{E} = \frac{\rho}{\epsilon_0} \tag{B.1}$$

$$\nabla \cdot \mathbf{B} = 0 \tag{B.2}$$

$$\nabla \times \mathbf{E} = -\frac{\partial \mathbf{B}}{\partial t} \tag{B.3}$$

$$\nabla \times \mathbf{B} = \mu_0 \mathbf{J} + \mu_0 \epsilon_0 \frac{\partial \mathbf{E}}{\partial t}. \tag{B.4}$$

Equation B.1 is known as Gauss' Law. It states that charge is the source of electric fields – the divergence of $\mathbf{E}$ at any point is determined by charge distributions. Equation B.2 is sometimes known as Gauss' Law for magnetism, showing the lack of magnetic monopoles. Equation B.3 is Faraday's Law and Equation B.4 is Ampere's Law with Maxwell's correction. By introducing scalar potential ϕ and vector potential $\mathbf{A}$ the electric and magnetic fields can be rewritten as

$$\mathbf{E} = -\frac{\partial \mathbf{A}}{\partial t} - \nabla \phi \tag{B.5}$$

$$\mathbf{B} = \nabla \times \mathbf{A} \tag{B.6}$$

Maxwell's equations implicitly conserve charge. By taking the divergence of Equation B.4 and using Equation B.1 the current conservation equation is found,

$$\frac{\partial \rho}{\partial t} + \nabla \cdot \mathbf{J} = 0. \tag{B.7}$$

By invoking $\mathbf{J} = -en_e\mathbf{v}$, Equation B.7 can be recast to read

$$\frac{\partial n_e}{\partial t} + \nabla \cdot (n_e \mathbf{v}) = 0. \tag{B.8}$$

B.2 Derivation of orbits of a single electron in an electromagnetic plane wave

To find the trajectory of a charged particle in the electromagnetic field of a laser,[1] we consider a laser pulse that is travelling in the positive z direction and is given by $\mathbf{A} = (\delta a_0 \sin\varphi, (1-\delta^2)^{1/2} a_0 \cos\varphi, 0)$, where δ is a polarisation parameter with $\delta = \{\pm 1, 0\}$ for linear and $\delta = \sqrt{2}/2$ for circular polarisation. The scalar potential $\phi = 0$ and the vector potential is thus a travelling function with $\varphi = \omega_0 t - k_0 z$.

We now proceed by applying normalisations outlined in Section A.2, with $t = \omega_0 t$ and $z = k_0 z$.[2] Due to $\mathbf{a}$ not being a function of x and y, transverse components of Equation 2.4 reduce to

$$\frac{\mathrm{d}}{\mathrm{d}t}\frac{\partial \mathcal{L}}{\partial \mathbf{v}_\perp} = 0, \tag{B.9}$$

where $\mathbf{v}_\perp = (v_x, v_y)$. With the definition of canonical momentum from Equation 2.6, Equation B.9 becomes a conservation law for canonical momentum. Hence, we have

$$\mathbf{p}_\perp - \mathbf{a} = \mathbf{p}_{\perp 0} \tag{B.10}$$

where $\mathbf{p}_{\perp 0}$ is the transverse momentum of the electron before arrival of the laser pulse. Taking $\mathbf{p}_{\perp 0} = 0$ for an electron initially at rest, we have

$$p_x = a_x, \tag{B.11}$$

$$p_y = a_y. \tag{B.12}$$

From the above it is apparent that a_0 is also a measure of the quiver momentum of the particle. Hence, as $a_0 \to 1$, the electron's transverse momentum becomes comparable to its rest-mass and motion of the particle is relativistic.

From the definition of the hamiltonian in terms of the lagrangian it can be shown that[90]

$$\frac{\mathrm{d}\mathcal{H}}{\mathrm{d}t} = -\frac{\partial \mathcal{L}}{\partial t}. \tag{B.13}$$

With $\omega = k = 1$ we can write $\frac{\partial \mathcal{L}}{\partial t} = -\frac{\partial \mathcal{L}}{\partial z}$. Recognising $\mathcal{H}$ as the particle energy and

[1] Following the derivation in Ref 83

[2] This is equivalent to setting $\omega = k = c = e = m_e = 1$.

[90] P. Bellan. *Fundamentals of Plasma Physics*. Cambridge University Press, 2008.

using z component of Euler-Lagrange equation 2.4 we obtain

$$\frac{\mathrm{d}\mathcal{E}}{\mathrm{d}t} = \frac{\partial \mathcal{L}}{\partial z} = \frac{\mathrm{d}}{\mathrm{d}t}\frac{\partial \mathcal{L}}{\partial v_z} = \frac{\mathrm{d}p_z}{\mathrm{d}t}, \tag{B.14}$$

which can be recast to obtain a conservation law for for $\mathcal{E} - p_z$:

$$\frac{\mathrm{d}}{\mathrm{d}t}\left(\mathcal{E} - p_z\right) = 0. \tag{B.15}$$

With $m_e = c = 1$, $\mathcal{E} = \gamma$ and thus

$$\gamma - p_z = \alpha, \tag{B.16}$$

where α is a constant of motion depending on electron state before arrival of the laser. Combining the definition $1 + p_\perp^2 + p_z^2 = \gamma^2$ and Equation B.16 we obtain

$$p_z = \frac{1 - \alpha^2 + p_\perp^2}{2\alpha}. \tag{B.17}$$

Finally, to determine the trajectories of the particle we integrate the equations of motion with respect to phase. We first note that with $p_z = \gamma v_z$ we have

$$\frac{\mathrm{d}\varphi}{\mathrm{d}t} = \frac{\partial \varphi}{\partial t} + v_z\frac{\partial \varphi}{\partial z} = 1 + \frac{p_z}{\gamma}\frac{\partial \varphi}{\partial z} = 1 - \frac{\gamma - \alpha}{\gamma} = \frac{\alpha}{\gamma}. \tag{B.18}$$

With the above result we can express the electron's momentum as

$$\mathbf{p} = \gamma\frac{\mathrm{d}\mathbf{r}}{\mathrm{d}t} = \gamma\frac{\mathrm{d}\varphi}{\mathrm{d}t}\frac{\mathrm{d}\mathbf{r}}{\mathrm{d}\varphi} = \alpha\frac{\mathrm{d}\mathbf{r}}{\mathrm{d}\varphi}. \tag{B.19}$$

We now proceed to calculate the electron's trajectory in the laboratory frame by noting that for an electron at rest before the laser arrives, $p_\perp = 0$ and $p_z = 0$ and thus from Equation B.17 we have $\alpha = 1$. Momentum of the particle is given by

$$p_x = \delta a_0 \sin\varphi, \tag{B.20}$$

$$p_y = (1 - \delta^2)^{1/2} a_0 \cos\varphi, \tag{B.21}$$

$$p_z = \frac{a_0^2}{4}\left[1 + (2\delta^2 - 1)\cos 2\varphi\right], \tag{B.22}$$

which leads to the trajectories

$$x = -\delta a_0 \cos\varphi, \tag{B.23}$$

$$y = (1-\delta^2)^{1/2} a_0 \sin\varphi, \tag{B.24}$$

$$z = \frac{a_0^2}{8}\left[2\varphi + (2\delta^2 - 1)\sin 2\varphi\right]. \tag{B.25}$$

From Equation B.25 we observe that the electron obtains cycle-averaged longitudinal momentum. This can be characterised by a drift momentum $p_D = \gamma_D v_D$. Remembering that $\gamma = 1 + a^2/2$ we have

$$v_D = \frac{\langle p_z \rangle}{\langle \gamma \rangle} = \frac{\langle a^2/2 \rangle}{\langle 1 + a^2/2 \rangle} = \frac{a_0^2/4}{1 + a_0^2/4} = \frac{a_0^2}{4 + a_0^2} \tag{B.26}$$

as $\langle \cos^2\varphi \rangle = 1/2$.

We can also analyse the electron's motion in its average rest frame. In this frame, $\langle p_z \rangle = 0$, and thus from Equation B.17 we have

$$\alpha = \sqrt{1 + \langle p_\perp^2 \rangle} = \sqrt{1 + \frac{a_0^2}{2}} \equiv \gamma_0. \tag{B.27}$$

The particle's momentum is given by

$$p_x = \delta a_0 \sin\varphi, \tag{B.28}$$

$$p_y = (1-\delta^2)^{1/2} a_0 \cos\varphi, \tag{B.29}$$

$$p_z = \frac{a_0^2}{4\gamma_0}(2\delta^2 - 1)\cos 2\varphi. \tag{B.30}$$

Using B.19, we now arrive at the electron trajectories:

$$x = -\delta \frac{a_0}{\gamma_0} \cos\varphi, \tag{B.31}$$

$$y = (1-\delta^2)^{1/2} \frac{a_0}{\gamma_0} \sin\varphi, \tag{B.32}$$

$$z = \frac{a_0^2}{8\gamma_0^2}(2\delta^2 - 1)\sin 2\varphi. \tag{B.33}$$

B.3 Derivation of the plasma frequency

To derive an expression for the electron plasma frequency, we make the following assumptions:[170] the plasma is unmagnetised, $\mathbf{B} = 0$; the plasma is cold, $k_b T = 0$; the

[170] F. Chen. *Introduction to Plasma Physics and Controlled Fusion*. Springer, 1984.

ions remain fixed and provide a neutralising background; the plasma is infinite; and electric field oscillates in the x direction, $\mathbf{E} = E\,\hat{\mathbf{i}}$. Equation 2.7 for the Lorentz force becomes

$$m_e \left(\frac{\partial \mathbf{v}}{\partial t} + \mathbf{v} \cdot \nabla \cdot \mathbf{v} \right) = -e\mathbf{E}, \tag{B.34}$$

where use has been made of the convective derivative.

Since we are dealing with small oscillations about the equilibrium, we proceed by linearising the equations governing the electron: Eq B.34 for the Lorentz force, the continuity equation B.8 and Gauss' Law B.1. We then write quantities of interest as the sum of an equilibrium value and a small perturbation:

$$n_e = n_{e0} + n_{e1}, \qquad \mathbf{v} = \mathbf{v}_1 + \mathbf{v}_1, \qquad \mathbf{E} = \mathbf{E}_0 + \mathbf{E}_1. \tag{B.35}$$

The equilibrium values of the velocity and electric field are zero. In addition to this we assume the perturbations behave sinusoidally. We then have

$$n_e = n_{e0} + n_{e1} e^{i(kx-\omega t)}, \qquad \mathbf{v} = v_1 e^{i(kx-\omega t)} \hat{\mathbf{i}}, \qquad \mathbf{E} = E_1 e^{i(kx-\omega t)} \hat{\mathbf{i}}. \tag{B.36}$$

The linearised equations now read

$$\frac{\partial n_{e0}}{\partial t} + \frac{\partial n_{e1}}{\partial t} + \nabla \left[\mathbf{v}_1 (n_{e0} + n_{e1}) \right] = 0 \tag{B.37}$$

$$m_e \left(\frac{\partial \mathbf{v}_1}{\partial t} + \mathbf{v}_1 \cdot \nabla \cdot \mathbf{v}_1 \right) = -e\mathbf{E}_1 \tag{B.38}$$

$$\nabla \cdot \mathbf{E}_1 = \frac{e(n_i - n_{e0} - n_{e1})}{\epsilon_0}. \tag{B.39}$$

The derivatives of all equilibrium values are zero by definition. Due to the perturbations being small, terms which involve the product of two perturbed values are negligible. Also, due to initial quasi-neutrality $n_i = n_{e0}$ and the ions being stationary, the RHS in B.39 becomes $-en_{e1}/\epsilon_0$. By using $\frac{\partial}{\partial t} \to -i\omega$ and $\nabla \to i\mathbf{k}$ we obtain

$$-i\omega n_{e1} + n_{e0} ikv_1 = 0 \tag{B.40}$$

$$m_e(-i\omega v_1) = -eE_1 \tag{B.41}$$

$$\epsilon_0 ikE_1 = -en_{e1}, \tag{B.42}$$

which, when k and E_1 are eliminated, yield

$$ik\epsilon_0 \frac{im_e \omega v_1}{e} = -e \frac{n_{e0} k v_1}{\omega}. \tag{B.43}$$

Requiring a non-zero v_1 we obtain the plasma frequency as

$$\omega_p = \left(\frac{n_e e^2}{\epsilon_0 m_e}\right)^{1/2}. \tag{B.44}$$

B.4 Derivation of dispersion relation for electromagnetic radiation in plasmas

Consider an infinite electromagnetic plane wave with $\mathbf{E} = E_0 e^{i(\mathbf{k}\cdot\mathbf{r}-\omega_0 t)}\hat{\mathbf{i}}$ and $\mathbf{B} = B_0 e^{i(\mathbf{k}\cdot\mathbf{r}-\omega_0 t)}\hat{\mathbf{j}}$ propagating in a plasma. For $a_0 < 1$ the equation of motion 2.7 reduces to

$$m\frac{\partial \mathbf{v}}{\partial t} = -e\mathbf{E}, \tag{B.45}$$

which in turn can be written as

$$-i\omega_0 m\mathbf{v} = -e\mathbf{E} \quad \Longrightarrow \quad \mathbf{v} = -i\frac{e\mathbf{E}}{m\omega_0}. \tag{B.46}$$

By taking a curl of Faraday's Law B.3 we obtain

$$-\mathbf{k}\times(\mathbf{k}\times\mathbf{E}) = \omega_0 \mathbf{k}\times\mathbf{B}, \tag{B.47}$$

which, when using the vector identity $\mathbf{k}\times(\mathbf{k}\times\mathbf{E}) = \mathbf{k}(\mathbf{k}\cdot\mathbf{E}) - k^2\mathbf{E}$ and remembering $\mathbf{k}\cdot\mathbf{E} = 0$ for transverse waves, becomes

$$-k_0^2\mathbf{E} = \omega_0 \mathbf{k}\times\mathbf{B}. \tag{B.48}$$

We now substitute B.46 and B.48 along with $\mathbf{J} = -en_e\mathbf{v}$ into Ampere's Law (Equation B.4) to obtain

$$\frac{1}{\mu_0}\left(-\frac{k_0^2\mathbf{E}}{\omega_0}\right) = -en_e\left(-\frac{ie\mathbf{E}}{m\omega_0}\right) + \epsilon_0(-i\omega_0)\mathbf{E}. \tag{B.49}$$

Rearranging and recognising Equation B.44 gives dispersion relation for infinite plane waves propagating in a plasma:

$$\omega_0^2 = \omega_p^2 + c^2 k_0^2 \tag{B.50}$$

B.5 Derivation of 3D linear laser driven plasma wave

We start by considering the Lorentz force on a fluid electron, along with the continuity equation B.7 and Gauss' Law B.1. Lorentz force on plasma fluid reads

$$m_e \left[\frac{\partial \mathbf{u}}{\partial t} + (\mathbf{u} \cdot \nabla)\, \mathbf{u} \right] = -e \left(\mathbf{E} + \mathbf{u} \times \mathbf{B} \right). \tag{B.51}$$

From the definition of $\mathbf{a}$ we have $\mathbf{a} \equiv \mathbf{u}_\perp / c$ such that we can write $\mathbf{u} = e\mathbf{A}/m_e$. With $\mathbf{B} = \nabla \times \mathbf{A}$ Equation B.51 becomes

$$m_e \frac{\partial \mathbf{u}}{\partial t} = -e\mathbf{E} - \frac{e^2}{m_e} \left[(\mathbf{A} \cdot \nabla)\, \mathbf{A} + \mathbf{A} \times (\nabla \times \mathbf{A}) \right]. \tag{B.52}$$

We now make use of the vector identity $\nabla \mathbf{A}^2/2 = \mathbf{A} \times (\nabla \times \mathbf{A}) + (\mathbf{A} \cdot \nabla)\, \mathbf{A}$ and normalise $\mathbf{A}$ to arrive at

$$m_e \frac{\partial \mathbf{u}}{\partial t} = -e\mathbf{E} - \frac{1}{2} m_e c^2 \nabla \mathbf{a}^2. \tag{B.53}$$

By evoking $\rho = -e(n_e - n_i)$ and $\mathbf{J} = -e n_e \mathbf{u}$ we can rewrite continuity equation as

$$-e \frac{\partial}{\partial t}(n_e - n_i) - e \nabla \left(n_e \mathbf{u} \right) = 0. \tag{B.54}$$

We also have Gauss' law that can be written as

$$\nabla \cdot \mathbf{E} = \frac{-e(n_e - n_i)}{\epsilon_0}. \tag{B.55}$$

We proceed by linearising[3] Equations B.53, B.54 and B.55 to yield

$$m_e \frac{\partial \mathbf{u}_1}{\partial t} = -e\mathbf{E}_1 - \frac{1}{2} m_e c^2 \nabla \mathbf{a} \tag{B.56}$$

$$\frac{\partial n_1}{\partial t} + n_0 \nabla \mathbf{u}_1 = 0 \tag{B.57}$$

$$\nabla \cdot \mathbf{E}_1 = -\frac{e n_1}{\epsilon_0}. \tag{B.58}$$

We now operate on Equation B.56 with the $\nabla\cdot$ operator and on B.57 with $\partial/\partial t$. We can then combine the resulting equations to yield

$$-m_e \frac{1}{n_0} \frac{\partial^2 n_1}{\partial t^2} = \frac{e^2}{m_e} n_1 - \frac{1}{2} m_e c^2 \nabla a^2 \tag{B.59}$$

[3] cf Section B.3

which can be rewritten as

$$\left(\frac{\partial^2}{\partial t^2} + \omega_p^2\right)\frac{n_1}{n_o} = \frac{1}{2}c^2\nabla a^2. \tag{B.60}$$

We can use Poisson's Equation to find describe the potential of the wave,

$$\nabla^2\phi = -\frac{\rho}{\epsilon_0}, \tag{B.61}$$

which under linearisation becomes $\nabla^2\phi = en_1/\epsilon_0$. Applying the normalisation outlined in Section A.2 we can write the normalised potential as

$$\nabla^2\phi = \frac{e^2 n_1}{m_e c^2 \epsilon_0} \implies \frac{n_1}{n_0} = \nabla^2\phi\frac{c^2}{\omega_p^2} \tag{B.62}$$

and thus Equation B.60, once integrated, becomes an equation for potential in the plasma wave:

$$\left(\frac{\partial^2}{\partial t^2} + \omega_p^2\right)\phi = \frac{\omega_p^2}{2}a^2. \tag{B.63}$$

Equations B.60 and B.63 are inhomogeneous Helmholtz equations and can be solved with Green's functions. The solutions, describing a 3D linear plasma wave, valid for $a_0 \ll 1$ are given by

$$\frac{n_1}{n_0} = \frac{c^2}{\omega_p}\int_0^t \mathrm{d}t' \sin[\omega_p(t-t')]\nabla^2\frac{a^2}{2} \tag{B.64}$$

$$\phi = \omega_p\int_0^t \mathrm{d}t' \sin[\omega_p(t-t')]\frac{a^2}{2} \tag{B.65}$$

B.6 Quasi static approximation

A very useful approximation to deal with short pulse phenomena in plasmas is the quasi static approximation[96,261]. When transforming into a frame comoving with the laser pulse, such that $\xi = z - v_g t$ and $\tau = t$, all plasma fluid equations are written in terms of ξ and τ. The assumption is that the laser pulse evolution is much slower than the time for plasma electron response. Hence, the plasma electrons feel a static laser pulse, ie the laser pulse does not evolve and $\partial/\partial\tau$ derivatives can be ignored. As the approximation only relates to plasma response, the $\partial/\partial\tau$ derivatives are not dropped in the wave equation.

The spatial and temporal derivatives for plasma quantities in the comoving frame

[96] P Sprangle *et al*, *Phys Rev Lett* **64**, 1990.
[261] A. Ting *et al*, *Phys Fluids B-Plasma* **2**, 1990.

thus become

$$\frac{\partial}{\partial t} = \frac{\partial \xi}{\partial t}\frac{\partial}{\partial \xi} + \frac{\partial \tau}{\partial t}\frac{\partial}{\partial \tau} = -v_g\frac{\partial}{\partial \xi} + \frac{\partial}{\partial \tau} \approx -c\frac{\partial}{\partial \xi}, \tag{B.66}$$

$$\frac{\partial}{\partial z} = \frac{\partial \xi}{\partial z}\frac{\partial}{\partial \xi} = \frac{\partial}{\partial \xi}, \tag{B.67}$$

where $v_g \approx c$ was used in Equation B.66.

APPENDIX C

Size and shape of focal spots

The focal spot profile, size and intensity play the highest role in determining the dynamics of high power laser plasma interactions. However, there exists a large disparity in the literature in reporting the parameters of the focal spot employed in the experiment. Authors most frequently report the beam waist, the radius at which intensity has fallen to $1/e^2$ of its peak value. However, often either the full-width-half-maximum (FWHM) or half-width-half-maximum is reported, with some reports only discussing the "size of the focal spot". Also, the energy contained within the FWHM contour is often quoted to be larger than is physically possible for standard focussing configurations (i.e. without using a phase plate).

With this in mind, we discuss some fundamental parameters of commonly used focal spots, namely the top-hat and gaussian near field. The focal spot size at different fractional intensities along with the fraction of energy contained within the contour is presented. The effects of using a limited dynamic range in measuring enclosed energy are discussed.

The distribution of radiation at the focal plane of a lens can be calculated by using the Fraunhofer approximation.[156] Assuming a 2D geometry with coordinates x and y in the near field, the diffraction pattern $U(p,q)$ in the far field, described by coordinates p and q, is given by

$$U(p,q) = \int_{\text{Aperture}} A(x,y) e^{-ik\frac{xp+yq}{F}} \mathrm{d}x\mathrm{d}y, \tag{C.1}$$

where $A(x,y)$ is the aperture function and F is the observation distance, set equal to focal length of the optic here.

[156] M. Born *et al.* *Principles of Optics: Electromagnetic Theory of Propagation, Interference and Diffraction of Light.* Cambridge University Press, 1999.

C.1 Gaussian nearfield

Firstly, it is instructive to discuss the behaviour and size focal spots formed by gaussian near fields. As the focal plane spatial distribution is a Fourier transform of the near field, the focus of a gaussian beam stays gaussian. Using polar coordinates, the intensity at the focal plane is a function of r alone, given by

$$I(r,\phi) = I_{\text{peak}} e^{-2\frac{r^2}{w_0^2}}. \tag{C.2}$$

Here, I_{peak} is peak intensity and w_0 is the beam waist. This is the distance at which the electric field falls to a value of $1/e$ of its peak; for the intensity distribution this is the radius at which $I = I_{\text{peak}}/e^2$. The beam waist is the standard way to describe gaussian beams and is ubiquitously in laser physics. Table C.1 provides conversion factors between other intensity levels for a gaussian beam. The most notable one is the FWHM, the full width of the intensity pattern, given by $\text{FWHM} = w_0\sqrt{2\log 2}$. In general, for an intensity level of Λ, the corresponding full-width in terms of the beam waist w_0 is $w_0\sqrt{2\log(1/\Lambda)}$.

Energy within a radius r_0 from the beam axis can be found by integrating the intensity over infinitesimal area elements. The fraction of energy enclosed in radius r_0 is given by

$$\eta(r_0) = \frac{1}{\mathcal{E}_0}\int_0^{2\pi}\int_0^{r_0} I(r,\phi)\cdot r\,\mathrm{d}r\,\mathrm{d}\phi, \tag{C.3}$$

where $\mathcal{E}_0$ is the total enclosed energy, given by letting $r_0 \to \infty$. Rearranging, and using Equation C.2, we obtain

$$\eta(r_0) = 1 - e^{-2\frac{r_0^2}{w_0^2}}. \tag{C.4}$$

Thus, within an intensity contour of 50% half of the total energy is enclosed. Different values of enclosed energy for various intensity contours are shown in Table C.2.

	FWHM ($I_{\text{peak}}/2$)	w_I (I_{peak}/e)	w_0 (I_{peak}/e^2)
FWHM	1	$2\sqrt{\log 2}$	$\sqrt{2\log 2}$
w_I	$\frac{1}{2\sqrt{\log 2}}$	1	$\sqrt{2}$
w_0	$\frac{1}{\sqrt{2\log 2}}$	$\frac{1}{\sqrt{2}}$	1

Table C.1: *Conversion factors between different extents of a gaussian intensity profile. As an example, the beam waist w_0 is calculated from the FWHM diameter as $w_0 = \text{FWHM}/\sqrt{2\log 2}$.*

C.2 Top hat nearfield

Most high power lasers use nearly top hat nearfield to extract maximum energy from crystals. The Fraunhofer integral in Equation C.1 becomes, for intensity in the far field:

$$I(r,\phi) = I_{\text{peak}} \left[\frac{2J_1(\rho)}{\rho}\right]^2, \tag{C.5}$$

where J_1 is the Bessel function of the first kind of order one and $\rho = k_L R \sin\theta$. The variable ρ describes a normalised radius in the far field and R is the radius of the aperture, i.e. the beam. Given the paraxial approximation, $\sin\theta = r/F$, we have $\rho = \pi D r/(\lambda_L F) = \pi r/(\lambda_L f)$ with $D = 2R$ being the diameter of the beam and F the focal length; the usual definition of the focal number f was also used. Unsurprisingly, the final result exhibits self-similarity and the spot size increases with increasing focal ratio. The peak intensity when focussing a beam of power P_L with an optic with $f/\#$ of f is given by

$$I_{\text{peak}} = \frac{P_L S}{\lambda_L^2 f^2}, \tag{C.6}$$

where $S = \pi D^2/4$ is the beam area.

The enclosed energy is again found by employing Equation C.3. Also making use of properties of Bessel functions, we arrive at

$$\eta(r_0) = 1 - J_0^2(\rho_0) - J_1^2(\rho_0), \tag{C.7}$$

with $\rho_0 = \pi r_0/(\lambda_L f)$. Figure C.1a shows an "oversatured" image of a calculated Airy pattern. With the maximum value of the image set to 0.005 of peak value the dark bands are clearly visible. Figure C.1b shows the intensity and enclosed dependence on radial coordinate ρ. The first three dark bands are at radii $1.22\pi, 2.233\pi$ and 3.238π and contain 83.8%, 91.0%, and 93.8% of the total energy,respectively. The radii of the first two dark bands are shown as the vertical dashed lines in Figure C.1b. The solid vertical line is plotted at the radius where intensity falls to 50%, showing that less than 50% of the total energy is contained within that radius. The exact values for amount

	I/I_0	Gaussian focus	Airy pattern
FWHM	50%	50%	47.4%
$1/e$	36.8%	63.2%	58.8%
$1/e^2$	13.5%	86.5%	76.6%

Table C.2: *Values of enclosed energy within the FWHM, $1/e$ and $1/e^2$ contours for gaussian focal spots and for the Airy pattern.*

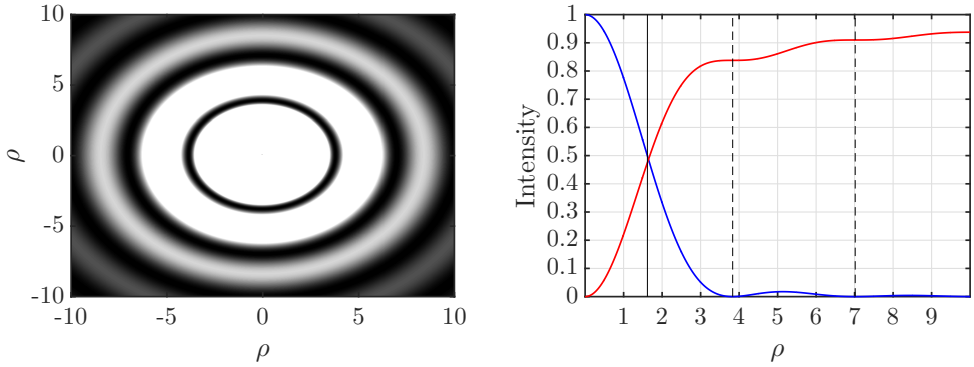

(a) *Intensity distribution* ***(b)*** *Radial intensity distribution*

Figure C.1: *Intensity distribution (a) and radial dependence of intensity and enclosed energy (b) for an Airy pattern type focal spot. The colourtable has been saturated to highlight the existence of the dark bands in Panel (a). The first dark band is centred on $\rho = 1.22\pi$ and 83.2% of the total energy is in the central spot.*

of energy within a contour are shown in Table C.2 and highlight the effect of energy displaced from the central spot. A gaussian spot contains 13% more energy within the $1/e^2$ contour than an Airy pattern. For a diffraction limited Airy pattern, the FWHM diameter of the spot is given by $d_{\mathrm{FWHM}} = 1.029\lambda_L f$. The $1/e$ and $1/e^2$ radii of the intensity pattern are given by $w_I = 0.610\lambda_L f$ and $w_0 = 0.823\lambda_L f$; here f is the focal ratio $f = F/D$.

Bibliography

[1] E. Rutherford. *Philosophical Magazine Series 6*. **21**, pp. 669–688. 1911. (see p. 17)
"LXXIX. The scattering of α and β particles by matter and the structure of the atom"
URL: http://dx.doi.org/10.1080/14786440508637080.

[2] T. Shears. *Philosophical Transactions of the Royal Society A*. **370**, pp. 805–817. 2012. (see p. 17)
"The Standard Model"
URL: http://rsta.royalsocietypublishing.org/cgi/doi/10.1098/rsta.2011.0314.

[3] G. Aad *et al.* *Physical Review Letters*. **114**, p. 191803. 2015. (see p. 17)
"Combined Measurement of the Higgs Boson Mass in pp Collisions at $\sqrt{s} = 7$ and 8 TeV with the ATLAS and CMS Experiments"
URL: http://link.aps.org/doi/10.1103/PhysRevLett.114.191803.

[4] *The Internatioal Linear Collider Technical Design Report*. Tech. rep. ILC, June 2013. URL: https://www.linearcollider.org/ILC/Publications/Technical-Design-Report (see pp. 17, 18).

[5] *A Multi-TeV Linear Collider based on CLIC Technology: CLIC Conceptual Design Report*. Tech. rep. CERN-2012-007. CERN, Jan. 2012. URL: http://project-clic-cdr.web.cern.ch/project-CLIC-CDR/CDR_Volume1.pdf (see pp. 17, 18, 21, 222).

[6] A. Ball *et al.* "Future Circular Collider Study". In: *Future Circular Collider Study Kickoff Meeting*. Feb. 2014 (see p. 17).

[7] W. H. Scharf. *Biomedical particle accelerators*. American Institute of Physics, 1993. (see p. 17).

[8] L. V. DE Broglie. *Annales de Physique*. **3**. 1925. (see p. 18)
"RECHERCHES SUR LA THE ORIE DES QUANTA".

[9] J. D. Cockcroft and E. T. S. Walton. *Proceedings of the Royal Society A: Mathematical, Physical and Engineering Sciences*. **129**, pp. 477–489. 1930. (see pp. 18, 19)
"Experiments with High Velocity Positive Ions"
URL: http://rspa.royalsocietypublishing.org/cgi/doi/10.1098/rspa.1930.0169.

[10] J. D. Cockcroft and E. T. S. Walton. *Proceedings of the Royal Society A: Mathematical, Physical and Engineering Sciences*. **136**, pp. 619–630. 1932. (see p. 19)
"Experiments with High Velocity Positive Ions. (I) Further Developments in the Method of Obtaining High Velocity Positive Ions"
URL: http://rspa.royalsocietypublishing.org/cgi/doi/10.1098/rspa.1932.0107.

[11] CERN. *The scale of the LHC*. URL: http://cds.cern.ch/record/42370 (visited on 09/18/2016) (see p. 19).

[12] V. I. Veksler. *J. Phys.* **9**, pp. 153–158. 1945. (see p. 19)
"A new method of acceleration of relativistic particles"
URL: http://cds.cern.ch/record/109364.

[13] E. M. McMillan. *Physical Review*. **68**, pp. 143–144. 1945. (see p. 19)
"The SynchrotronA Proposed High Energy Particle Accelerator"
URL: http://link.aps.org/doi/10.1103/PhysRev.68.143.

[14] N. Christofilos. *Focussing system for ions and electrons*. US Patent 2,736,799. 1956. URL: http://www.google.co.uk/patents/US2736799 (see p. 19).

[15] E. D. Courant, M. S. Livingston, and H. S. Snyder. *Physical Review*. **88**, pp. 1190–1196. 1952. (see p. 19)
"The Strong-Focusing SynchrotonA New High Energy Accelerator"
URL: http://link.aps.org/doi/10.1103/PhysRev.88.1190.

[16] S. M. Livingston. *High-energy accelerators*. Interscience Publishers, 1954. (see p. 19).

[17] W. K. Panofsky. *SLAC Beam Line*. 1997. (see p. 20)
"Evolution of Particle Accelerators".

[18] A. Chao *et al. eConf*. **C010630**, MT1001. 2001. (see p. 20)
"2001 Snowmass Accelerator R & D report"
URL: http://www.slac.stanford.edu/econf/C010630/proceedings.shtml.

[19] M. Tigner. *Physics Today*. **54**, pp. 36–40. 2001. (see p. 20)
"Does accelerator-based particle physics have a future?"
URL: http://scitation.aip.org/content/aip/magazine/physicstoday/article/54/1/10.1063/1.1349610.

[20] A. Grudiev, S. Calatroni, and W. Wuensch. *Physical Review Special Topics - Accelerators and Beams*. **12**, p. 102001. 2009. (see p. 21)
"New local field quantity describing the high gradient limit of accelerating structures"
URL: http://link.aps.org/doi/10.1103/PhysRevSTAB.12.102001.

[21] R. W. Aßmann. "Review of Ultra high-gradient acceleration schemes, results of experiments". In: *Proceedings of EPAC 2002*. 2002 (see p. 21).

[22] T. Tajima and J. Dawson. *Physical Review Letters*. **43**, pp. 267–270. 1979. (see pp. 21, 23, 24, 54, 59)
"Laser electron accelerator"
URL: http://link.aps.org/doi/10.1103/PhysRevLett.43.267.

[23] P. Chen *et al. Physical Review Letters*. **54**, pp. 693–696. 1985. (see p. 21)
"Acceleration of Electrons by the Interaction of a Bunched Electron Beam with a Plasma"
URL: http://link.aps.org/doi/10.1103/PhysRevLett.54.693.

[24] Y. B. Fainberg *et al. Fizika Plazmy*. **20**, pp. 674–681. 1994. (see p. 22)
"Wakefield acitation in plasma by a train of relativistic electron bunches".

[25] J. B. Rosenzweig *et al. Physical Review Letters*. **61**, pp. 98–101. 1988. (see p. 22)
"Experimental Observation of Plasma Wake-Field Acceleration"
URL: http://link.aps.org/doi/10.1103/PhysRevLett.61.98.

[26] I. Blumenfeld *et al. Nature*. **445**, pp. 741–4. 2007. (see p. 22)
"Energy doubling of 42 GeV electrons in a metre-scale plasma wakefield accelerator."
URL: http://www.ncbi.nlm.nih.gov/pubmed/17301787.

[27] DESY. *The FLASHForward Project*. URL: https://vi-pwfa.desy.de/e192843/ (visited on 09/18/2016) (see p. 22).

[28] R Assmann *et al. Plasma Physics and Controlled Fusion*. **56**, p. 084013. 2014. (see p. 22)
"Proton-driven plasma wakefield acceleration: a path to the future of high-energy particle physics"
URL: http://iopscience.iop.org/article/10.1088/0741-3335/56/8/084013/meta.

[29] Diamond. *Diamond facts*. URL: http://www.diamond.ac.uk/Home/About/FAQs/General.html (visited on 09/18/2016) (see pp. 22, 23).

[30] M. Rosenbluth and C. Liu. *Physical Review Letters*. **29**. 1972. (see p. 23)
"Excitation of plasma waves by two laser beams"
URL: http://link.aps.org/doi/10.1103/PhysRevLett.29.701.

[31] Y Kitagawa, T Matsumoto, and T Minamihata. *Physical Review Letters*. **68**, pp. 8–11. 1992. (see p. 23)
"Beat-wave excitation of plasma wave and observation of accelerated electrons"
URL: http://link.aps.org/doi/10.1103/PhysRevLett.68.48.

[32] C. E. Clayton *et al. Physics of Plasmas*. **1**, p. 1753. 1994. (see pp. 23, 26)
"Acceleration and scattering of injected electrons in plasma beat wave accelerator experiments"
URL: http://scitation.aip.org/content/aip/journal/pop/1/5/10.1063/1.870679.

[33] S. Y. Tochitsky *et al. Physical Review Letters*. **92**, p. 095004. 2004. (see p. 23)
"Enhanced Acceleration of Injected Electrons in a Laser-Beat-Wave-Induced Plasma Channel"
URL: http://link.aps.org/doi/10.1103/PhysRevLett.92.095004.

[34] C. Joshi. *Physics of Plasmas*. **14**, p. 055501. 2007. (see p. 23)
"The development of laser- and beam-driven plasma accelerators as an experimental field"
URL: http://scitation.aip.org/content/aip/journal/pop/14/5/10.1063/1.2721965.

[35] E. Esarey and A. Ting. *Physical Review Letters*. **65**, pp. 1961–1961. 1990. (see p. 24)
"Comment on "Cascade Focusing in the Beat-Wave Accelerator""
URL: http://link.aps.org/doi/10.1103/PhysRevLett.65.1961.

[36] J. Krall *et al. Physical Review E.* **48**, pp. 2157–2161. 1993. (see p. 24)
"Enhanced acceleration in a self-modulated-laser wake-field accelerator"
URL: http://link.aps.org/doi/10.1103/PhysRevE.48.2157.

[37] K. Nakajima, D. Fisher, and T. Kawakubo. *Physical Review Letters.* **74**, pp. 4428–4431. 1995. (see p. 24)
"Observation of ultrahigh gradient electron acceleration by a self-modulated intense short laser pulse"
URL: http://link.aps.org/doi/10.1103/PhysRevLett.74.4428.

[38] A. Modena *et al. Nature.* **377**, pp. 606–608. 1995. (see pp. 24, 65)
"Electron acceleration from the breaking of relativistic plasma waves"
URL: http://www.nature.com/doifinder/10.1038/377606a0.

[39] D. Gordon *et al. Physical Review Letters.* **80**, pp. 2133–2136. 1998. (see p. 24)
"Observation of Electron Energies Beyond the Linear Dephasing Limit from a Laser-Excited Relativistic Plasma Wave"
URL: http://link.aps.org/doi/10.1103/PhysRevLett.80.2133.

[40] V. Malka *et al. Physics of Plasmas.* **8**, p. 2605. 2001. (see p. 24)
"Characterization of electron beams produced by ultrashort (30 fs) laser pulses"
URL: http://scitation.aip.org/content/aip/journal/pop/8/6/10.1063/1.1374584.

[41] L. Gorbunov and V. Kirsanov. *Soviet Physics JETP.* **66**, pp. 290–294. 1987. (see pp. 24, 40, 43, 55)
"Excitation of plasma waves by an electromagnetic wave packet"
URL: http://www.jetp.ac.ru/cgi-bin/e/index/e/66/2/p290?a=list.

[42] P. Sprangle *et al. Applied Physics Letters.* **53**, p. 2146. 1988. (see pp. 24, 40)
"Laser wakefield acceleration and relativistic optical guiding"
URL: http://scitation.aip.org/content/aip/journal/apl/53/22/10.1063/1.100300.

[43] H Hamster *et al. Physical Review Letters.* **71**, pp. 2725–2728. 1993. (see p. 24)
"Subpicosecond, electromagnetic pulses from intense laser-plasma interaction"
URL: http://link.aps.org/doi/10.1103/PhysRevLett.71.2725.

[44] J. R. Marquès *et al. Physical Review Letters.* **76**, pp. 3566–3569. 1996. (see pp. 24, 115)
"Temporal and Spatial Measurements of the Electron Density Perturbation Produced in the Wake of an Ultrashort Laser Pulse"
URL: http://link.aps.org/doi/10.1103/PhysRevLett.76.3566.

[45] C. W. Siders *et al. Physical Review Letters.* **76**, pp. 3570–3573. 1996. (see pp. 24, 115)
"Laser Wakefield Excitation and Measurement by Femtosecond Longitudinal Interferometry"
URL: http://link.aps.org/doi/10.1103/PhysRevLett.76.3570.

[46] F. Amiranoff *et al. Physical Review Letters.* **81**, pp. 995–998. 1998. (see pp. 24–26)
"Observation of Laser Wakefield Acceleration of Electrons"
URL: http://link.aps.org/doi/10.1103/PhysRevLett.81.995.

[47] Y. Kitagawa *et al. Physical Review Letters.* **92**, p. 205002. 2004. (see p. 24)
"Electron Acceleration in an Ultraintense-Laser-Illuminated Capillary"
URL: http://link.aps.org/doi/10.1103/PhysRevLett.92.205002.

[48] P. Mora and T. M. Antonsen. *Physical Review E.* **53**, pp. 2068–2071. 1996. (see pp. 25, 44, 111)
"Electron cavitation and acceleration in the wake of an ultraintense, self-focused laser pulse"
URL: http://link.aps.org/doi/10.1103/PhysRevE.53.R2068.

[49] A. Pukhov and J. Meyer-ter Vehn. *Applied Physics B: Lasers and Optics.* **74**, pp. 355–361. 2002. (see pp. 25, 44, 65, 111)
"Laser wake field acceleration: the highly non-linear broken-wave regime"
URL: http://link.springer.com/10.1007/s003400200795.

[50] S. P. D. Mangles *et al. Nature.* **431**, pp. 535–538. 2004. (see pp. 25, 26, 66, 67)
"Monoenergetic beams of relativistic electrons from intense laserplasma interactions"
URL: http://www.nature.com/nature/journal/v431/n7008/abs/nature02939.html.

[51] J. Faure *et al. Nature.* **431**, pp. 541–544. 2004. (see pp. 25, 26, 66, 67)
"A laserplasma accelerator producing monoenergetic electron beams"
URL: http://www.nature.com/nature/journal/v431/n7008/abs/nature02963.html.

[52] C. G. R. Geddes *et al. Nature.* **431**, pp. 538–541. 2004. (see pp. 25, 26)
"High-quality electron beams from a laser wakefield accelerator using plasma-channel guiding"
URL: http://www.nature.com/nature/journal/v431/n7008/abs/nature02900.html.

[53] W. P. Leemans *et al. Physical Review Letters.* **113**, p. 245002. 2014. (see pp. 25, 27, 183, 229)
"Multi-GeV Electron Beams from Capillary-Discharge-Guided Subpetawatt Laser Pulses in the Self-Trapping Regime"
URL: http://link.aps.org/doi/10.1103/PhysRevLett.113.245002.

[54] W. P. Leemans *et al. Nature Physics.* **2**, pp. 696–699. 2006. (see pp. 25, 224)
"GeV electron beams from a centimetre-scale accelerator"
URL: http://www.nature.com/doifinder/10.1038/nphys418.

[55] C. E. Clayton *et al. Physical Review Letters.* **105**, p. 105003. 2010. (see pp. 25, 26, 166, 172)
"Self-Guided Laser Wakefield Acceleration beyond 1 GeV Using Ionization-Induced Injection"
URL: http://link.aps.org/doi/10.1103/PhysRevLett.105.105003.

[56] X. Wang *et al. Nature Communications.* **4**. 2013. (see pp. 25, 66, 67, 183)
"Quasi-monoenergetic laser-plasma acceleration of electrons to 2 GeV"
URL: http://www.nature.com/doifinder/10.1038/ncomms2988.

[57] J. Osterhoff *et al. Physical Review Letters.* **101**, p. 085002. 2008. (see pp. 25, 103)
"Generation of Stable, Low-Divergence Electron Beams by Laser-Wakefield Acceleration in a Steady-State-Flow Gas Cell"
URL: http://link.aps.org/doi/10.1103/PhysRevLett.101.085002.

[58] S. P. D. Mangles *et al. Plasma Physics and Controlled Fusion.* **48**, B83–B90. 2006. (see p. 25)
"Effect of laser contrast ratio on electron beam stability in laser wakefield acceleration experiments"
URL: http://iopscience.iop.org/article/10.1088/0741-3335/48/12B/S08/meta.

[59] S. Banerjee *et al. Physical Review Special Topics - Accelerators and Beams.* **16**, p. 031302. 2013. (see p. 25)
"Stable, tunable, quasimonoenergetic electron beams produced in a laser wakefield near the threshold for self-injection"
URL: http://link.aps.org/doi/10.1103/PhysRevSTAB.16.031302.

[60] J. M. Cole. "Diagnosis and Application of Laser Wakefield Accelerators". Imperial College London, 2015. (see pp. 25, 92, 106).

[61] I. Kostyukov *et al. Physical Review Letters.* **103**, p. 175003. 2009. (see pp. 26, 65, 229)
"Electron Self-Injection in Multidimensional Relativistic-Plasma Wake Fields"
URL: http://link.aps.org/doi/10.1103/PhysRevLett.103.175003.

[62] S. Kalmykov *et al. Physical Review Letters.* **103**, p. 135004. 2009. (see pp. 26, 66, 67)
"Electron Self-Injection and Trapping into an Evolving Plasma Bubble"
URL: http://link.aps.org/doi/10.1103/PhysRevLett.103.135004.

[63] W. Lu *et al. Physical Review Special Topics - Accelerators and Beams.* **10**, p. 061301. 2007. (see pp. 26, 55, 58–60, 127, 129, 138, 140, 229)
"Generating multi-GeV electron bunches using single stage laser wakefield acceleration in a 3D nonlinear regime"
URL: http://link.aps.org/doi/10.1103/PhysRevSTAB.10.061301.

[64] E. Esarey *et al. Physical Review Letters.* **79**, pp. 2682–2685. 1997. (see p. 26)
"Electron injection into plasma wakefields by colliding laser pulses"
URL: http://link.aps.org/doi/10.1103/PhysRevLett.79.2682.

[65] J Faure *et al. Nature.* **444**, pp. 737–739. 2006. (see p. 26)
"Controlled injection and acceleration of electrons in plasma wakefields by colliding laser pulses"
URL: http://www.nature.com/doifinder/10.1038/nature05393.

[66] S. Bulanov *et al. Physical Review E.* **58**, R5257–R5260. 1998. (see p. 26)
"Particle injection into the wave acceleration phase due to nonlinear wake wave breaking"
URL: http://link.aps.org/doi/10.1103/PhysRevE.58.R5257.

[67] A Buck *et al. Physical Review Letters.* **110**, p. 185006. 2013. (see p. 26)
"Shock-Front Injector for High-Quality Laser-Plasma Acceleration"
URL: http://link.aps.org/doi/10.1103/PhysRevLett.110.185006.

[68] M. Burza *et al. Physical Review Special Topics - Accelerators and Beams.* **16**, p. 011301. 2013. (see p. 26)
"Laser wakefield acceleration using wire produced double density ramps"
URL: http://link.aps.org/doi/10.1103/PhysRevSTAB.16.011301.

[69] D. Umstadter, J. K. Kim, and E. Dodd. *Physical Review Letters.* **76**, pp. 2073–2076. 1996. (see p. 26)
"Laser Injection of Ultrashort Electron Pulses into Wakefield Plasma Waves"
URL: http://link.aps.org/doi/10.1103/PhysRevLett.76.2073.

[70] C. Max, J Arons, and A. Langdon. *Physical Review Letters*. **33**, pp. 209–212. 1974. (see pp. 27, 51)
"Self-modulation and self-focusing of electromagnetic waves in plasmas"
URL: http://link.aps.org/doi/10.1103/PhysRevLett.33.209.

[71] G. Z. Sun *et al*. *Physics of Fluids*. **30**, p. 526. 1987. (see pp. 27, 52)
"Self-focusing of short intense pulses in plasmas"
URL: http://link.aip.org/link/?PFLDAS/30/526/1.

[72] J. E. Ralph *et al*. *Physical Review Letters*. **102**, p. 175003. 2009. (see pp. 27, 115)
"Self-Guiding of Ultrashort, Relativistically Intense Laser Pulses through Underdense Plasmas in the Blowout Regime"
URL: http://link.aps.org/doi/10.1103/PhysRevLett.102.175003.

[73] A. Butler, D. J. Spence, and S. M. Hooker. *Physical Review Letters*. **89**, p. 185003. 2002. (see p. 27)
"Guiding of High-Intensity Laser Pulses with a Hydrogen-Filled Capillary Discharge Waveguide"
URL: http://link.aps.org/doi/10.1103/PhysRevLett.89.185003.

[74] A. Sävert *et al*. *Physical Review Letters*. **115**, p. 055002. 2015. (see pp. 27, 66, 67, 85, 163, 200, 233)
"Direct Observation of the Injection Dynamics of a Laser Wakefield Accelerator Using Few-Femtosecond Shadowgraphy"
URL: http://link.aps.org/doi/10.1103/PhysRevLett.115.055002.

[75] W. P. Leemans and E. Esarey. *Physics Today*. **62**, pp. 44–49. 2009. (see pp. 28, 165)
"Laser-driven plasma-wave electron accelerators"
URL: http://scitation.aip.org/content/aip/magazine/physicstoday/article/62/3/10.1063/1.3099645.

[76] S. Steinke *et al*. *Nature*. **530**, pp. 190–193. 2016. (see p. 28)
"Multistage coupling of independent laser-plasma accelerators"
URL: http://www.nature.com/doifinder/10.1038/nature16525.

[77] L. V. Keldysh. *Soviet Physics JETP*. **20**, pp. 1307–1314. 1965. (see p. 30)
"Ionization in the field of a strong electromagnetic wave"
URL: http://www.jetp.ac.ru/cgi-bin/e/index/e/20/5/p1307?a=list.

[78] A. M. Perelomov, V. S. Popov, and M. Terent'ev. *Soviet Physics JETP*. **23**, p. 924. 1966. (see p. 30)
"Ionization of atoms in an alternating electrical field"
URL: http://www.jetp.ac.ru/cgi-bin/e/index/e/23/5/p924?a=list.

[79] H. R. Reiss. *Physical Review A*. **1**, p. 803. 1970. (see p. 30)
"Semiclassical Electrodynamics of Bound Systems in Intense Fields"
DOI: 10.1017/CBO9781107415324.004.

[80] S Augst *et al*. *Physical Review Letters*. **63**, pp. 2212–2215. 1989. (see p. 31)
"Tunneling ionization of noble gases in a high-intensity laser field."
URL: http://journals.aps.org/prl/abstract/10.1103/PhysRevLett.63.2212.

[81] J. D. Jackson. *Classical Electrodynamics*. John Wiley and Sons, 1998. (see p. 32).

[82] T. Kibble and F. Berkshire. *Classical Mechanics*. Imperial College Press, 2004. (see pp. 32, 178).

[83] P. Gibbon. *Short Pulse Laser Interactions with Matter*. Imperial College Press, 2005. (see pp. 33, 238).

[84] J. N. Bardsley, B. M. Penetrante, and M. H. Mittleman. *Physical Review A*. **40**, pp. 3823–3835. 1989. (see p. 33)
"Relativistic dynamics of electrons in intense laser fields"
DOI: 10.1103/PhysRevA.40.3823.

[85] B. Quesnel and P. Mora. *Physical Review E*. **58**, pp. 3719–3732. 1998. (see p. 35)
"Theory and simulation of the interaction of ultraintense laser pulses with electrons in vacuum"
DOI: 10.1103/PhysRevE.58.3719.

[86] E. A. Startsev and C. J. McKinstrie. *Physical Review E*. **55**, pp. 7527–7535. 1997. (see p. 35)
"Multiple scale derivation of the relativistic ponderomotive force"
DOI: 10.1103/PhysRevE.55.7527.

[87] W. L. Kruer. *The Physics of laser plasma interactions*. Westview Press, 1987. (see p. 35).

[88] H. A. H. Boot and R. B. Harvie. *Nature*. **180**, p. 1187. 1957. (see p. 35)
"Charged particles in a non-uniform radio-frequency field"
DOI: doi:10.1038/1801187a0.

[89] E. N. Nerush and I. Kostyukov. *Physical Review Letters*. **103**, p. 035001. 2009. (see p. 36)
"Carrier-Envelope Phase Effects in Plasma-Based Electron Acceleration with Few-Cycle Laser Pulses"
DOI: 10.1103/PhysRevLett.103.035001.

[90] P. Bellan. *Fundamentals of Plasma Physics*. Cambridge University Press, 2008. (see pp. 37, 238).

[91] J. M. Dawson. *Physical Review*. **113**, pp. 383–387. 1959. (see pp. 38, 44)
"Nonlinear electron oscillations in a cold plasma"
DOI: 10.1103/PhysRev.113.383.

[92] A. I. Akhiezer and R. V. Polovin. *JETP Letters*. **3**, pp. 696–705. 1959. (see p. 39)
"Theory of Wave Motion of an Electron Plasma"
URL: http://www.jetp.ac.ru/cgi-bin/e/index/e/3/5/p696?a=list.

[93] T. Katsouleas and W. B. Mori. *Physical Review Letters*. **61**, pp. 90–93. 1988. (see p. 39)
"Wave-Breaking Amplitude of Relativistic Oscillations in a Thermal Plasma"
URL: http://link.aps.org/doi/10.1103/PhysRevLett.61.90.

[94] W. K. H. Panofsky and W. A. Wenzel. *Review of Scientific Instruments*. **27**, p. 967. 1956. (see p. 43)
"Some considerations concerning the transverse deflection of charged particles in radio-frequency fields"
DOI: 10.1063/1.1715427.

[95] R. Keinigs and M. E. Jones. *Physics of Fluids*. **30**, p. 252. 1987. (see p. 43)
"Two-dimensional dynamics of the plasma wakefield accelerator"
URL: http://scitation.aip.org/content/aip/journal/pof1/30/1/10.1063/1.866183.

[96] P Sprangle, E Esarey, and A Ting. *Physical Review Letters*. **64**, pp. 2011–2014. 1990. (see pp. 44, 47, 55, 58, 130, 244)
"Nonlinear theory of intense laser-plasma interactions"
URL: http://link.aps.org/doi/10.1103/PhysRevLett.64.2011.

[97] P Sprangle, E Esarey, and A Ting. *Physical Review A*. **41**. 1990. (see pp. 44, 130, 136)
"Nonlinear interaction of intense laser pulses in plasmas"
URL: http://journals.aps.org/pra/abstract/10.1103/PhysRevA.41.4463.

[98] S. V. Bulanov, V. I. Kirsanov, and A. S. Sakharov. *JETP Letters*. **50**, pp. 176–178. 1989. (see p. 44)
"Excitation of ultrarelativistic plasma waves by pulse of electromagnetic radiation"
URL: http://adsabs.harvard.edu/abs/1989ZhPmR..50..176B.

[99] F. S. Tsung *et al.* *Physical Review Letters*. **93**, p. 185002. 2004. (see pp. 44, 159)
"Near-GeV-Energy Laser-Wakefield Acceleration of Self-Injected Electrons in a Centimeter-Scale Plasma Channel"
URL: http://link.aps.org/doi/10.1103/PhysRevLett.93.185002.

[100] W. Lu *et al.* *Physical Review Letters*. **96**, p. 165002. 2006. (see p. 45)
"Nonlinear Theory for Relativistic Plasma Wakefields in the Blowout Regime"
URL: http://link.aps.org/doi/10.1103/PhysRevLett.96.165002.

[101] W. Lu *et al.* *Physics of Plasmas*. **13**, p. 056709. 2006. (see pp. 45, 46, 55)
"A nonlinear theory for multidimensional relativistic plasma wave wakefields"
URL: http://scitation.aip.org/content/aip/journal/pop/13/5/10.1063/1.2203364.

[102] Y. R. Shen. *The Principles of nonlinear optics*. Wiley, 1984. (see p. 47).

[103] W. B. Mori. *IEEE Journal of Quantum Electronics*. **33**, pp. 1942–1953. 1997. (see pp. 47, 48)
"The physics of the nonlinear optics of plasmas at relativistic intensities for short-pulse lasers"
URL: http://ieeexplore.ieee.org/lpdocs/epic03/wrapper.htm?arnumber=641309.

[104] J. T. Mendonça. *Theory of photon acceleration*. Institute of Physics Publishing, 2001. (see p. 48).

[105] J. Faure *et al.* *Physical Review Letters*. **95**, p. 205003. 2005. (see p. 49)
"Observation of Laser-Pulse Shortening in Nonlinear Plasma Waves"
URL: http://link.aps.org/doi/10.1103/PhysRevLett.95.205003.

[106] J. Schreiber *et al.* *Physical Review Letters*. **105**, p. 235003. 2010. (see pp. 49, 136)
"Complete Temporal Characterization of Asymmetric Pulse Compression in a Laser Wakefield"
URL: http://link.aps.org/doi/10.1103/PhysRevLett.105.235003.

[107] E. Hecht. *Optics*. 4th ed. Addison Wesley, 2002. (see p. 49).

[108] A. Zigler *et al.* *Journal of the Optical Society of America B*. **13**, p. 68. 1996. (see p. 51)
"Optical guiding of high-intensity laser pulses in a long plasma channel formed by a slow capillary discharge"
URL: http://www.opticsinfobase.org/abstract.cfm?URI=josab-13-1-68.

[109] P. Sprangle, C.-M. Tang, and E. Esarey. *IEEE Transactions on Plasma Science*. **15**, pp. 145–153. 1987. (see pp. 52, 127, 129)
"Relativistic Self-Focusing of Short-Pulse Radiation Beams in Plasmas"
URL: http://ieeexplore.ieee.org/lpdocs/epic03/wrapper.htm?arnumber=4316677.

[110] A. G. R. Thomas *et al.* *Physical Review Letters*. **98**, p. 095004. 2007. (see pp. 52, 126, 127, 129)
"Effect of Laser-Focusing Conditions on Propagation and Monoenergetic Electron Production in Laser-Wakefield Accelerators"
URL: http://link.aps.org/doi/10.1103/PhysRevLett.98.095004.

[111] T. P. Wangler. *RF Linear Accelerators*, p. 284. Wiley, 2008. (see p. 55).

[112] C. Decker and W. B. Mori. *Physical Review Letters*. **72**, pp. 490–493. 1994. (see p. 56)
"Group velocity of large amplitude electromagnetic waves in a plasma"
URL: http://link.aps.org/doi/10.1103/PhysRevLett.72.490.

[113] C. D. Decker *et al.* *Physics of Plasmas*. **3**, p. 2047. 1996. (see pp. 56, 58, 136, 229)
"The evolution of ultra-intense, short-pulse lasers in underdense plasmas"
URL: http://scitation.aip.org/content/aip/journal/pop/3/5/10.1063/1.872001.

[114] B. A. Shadwick, C. B. Schroeder, and E. Esarey. *Physics of Plasmas*. **16**, p. 056704. 2009. (see p. 58)
"Nonlinear laser energy depletion in laser-plasma accelerators"
URL: http://scitation.aip.org/content/aip/journal/pop/16/5/10.1063/1.3124185.

[115] E. Esarey and M. Pilloff. *Physics of Plasmas*. **2**, p. 1432. 1995. (see pp. 59, 64)
"Trapping and acceleration in nonlinear plasma waves"
DOI: 10.1063/1.871358.

[116] S. P. D. Mangles *et al.* *IEEE Transactions on Plasma Science*. **36**, pp. 1715–1721. 2008. (see p. 60)
"Self-Guided Wakefield Experiments Driven by Petawatt-Class Ultrashort Laser Pulses"
URL: http://ieeexplore.ieee.org/lpdocs/epic03/wrapper.htm?arnumber=4599096.

[117] S. Kneip *et al.* *Physical Review Letters*. **103**, p. 035002. 2009. (see pp. 62, 66, 67, 115, 130, 182)
"Near-GeV Acceleration of Electrons by a Nonlinear Plasma Wave Driven by a Self-Guided Laser Pulse"
URL: http://link.aps.org/doi/10.1103/PhysRevLett.103.035002.

[118] I. Kostyukov, A. Pukhov, and S. Kiselev. *Physics of Plasmas*. **11**, p. 5256. 2004. (see pp. 65, 178)
"Phenomenological theory of laser-plasma interaction in bubble regime"
URL: http://scitation.aip.org/content/aip/journal/pop/11/11/10.1063/1.1799371.

[119] A. G. R. Thomas. *Physics of Plasmas*. **17**, p. 056708. 2010. (see pp. 65, 163, 178–180, 229)
"Scalings for radiation from plasma bubbles"
URL: http://scitation.aip.org/content/aip/journal/pop/17/5/10.1063/1.3368678.

[120] S. P. D. Mangles *et al.* *Physical Review Special Topics - Accelerators and Beams*. **15**, pp. 2–7. 2012. (see pp. 66, 68, 203, 216)
"Self-injection threshold in self-guided laser wakefield accelerators"
URL: http://link.aps.org/doi/10.1103/PhysRevSTAB.15.011302.

[121] S. A. Yi *et al.* *Plasma Physics and Controlled Fusion*. **53**. 2011. (see p. 66)
"Hamiltonian analysis of electron self-injection and acceleration into an evolving plasma bubble"
DOI: 10.1088/0741-3335/53/1/014012.

[122] M. R. Islam *et al.* *New Journal of Physics*. **17**, p. 93033. 2015. (see pp. 67, 163)
"Near-threshold electron injection in the laser-plasma wakefield accelerator leading to femtosecond bunches"
URL: http://dx.doi.org/10.1088/1367-2630/17/9/093033.

[123] M. Chen *et al.* *Physics of Plasmas*. **19**, p. 033101. 2012. (see pp. 68, 167)
"Theory of ionization-induced trapping in laser-plasma accelerators"
URL: http://scitation.aip.org/content/aip/journal/pop/19/3/10.1063/1.3689922.

[124] A. Pak *et al.* *Physical Review Letters*. **104**, p. 025003. 2010. (see pp. 68, 163, 166)
"Injection and Trapping of Tunnel-Ionized Electrons into Laser-Produced Wakes"
URL: http://link.aps.org/doi/10.1103/PhysRevLett.104.025003.

[125] J. E. Leiss. *IEEE Transactions on Nuclear Science*, p. 566. 1965. (see p. 69)
"Beam loading in linear accelerators".

[126] T. Katsouleas *et al.* *Particle Accelerators*. **22**. 1987. (see pp. 69, 71)
"Beam Loading in Plasma Accelerators"
URL: https://cds.cern.ch/record/898463/files/p81.pdf.

[127] S. Wilks *et al.* *IEEE Transactions on Plasma Science*. **15**, pp. 210–217. 1987. (see pp. 69, 70)
"Beam loading in plasma waves"
DOI: http://dx.doi.org/10.1109/TPS.1987.4316687.

[128] M. Tzoufras *et al.* *Physical Review Letters*. **101**, p. 145002. 2008. (see p. 71)
"Beam Loading in the Nonlinear Regime of Plasma-Based Acceleration"
URL: http://link.aps.org/doi/10.1103/PhysRevLett.101.145002.

[129] M. Tzoufras *et al.* *Physics of Plasmas*. **16**, p. 056705. 2009. (see pp. 71, 72)
"Beam loading by electrons in nonlinear plasma wakes"
URL: http://scitation.aip.org/content/aip/journal/pop/16/5/10.1063/1.3118628.

[130] T. H. Maiman. *Nature*. **187**, pp. 493–494. 1960. (see pp. 73, 74)
"Stimulated Optical Radiation in Ruby"
DOI: 10.1038/187493a0.

[131] C. H. Townes. "The first laser". In: *A Century of Nature: Twenty-One Discoveries that Changed Science and the World*. Ed. by L. Garwin and T. Lincoln. University of Chicago Press, 2004, pp. 105–119 (see p. 73).

[132] O. A. Hurricane *et al.* *Nature*. **506**, pp. 343–8. 2014. (see p. 74)
"Fuel gain exceeding unity in an inertially confined fusion implosion."
URL: http://www.nature.com/nature/journal/v506/n7488/full/nature13008.html.

[133] R. F. Smith *et al.* *Nature*. **511**, pp. 330–333. 2014. (see p. 74)
"Ramp compression of diamond to five terapascals"
URL: http://www.nature.com/nature/journal/v511/n7509/full/nature13526.html.

[134] M. Dunne. *Science*. **213**, pp. 374–377. 2006. (see p. 74)
"Laser-Driven Particle Accelerators"
URL: http://science.sciencemag.org/content/312/5772/374.

[135] A Einstein. *Physikalische Zeitschrift*. **18**, pp. 121–128. 1917. (see p. 74)
"On the quantum theory of radiation".

[136] D. Kleppner. *Physical Review Letters*. **47**, pp. 233–236. 1981. (see p. 74)
"Inhibited spontaneous emission"
DOI: 10.1103/PhysRevLett.47.233.

[137] A. Siegman. *Lasers*. University Science Books, 1990. (see pp. 74, 82).

[138] J. D. Sethian *et al.* *Physics of Plasmas*. **10**, p. 2142. 2003. (see p. 74)
"Electron beam pumped KrF lasers for fusion energy"
URL: http://scitation.aip.org/content/aip/journal/pop/10/5/10.1063/1.1564082.

[139] J. Tulip and H. Seguin. *Applied Physics Letters*. **19**, p. 263. 1971. (see p. 74)
"Explosion-Pumped Gas-Dynamic CO2 Laser"
URL: http://scitation.aip.org/content/aip/journal/apl/19/8/10.1063/1.1653911.

[140] S. Banerjee *et al.* *Optics Letters*. **37**, p. 2175. 2012. (see p. 74)
"High-efficiency 10 J diode pumped cryogenic gas cooled Yb:YAG multislab amplifier"
URL: https://www.osapublishing.org/abstract.cfm?URI=ol-37-12-2175.

[141] F. J. McClung and R. W. Hellwarth. *Journal of Applied Physics*. **33**, pp. 828–829. 1962. (see p. 74)
"Giant optical pulsations from ruby"
URL: http://scitation.aip.org/content/aip/journal/jap/33/3/10.1063/1.1777174.

[142] S. Hooker and C. Webb. *Laser Physics*. Oxford University Press, 2010. (see pp. 75, 81, 82).

[143] D. E. Spence, P. N. Kean, and W Sibbett. *Optics Letters*. **16**, pp. 42–4. 1991. (see p. 76)
"60-fsec pulse generation from a self-mode-locked Ti:sapphire laser."
DOI: 10.1364/OL.16.000042.

[144] L. Cohen. *Time-Frequency analysis*. Prentice Hall, 1995. (see pp. 76, 78).

[145] C. Iaconis and I. A. Walmsley. *IEEE Journal of Quantum Electronics*. **35**, pp. 501–509. 1999. (see p. 76)
"Self-referencing spectral interferometry for measuring ultrashort optical pulses"
URL: http://ieeexplore.ieee.org/lpdocs/epic03/wrapper.htm?arnumber=753654.

[146] A. Monmayrant, S. Weber, and B. Chatel. *Journal of Physics B: Atomic, Molecular and Optical Physics*. **43**, p. 103001. 2010. (see p. 77)
"A newcomer's guide to ultrashort pulse shaping and characterization"
URL: http://iopscience.iop.org/article/10.1088/0953-4075/43/10/103001/meta.

[147] R. Bracewell. *The Fourier transform and its applications*. McGraw-Hill Higher Education, 2000. (see p. 77).

[148] J. Diels and W. Rudolph. *Ultrashort Laser Pulse Phenomena*. Academic Press, 2006. (see p. 78).

[149] D Strickland and G Mourou. *Optics Communications*. **56**, pp. 219–221. 1985. (see p. 78)
"Compression of amplified chirped optical pulses"
URL: http://www.sciencedirect.com/science/article/pii/0030401885901518.

[150] P. Maine *et al.* *IEEE Journal of Quantum Electronics*. **24**, pp. 398–403. 1988. (see p. 78)
"Generation of ultrahigh peak power pulses by chirped pulse amplification"
URL: http://ieeexplore.ieee.org/lpdocs/epic03/wrapper.htm?arnumber=137.

[151] STFC. *Astra Gemini laser system*. URL: http://www.clf.stfc.ac.uk/CLF/Facilities/Astra/12254.aspx (visited on 05/10/2016) (see p. 79).

[152] C.J. Hooker *et al.* *J. Phys. IV France*. **133**, pp. 673–677. 2006. (see p. 79)
"The Astra Gemini project A dual-beam petawatt Ti:Sapphire laser system"
URL: http://dx.doi.org/10.1051/jp4:2006133135.

[153] E. J. Divall. *Central Laser Facility Annual Report*. 2008. (see p. 79)
"Laser performance analysis tool"
URL: http://www.clf.stfc.ac.uk/resources/PDF/ar07-08_s7_laser_performance_data_analysis.pdf.

[154] V. Yanovsky *et al.* *Opt. Express*. **16**, pp. 2109–2114. 2008. (see p. 79)
"Ultra-high intensity- 300-TW laser at 0.1 Hz repetition rate."
URL: http://www.opticsexpress.org/abstract.cfm?URI=oe-16-3-2109.

[155] S Feng and H. G. Winful. *Optics letters*. **26**, pp. 485–7. 2001. (see p. 82)
"Physical origin of the Gouy phase shift."
URL: https://www.osapublishing.org/ol/abstract.cfm?uri=ol-26-8-485.

[156] M. Born and E. Wolf. *Principles of Optics: Electromagnetic Theory of Propagation, Interference and Diffraction of Light*. Cambridge University Press, 1999. (see pp. 83, 246).

[157] S. P. D. Mangles *et al.* *Applied Physics Letters*. **95**, p. 181106. 2009. (see p. 84)
"Controlling the spectrum of x-rays generated in a laser-plasma accelerator by tailoring the laser wavefront"
URL: http://scitation.aip.org/content/aip/journal/apl/95/18/10.1063/1.3258022.

[158] G. Genoud *et al.* *Physics of Plasmas*. **20**, p. 064501. 2013. (see pp. 84, 124)
"Increasing energy coupling into plasma waves by tailoring the laser radial focal spot distribution in a laser wakefield accelerator"
URL: http://scitation.aip.org/content/aip/journal/pop/20/6/10.1063/1.4810795.

[159] A. Buck *et al.* *Nature Physics*. **7**, pp. 543–548. 2011. (see p. 85)
"Real-time observation of laser-driven electron acceleration"
URL: http://www.nature.com/doifinder/10.1038/nphys1942.

[160] Andor. *Andor Ixon-Ultra 888*. URL: http://www.andor.com/scientific-cameras/ixon-emccd-camera-series/ixon-ultra-888 (visited on 12/11/2016) (see p. 88).

[161] Andor. *Andor Shamrock 303i*. URL: http://www.andor.com/spectrograph/shamrock-spectrograph-series/shamrock-303i (visited on 12/11/2016) (see p. 88).

[162] P. Instruments. *SpectraPro*. URL: http://www.princetoninstruments.com/products/SpectraPro (visited on 12/11/2016) (see p. 88).

[163] Gentec. *Energy detectors*. URL: https://www.gentec-eo.com/products/energy-detectors/QE25 (visited on 12/11/2016) (see p. 89).

[164] I. A. Walmsley and C. Dorrer. *Advances in Optics and Photonics*. **1**, p. 308. 2009. (see p. 89)
"Characterization of ultrashort electromagnetic pulses"
URL: http://www.opticsinfobase.org/abstract.cfm?URI=aop-1-2-308.

[165] F Salin *et al.* *Applied optics*. **26**, pp. 4528–31. 1987. (see p. 89)
"Single-shot measurement of a 52-fs pulse."
URL: http://www.ncbi.nlm.nih.gov/pubmed/20523397.

[166] D. J. Kane and R. Trebino. *Optics letters*. **18**, pp. 823–5. 1993. (see p. 90)
"Single-shot measurement of the intensity and phase of an arbitrary ultrashort pulse by using frequency-resolved optical gating."
URL: https://www.osapublishing.org/ol/abstract.cfm?id=11717.

[167] R. Trebino *et al.* *Review of Scientific Instruments*. **68**, pp. 3277–3295. 1997. (see p. 90)
"Measuring ultrashort laser pulses in the time-frequency domain using frequency-resolved optical gating"
DOI: 10.1063/1.1148286.

[168] C. Iaconis and I. A. Walmsley. *Optics letters*. **23**, pp. 792–4. 1998. (see p. 90)
"Spectral phase interferometry for direct electric-field reconstruction of ultrashort optical pulses."
URL: http://www.ncbi.nlm.nih.gov/pubmed/18087344.

[169] T. Witting *et al. Optics letters*. **36**, pp. 1680–2. 2011. (see pp. 90, 187)
"Characterization of high-intensity sub-4-fs laser pulses using spatially encoded spectral shearing interferometry."
URL: https://www.osapublishing.org/ol/abstract.cfm?uri=ol-36-9-1680.

[170] F. Chen. *Introduction to Plasma Physics and Controlled Fusion*. Springer, 1984. (see pp. 91, 240).

[171] H. M. Ltd. *GM08 Gaussmeter*. URL: http://www.hirst-magnetics.com/instruments/gm08_p1.shtml (visited on 06/20/2016) (see p. 92).

[172] J. Dormand and P. Prince. *Journal of Computational and Applied Mathematics*. **6**, pp. 19 –26. 1980. (see p. 93)
"A family of embedded Runge-Kutta formulae"
URL: http://www.sciencedirect.com/science/article/pii/0771050X80900133.

[173] L. F. Shampine and M. W. Reichelt. *SIAM Journal on Scientific Computing*. **18**, pp. 1–22. 1997. (see p. 93)
"The MATLAB ODE Suite"
URL: http://dx.doi.org/10.1137/S1064827594276424.

[174] H. J. Cha *et al. Review of Scientific Instruments*. **83**, p. 063301. 2012. (see p. 96)
"Absolute energy calibration for relativistic electron beams with pointing instability from a laser-plasma accelerator."
URL: http://www.ncbi.nlm.nih.gov/pubmed/22755616.

[175] A. A. Soloviev *et al. Review of Scientific Instruments*. **82**, p. 043304. 2011. (see p. 96)
"Two-screen single-shot electron spectrometer for laser wakefield accelerated electron beams"
URL: http://scitation.aip.org/content/aip/journal/rsi/82/4/10.1063/1.3585862.

[176] J. C. Wood. private communication (see pp. 98, 99).

[177] A Buck *et al. Review of Scientific Instruments*. **81**, p. 033301. 2010. (see pp. 98, 99)
"Absolute charge calibration of scintillating screens for relativistic electron detection."
URL: http://scitation.aip.org/content/aip/journal/rsi/81/3/10.1063/1.3310275.

[178] Y. Glinec *et al. Review of Scientific Instruments*. **77**, p. 103301. 2006. (see pp. 99, 224)
"Absolute calibration for a broad range single shot electron spectrometer"
URL: http://scitation.aip.org/content/aip/journal/rsi/77/10/10.1063/1.2360988.

[179] N. Kotera *et al. Method of and apparatus for reading out a radiation image recorded in a stimulable phosphor*. US Patent 4,258,264. 1981. URL: https://www.google.com/patents/US4258264 (see p. 99).

[180] H. von Seggern *et al. Journal of Applied Physics*. **64**, pp. 1405–1412. 1988. (see p. 99)
"Physical model of photostimulated luminescence of x-ray irradiated BaFBr:Eu2+"
DOI: 10.1063/1.341838.

[181] B. Hidding *et al. Review of Scientific Instruments*. **78**, p. 083301. 2007. (see p. 99)
"Novel method for characterizing relativistic electron beams in a harsh laser-plasma environment"
URL: http://scitation.aip.org/content/aip/journal/rsi/78/8/10.1063/1.2775668.

[182] K. Zeil *et al. Review of Scientific Instruments*. **81**, p. 013307. 2010. (see p. 99)
"Absolute response of Fuji imaging plate detectors to picosecond-electron bunches"
URL: http://scitation.aip.org/content/aip/journal/rsi/81/1/10.1063/1.3284524.

[183] S. Masuda *et al. Review of Scientific Instruments*. **79**, p. 083301. 2008. (see p. 99)
"Absolute calibration of an electron spectrometer using high energy electrons produced by the laser-plasma interaction"
URL: http://scitation.aip.org/content/aip/journal/rsi/79/8/10.1063/1.2969655.

[184] K. A. Tanaka *et al. Review of Scientific Instruments*. **76**, p. 13507. 2005. (see p. 99)
"Calibration of imaging plate for high energy electron spectrometer"
URL: http://scitation.aip.org/content/aip/journal/rsi/76/1/10.1063/1.1824371.

[185] T. Scheimpflug. *Improved Method and apparatus for the Systematic Alteration or Distortion of Plane Pictures and Images by Means of Lenses and Mirrors for Photography and for other purposes*. 1904. URL: http://www.trenholm.org/hmmerk/TSBP.pdf (see p. 100).

[186] H. D. Zhang *et al. Physical Review Special Topics - Accelerators and Beams*. **15**, p. 072803. 2012. (see p. 100)
"Beam halo imaging with a digital optical mask"
URL: http://link.aps.org/doi/10.1103/PhysRevSTAB.15.072803.

[187] S. Semushin and V. Malka. *Review of Scientific Instruments*. **72**, p. 2961. 2001. (see p. 101)
"High density gas jet nozzle design for laser target production"
URL: http://scitation.aip.org/content/aip/journal/rsi/72/7/10.1063/1.1380393.

[188] Peter-Paul Electronics Co., Inc. *2-way, normally-closed solenoid*. URL: https://peterpaul.com/valves/2-way-normally-closed/series-20-model-eh22 (visited on 06/21/2016) (see p. 102).

[189] R. Weingartner *et al*. *Physical Review Special Topics - Accelerators and Beams*. **15**, p. 111302. 2012. (see p. 103)
"Ultralow emittance electron beams from a laser-wakefield accelerator"
URL: http://link.aps.org/doi/10.1103/PhysRevSTAB.15.111302.

[190] A. Martinez de la Ossa *et al*. *Physical Review Letters*. **111**, p. 245003. 2013. (see p. 103)
"High-Quality Electron Beams from Beam-Driven Plasma Accelerators by Wakefield-Induced Ionization Injection"
URL: http://link.aps.org/doi/10.1103/PhysRevLett.111.245003.

[191] A. J. Gonsalves *et al*. *Nature Physics*. **7**, pp. 862–866. 2011. (see p. 103)
"Tunable laser plasma accelerator based on longitudinal density tailoring"
URL: http://www.nature.com/doifinder/10.1038/nphys2071.

[192] G. S. Settles. *Schlieren and Shadowgraph Techniques*, p. 29. 2nd ed. Springer, 2006. (see p. 106).

[193] V. Malka *et al*. *Review of Scientific Instruments*. **71**, p. 2329. 2000. (see p. 106)
"Characterization of neutral density profile in a wide range of pressure of cylindrical pulsed gas jets"
URL: http://scitation.aip.org/content/aip/journal/rsi/71/6/10.1063/1.1150619.

[194] B. Fryxell *et al*. *The Astrophysical Journal Supplement Series*. **131**, pp. 273–334. 2000. (see p. 107)
"FLASH: An Adaptive Mesh Hydrodynamics Code for Modeling Astrophysical Thermonuclear Flashes"
DOI: 10.1086/317361.

[195] P. Woodward and P. Colella. *Journal of Computational Physics*. **54**, pp. 115–173. 1984. (see p. 107)
"The numerical simulation of two-dimensional fluid flow with strong shocks"
DOI: 10.1016/0021-9991(84)90142-6.

[196] J. Dawson. *Reviews of Modern Physics*. **55**, pp. 403–447. 1983. (see p. 111)
"Particle simulation of plasmas"
URL: http://link.aps.org/doi/10.1103/RevModPhys.55.403.

[197] N. Jain, T. M. Antonsen, and J. Palastro. *Physical Review Letters*. **115**, p. 195001. 2015. (see p. 111)
"Positron Acceleration by Plasma Wakefields Driven by a Hollow Electron Beam"
URL: http://link.aps.org/doi/10.1103/PhysRevLett.115.195001.

[198] Kane Yee. *IEEE Transactions on Antennas and Propagation*. **14**, pp. 302–307. 1966. (see p. 111)
"Numerical solution of initial boundary value problems involving maxwell's equations in isotropic media"
URL: http://ieeexplore.ieee.org/lpdocs/epic03/wrapper.htm?arnumber=1138693.

[199] J. P. Boris. "Relativistic plasma simulation-optimization of a hybrid code". In: *Proceedings of the 4th Conference on Numerical Simulation of Plasmas*. 1970, pp. 3–67 (see p. 111).

[200] F. Fiuza *et al*. *Record simulations conducted on Lawrence Livermore supercomputer*. URL: https://www.llnl.gov/news/record-simulations-conducted-lawrence-livermore-supercomputer (visited on 06/23/2016) (see p. 112).

[201] R. Courant, K. Friedrichs, and H. Lewy. *IBM Journal of Research and Development*. **11**, pp. 215–234. 1967. (see p. 112)
"On the Partial Difference Equations of Mathematical Physics"
DOI: 10.1147/rd.112.0215.

[202] S. C. Rae. *Optics Communications*. **97**, pp. 25–28. 1993. (see p. 113)
"Ionization-induced defocusing of intense laser pulses in high-pressure gases"
DOI: 10.1016/0030-4018(93)90611-8.

[203] S. Wilks, J. Dawson, and W. B. Mori. *Physical Review Letters*. **61**, pp. 337–341. 1988. (see pp. 113, 119, 167)
"Frequency up-conversion of electromagnetic radiation with use of an overdense plasma"
URL: http://link.aps.org/doi/10.1103/PhysRevLett.61.337.

[204] T. P. Rowlands-Rees *et al*. *Physical Review Letters*. **100**, p. 105005. 2008. (see p. 113)
"Laser-Driven Acceleration of Electrons in a Partially Ionized Plasma Channel"
URL: http://link.aps.org/doi/10.1103/PhysRevLett.100.105005.

[205] C. McGuffey *et al*. *Physical Review Letters*. **104**, p. 025004. 2010. (see pp. 113, 166, 173, 180, 181)
"Ionization Induced Trapping in a Laser Wakefield Accelerator"
URL: http://link.aps.org/doi/10.1103/PhysRevLett.104.025004.

[206] T. D. Arber *et al. Plasma Physics and Controlled Fusion*. **57**, p. 113001. 2015. (see p. 113)
"Contemporary particle-in-cell approach to laser-plasma modelling"
URL: http://dx.doi.org/10.1088/0741-3335/57/11/113001.

[207] C. P. Ridgers *et al. Journal of Computational Physics*. **260**, pp. 273–285. 2014. (see p. 113)
"Modelling gamma-ray photon emission and pair production in high-intensity lasermatter interactions"
URL: http://www.sciencedirect.com/science/article/pii/S0021999113008061.

[208] P. A. Jaanimagi. *SPIE Proceedings*. **5194**, pp. 171–182. 2004. (see p. 114)
"Breaking the 100-fs barrier with a streak camera"
URL: http://dx.doi.org/10.1117/12.512747.

[209] N. E. Andreev and M. V. Chegotov. *Journal of Experimental and Theoretical Physics*. **101**, pp. 56–63. 2005. (see pp. 115, 124, 228)
"Wakefield generation as the mechanism behind spectral shift of a short laser pulse"
URL: http://link.springer.com/10.1134/1.2010661.

[210] F. Wojda *et al. Physical Review E*. **80**, p. 066403. 2009. (see pp. 115, 124)
"Laser-driven plasma waves in capillary tubes"
URL: http://link.aps.org/doi/10.1103/PhysRevE.80.066403.

[211] N. E. Andreev *et al. New Journal of Physics*. **12**, p. 045024. 2010. (see p. 115)
"Analysis of laser wakefield dynamics in capillary tubes"
URL: http://iopscience.iop.org/article/10.1088/1367-2630/12/4/045024/meta.

[212] S. Shiraishi *et al. Physics of Plasmas*. **20**, p. 063103. 2013. (see pp. 115, 124, 228)
"Laser red shifting based characterization of wakefield excitation in a laser-plasma accelerator"
URL: http://scitation.aip.org/content/aip/journal/pop/20/6/10.1063/1.4810802.

[213] S. C. Wilks *et al. Physical Review Letters*. **62**, pp. 2600–2603. 1989. (see p. 115)
"Photon accelerator"
URL: http://link.aps.org/doi/10.1103/PhysRevLett.62.2600.

[214] L. Silva *et al. IEEE Transactions on Plasma Science*. **28**, pp. 1128–1134. 2000. (see p. 115)
"Photon kinetics for laser-plasma interactions"
URL: http://ieeexplore.ieee.org/lpdocs/epic03/wrapper.htm?arnumber=893299.

[215] C. D. Murphy *et al. Physics of Plasmas*. **13**, p. 033108. 2006. (see p. 115)
"Evidence of photon acceleration by laser wake fields"
URL: http://scitation.aip.org/content/aip/journal/pop/13/3/10.1063/1.2178650.

[216] C. B. Schroeder *et al. Physics of Plasmas*. **10**, p. 2039. 2003. (see p. 116)
"Frequency chirp and pulse shape effects in self-modulated laser wakefield accelerators"
URL: http://scitation.aip.org/content/aip/journal/pop/10/5/10.1063/1.1560614.

[217] A. G. Khachatryan, F. A. Van Goor, and K. J. Boller. *Physical Review E*. **70**, pp. 13–16. 2004. (see p. 116)
"Interaction of free charged particles with a chirped electromagnetic pulse"
DOI: 10.1103/PhysRevE.70.067601.

[218] V. B. Pathak *et al. New Journal of Physics*. **14**, p. 023057. 2012. (see pp. 116, 131, 137)
"Effect of the frequency chirp on laser wakefield acceleration"
URL: http://iopscience.iop.org/article/10.1088/1367-2630/14/2/023057/meta.

[219] S. Y. Kalmykov *et al. New Journal of Physics*. **14**, p. 033025. 2012. (see pp. 116, 131)
"Laser plasma acceleration with a negatively chirped pulse: all-optical control over dark current in the blowout regime"
URL: http://iopscience.iop.org/article/10.1088/1367-2630/14/3/033025/meta.

[220] D VON DER Linde and H Schüler. *JOSA B*. **13**, pp. 216–222. 1996. (see p. 117)
"Breakdown threshold and plasma formation in femtosecond lasersolid interaction"
URL: http://www.opticsinfobase.org/abstract.cfm?id=33682.

[221] P. Tournois. *Optics communications*. **140**, pp. 245–249. 1997. (see p. 117)
"Acousto-optic programmable dispersive filter for adaptive compensation of group delay time dispersion in laser systems"
URL: http://www.sciencedirect.com/science/article/pii/S0030401897001533.

[222] J. Dias *et al. Physical Review Letters*. **78**, pp. 4773–4776. 1997. (see p. 119)
"Experimental evidence of photon acceleration of ultrashort laser pulses in relativistic ionization fronts"
URL: http://link.aps.org/doi/10.1103/PhysRevLett.78.4773.

[223] B. M. Penetrante *et al. Journal of the Optical Society of America B.* **9**, p. 2032. 1992. (see p. 120)
"Ionization-induced frequency shifts in intense femtosecond laser pulses"
URL: http://www.opticsinfobase.org/abstract.cfm?URI=josab-9-11-2032.

[224] J. Paye. *IEEE Journal of Quantum Electronics.* **28**, pp. 2262–2273. 1992. (see p. 122)
"The chronocyclic representation of ultrashort light pulses"
URL: http://ieeexplore.ieee.org/lpdocs/epic03/wrapper.htm?arnumber=159533.

[225] E. Esarey *et al. IEEE Journal of Quantum Electronics.* **33**, pp. 1879–1914. 1997. (see pp. 126, 130)
"Self-focusing and guiding of short laser pulses in ionizing gases and plasmas"
URL: http://ieeexplore.ieee.org/lpdocs/epic03/wrapper.htm?arnumber=641305.

[226] W. P. Leemans *et al. Physical Review Letters.* **89**, p. 174802. 2002. (see pp. 137, 229)
"Electron-Yield Enhancement in a Laser-Wakefield Accelerator Driven by Asymmetric Laser Pulses"
URL: http://link.aps.org/doi/10.1103/PhysRevLett.89.174802.

[227] T. Z. Zhao *et al. Plasma Physics and Controlled Fusion.* **58**, p. 105003. 2016. (see pp. 137, 229)
"Characterization of electrons and x-rays produced using chirped laser pulses in a laser wakefield accelerator"
URL: http://iopscience.iop.org/article/10.1088/0741-3335/58/10/105003/meta.

[228] S. De Silvestri, P Laporta, and O Svelto. *IEEE Journal of Quantum Electronics.* **20**, pp. 533–539. 1984. (see p. 138)
"The role of cavity dispersion in CW mode-locked dye lasers"
URL: http://ieeexplore.ieee.org/document/1072432/.

[229] T. Mehrling *et al. Physical Review Special Topics - Accelerators and Beams.* **15**, p. 111303. 2012. (see p. 141)
"Transverse emittance growth in staged laser-wakefield acceleration"
URL: http://link.aps.org/doi/10.1103/PhysRevSTAB.15.111303.

[230] Allied Vision Technologies. *Stingray F-033 documentation.* URL: https://www.alliedvision.com/en/products/cameras/detail/Stingray/F-033.html (visited on 05/10/2016) (see p. 142).

[231] Edmund Optics. *Mitutoyo 10x NIR.* URL: http://www.edmundoptics.co.uk/microscopy/infinity-corrected-objectives/mitutoyo-nir-nuv-uv-infinity-corrected-objectives/46403/ (visited on 05/10/2016) (see pp. 143, 186).

[232] Z.-H. He *et al. Nature Communications.* **6**, p. 7156. 2015. (see p. 158)
"Coherent control of plasma dynamics"
URL: http://www.nature.com/doifinder/10.1038/ncomms8156.

[233] J. Ferri *et al. Scientific Reports.* **6**, p. 27846. 2016. (see p. 158)
"Effect of experimental laser imperfections on laser wakefield acceleration and betatron source"
URL: http://www.nature.com/articles/srep27846.

[234] B. Beaurepaire *et al. Physical Review X.* **5**, pp. 1–7. 2015. (see p. 158)
"Effect of the laser wave front in a laser-plasma accelerator"
DOI: 10.1103/PhysRevX.5.031012.

[235] F. S. Tsung *et al. Physics of Plasmas.* **13**, p. 056708. 2006. (see pp. 159, 200)
"Simulation of monoenergetic electron generation via laser wakefield accelerators for 525 TW lasers"
URL: http://link.aip.org/link/PHPAEN/v13/i5/p056708/s1{\&}Agg=doi.

[236] S. A. Yi *et al. Physics of Plasmas.* **20**. 2013. (see p. 163)
"Analytic model of electromagnetic fields around a plasma bubble in the blow-out regime"
DOI: 10.1063/1.4775774.

[237] K. Nakajima *et al. Physical Review Special Topics - Accelerators and Beams.* **14**, pp. 1–12. 2011. (see p. 165)
"Operating plasma density issues on large-scale laser-plasma accelerators toward high-energy frontier"
DOI: 10.1103/PhysRevSTAB.14.091301.

[238] M. Z. Mo *et al. Applied Physics Letters.* **102**, p. 134102. 2013. (see pp. 167, 173)
"Generation of 500 MeV–1 GeV energy electrons from laser wakefield acceleration via ionization induced injection using CO2 mixed in He"
URL: http://scitation.aip.org/content/aip/journal/apl/102/13/10.1063/1.4799280.

[239] F. G. Desforges *et al. Physics of Plasmas.* **21**, p. 120703. 2014. (see p. 167)
"Dynamics of ionization-induced electron injection in the high density regime of laser wakefield acceleration"
URL: http://scitation.aip.org/content/aip/journal/pop/21/12/10.1063/1.4903845.

[240] C. Xia *et al. Physics of Plasmas.* **18**, p. 113101. 2011. (see p. 167)
"Effects of self-focusing on tunnel-ionization-induced injection in a laser wakefield accelerator"
URL: http://scitation.aip.org/content/aip/journal/pop/18/11/10.1063/1.3656958.

[241] H. R. Griem. *Principles of Plasma Spectroscopy:* Cambridge University Press, 1997. (see p. 170).

[242] J. Faure. *CERN Yellow Reports*. **1**. 2016. (see p. 175)
"Plasma Injection Schemes for Laser-Plasma Accelerators"
URL: https://cds.cern.ch/record/2203634.

[243] M. Zeng *et al.* *Physics of Plasmas*. **21**, p. 030701. 2014. (see p. 176)
"Self-truncated ionization injection and consequent monoenergetic electron bunches in laser wakefield acceleration"
URL: http://scitation.aip.org/content/aip/journal/pop/21/3/10.1063/1.4868404.

[244] M Mirzaie *et al.* *Scientific Reports*. **5**, p. 14659. 2015. (see p. 176)
"Demonstration of self-truncated ionization injection for GeV electron beams"
URL: http://www.nature.com/articles/srep14659.

[245] A. J. W. Reitsma and D. A. Jaroszynski. *Laser and Particle Beams*. **22**, pp. 1–7. 2004. (see p. 178)
"Coupling of longitudinal and transverse motion of accelerated electrons in laser wakefield acceleration"
DOI: 10.10170S0263034604040054.

[246] G. Sarri *et al.* *Physical Review Letters*. **113**, p. 224801. 2014. (see p. 183)
"Ultrahigh Brilliance Multi-MeV γ-Ray Beams from Nonlinear Relativistic Thomson Scattering"
URL: http://link.aps.org/doi/10.1103/PhysRevLett.113.224801.

[247] G. Sarri *et al.* *Nature Communications*. **6**, pp. 1–11. 2015. (see p. 183)
"Neutral and high-density electron-positron pair plasmas in the laboratory"
URL: http://dx.doi.org/10.1038/ncomms7747.

[248] J. M. Cole *et al.* *Scientific Reports*. **5**, p. 13244. 2015. (see pp. 183, 216)
"Laser-wakefield accelerators as hard x-ray sources for 3D medical imaging of human bone."
URL: http://www.nature.com/srep/2015/150818/srep13244/full/srep13244.html.

[249] J. C. Wood *et al.* *Central Laser Facility Annual Reports*. 2015. (see p. 184)
"Ultrafast Imaging of Laser Driven Shocks using Betatron X-rays from a Laser Wakefield Accelerator"
URL: http://www.clf.stfc.ac.uk/CLF/resources/PDF/ar14-15_High_Intensity_Wood.pdf.

[250] Imagine Optic. *ILAO deformable mirror*. URL: http://www.imagine-optic.com/en/product/ilao (visited on 08/09/2016) (see p. 186).

[251] A. S. Wyatt *et al.* *Optics Letters*. **31**, p. 1914. 2006. (see p. 187)
"Sub-10 fs pulse characterization using spatially encoded arrangement for spectral phase interferometry for direct electric field reconstruction"
URL: https://www.osapublishing.org/abstract.cfm?URI=ol-31-12-1914.

[252] D. E. Cardenas *et al.* *ArXiv e-prints*. 2015. (see p. 194)
"Energy limitation of laser-plasma electron accelerators"
arXiv: 1505.05732 [physics.acc-ph] URL: http://arxiv.org/abs/1505.05732.

[253] S Corde *et al.* *Nature Communications*. **4**, p. 1501. 2013. (see p. 204)
"Observation of longitudinal and transverse self-injections in laser-plasma accelerators"
URL: http://www.nature.com/doifinder/10.1038/ncomms2528.

[254] J. C. Wood. "Betatron radiation from laser wakefield accelerators and its applications". Imperial College London, 2016. (see p. 209).

[255] M. J. V. Streeter. "Ultrafast Dynamics of Relativistic Laser Plasma Interactions". Imperial College London, 2013. (see p. 211).

[256] C. Benedetti *et al.* *Physics of Plasmas*. **20**, p. 103108. 2013. (see p. 211)
"Numerical investigation of electron self-injection in the nonlinear bubble regime"
URL: http://scitation.aip.org/content/aip/journal/pop/20/10/10.1063/1.4824811.

[257] S. P. D. Mangles. *CERN Yellow Reports*. **1**, p. 289. 2016. (see pp. 212, 213, 224)
"An Overview of Recent Progress in LaserWakefield Acceleration Experiments"
URL: https://e-publishing.cern.ch/index.php/CYR/article/view/224.

[258] E. Guillaume *et al.* *Physical Review Letters*. **115**, p. 155002. 2015. (see p. 225)
"Electron Rephasing in a Laser-Wakefield Accelerator"
URL: http://link.aps.org/doi/10.1103/PhysRevLett.115.155002.

[259] C. B. Schroeder *et al.* *Physical Review Special Topics - Accelerators and Beams*. **13**, p. 101301. 2010. (see p. 233)
"Physics considerations for laser-plasma linear colliders"
URL: http://journals.aps.org/prab/abstract/10.1103/PhysRevSTAB.13.101301.

[260] J Vieira *et al.* *Plasma Physics and Controlled Fusion*. **54**, p. 055010. 2012. (see p. 233)
"Influence of realistic parameters on state-of-the-art laser wakefield accelerator experiments"
URL: http://iopscience.iop.org/article/10.1088/0741-3335/54/5/055010/meta.

[261] A. Ting, E. Esarey, and P. Sprangle. *Physics of Fluids B: Plasma Physics*. **2**, p. 1390. 1990. (see p. 244)
"Nonlinear wake-field generation and relativistic focusing of intense laser pulses in plasmas"
URL: http://scitation.aip.org/content/aip/journal/pofb/2/6/10.1063/1.859561.